

Fundamental Understanding of Poly(ether ketone ketone) for High Temperature Laser Sintering

Submitted by

Luiza Benedetti

to the University of Exeter as a thesis for the degree of Doctor of
Philosophy in Engineering, June 2020

This thesis is available for Library use on the understanding that it is copyright material and that no quotation from the thesis may be published without proper acknowledgement.

I certify that all material in this thesis which is not my own work has been identified and that no material has previously been submitted and approved for the award of a degree by this or any other University.

Luiza Benedetti

Abstract

High-Temperature Laser Sintering (HT-LS) is a powder bed fusion technique employed to manufacture polymers with high service temperature, usually above 150 °C. The aerospace, automotive, and medical industries have driven the demand for processing high-performance polymers, as they could offer a lighter and cheaper alternative while maintaining the mechanical and chemical performance required to replace metallic parts in particular environments.

Kepstan 6002 poly(ether ketone ketone) (PEKK) belongs to poly(aryl ether ketone)s (PAEKs) family and has a promising application in LS. The lower melting temperature united to the high glass transition temperature of PEKK (similar to PEK HP3, first commercially available HT-LS grade) enabled processing at lower temperatures whilst maintaining the high-temperature resistance of the polymer. Furthermore, the kinetics of crystallisation of Kepstan 6002 PEKK is very slow, which can assist layer adhesion during LS and improve mechanical properties in Z orientation.

The present research project was developed in collaboration with Arkema. Three different grades of Kepstan 6002 PEKK were selected for initial analyses – HL1327, HL1320, and P12S959a. The powders were characterised for powder size, distribution, morphology, flow, moisture effect, and coalescence behaviour. This screening enabled the selection of HL1327 grade as the most promising for HT-LS application.

The PEKK particle and powder analyses continued with an in-depth study of particle size and shape changes as a function of temperature and coalescence. The study revealed individual particle shrinkage prior to melting, followed by increased growth. The same phenomenon was observed for pairs of particles during coalescence and was attributed to the recovering of elastic deformation of the polymeric chains.

The effect of intrinsic PEKK characteristics was successfully evaluated and quantified in the overall shrinkage in LS. The results identified powder properties as the main factor causing shrinkage of PEKK, as opposed to crystallisation. These results are supported by the powder characterisation developed in previous chapters.

The interaction between material and process was investigated and optimised by testing different combinations of laser parameters and processing temperatures. The resulting properties were monitored regarding mechanical performance, surface topography, porosity, and crystallisation. The optimised PEKK specimens showed excellent mechanical strength (~90 MPa) and modulus, but poor elongation, a common drawback from the LS process.

The combination of fundamental material properties and process optimisation led to the development of a novel route to improve elongation and control the mechanical performance of LS PEKK. The experimental method successfully related cooling time, mechanical properties, and crystallisation of PEKK, and was able to increase elongation at break by 5.4 times. The improvement of elongation at break was attributed to the largely amorphous phase of PEKK when subjected to short cooling times.

Lastly, powder recyclability was investigated from a chemical and physical perspective. PEKK can be reused following additional treatment steps, e.g., sieving. The potential for recyclability is an important remark as the material cost is significantly reduced and therefore preferred over the use of metals for high-performance applications.

"Wonder is the desire for knowledge."

(Saint Thomas Aquinas)

- To mom and dad, who showed me the wonder of life since childhood.

Acknowledgements

I would not have been able to complete this thesis without the help of extraordinary people, which I will dedicate this section, in order to express my deep gratitude.

First of all, I would like to acknowledge the tireless and wonderful work of my supervisor, professor Oana Ghita, who dedicated countless hours of her time to guide, assist and supervise me and this research project. Her example of work discipline, dedication, and passion for the field is an inspiration for my personal and professional development, and will surely make an impact throughout the rest of my life. I would also like to thank professor Ken Evans for the co-supervision, ideas, and questions, which made my research time more interesting and definitely more academic. I am grateful for the opportunity to start and successfully accomplish this research whilst being supervised by these brilliant minds. It was a pleasure to work with you!

This Ph.D. would not be possible without the sponsorship of Arkema and the support of Benoit Brulé and Nadine Decreamer, who were always available to meet and provide interesting insights to successfully develop this work. They have my deep gratitude for relying on my work and sharing my enthusiasm with this research.

My daily work would not be the same without the incredible colleagues and friends, which I was able to meet at ETG/CALM. I would like to thank Richard Davies for the training, advice and company, and his willingness to work outside the usual schedules. I would also like to thank Tommy for the impressive availability and prompt help with training, potential problems, and methods to put into action my crazy ideas. Beyond that, he has shown to be a great friend throughout this period, and I am very grateful for the laughs and good stories that brightened my days/evenings in the lab. Special thanks to Linda, for sorting any financial problem in a 'blink of an eye', and Paul for his availability to help when needed.

To all the old and new CALM team - Andy, Binling, Cleiton, Dieter, Maria, Nan Ye, Paul, Shaz, Yaan, Yas, Zoltan. Thank you all for sharing your experiences, ideas, and time, fun times. I would especially like to thank Cleiton, Dieter, Maria, and Nick, for being infallible lunch mates (even when I failed so many times) and friends inside and beyond the office. Your friendship has made work both pleasant and a great place to be during these years; keep glowing wherever you go!

Other people in the office deserve acknowledgement - to Anhad and Sam, for the fun times spent together, and for their help with the university system and computer/software

problems. They, Binling and Cleiton have shown to be great squash buddies too. I should not forget Amir, for his advice, support, and deep conversations.

To Hong, for her efficiency and amazing help with training. Her smile and kindness made Image Suite lab a very pleasant work environment. I should not forget her help with SEM, WXR and Micro-CT, all of them of great importance to accomplish this work. To Ana, for her kind help with TEM analysis, even at busy times. To Robert, for assisting with particle size distribution analysis at the Camborne School College.

My Ph.D. experience was even more rewarding due to the fantastic people I was able to meet in Exeter, some of them I cannot thank enough. To my favourite British girls, Caroline, Louisa (or soul sistah) and Miriam - for the cafes, trips, plays, company, conversations, and for understanding and being the best support I could ever have during some difficult times in Exeter - I am already missing you and hope we can get together soon. To my amazing housemates throughout these years, especially Ed, Giorgio, Jan, Jonjo, Maria, Michael, Miriam, and Susan. You are incredible, and I could not thank you enough for having the opportunity to be able to live with you. Special thanks to Jan, for being just the best company/housemate/problem in all these moments (apart from mornings, because you know...). I would also like to thank other friends from Exeter for the fun and unforgettable moments together - Barnaby, Benjamin, Joseph, Justine, Inés, Pierre, Ted, and several others - you are all in my heart.

To my friends from Ashwell, especially Barbs, Blanca, Catherine, Claudia, Chinwe, Joanne, and Montse - you provided the best experiences and trips I had in my life, and I would not be able to have better company than you! Thank you for expanding the technical/professional growth acquired during this Ph.D. to huge personal growth. Barbs, thank you for being a bit of 'home' in the UK. You are always in my thoughts and prayers.

To Ann, for being like a mother away from home - you are a star in everything you do, keep encouraging others with your generous heart. To Donna, Fr. Michael, and Fr. Jonathan - you are true witnesses of Christ on Earth, thank you for all the support.

To my long-distance and long-time friends, who were able to understand and support my steps, even when that involves being quite far from them throughout most of the year. To Amanda, Julia and João Pedro, for reminding me of the great times we had at school every time I go back home. To Anara, Bruna, Francis, and Mariele - I could not have asked for better friends in my life. Thank you for rejoicing with my success, checking in on me and surprising me with cards, presents, and love. Your friendship was everything I needed to accomplish this Ph.D. without getting crazy. Mari, thank you for being my best(ie) (future) cousin. To my godparents, Danilo and Lena, and cousins, Marco and Vitor, for transmitting encouragement, happiness, and entertainment throughout this journey. To my extended family members, especially my grandmother, Leocadia, for the support throughout this phase.

To Victor Magri, I cannot express my gratitude for the support much beyond the expected, especially in the final and difficult months of my Ph.D. You have shown true love and an outstanding capability of understanding, listening, and being there for me, even being far. I love you.

I could not have traced this path without all the support of my amazing family. To my brothers, Victor and Arthur, growing at your side could have been anything but boring - thank you for the deep and random conversations, and the time we spent together. To my parents, Aloisio and Tania, you will always be my heroes, and I am really proud to be your daughter. Thank you for your example, effort, and love. You are incredible human beings and parents, and I would not be able to reach this level of education if it were not for your dedication, guidance, and support.

To Saint Thomas Aquinas, a true Doctor and inspiration for me to develop this work by giving my best as much as possible. Finally, 'there is life beyond a Ph.D.', indeed. To God, Creator of everything, co-creator of this work. Constant thoughts of being your daughter have reminded me that life is too short to be stressed about work.

Publications

1. **Benedetti, L.**, Brulé, B., Decraemer, N., Davies, R., Evans, K. E., Ghita, O. (2020). A Route to Improving Elongation of High-Temperature Laser Sintered PEKK, Additive Manufacturing, 36, 1–10. doi: <https://doi.org/10.1016/j.addma.2020.101540>.
2. **Benedetti, L.**, Brulé, B., Decreamer, N., Evans, K. E., & Ghita, O. (2019). Shrinkage behaviour of semi-crystalline polymers in laser sintering: PEKK and PA12. Materials & Design, 181, 107906. <https://doi.org/10.1016/j.matdes.2019.107906>.
3. **Benedetti, L.**, Brulé, B., Decraemer, N., Evans, K. E., & Ghita, O. (2019). Evaluation of particle coalescence and its implications in laser sintering. Powder Technology, 342, 917–928. <https://doi.org/10.1016/j.powtec.2018.10.053>.
4. **Benedetti, L.**, Brulé, B., Decraemer, N., Davies, R., & Evans, K. (2019). Mechanical Performance of Laser Sintered Poly (Ether Ketone Ketone). 30th Annual International Solid Freeform Fabrication Symposium, 44(0), 1–14.
5. Haeri, S., **Benedetti, L.**, & Ghita, O. (2020). Effects of particle elongation on the binary coalescence dynamics of powder grains for Laser Sintering applications. Powder Technology, 363, 245–255. <https://doi.org/10.1016/j.powtec.2019.12.025>.
6. Chen, B., Yazdani, B., **Benedetti, L.**, Chang, H., Zhu, Y., & Ghita, O. (2019). Fabrication of nanocomposite powders with a core-shell structure. Composites Science and Technology, 170(November 2018), 116–127. <https://doi.org/10.1016/j.compscitech.2018.11.046>.
7. Yazdani, B., Chen, B., **Benedetti, L.**, Davies, R., Ghita, O., & Zhu, Y. (2018). A new method to prepare composite powders customized for high temperature laser sintering. Composites Science and Technology, 167(June), 243–250. <https://doi.org/10.1016/j.compscitech.2018.08.006>.

Table of Contents

List of Figures	19
List of Tables	29
Nomenclature	33
1 Introduction	39
1.1 Research Context	40
1.2 Objectives	41
1.3 Thesis Outline	41
2 Literature Review	45
2.1 Introduction	46
2.2 Material: Poly(aryl ether ketone)s (PAEKs)	46
2.2.1 Structure and classification	47
2.2.2 Synthesis	48
2.2.3 Fundamentals of crystallisation	51
2.3 Particle and Powder Bulk Properties	58
2.3.1 Particle properties	60
2.3.2 Powder flow: methods & properties	64
2.3.3 Powder bulk density: methods & properties	67
2.3.4 Other factors affecting powder flow	69
2.3.5 Methods for improving particle and powder properties for LS	72
2.4 Particle Coalescence of Polymers	73
2.4.1 Fundamentals of coalescence	73
2.4.2 Mechanisms of coalescence	75
2.4.3 Coalescence under hot stage microscopy (HSM) and in laser sintering	78
2.5 Process: Additive Manufacturing (AM)	80
2.5.1 High temperature laser sintering (HT-LS)	81
2.5.2 Configuration	83
2.5.3 Parameters	87
2.6 Properties: Mechanical Behaviour	94
2.6.1 Influence of crystallisation in mechanical performance	94

2.6.2	Influence of molecular weight in mechanical performance	95
2.6.3	Effect of part orientation in mechanical performance	96
2.7	Applications	96
2.7.1	Aerospace Industry	97
2.7.2	Other fields	98
3	Materials and Methods	101
3.1	Summary	102
3.2	Materials	102
3.3	Experimental Methods	104
3.3.1	Scanning electron microscopy (SEM)	104
3.3.2	Particle size distribution (PSD) and shape analysis	104
3.3.3	Particle size and shape descriptors	105
3.3.4	Hot stage microscopy (HSM)	106
3.3.5	Powder rheometry	108
3.3.6	Differential scanning calorimetry (DSC)	111
3.3.7	Dynamic mechanical analysis (DMA)	112
3.3.8	Thermomechanical analysis (TMA)	113
3.3.9	Wide angle X-ray diffraction (WXR)	113
3.3.10	Transmission electron microscopy (TEM)	114
3.3.11	Tensile testing	114
3.3.12	Flexural testing	115
3.3.13	Compressive testing	115
3.3.14	Micro-computer tomography (Micro-CT)	116
3.3.15	Surface analysis	116
3.3.16	ANOVA statistical analysis	116
3.3.17	Cake analysis under optical microscopy	117
3.3.18	<i>In situ</i> bulk density	118
3.3.19	Thermogravimetric analysis (TGA)	118
4	Powder Characterisation	119
4.1	Summary	120
4.2	Particle Characteristics	120
4.2.1	Scanning electron microscopy (SEM) analysis	120
4.2.2	Particle size distribution analysis	123
4.2.3	Shape analysis	124
4.3	Powder Properties	124
4.3.1	Powder rheometry results	124
4.3.2	The effect of moisture on powder flow	128
4.4	Conclusions	133

5	An experimental Investigation of PAEKs Behaviour at High-Temperature	135
5.1	Summary	136
5.2	Methods of Evaluating Individual Particles Behaviour with Temperature .	137
5.2.1	Method S1	137
5.2.2	Method S2	137
5.2.3	Method S3	138
5.3	Methods of Assessing Neck Growth with Temperature	138
5.3.1	Method N1	138
5.3.2	Method N2	138
5.3.3	Method N3	139
5.4	Individual Particles Changes with Temperature	139
5.4.1	By method	139
5.4.2	By PAEK grade	140
5.4.3	By substrate	142
5.4.4	Shape comparison	143
5.5	Hot Stage Microscopy Analysis for Neck Growth	144
5.5.1	By method	144
5.5.2	By PAEK grade	146
5.5.3	By substrate	148
5.6	Particles Behaviour at Processing Temperature: Isothermal Investigation .	150
5.7	Conclusions	151
6	Thermal and Crystallisation Properties of PEKK	153
6.1	Summary	154
6.2	Dynamic Differential Scanning Calorimetry (DSC)	154
6.3	Isothermal Crystallisation of PEKK	157
6.4	Wide Angle X-ray Diffraction (WXR) Results	158
6.5	Conclusions	158
7	Process Optimisation	163
7.1	Summary	164
7.2	Processing Parameters & Optimisation	165
7.2.1	Laser parameters	165
7.2.2	Processing temperatures	166
7.2.3	Screening of laser parameters	166
7.3	Effect of Building Orientation	171
7.4	Effect of Different Processing Temperatures	177
7.5	Effect of Multiple Laser Exposures	181
7.6	Conclusions	189

8 Shrinkage Behaviour of PEKK in High-Temperature Laser Sintering	191
8.1 Summary	192
8.2 Shrinkage Factors	192
8.2.1 Measuring shrinkage in laser sintering: β_{total}	193
8.3 Results and Discussions	194
8.3.1 Shrinkage in laser sintering: β_{total}	194
8.3.2 Shrinkage due to thermal contraction: β_T	196
8.3.3 Shrinkage due to crystallisation: β_c	196
8.3.4 Calculation of powder bulk effect: β_{powder}	197
8.4 Conclusions	198
9 Crystallisation, Mechanical Performance and Cooling Time of PEKK in LS	201
9.1 Summary	202
9.2 Cooling in High-Temperature Laser Sintering	203
9.3 Build Setup	205
9.4 Results and Discussions	206
9.4.1 Mechanical performance varying with cooling time	206
9.4.2 Crystallisation varying with cooling time	211
9.4.3 Crystal structure varying with cooling time	217
9.5 Conclusions	220
10 Recyclability of LS PEKK Powder	223
10.1 Summary	224
10.2 Results and Discussions	225
10.2.1 Investigation of bulk density	225
10.2.2 SEM analysis	226
10.2.3 Particle size distribution	228
10.2.4 Morphology investigation	229
10.2.5 Powder flow performance	231
10.2.6 Thermal changes	233
10.2.7 Crystallisation changes	235
10.3 Conclusions	236
11 Conclusions and Future Remarks	239
11.1 General Conclusions	240
11.2 Specific Conclusions	241
11.2.1 Powder and particle behaviour at room temperature	241
11.2.2 Particle and powder behaviour during coalescence and at processing temperature	242
11.2.3 Crystallisation properties of PEKK	243
11.2.4 Process optimisation	243
11.2.5 Shrinkage in laser sintering	244

11.2.6	Crystallisation affecting the performance of LS PEKK	244
11.2.7	Recyclability of PEKK powder	245
11.3	Limitations	246
11.3.1	Limitations of experimental methods	246
11.3.2	Limitations of PEKK optimisation for HT-LS	247
11.4	Future Work	248
Appendix A Summary of Coalescence Mechanisms driven by Viscous Flow		251
Appendix B Polymorphism of PEKK produced by LS		259
Appendix C Replicating Final Performance of Optimised Quenched Specimens under Scalable LS Setup		265
Appendix D Molecular Weight Change with Powder Reuse		269
References		271

List of Figures

Fig. 1.1	Diagram illustrating the effect of material properties in LS performance. The colour of each box is linked with the chapter in which the topic is explored. The boxes in white include other aspects not explored in this work.	43
Fig. 2.1	Literature review structure showing the main sections of this study. . .	46
Fig. 2.2	Chemical structure of PEKK [13].	48
Fig. 2.3	Electrophilic acylation reaction [20].	50
Fig. 2.4	Nucleophilic substitution reaction. Adapted from [20].	51
Fig. 2.5	Energy change to form spherical nuclei during crystallisation. The difference between the surface energy and the heat of crystallisation gives the total energy ΔG [50].	52
Fig. 2.6	Representation of spherulites configuration in (1) PEEK and in (2) typical polymers [75].	57
Fig. 2.7	Different morphology configurations of PEKK, view from the top of the crystal structure. (1) Form I and (2) form II [80].	57
Fig. 2.8	Diagram illustrating the effect of particle and powder properties and environmental conditions in the final LS performance.	58
Fig. 2.9	Effect of particle morphology in powder bulk density [122]. Relative roundness R is defined as the ratio between the surface area of a sphere with the same volume as the test particle (S_s) and the actual surface area (S). 62	
Fig. 2.10	SEM images of PEEK 150PF indicating (1) pores within the particle and (2) a porous particle structure. Adapted from [117].	63
Fig. 2.11	Modern systems to assess powder flow. (1) Configuration of the revolution powder analyser indicating the avalanche angle (adapted from [145]) and (2) FT-4 powder rheometer indicating forces acting in the system and the angles of the blade (adapted from [144]).	66
Fig. 2.12	Illustration of the different types of density measurements and their packing information [140].	68
Fig. 2.13	Addition of small particles to enhance bulk density. f_s is the solid fraction of small particles, f_L is the solid fraction of large particles, and the maximum solid fraction f^* is achieved with a bi-modal distribution of small and larger particles [115].	69

Fig. 2.14 Illustration of the downer reactor configuration to round polymer particles for LS application [181].	72
Fig. 2.15 The different stages of micron-sized polymer particles under coalescence, adapted from [186].	74
Fig. 2.16 Schematic illustration of contact growth modes adapted from Jagota et al. [208]. (1) Elastic adhesion driving contact growth in a zipping mode; (2) tractions viscous sintering driving contact growth in a stretching mode.	76
Fig. 2.17 SEM micrographs of UHMWPE particles showing nodular structures aggregated into larger structure units [221].	79
Fig. 2.18 Illustration of the LS process and the main components in the system [233].	81
Fig. 2.19 The EOS P 800 HT-LS system [234].	82
Fig. 2.20 Build dimensions of EOS P 8000 HT-LS system in the maximum capacity (yellow) compared to the two reduced configuration options (green and blue).	84
Fig. 2.21 Illustration of the deposition systems commercially available for LS; (1) counter-rotation roller and (2) translational blade system [115].	85
Fig. 2.22 Schematic illustration of the EOS P 800 system showing (a) process chamber temperature; (b) exchangeable build frame temperature and (c) building platform temperature.	86
Fig. 2.23 Comparison of the change in volume between amorphous and semi-crystalline polymers.	91
Fig. 2.24 (1) DSC of different PAEK grades showing no operating window. The processing temperature is set within the melting peak and corresponds to the minimum of the first derivative of the heating curve in the DSC. These curves are shown for (2) PEK HP3 and (3) PEEK 450PF [152].	93
Fig. 3.1 Schematic illustration of the characterisation methodologies performed to describe general properties of PEKK in powder and specimen format.	103
Fig. 3.2 Stages performed in ImageJ software to describe particles under HSM. (1) Image capture, (2) scale conversion, (3) manual contour, (4) binary conversion, (5) threshold application, and (6) measurement of the neck and/or particle size and morphology.	107
Fig. 3.3 Illustration of the different orientations of manufacturing, (1) X, (2) Y, and (3) Z. The specimens manufactured in X and Y orientation were placed at 0° in relation to the powder deposition direction, whilst Z specimens were manufactured at 0° and 90° rotation in relation to the direction of powder deposition.	115
Fig. 3.4 Areas selected for the inspection of surface roughness on specimens manufactured in different orientations.	117

Fig. 3.5 (1) Optical image of the cake and (2) conversion of the image into binary colours.	117
Fig. 3.6 Laser sintered boxes manufactured to assess powder bulk density of Kepstan 6002 PEKK. (1) .STL file, (2) manufactured boxes filled with powder after removal from the LS system; (3) empty boxes (after sandblasting and cleaning).	118
Fig. 4.1 Typical SEM images of HL1327 powder (Kepstan 6002 PEKK) at increasing magnification. Note the scale bars of (1) 100 μm and (2) 50 μm .	121
Fig. 4.2 Typical SEM images of P12S959a powder at different magnifications. Note the scale bars of (1) 200 μm and (2) 40 μm	121
Fig. 4.3 Typical SEM images of HL1320 powder at different magnifications. Note the scale bars of (1) 200 μm and (2) 40 μm	121
Fig. 4.4 Typical SEM images of Orgasol PA12 powder at different magnifications. Note the scale bars of (1) 200 μm and (2) 50 μm	122
Fig. 4.5 Typical SEM images of PEK HP3 powder at different magnifications. Note the scale bars of (1) 200 μm and (2) 40 μm	122
Fig. 4.6 Particle size distribution results of different PEKK grades. PEK HP3 and Orgasol PA12 were added for comparison. (1) Volumetric distribution and (2) cumulative distribution of particle size.	123
Fig. 4.7 Shape descriptor results for (a) different PEKK grades and (b) Kepstan 6002 PEKK compared with well-established LS grades. The shape was described in terms of particle diameter against (1) perimeter, (2) circularity, (3) roundness, and (4) convexity.	125
Fig. 4.8 Stability test curves for PEKK grades. PEK HP3 and Orgasol PA12 were introduced for comparison.	126
Fig. 4.9 Flow rate curves of PAEKs and Orgasol PA12 varying with tip speed.	127
Fig. 4.10 Compressibility behaviour of PAEKs and Orgasol PA12.	128
Fig. 4.11 Stability test results for (1) HL1327, (2) P12S959a, and (3) PEK HP3 at different environmental conditions. Note that the standard stability test was used.	129
Fig. 4.12 Flow rate test results of (1) HL1327, (2) P12S959a, and (3) PEK HP3 subjected to different environmental conditions.	130
Fig. 4.13 Flow rate test results of (1) HL1327, (2) P12S959a, and (3) PEK HP3 subjected to different environmental conditions.	131
Fig. 5.1 Schematic illustration of Chapter 5.	137
Fig. 5.2 Particles of HL1327 at (1) room temperature, (2) sintering temperature (T), and (3) maximum test temperature of 96 °C above (T).	139
Fig. 5.3 Change in particle size of HL1327 PEKK grade with temperature increase. (1) Method S1 and (2) methods S2 and S3.	140
Fig. 5.4 Change in normalised perimeter (method S3) of different PAEK grades.	141

Fig. 5.5	Particle change with temperature. The darkest image corresponds to the particle at room temperature, followed by the image at (T), whilst the lightest colour corresponds to the particle at the maximum experimental temperature.	142
Fig. 5.6	Change in normalised perimeter of HL1327 particles on different substrates.	143
Fig. 5.7	Change in particle shape of different PAEK grades. The shape was described in terms of (1) circularity and (2) roundness.	144
Fig. 5.8	A pair of particles of HL1327 grade under coalescence at (1) room temperature, (2) neck formation temperature (T), and (3) maximum test temperature of 88 °C above (T).	145
Fig. 5.9	Evaluation of different methods to monitor neck growth of HL1327 particles on a glass substrate.	145
Fig. 5.10	Neck growth and change in normalised particle perimeter with temperature for HL1327 grade.	146
Fig. 5.11	Coalescence of different PAEK grades on a glass substrate according to method N3 (neck growth normalised by the average perimeter of the particles).	147
Fig. 5.12	Progress of particle coalescence. The darkest images correspond to the particles at room temperature, followed by the particles at (T), and the lightest colour images correspond to the particles at maximum experimental temperature.	148
Fig. 5.13	Average neck growth of HL1327 grade on different substrates using method N3 (neck normalised by perimeter as temperature increases).	149
Fig. 5.14	Progress of coalescence of HL1327 particles on PEKK film.	149
Fig. 5.15	PEKK particles exposed to HSM under the isothermal condition at 292 °C for six hours. The results were monitored in terms of (1) average perimeter, (2) normalised perimeter for each individual particle.	150
Fig. 6.1	Heating and cooling profiles of standard DSC runs for the three different PEKK grades compared with PEK HP3. The melting peak is visible for all the grades, but no sign of crystallisation is found except for PEK HP3.	155
Fig. 6.2	DSC profiles for HL1327 grade at different (1) heating and (2) cooling rates.	156
Fig. 6.3	Magnified DSC cooling curves of HL1327 PEKK. Crystallisation peaks are found for PEKK cooled at 1.5 °C min ⁻¹ and 1°C min ⁻¹	156
Fig. 6.4	Heating and cooling DSC profiles for PEK HP3. Melting and crystallisation peaks are observed despite the test rate selected.	157
Fig. 6.5	DSC heating thermoscan of Kepstan 6002 PEKK indicating melting and the first derivative of the melt (in red).	158

Fig. 6.6	Relative volumetric crystallinity of Kesptan 6002 PEKK, HL1327 grade, at different isotherms.	159
Fig. 6.7	Time taken to crystallise half of the maximum crystallisation of Kesptan 6002 PEKK, HL1327 grade, at different isotherms, also known as the half-time crystallisation curve.	160
Fig. 6.8	Enthalpy of fusion of HL1327 PEKK at different isotherms. Note the maximum enthalpy at 240 °C.	160
Fig. 6.9	WXR D spectra for different PAEK grades.	161
Fig. 7.1	Schematic representation of processing parameters and characterisation methods employed to assess LS quality of PEKK.	164
Fig. 7.2	DSC profile of Kepstan 6002 PEKK indicating melting and the first derivative of the heating (dashed curve). The T_{bed} (292 °C) and T_{bp} (265 °C) were extracted from the DSC curves.	167
Fig. 7.3	Usual build configuration for specimens manufactured in the X orientation.	168
Fig. 7.4	Average UTS of LS HL1327 PEKK specimens manufactured at different laser powers.	169
Fig. 7.5	Average UTS of LS HL1327 PEKK specimens manufactured at different laser scan speeds.	169
Fig. 7.6	Average UTS (1) and elongation at break (2) of LS HL1327 PEKK manufactured using different energy densities.	170
Fig. 7.7	SEM images of films produced using different laser powers and energy densities. (1) 3 W and 5.9 mJ mm ⁻² , (2) 6 W and 11.8 mJ mm ⁻² , and (3) 12 W and 23.5 mJ mm ⁻² . Note the different scale bars of (a) 1 and 2 mm and (b) 500 μm and 200 μm.	170
Fig. 7.8	Relation between laser power and surface topology (S_a) of PEKK films.	171
Fig. 7.9	Build configuration of specimens manufactured in (1) Y, and (2) Z orientation.	172
Fig. 7.10	(1) Ultimate tensile strength and (2) elongation at break of Kepstan 6002 PEKK manufactured in different orientations.	172
Fig. 7.11	Flexural strength of Kepstan 6002 PEKK specimens manufactured in different orientations.	173
Fig. 7.12	(1) Compressive strength of PEKK specimens manufactured in different orientations. The curves were separated into (i) elastic region, (ii) plastic region up to 50%, and (iii) plastic region >50%; (2) example of a specimen after being subjected to compressive testing.	174
Fig. 7.13	Tensile testing fracture of LS Kepstan 6002 PEKK specimens produced at (1-3) X, (4-6) Y, and (7-9) Z orientation. Note the scale bars of 1 mm (left column), 200 μm (centre) and 50 μm (right column).	175

Fig. 7.14 Micro-CT scan of a specimen manufactured in X orientation. (1) Section showing internal porosity and (2) volumetric reconstruction of the scan.	176
Fig. 7.15 Volumetric porosity of Kepstan 6002 PEKK specimens measured using a Micro-CT scan.	176
Fig. 7.16 Comparison of the (1) ultimate tensile strength and (2) elongation at break of Kepstan 6002 PEKK specimens processed at different building platform temperatures.	177
Fig. 7.17 Tensile strength fracture of LS Kepstan 6002 PEKK specimens manufactured using T_{bp} of 286 °C at (1-3) X and (4-6) Y orientation. Note the scale bars of 1 mm (left column), 200 μm (centre) and 50 μm (right column).	178
Fig. 7.18 WXR spectra of LS specimens of Kepstan 6002 PEKK manufactured at different T_{bp} and compared with the virgin PEKK powder.	180
Fig. 7.19 The average degree of crystallinity obtained with WXR for specimens manufactured in X orientation at different T_{bp}	181
Fig. 7.20 TEM images of LS specimens manufactured at T_{bp} of (1) 265 °C and (2) 286 °C at different magnifications, as shown by the scale bars. The spherulites obtained at T_{bp} of 265 °C are overall smaller and vary between 2.8 and 5.8 μm in diameter, whilst the spherulites resulting from a T_{bp} of 286 °C are larger and vary between 3.7 and 7.5 μm in diameter.	182
Fig. 7.21 Relation between scan strategy, tensile strength, and elongation at break of PEKK specimens produced with different ED and laser exposures.	185
Fig. 7.22 SEM images of films produced with double laser exposure and the same ED (23.5 mJ mm^{-2}). (1) 3 + 9 W, (2) 4 + 8 W and (3) 8 + 4 W. Note the different scale bars of (a) 1 mm and (b) 500 μm	186
Fig. 7.23 SEM images of films produced with three laser exposures and the same ED (23.5 mJ mm^{-2}). (1) 3 + 3 + 6 W and (2) 6 + 3 + 3 W. Note the different scale bars of (a) 1 mm and (b) 500 μm	187
Fig. 7.24 Relation between scan strategy, tensile strength, and surface topology of PEKK specimens produced with different ED and laser exposures.	188
Fig. 8.1 Change in volume of semi-crystalline polymers subjected to heating and cooling.	192
Fig. 8.2 (1) Shrinkage in Z orientation for PEKK and PA12 parallelepipeds; (2) downskin and upskin effect observed in the PEKK parts.	194
Fig. 8.3 Dimension change due to crystallisation of Kepstan 6002 PEKK at (1) slow cooling rate and (2) rapid cooling rate.	197
Fig. 9.1 Illustration of the topics discussed in Chapter 9.	202

Fig. 9.2	Examples of the amorphous behaviour of Kepstan 6002 PEKK grade when processed by conventional polymer techniques such as (1) injection moulding, (2) extrusion calendaring, and (3) sheet thermoforming. The slow cooling of LS, however, provides enough time for PEKK crystallisation, as shown in (4).	203
Fig. 9.3	Schematic representation of the cooling profile in an HT-LS system. Once the part production is finished (1-2), the system goes through the standard machine cooling (3), which comprises two cooling stages with different rates.	204
Fig. 9.4	Crystallisation build setup. The temperatures of manufacturing, T_{bed} and T_{bp} , are indicated on the right. Group one was the first to be built, following a sequential order until group 16 is completed. Therefore, the first group was exposed to the longest time of cooling, as opposed to group 16. The colour of the specimens attempted to match their real colours when removed from quenching.	206
Fig. 9.5	Relationship between cooling time and groups of specimens in the build setup.	207
Fig. 9.6	Specimens removed from the cake, cleaned, and sandblasted. Note the change in color with cooling time. The specimens of lighter color remained cooling in the system for a longer time; therefore, they are more crystalline. In contrast, the darker specimens are less crystalline due to the shorter cooling time.	207
Fig. 9.7	Mechanical performance of specimens produced at different cooling times; (1) average tensile strength and elongation at break for each cooling time and (2) average mechanical performance separated by location in the powder bed, corner, and middle.	208
Fig. 9.8	Average elastic modulus versus elongation at break for specimens produced at different cooling times.	210
Fig. 9.9	SEM images of the fracture for specimens manufactured at (1) 9.25 h, (2) 6.25 h, (3) 4.75 h, (4) 1 h, and (5) 0 h of cooling time. Note the scale bars of (a) 1 mm, (b) 200 μm and (c) 50 μm .	212
Fig. 9.9	SEM images of the fracture for specimens manufactured at (1) 9.25 h, (2) 6.25 h, (3) 4.75 h, (4) 1 h, and (5) 0 h of cooling time. Note the scale bars of (a) 1 mm, (b) 200 μm and (c) 50 μm (cont.).	213
Fig. 9.10	Degree of crystallinity measured using WXRd for specimens produced at different cooling times.	214
Fig. 9.11	Average degree of crystallinity versus (1) tensile strength and (2) elongation at break for specimens produced at different cooling times.	214
Fig. 9.12	Relative volumetric crystallinity of isothermally crystallised Kepstan 6002 PEKK compared with the LS process. The time to crystallise some of the LS groups is highlighted in the LS line by points of different colours and shapes.	216

Fig. 9.13 PEKK spherulites formed after 10 h of cooling in LS. (1) General morphology of the spherulites and (2) magnified images of individual spherulites. The spherulites are homogeneously distributed at varying sizes from 5.4 to 5.7 μm in diameter.	217
Fig. 9.14 PEKK spherulites formed after 5.5 h of cooling in LS. (1) General morphology of the spherulites, (2) magnified images of the core structures, (3) magnified images of the spherulites' structure. The spherulites assume a larger diameter, which starts growing from very clear cores.	218
Fig. 9.15 PEKK spherulites formed with minimal LS cooling time approaching 0 h. (1) General morphology of the crystallised region, (2) image of the amorphous region, and (3) magnified images of the nuclei being formed. The quenching was not enough to prevent crystallisation.	218
Fig. 9.16 WXR D spectra of LS Kepstan 6002 PEKK specimens subjected to different cooling times.	219
Fig. 10.1 Schematic illustration of Chapter 10 structure and the characterisation techniques employed to investigate powder, particle, and material properties.	224
Fig. 10.2 Optical analysis of cakes processed at (1) 265 $^{\circ}\text{C}$ and (2) 286 $^{\circ}\text{C}$ of T_{bp} .	225
Fig. 10.3 Typical SEM images of Kepstan 6002 PEKK powder. Note the scale bars of 100 μm (left), 20 μm (middle) and 2 μm (right) for (1-3) virgin particles, (4-6) processed particles at T_{bp} of 265 $^{\circ}\text{C}$ and (7-9) processed particles at T_{bp} of 286 $^{\circ}\text{C}$	227
Fig. 10.4 Particle size distribution analysis for virgin and processed Kepstan 6002 PEKK powder at 265 $^{\circ}\text{C}$ and 286 $^{\circ}\text{C}$ of T_{bp}	228
Fig. 10.5 Images of semi-sintered particles from the processed cake at (1-2) 265 $^{\circ}\text{C}$ and (3-4) 286 $^{\circ}\text{C}$. The dashed lines represent the assumed partial sintering region between particles in the processed powder.	229
Fig. 10.6 Perimeter varying with particle diameter for virgin and processed PEKK.	230
Fig. 10.7 Convexity varying with particle diameter for virgin and processed PEKK.	230
Fig. 10.8 Stability results of Kepstan 6002 PEKK powder processed at different conditions and tested (1) before and (2) after sieving.	232
Fig. 10.9 Flow rate performance of Kepstan 6002 PEKK powder processed at different conditions and tested (1) before and (2) after sieving.	232
Fig. 10.10 DSC thermoscan of the heating curve for Kepstan 6002 PEKK powder processed at different T_{bp}	234
Fig. 10.11 (1) TGA profile of Kepstan 6002 PEKK powder processed at different T_{bp} and (2) the first derivative of the TGA curves.	234
Fig. 10.12 Half-time crystallisation curve of Kepstan 6002 PEKK powder before and after being processed at different T_{bp}	235
Fig. 10.13 WXR D spectra of Kepstan 6002 PEKK powder before and after being processed at different T_{bp}	236

Fig. 10.14 Average degree of crystallinity of Kepstan 6002 PEKK powder processed at different conditions and compared with the virgin powder. . . .	237
Fig. 11.1 Virgin PEKK powder agglomerating in the (1) hopper damper and (2) around the recoater during manufacturing using the EOS P 800 system. . .	247
Fig. B.1 WXR D patterns of LS Kepstan 6002 PEKK specimens subjected to different cooling times. (1) 10.75 h, 10 h, 9.25 h and 8.5 h; (2) 7.75 h, 7 h, 6.25 h and 5.5 h; (3) 4.75 h, 4 h, 3.25 h and 2.5 h; (4) 1.75 h, 1 h, 0.25 h, and 0 h.	259
Fig. B.2 WXR D patterns of LS Kepstan 6002 PEKK specimens analysed along Z orientation with varying cooling time. (1) 10.75 h, 10 h, 9.25 h and 8.5 h; (2) 7.75 h, 7 h, 6.25 h and 5.5 h; (3) 4.75 h, 4 h, 3.25 h and 2.5 h; (4) 1.75 h, 1 h, 0.25 h, and 0 h.	260
Fig. B.3 DSC thermograms of the melt for LS Kepstan 6002 PEKK specimens produced at different cooling times. (1) 10.75 h, 10 h, 9.25 h and 8.5 h; (2) 7.75 h, 7 h, 6.25 h and 5.5 h; (3) 4.75 h, 4 h, 3.25 h and 2.5 h; (4) 1.75 h, 1 h, 0.25 h, and 0 h.	261
Fig. B.4 DSC thermograms of the melt for LS Kepstan 6002 PEKK specimens. The thermograms were repeated for different samples subjected to the same cooling time. (1) 10.75 h and 7 h samples and (2) 5.5 and 3.25 h samples. Note that different phenomena are occurring despite the samples being subjected to the same cooling time.	263
Fig. C.1 Configuration of the experimental build. The temperatures of manufacturing, T_{bed} and T_{bp} are indicated on the right. The half of the build located on the upper left region remained in the system for 3.5 h, whilst the other half was removed and placed in the oven at 230 °C for the same period.	266
Fig. C.2 (1) UTS and (2) strain at break properties of specimens produced with the two different setups - cooling in the machine and placed in the oven at 230 °C. The results were compared for the specimens produced at standard LS cooling, and for the specimens subjected to 5.5 and 6.25 h of cooling before quenching in water.	267
Fig. C.3 Degree of crystallinity obtained with the specimens left in the system and placed in the oven for 3.5 h. The results were compared with the specimens quenched in water and with the standard LS process with a cooling time of 9 h.	267

List of Tables

Table 2.1	Polymers from the PAEK family and their main thermal properties [20].	47
Table 2.2	General properties of three Arkema’s PEKK set of grades of different series [12, 34, 33].	49
Table 2.3	Lattice parameters of PAEKs [13, 74].	56
Table 2.4	Processes available to produce powder for LS.	59
Table 2.5	Effect of humidity in interparticulate forces [153].	71
Table 2.6	Some of the mechanical properties of LS PEK HP3, IM PEEK 450 and LS PA2200 [277, 10, 278–280].	97
Table 2.7	The advantages of using AM to manufacture aerospace and defence parts compared to conventional processes [282].	98
Table 3.1	General properties of different grades investigated in this study. Three grades referred as Kepstan 6002 PEKK were compared with the LS PEK HP3 [280] and Orgasol PA12 [295] grades.	103
Table 3.2	Criteria used to select the images for ImageJ analysis.	108
Table 3.3	Description of the parameters measured with stability and flow rate test [144].	110
Table 3.4	Enthalpy of fusion of the fully crystallised PEKK, PEEK and PA12 polymers at the equilibrium temperature [299, 66, 300].	111
Table 3.5	Methods for dilatometry analysis.	113
Table 4.1	Summary of particle size distribution analysis of PEK HP3, Orgasol PA12, and different PEKK grades.	123
Table 4.2	Summary of powder rheology results for different PEKK grades. PEK HP3 and Orgasol PA12 were included for comparison.	126
Table 4.3	Summary of FT-4 powder rheometry results of PAEK grades subjected to different environmental conditions.	132
Table 5.1	Corresponding (T) values for each PAEK grade in the analysis.	142
Table 6.1	Degree of crystallinity for different PAEK grades using the WXR technique.	159

Table 7.1	Standard laser sintering parameters for PEK HP3 [263].	165
Table 7.2	Processing temperatures selected to perform LS trials according to each section of this chapter.	167
Table 7.3	Average surface roughness of Kepstan 6002 PEKK specimens manufactured at different orientations.	175
Table 7.4	Volumetric porosity of Kepstan 6002 PEKK specimens processed at different T_{bp}	179
Table 7.5	Surface roughness of Kepstan 6002 PEKK specimens manufactured at different orientations.	179
Table 7.6	Design of experiment showing different laser power combinations used to study the effect of multiple laser exposures.	183
Table 7.7	Average mechanical strength of specimens produced with different laser powers and laser exposure strategies.	184
Table 7.8	Average elongation at break of specimens produced with different laser powers and laser exposure strategies.	185
Table 7.9	Average R_a values of films produced with different laser powers and laser exposure strategies.	186
Table 8.1	Laser sintering parameters for PEKK and PA12.	194
Table 8.2	Average shrinkage in the laser sintering of PEKK and PA12.	195
Table 8.3	Thermal contraction during cooling for PEKK and PA12.	196
Table 8.4	Shrinkage due to crystallisation of Kepstan 6002 PEKK and Orgasol PA12 [142].	197
Table 8.5	Shrinkage (%) in Laser Sintering and the effect of powder bulk.	198
Table 9.1	One-way ANOVA analysis of the elongation at break of specimens subjected to different cooling times. The specimens manufactured at a specific cooling time (left column) were compared with the other specimens of the build in terms of their cooling time.	209
Table 9.2	One-way ANOVA analysis of the degree of crystallinity of specimens subjected to different cooling times. The specimens manufactured at a specific cooling time (left column) were compared with the other specimens of the build in terms of cooling time.	215
Table 10.1	Bulk density of Kepstan 6002 PEKK achieved with different methods and conditions.	226
Table 10.2	Summary of the particle size distribution of Kepstan 6002 PEKK powder.	228
Table 10.3	Summary of flow performance for Kepstan 6002 PEKK processed at different conditions.	231
Table 10.4	Summary of flow performance for sieved Kepstan 6002 PEKK powder processed at different conditions.	231

Table 10.5 Summary of thermal and degradation properties of virgin and processed PEKK powder.	233
Table A.1 Analytical solutions and numerical studies to predict particle coalescence driven by viscous sintering.	252
Table B.1 Relation between thermogram peaks and crystallisation phenomenon of PEKK [13].	263
Table D.1 GPC values for PEKK powder processed at different conditions and compared with the virgin powder.	269

Nomenclature

List of Acronyms / Abbreviations

ABS	acrylonitrile Butadiene Styrene
AM	Additive Manufacturing
AoR	Angle of Repose
AR	Aspect Ratio
BET	Brunauer-Emmett-Teller
BFE	Basic Flowability Energy
CAD	Computer Aided Design
CBD	Conditioned Bulk Density
CIB	Chemical Induced Binding
CPS	Compressibility
CT	Computed Topography
DMA	Dynamic Mechanical Analysis
DMA	Dynamic Mechanical Analysis
DMSO	Dimethyl Sulfoxide
DPE	Diphenyl Ether
DPS	Diphenyl Sulfone
DSC	Differential Scanning Calorimetry
EMR	Energy Melt Ratio
FCC	Face-centred cubic
FDM	Fused Deposition Modeling

FEM	Finite Element Method
FRI	Flow Rate Index
GPC	Gel permeation chromatography
HDPE	High-density Polyethylene
HR	Hausner Ratio
HSM	Hot-stage Microscopy
HT-LS	High-Temperature Laser Sintering
<i>I</i>	Isophthalic acid
IM	Injection Moulding
IR	Infrared
IV	Inherent Viscosity
LDPE	Low-density Polyethylene
LPS	Liquid Phase Sintering
LS	Laser Sintering or Laser Sintered
PA11	Polyamide 11
PAEK	Poly(aryl ether ketone)
PA	Poly(amide)
PBF	Powder Bed Fusion
PBT	Polybutylene Terephthalate
PC	Polycarbonate
PEEK	Poly(ether ether ketone)
PEI	Poly(ethylenimine)
PEKK	Poly(ether ketone ketone)
PEK	Poly(ether ketone)
PE	Polyethylene
PMMA	Poly(methyl methacrylate)
POM	Poly(oxymethylene)

PP	Polypropylene
PSD	Particle Size Distribution
PS	Polystyrene
PTFE	Polytetrafluoroethylene
PVDF	Polyvinylidene Fluoride
RMWPE	Regular Molecular Weight Polyethylene
RPA	Revolution Powder Analyser
SEM	Scanning Electron Microscopy
SE	Specific Energy
SI	Stability Index
SLA	Stereolithography
SLM	Selective Laser Melting
SLS	Selective Laser Sintering
SSS	Solid State Sintering
<i>T</i>	Terephthalic acid
TEM	Transmission Electron Microscopy
TGA	Thermogravimetric Analysis
TMA	Thermomechanical analysis
TPE	Thermoplastic Elastomer
TPE	Thermoplastic Elastomers
TPU	Thermoplastic Polyurethane
UHMWPE	Ultra-high Molecular Weight Polyethylene
UTS	Ultimate Tensile Strength
WXR	Wide X-ray Diffraction

List of Symbols

β_c	Shrinkage due to Crystallisation
β_{powder}	Shrinkage due to Powder Bulk

β_{total}	Total Shrinkage due to Laser Sintering
β_T	Shrinkage due to Temperature
CO_2	Carbon Dioxide
ΔH_f	Heat of Fusion
ΔH_f^0	Heat of Fusion of the fully crystalline polymer
ED	Energy Density
γ	Surface Tension
H_c	Critical Humidity
H_{min}	Lower Limit of Humidity
h_s	Scan spacing
λ	Wavelength
M_w	Molecular Weight
η	Viscosity
η_0	Zero-shear Viscosity
P_L	Laser Power
R	Relative Roundness
R_a	Arithmetical Mean Height of a Line
R_t	Total Mean Height of a Line
S	Surface area
S_a	Arithmetical Mean Height of a Surface
σ	Surface Tension
S_s	Surface area of a sphere
S_t	Total Mean Height of a Surface
T	Temperature
t	Time
T_{bed}	Bed Temperature
T_{bp}	Building Platform Temperature

T_c	Crystallisation Temperature
T_{ebf}	Exchangeable Build Frame Temperature
T_c	Crystallisation Temperature
T_g	Glass Transition Temperature
T_m	Melting Temperature
T_{max}	Maximum Experimental Temperature
T	Temperature of Coalescence
v_s	Scan speed
X_r	Degree of crystallinity

Chapter 1

Introduction

1.1 Research Context

The increasing interest in producing complex and customised parts, integrated systems, in combination with reducing cost and accelerating part production, has led to the rapid growth of Additive Manufacturing (AM) in the past decades. Structures of impossible manufacturing have been recently getting shape and replacing final-used parts in multiple sectors of industry, including medical, aerospace, and automotive [1].

Amongst the polymeric AM, Fused Deposition Modeling (FDM) and Laser Sintering (LS) are the most widely employed techniques. The LS process uses a laser as a heat source to selectively fuse particles and build a three-dimensional part, layer-by-layer [2]. In comparison to FDM, LS parts are more accurate and allow serial production with a range of materials varying from polymers, metals, ceramic, and composites.

Despite the capability of processing powders with broad properties, the growing but still limited options of LS grades prevent the spreading of this technology to applications in which high performance is desired. Recent studies showed that polyamides take from 90 to 95% of the total market of polymers for LS [3–5]. This scenario is gradually reversing by the development of other materials; they include thermoplastic elastomers (TPE) [6], polycarbonate (PC) [7], polybutylene terephthalate (PBT) [8] and poly(aryl ether ketone)s (PAEKs) [9–11].

The development of PAEKs for LS started in 2010 with the launching of PEEK HP3 grade in parallel to the EOS P 800, the first commercially available high-temperature laser sintering (HT-LS) system. Since then, different PAEK grades have been investigated to reduce cost and improve performance [9]. Poly(ether ketone ketone) (PEKK) is an alternative option of a high-performance polymer able to be processed at significantly lower temperatures. Compared to PEEK HP3, melting is reduced by ~ 70 °C whilst maintaining the high glass transition temperature (T_g) required for high service temperature applications [12].

In particular, Kepstan 6002 PEKK grade has slow kinetics of crystallisation [13], which results in a completely amorphous structure when processed by conventional technologies such as injection moulding (IM). The prolonged time of cooling in LS, however, is sufficient for crystallisation to take place without compromising layer bonding. This property is essential to improve final part performance in Z orientation.

PEKK applications include the medical, aerospace, and automotive industries. As a highly chemical resistant biomaterial, PEKK can be used in orthopedic and maxillofacial surgeries, prosthetics, scaffolds, and tissue regeneration [14, 15]. For aerospace and automotive applications, the low density of PEKK combined with high thermal, mechanical, chemical, and fire resistance can replace metals in structural components in contact with hydraulic fluids and synthetic lubricants [16, 17].

1.2 Objectives

This thesis was developed in collaboration with Arkema to improve Kepstan 6002 PEKK properties for the LS use. The main property of interest is the mechanical performance of the LS parts, which requires optimisation to achieve the needs of the desired markets, especially the aerospace industry. The improvement of the final LS parts depends on understanding the fundamental material and particle/powder properties for successful HT-LS processing. Therefore, through a material and process in-depth investigation and understanding, this research project attempts to improve the mechanical properties of HT-LS PEKK for different applications.

1.3 Thesis Outline

The structure of this thesis comprises five main areas: Introduction and state of the art (Chapters 1 & 2), material characterisation (Chapters 3-6), process optimisation (Chapters 7-9), powder recyclability (Chapter 10), and overall discussion and conclusions (Chapter 11).

The state of the art focuses on the description of PAEK polymers, the LS process, mechanical properties obtained with LS parts, and future applications. The topics explored to relate material and process properties include particle and powder properties assessed at room temperature and processing temperatures.

The understanding of the physical and chemical properties of PEKK polymer is vital to optimising the final performance of LS parts. This relationship is illustrated in Fig.1.1, which presents a diagram associating all material and powder properties affecting the LS process, and therefore final component performance.

The illustration of Fig.1.1 separates each chapter by colour; the topics explored in the corresponding chapter share the same colour. The experiments involving fundamental particle and powder characteristics, thermal behaviour, crystallisation, mechanical properties, consolidation, and surface analysis were described in the initial part of this study (Chapter 3).

In Chapter 4, the particle and powder properties were firstly assessed at room temperature for individual particles of three different grades in terms of their size, distribution, and morphology. The results were compared with commercial LS grades. Then, the effect of moisture in powder bulk density and flow performance was investigated.

Powder behaviour may change with temperature, and particle characteristics at room temperature can be significantly different than at processing temperatures, especially near the melting peak (T_m), range in which pre-heating in LS of PAEKs operates. The effect of temperature was therefore monitored before and during the melt, for individual particles and a pair of particles under coalescence. This was explored for different PEKK grades in Chapter 5, which concludes particle and powder characterisation by selecting the most suitable PEKK grade for LS.

In Chapter 6, the crystallisation properties of PEKK were explored under dynamic and isothermal conditions using differential scanning calorimetry (DSC). Crystallisation was also investigated under wide X-ray diffraction (WXR) to support the DSC data.

Chapter 7 is the first of three chapters on PEKK optimisation for LS. In this chapter, different combinations of laser parameters and processing temperatures were evaluated to improve PEKK parts regarding their consolidation, mechanical properties, surface roughness, and crystallisation. At last, this chapter investigates the effect of multiple laser exposures.

In Chapter 8, an equation was proposed to assess the shrinkage associated with intrinsic material properties in LS. The parameters - thermal retraction, shrinkage due to crystallisation, and powder bulk - were experimentally measured and quantified for Kepstan 6002 PEKK, and then compared with Orgasol PA12 grade.

In an attempt to improve the brittle behaviour achieved with LS, a novel procedure was developed to improve the elongation of LS PEKK parts. The optimisation of elongation is described in Chapter 9, which associates cooling time with elongation at break but also kinetics of crystallisation. For this reason, the degree of crystallinity and crystal structures were further explored and reported in the same chapter, which concludes LS optimisation of PEKK.

The main industrial advantage of replacing metals for polymer parts processed by LS is the potential for cost reduction with powder recycling. Maintaining the properties of the virgin material is, therefore, crucial when processing PEKK by LS. The used powders processed at different temperatures were then assessed regarding changes in particle and powder behaviour and thermal, physical, and chemical properties. The results are presented and discussed in Chapter 10.

Finally, Chapter 11 summarises the main results and remarks achieved with HT-LS of PEKK and suggests future investigations in the same field.

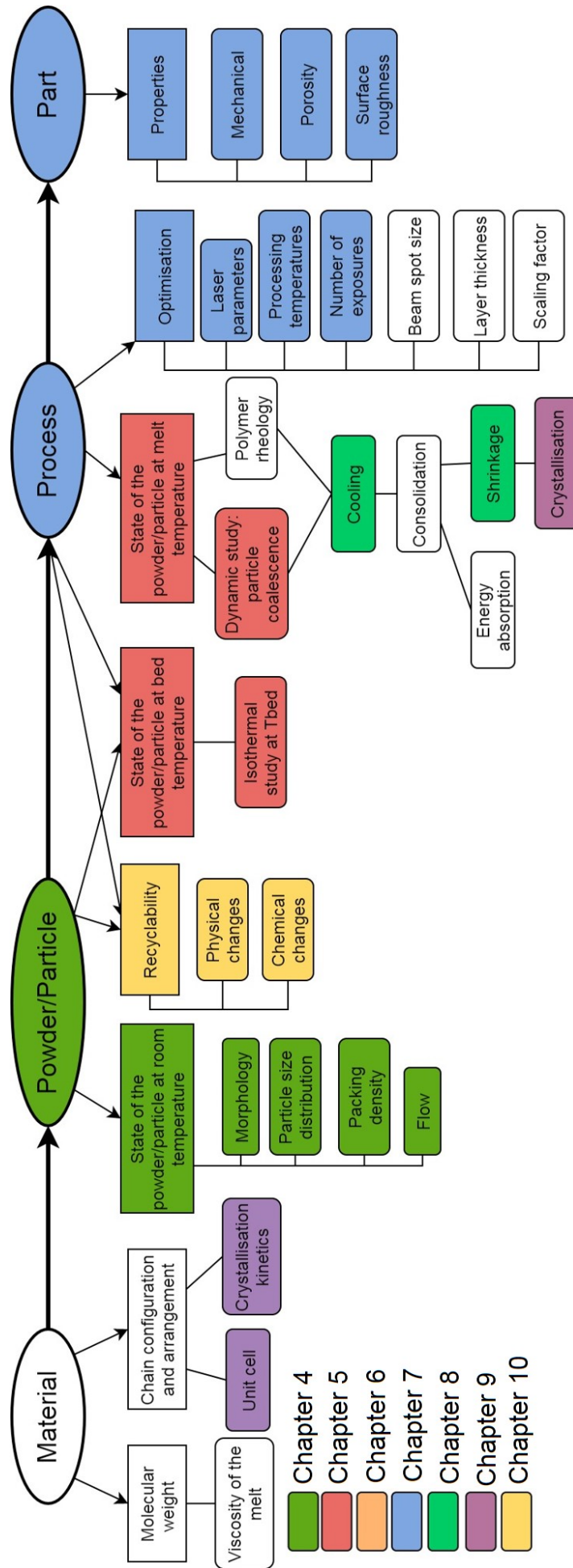


Fig. 1.1 Diagram illustrating the effect of material properties in LS performance. The colour of each box is linked with the chapter in which the topic is explored. The boxes in white include other aspects not explored in this work.

Chapter 2

Literature Review

2.1 Introduction

Following a similar structure to this thesis, the literature review comprises six main sections: material, particle & powder properties, coalescence, process, properties, and applications. Different topics will be discussed in each of these sections, according to their relevance for this thesis. A schematic representation of the literature review structure is shown in Fig.2.1.

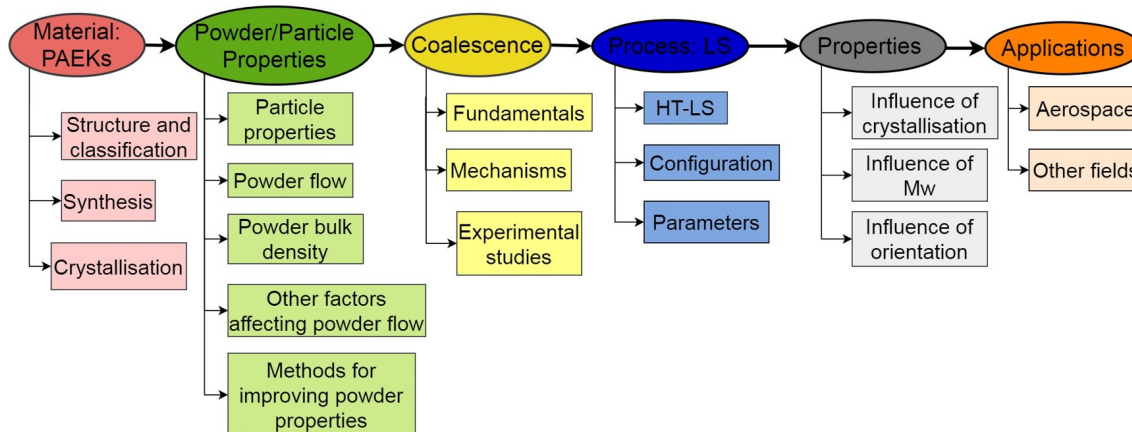


Fig. 2.1 Literature review structure showing the main sections of this study.

2.2 Material: Poly(aryl ether ketone)s (PAEKs)

This section will focus on the study of PAEK polymers by considering their structure, synthesis, and then crystallisation kinetics and crystal morphology. According to the National Research Council [18], the national academy of sciences and engineering in the USA, thermoplastic polymers are often classified regarding their mechanical performance as conventional/commodity thermoplastics, engineering polymers, or high-performance polymers. Among the high-performance group, PAEK family stands out for having a unique combination of excellent thermal stability and mechanical properties at a broad temperature range; low flammability and low emission of smoke and toxic gases; chemical, radiation and solvent resistance; abrasion resistance, low water absorption, good impact properties, and good electrical performance [19, 9, 20]. Furthermore, PAEKs are biocompatible polymers [21].

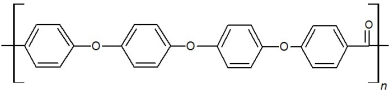
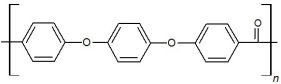
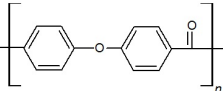
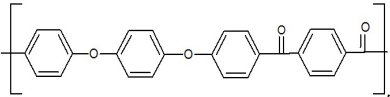
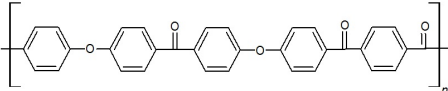
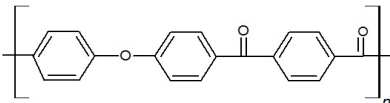
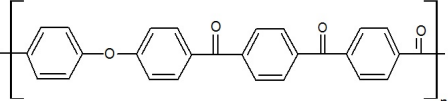
As a result of these properties, PAEK is widely used in engineering applications such as bearings, piston parts, pumps, compressor plate valves, cable insulation, and ultra-high vacuum systems [22]. PAEKs are also applicable in electrical and electronic parts, military equipment wires, nuclear plants, underground railways, and oil wells [17]. In the aerospace and automotive sectors, the importance of lightweight, thermal resistance, fire-resistant properties, and sustainable structures have triggered an interest in thermoplastics and thermoplastic composites [23]. As opposed to thermosets, PAEK is weldable and can be recycled, in addition to displaying a better mechanical performance and solvent resistance than epoxies and polyimides [17].

2.2.1 Structure and classification

The PAEK family consists of polymers with the phenyl group and ether or keto linkage in the repeating structural units. The aromatic ring in the monomer structure promotes chemical and heat resistance for prolonged times, whilst ketone groups increase molecular stiffness due to a higher barrier for rotational conformation. Therefore, an increase in ketone content increases glass transition temperature (T_g) in PAEK polymers, whilst an increase in ether content increases chain flexibility due to a lower energy barrier for conformation. A higher ketone content usually enhances the packing fraction of the unit-cell structure, resulting in higher cohesive energy and melting temperature (T_m) [13]. Different arrangements and concentrations of isomers, however, can change these properties.

The PAEK family is mainly known for three different polymers: poly(ether ketone) (PEK), poly(ether ether ketone) (PEEK), and poly(ether ketone ketone) PEKK. Other polymers share similar structures; they are shown in Table 2.1.

Table 2.1 Polymers from the PAEK family and their main thermal properties [20].

Polymer	Structure	T_g (°C)	T_m (°C)
PEEEK [24]		129	324
PEEK [25]		143	343
PEK [19]		153	365.5
PEEKK [24]		154	358
PEKEKK [26]		173	371
PEKK [27]		156	300
PEKKK [28]		175	439

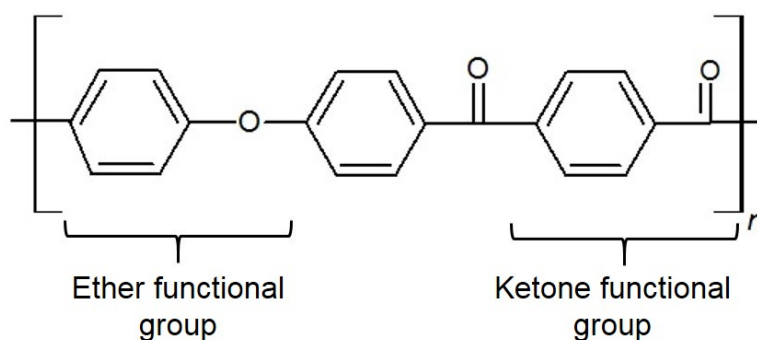


Fig. 2.2 Chemical structure of PEKK [13].

2.2.1.1 Poly(ether ketone ketone)

PEKK belongs to the PAEK family and is formed by an aromatic backbone chain connected with ketone and ether functional groups in a ratio of 2:1 ketones/ether linkage. Fig.2.2 shows the chemical structure of PEKK. The concentration of ketone in the structure varies from 33% for PEEK, 50% for PEK, and 67% for PEKK. The growth in ketone content increases chain stiffness and T_g , which leads to a slightly better mechanical performance [13].

PEKK was patented by DuPont in 1962 but was less studied if compared to other polymers from the PAEK family. Most PEKK studies concerned kinetics of crystallisation and crystal formation either as a matrix for carbon-fibre composites [29] or by varying the concentration of T and I isomers [30, 27, 13].

Currently, Arkema is one of the leading suppliers of PEKK, commercialising this polymer in the neat form, with glass-fibre or carbon-fibre. The neat PEKK form is sold in three different series: Kepstan 6000, Kepstan 7000, and Kepstan 8000. The properties of one grade of each series are presented in Table 2.2 [31–33].

2.2.2 Synthesis

The high melting temperature and insolubility of PAEKs have several positive aspects regarding performance (Section 2.2); however, they complicate the synthesis of high molecular weight chains unless reaction conditions are used [20]. Some attempts started by DuPont in the 1960s with the synthesis of PEKK using Friedel-Crafts acylation method, but only low molecular weight PEKK was obtained [35]. Although different methods were developed, they also present limitations that need to be considered when deciding the best synthesis route.

Two main routes are used to synthesise PAEKs: electrophilic acylation and nucleophilic substitution reaction. The electrophilic acylation, also known as Friedel Crafts acylation, was developed by DuPont in 1962. It consists of condensing one aromatic compound from the group of aryl ethers (e.g., diphenyl ether) with a diacid halide from the aromatic hydrocarbon dicarbonyl halide group (e.g., isophthalic chloride or terephthalic chloride). The reaction is carried out in the presence of Friedel-Crafts catalyst (aluminium chloride

Table 2.2 General properties of three Arkema's PEKK set of grades of different series [12, 34, 33].

Properties	6002 [12]	7002 series [33]	8002 [34]
Flow level	Medium	Medium	Medium
Density (g cm ⁻³)	1.27	1.29	1.29
Water absorption (%) [2mm thick, immersed in water at 23 °C for 24h]	0.2	0.2	0.2
Melt volume flow rate (cm ³ 10 min ⁻¹) [380 °C 5kg ⁻¹]	35	35	35
Melting point (°C) [20 °C min ⁻¹ , 2 nd heating]	n/a	331	360
Melting point (°C) [After cooling below 0.5 °C min ⁻¹]	300-305	n/a	n/a
Glass transition temperature (°C) [20 °C min ⁻¹]	160	162	165
Tensile Modulus* (GPa) [23 °C, 5mm min ⁻¹]	2.9	3.8	3.8
Ultimate tensile strength (MPa) [23 °C, 5mm min ⁻¹]	88	110	112
Elongation at break (%) [23 °C, 5mm min ⁻¹]	>80	20	20
Tensile strength at yield (MPa) [125 °C, 25 mm min ⁻¹]	53	61	63
Flexural modulus (GPa) [23 °C]	3.0	3.9	3.9
Flexural strength max. (MPa) [23 °C]	128	168	171
Flammability rating [UL-94, 0.8 mm]	V-0	V-0	V-0
Processing temperature (°C)	320-360	340-360	375-385

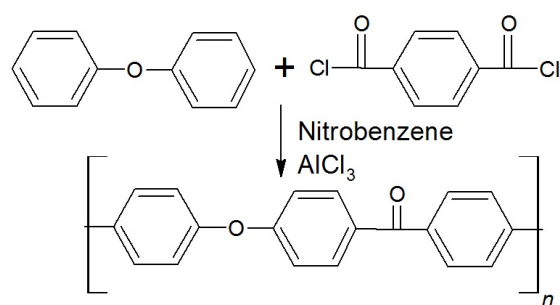


Fig. 2.3 Electrophilic acylation reaction [20].

is preferred) using nitrobenzene as solvent at a temperature range between 50 and 125 °C. This reaction is shown in Fig.2.3 [35]. Friedel-Crafts acylation is currently employed in PEKK synthesis, where diphenyl ether (DPE) is prepared with terephthalic acid (T) and isophthalic acid (I) in different ratios [13, 27]. This is a low-cost route, but only low molecular weight polymers can be obtained, with inherent viscosity (IV) of 0.18 dL g⁻¹ [35].

In 1964, Goodman at ICI (current Victrex) developed a self-condensation method that could provide higher molecular weight and IV of 0.5d L g⁻¹ [16, 36]. Further development was performed aiming to achieve even higher molecular weight (1.02 - 2.76 dL g⁻¹) PAEEKs using liquid hydrogen fluoride as solvent [37] to synthesise perfectly alternating copolymer with resistance to high heat deformation [38].

The nucleophilic substitution reaction uses activated aromatic dihalides and aromatic di(phenolates) to make PEEK. The activation of the aromatic dihalide is obtained using a strong electron-withdrawing group, such as carbonyl, sulfone, or phosphine oxide [20]. Johnson et al. [39] first attempted to produce PEEK by nucleophilic substitution reaction. They synthesised PEEK from bis(phenolate) with activated aromatic dihalides using dimethyl sulfoxide (DMSO) as solvent and NaOH or KOH as base. They found it challenging to achieve high molecular weight through this process because of the crystallinity and insolubility of PEEK in the DMSO solvent. In 1981, Attwood et al. [36] prepared PEK from the polycondensation of fluorophenoxide and bis-4-fluorophenyl ketone. The reaction used diphenyl sulfone (DPS) as solvent and it was performed at temperatures between 280 °C and 340 °C to obtain solubility. Fig.2.4 illustrates this process. In 1982, ICI first commercialised Victrex PEEK using this method. Despite achieving high molecular weight, this route is quite expensive, and careful optimisation is required at high temperatures since side reactions, such as ether exchange and cleavage, can occur.

Aiming to reduce the cost for PEK synthesis, Fukawa et al. [40] replaced the fluoro monomers proposed by Attwood [36] by activated chloride monomers in a reaction of 4,4'-dichlorobenzophenone with sodium carbonate at high temperatures and in the presence of silica/copper salt catalyst. They successfully achieved PEK polymer with an IV of 1.15 dL g⁻¹, and other PAEK copolymers with an IV equal or higher than 0.85. Further

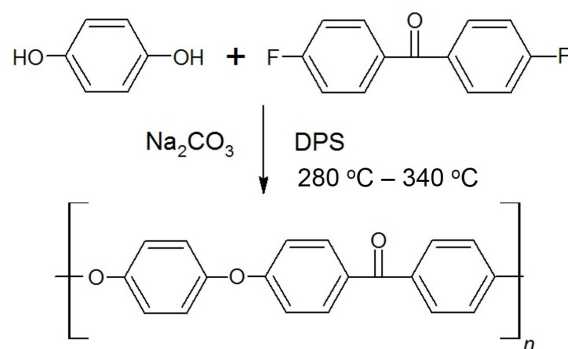


Fig. 2.4 Nucleophilic substitution reaction. Adapted from [20].

improvements were conducted to reduce the time of polymerisation and remove the use of base and solvent, as referred by Jinlian Yang and Kricheldorf et al. [20, 41].

Other studies attempted to synthesise PAEKs using soluble precursors to overcome the low molecular weight obtained by both routes - electrophilic and nucleophilic reactions. The soluble precursors route consists of synthesising amorphous PAEK by attaching a side group to the structure; a second reaction later removes this group. In 1987, Kelsey et al. [42] polymerised polyketide from cyclic ketal of 4,4'-dihydroxy benzophenone and 4,4'-difluorobenzophenone at 150 °C using dimethylacetamide as solvent. Polyketal structure was then converted to PEK by acid-catalysed hydrolysis. As the process was carried out at a relatively low temperature, they obtained PEK with minimum defect, excellent physical properties, a high degree of crystallinity, and high T_g , suggesting a uniform linear backbone structure.

In 1990, Risse and Sogah [43] obtained PEEK with t-butyl as side group by reacting t-butyl hydroquinone with 4,4'-difluorobenzophenone. The reaction took place at low temperatures using DMSO as solvent. The t-butyl side group was removed by retro Friedel-Crafts alkylation in the presence of Lewis acid catalyst (e.g., $\text{CF}_3\text{SO}_3\text{H}$). With this method, they achieved high molecular weight PEEK with an IV of 2.7 dL g⁻¹. In 1994, Pandya et al. [44] reported a novel method to produce polyketone by reacting bis(α -aminonitrile) derivatives with activated aromatic dihalides to form a carbon-carbon bond. The second step consisted of reacting isophthalamonitrile with 4,4'-difluorophenyl sulfone to produce poly aminonitrile. This reaction was conducted at room temperature using dimethylformamide as solvent and NaH as base. Finally, acid hydrolysis of polyaminonitrile was carried out to provide high molecular weight poly(ketone ketone sulfone).

PAEKs can also be produced by other routes, such as carbon-carbon coupling and ring-opening polymerisation. They are not the focus of this work but can be widely found in the literature [45–49].

2.2.3 Fundamentals of crystallisation

Crystallisation is the process of transforming a random liquid phase into an organised and periodic crystalline structure. It starts at T_m for crystallisation from the melt, but crys-

tallisation from solution is also possible. In polymers, crystallisation is highly dependent on the rate of cooling - the faster the cooling, the less time the chains have to organise, often solidifying into glassy solids. As polymers do not achieve a perfectly regular crystal lattice, they are never entirely crystalline but measured in terms of degree of crystallinity [50].

Understanding crystallisation is essential to control the mechanical properties of semicrystalline polymers. This property is often divided into two stages: nucleation and growth. Several studies attempted to describe crystallisation, starting from Gibbs theory and later extended by Becker and Döring (1935) [51], Avrami (1939-1941) [52–54], Turnbull and Fisher (1949) [55], Hillier (1965) [56] and Hoffman and Lauritzen (1961/1973) [57, 58]. These theories are based on the creation of a new phase when a polymer is cooled from the melt. This phase is formed when the decrease in free energy due to phase transition (heat of crystallisation) overcomes the increase in interfacial free energy, as reported by Gibbs's theory. Therefore, the growth of new particles depends on the ratio between surface area and volume. When the critical size is achieved, nuclei tend to stable and grow, whilst lower size particles tend to re-dissolve. Fig.2.5 illustrates this change in energy and the critical radius to form a stable nucleus.

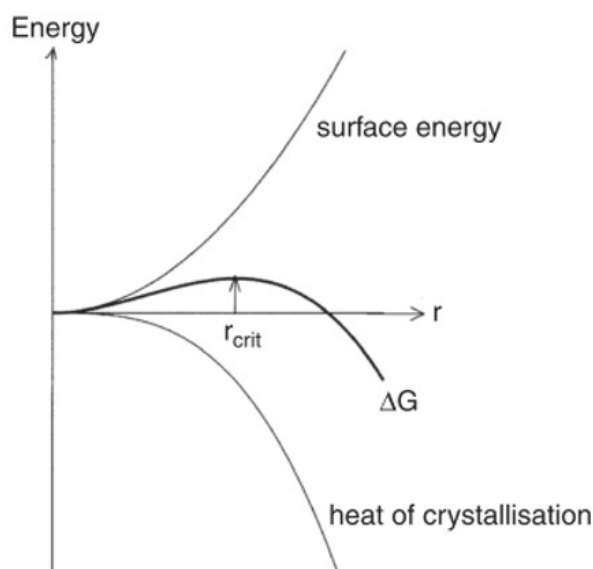


Fig. 2.5 Energy change to form spherical nuclei during crystallisation. The difference between the surface energy and the heat of crystallisation gives the total energy ΔG [50].

The rate of crystallisation is determined by the rate of nuclei formation and their rate of growth. The range of temperature for crystallisation is an intrinsic property of the polymer, but is usually from 10 °C below T_m to 30 °C above T_g , being quite slow close to T_m due to the decrease of driving force, accelerating up to a limit and then slowing down close to T_g as the diffusion of the polymer chains is hindered [50, 59].

From the several theories developed to describe crystallisation, Avrami's model [54, 53, 52] is possibly the most popular. This model predicts the degree of crystallinity by

assuming a solid-to-solid transformation in a stationary isothermal condition [60, 61] according to Eq.(2.1) [62, 60, 54, 53, 52],

$$1 - X_r = \exp(-Kt^n), \quad (2.1)$$

in which X_r corresponds to the maximum achievable degree of crystallinity (%), t is the crystallisation time (s), n is the Avrami exponent, and K is the Arrhenius-type rate constant. The constant n depends on the mechanism of nucleation and the form of crystal growth: $n \sim 1$ infers heterogeneous nucleation with stick growth type, n values of 2 suggest heterogeneous nucleation with disc-type growth [63], n of 3 refers to instantaneous nucleation of spheres, and n is equal to 4 when spherulites nucleate sporadically [64]. K constant takes into account nucleation and growth parameters and can be calculated through Eq.(2.2) [50]:

$$K = \frac{4}{3} (\pi v^3 N \rho^*), \quad (2.2)$$

in which v is the rate of crystal growth (nm s^{-1}); N is the number of nuclei per unit volume, and ρ^* is the relative density. Nonetheless, predicting crystallisation can be quite a complex task, and very often, the results do not match the theory. The Avrami constant n usually starts between 3 and 4 but drops as crystallisation progresses. Therefore, it is often divided into primary and secondary crystallisation. The primary crystallisation refers to the initial stage where theory and experiment data match, whilst secondary crystallisation starts when the Avrami equation cannot predict crystallisation [64]. More recent studies have created different models in order to predict secondary crystallisation [29, 65, 56]. Velisaris and Seferis [65] assumed two Avrami type crystallisation processes occurring in parallel and independently. In contrast, the Hillier model starts from the premise of constant radial growth of spherulites (Avrami postulate), followed by an increase in crystallinity within them to account for secondary crystallisation [56]. Hsiao et al. applied Hillier's model to PEKK polymer by creating a two-stage kinetics model in which nucleation growth is assumed sporadic and three-dimensional during primary crystallisation, while the second stage considers a two-dimensional or diffusion-controlled crystallisation with n equals to 2. They concluded that the modified Hillier model is more suitable to describe secondary crystallisation than the Velisaris and Seferis model [29].

Several experimental studies were developed in parallel with crystallisation models applied to PAEK polymers [66, 61, 67]. Blundell and Osborn [67] compared the crystallisation behaviour of PEEK with PET, and found very similar kinetics for both polymers, but with the main transitions of PEEK being ~ 75 °C higher. When investigating the crystallisation behaviour of PEEK, Cebe and Hong [61] found that most of the crystallinity fraction (from 0.45 to 0.7) is developed in the secondary process, and n and K factors are only constant between 0.03 and 0.2, in which crystallisation is driven by the primary process alone. Basset et al. [66] attributed the primary process to the formation of lamellae, whilst the secondary process is caused by their subsequent infilling; Wang et al. [68] confirmed these results for PEKK blends. In these studies, the two processes are identified

as two different peaks recorded during heating in the DSC; the highest peak corresponds to the lamellae formation.

According to Könnecke [69], the Avrami exponent n is always between 2 and 2.8 for all the PAEK structures crystallised from the melt or subjected to cold-crystallisation. Nonetheless, Vasconcelos et al. [63] claim that these values of n are only achieved in the absence of a secondary crystallisation, which is observed at temperatures equal or below 305 °C. At 305 °C, the first crystallisation has an n value of 1.4 with stick growth type geometry and heterogeneous nucleation, whilst the second stage of crystallisation cannot fit into Avrami's model of crystallisation [63].

Tardif et al. [70] were able to describe PEEK crystallisation kinetics using the Hillier model to account for secondary crystallisation. They ran a series of isotherms in flash-DSC and found a maximum crystallisation rate at 230 °C with n of 3, indicating instantaneous nucleation with subsequent spherical growth. At isotherms below 200 °C or above 300 °C, crystallisation was minimum and challenging to assess under flash-DSC.

Choupin et al. [71, 27] developed a kinetic model to predict the crystallisation of PEKK copolymer based on the derivative of the Hillier crystallisation model. They applied Avrami crystallisation in the first stage and a modified Hillier model to predict secondary crystallisation, with the assumption that the secondary crystallisation process starts from the first element that has been included in the lamellae at time θ . This is described by Eq.(2.3):

$$\alpha_2(t) = \int_0^t \alpha(\theta) \frac{d}{dt} (\alpha_2(t - \theta)) d\theta, \quad (2.3)$$

in which $\alpha_2(t - \theta)$ is the relative volume fraction at time t . The model fitted the kinetics of crystallisation of PEKK by considering changes in the heat flow during isothermal experiments in the DSC. They achieved an Avrami exponent of 2 for the primary crystallisation stage, and an exponent equals 1 for the secondary stage, which was found to be an instantaneous one-dimensional nucleation growth. For PEKK with a T/I concentration of 60/40, they observed a delay in nucleation initiation attributed to the slow crystallisation kinetics, which is maximum at ~ 230 °C [27]. This delay was accounted for in the model, which successfully predicted kinetics of crystallisation of PEKK with T/I ratios of 70/30 and 60/40 [27, 71].

Other studies focused on investigating the physical phenomenon behind nucleation and crystal growth of polymers [57]. Close to T_m , the ability of chain realignment is facilitated by the reduced viscosity of the liquid phase and the increase of free energy within the system. These factors are so strong that any potential nuclei are disrupted before growth takes place, therefore increasing the time for polymer nucleation and formation of spherulitic crystallites. On the other hand, temperatures close to T_g significantly reduce chain mobility and increase liquid phase viscosity. These factors decrease the chances for nuclei formation.

Primary nucleation can be either homogeneous or heterogeneous. Homogeneous nucleation starts randomly from the melt as a result of thermal fluctuations in the local

order. In practice, however, it is almost impossible to exclude foreign particles from the system; therefore, heterogeneous nucleation is dominant as it starts from the surface of microscopic and insoluble particles randomly disposed in the melt [72]. Secondary nucleation is the predominant mechanism of nucleation and only occurs in the presence of crystals from the crystallised material.

The degree of crystallinity of PEEK strongly depends on chain rearrangement, which occurs in the presence of large surface/volume ratios and high free enthalpies at the surface of lamellae, therefore enabling crystallisation of metastable lamellae. Gardner et al. [13] investigated the crystallisation of PEKK using wide X-ray diffraction (WXR) and Differential Scanning Calorimetry (DSC) techniques. They found two endotherm peaks; the broad peak corresponds to the actual melting of the lamellae, which are able to reorganise at higher temperatures, whilst the second peak refers to chains that were not able to rearrange fully as a result of high cooling rates. They concluded that it is possible to shift the lower endotherm to the higher endotherm by increasing the lamellae thickness of PEKK, which decreases the chemical potential of the system and enables more chains to rearrange. This shift can be achieved either by partial melt followed by sufficient time for recrystallisation, or can also involve fractionation of molecular length.

Basset [64] specifies the different crystal formation in semicrystalline polymers exposed to melt-growth or solution growth. In solidification from the melt, there is a complete reorganisation of the structure, while in solution growth, molecular conformation remains except for minor readjustments. Olley et al. [73] noticed that at temperatures well below T_c , PEEK only shows a small-scale organisation of the structure. The samples cooled from the melt, however, presented uniform microspherulites with stacked lamellae of ~ 15 nm of periodicity, whilst cold-crystallised samples showed more heterogeneous structure with thinner and smaller lamellae of ~ 10 nm, a result of a much higher nucleation density. They also observed an increase in lamellae thickness with the increase of temperature below and above T_m , which suggests the dual composition of the lamellae (amorphous and crystalline regions).

Motz and Schultz [59] investigated the solidification and kinetics behaviour of PEEK. They concluded that at slow cooling rates of 1.25 °C min^{-1} , PEEK starts crystallising at 315 °C and the crystallisation occurs at a narrow temperature range of 10 °C. In a fast solidification of 160 °C min^{-1} , crystallisation process starts at 285 °C, 30 °C lower than at slow cooling rates. Interestingly, the cooling rate seems to have a limiting effect on the degree of crystallinity, possibly due to the high nucleation density of this polymer. Cebe and Hong [61] confirmed this phenomenon and found a degree of crystallinity of about 29% for PEEK cooled from the melt at cooling rates varying between 10 °C min^{-1} and 160 °C min^{-1} . However, Motz and Schultz [59] added that a faster cooling rate than crystallisation rate might lead to incomplete crystallisation, and they highlighted that different cooling rates affect final crystal morphology.

So far, crystallisation and different theories applied to predict crystallisation were discussed. As briefly stated, by controlling crystallisation, it is possible to achieve different

morphologies as spherulites size and thickness may vary. Section 2.3.1.2 will investigate the morphology of PAEKs.

2.2.3.1 Morphology

The PAEK family has an orthorhombic crystal structure and crystallises in the form of spherulites [74, 36, 75]. The chains are arranged at the corner $(0,0,Z)$ and centre $(\frac{1}{2}, \frac{1}{2}, Z')$ of the unit cell and exhibit an extended conformation with adjacent phenylene groups rotating $\pm\gamma$ out of the plane of the linkage groups, in which γ varies from 30 to 50° [13]. The diffraction pattern of PAEKs is similar when crystallised from the melt; however, a shift to lower angles is observed with the increase of ketone content in the molecule. This shift changes the unit-cell parameters slightly, which are shown in Table 2.3 [13, 74].

Table 2.3 Lattice parameters of PAEKs [13, 74].

Polymer	Ketone content (%)	Crystal structure	Lattice parameters (Å)		
			a	b	c
PEK [74]	50%	Orthorhombic	7.63	5.96	10.00
PEEK [74]	33%	Orthorhombic	7.75	5.86	10.00
PEKK [13]	67%	Orthorhombic	7.69 (form I) and 3.93 (form II)	6.06 (form I) and 5.75 (form II)	10.16 (form I and II)

The thermal history directly influences the degree of crystallinity of PAEKs, which can vary from 0% for samples quenched in cold water to 42% for samples of PEEK crystallised at temperatures around 320 °C [76, 75]. The arrangement of PEEK is energetically favoured to be a zigzag plane with the same orientation to all molecules. Therefore, bc planes become the favoured nucleation faces with b as the preferred growth direction and a as the width of the lamellae [75]. As opposed to polyethylene, PEEK has a lower degree of crystallinity; this is possibly due to the rigidity of the chains [77].

Lovinger and Davis [75] investigated the morphology of thin films of PEEK crystallised from the melt. They noticed that PEEK shows a strong tendency to superimpose a uniplanar lamellar orientation to the growing spherulites, as shown in the configuration (1) of Fig.2.6. The superposition is due to constraints in lamellae growth, whilst the morphology of typical polymers (Fig.2.6(2)) can grow in any orientation. At lower crystallisation temperatures, the lamellae are disposed in a more random pattern, although the cylindrical symmetry is still dominant. The quenching of PEEK leads to random lamellar aggregates and small spherulites. A similar conclusion was drawn by Jonas and Legras [78], who observed that PEEK is not able to make sharp folds when exposed to high supercooling rates. Deslandes et al. [79] confirmed the significant changes in the crystallisation of PEEK with thermal history, and pointed different phenomena - destruction/formation of nuclei, chain branching - occurring at different times and temperatures.

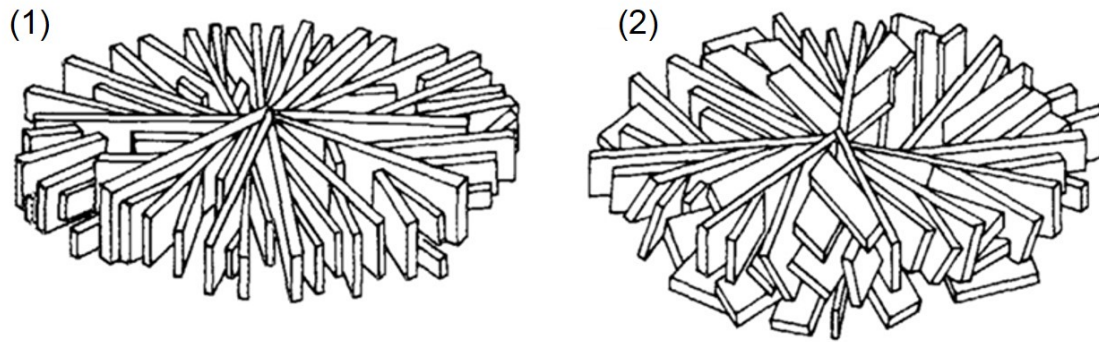


Fig. 2.6 Representation of spherulites configuration in (1) PEEK and in (2) typical polymers [75].

PEKK is a polymorph and can crystallise in two different forms: form I and form II. A top view of these crystal structures are represented in Fig.2.7 [80]. Both forms have the alignment of the chains limited by interchain interactions of weak dipoles and phenyl-phenyl interactions. Form I is the conventional structure, in which phenyl-phenyl interactions among chains are aligned edge-to-face [13]. Form II is achieved by solvent crystallisation or cold crystallisation [81, 82] and is shown by the WXR peak at 2θ equals to 15.6° . In this form, phenyl-phenyl interactions are aligned face-to-face. Form II seemed to be exclusive for PAEKs with a higher concentration of ketone. Nonetheless, Liu et al. [83] could produce PEEK with form II through strain-induced crystallisation. Garcia-Leiner et al. [84] claim that both forms can be found under certain conditions in LS and Fused Deposition Modelling (FDM) of PEKK. However, they do not provide further explanation.

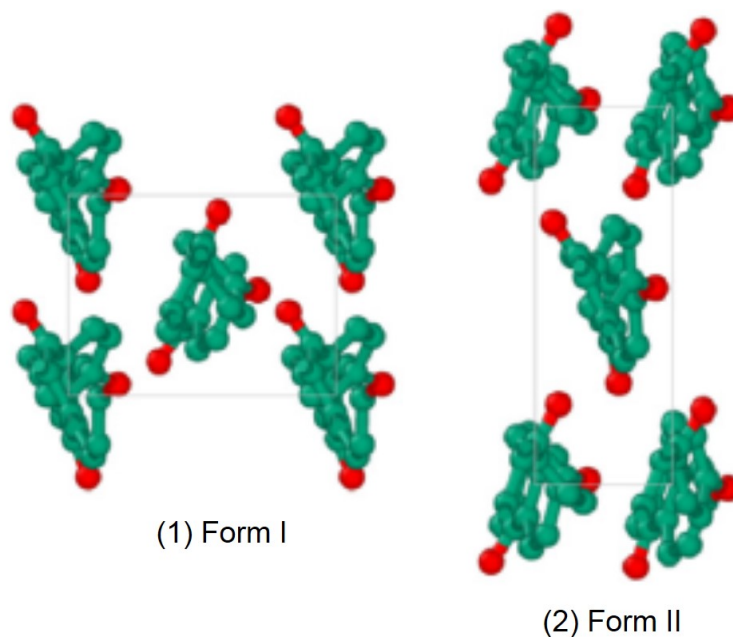


Fig. 2.7 Different morphology configurations of PEKK, view from the top of the crystal structure. (1) Form I and (2) form II [80].

The two crystalline forms are associated with different melting peaks of PEKK. Gardner et al. [13] carried out DSC scans of PEKK with different thermal histories and concluded that the endotherms at 300 °C and 330 °C are related to the melting of form I, whilst the endotherm at 280 °C is associated with the melting of form II. They found another endotherm at 225 °C, which they attributed to a mixture of form I and form II. The melting of form I at 330 °C leads to a recrystallisation or reorganisation process of the crystal structure, which is explained by the increase in chain flexibility of PEKK with the same concentration of T and I moieties (50/50). They also noticed another endotherm at 220 °C for annealed specimens, which they associated with the double-melt behaviour of PEKK that seems to occur repeatedly at 10 °C above the annealing temperature. This behaviour refers to the growth of an interlamellar crystalline structure within the lamellae [56].

2.3 Particle and Powder Bulk Properties

The rapid evolution of LS as a manufacturing technology to produce final parts led to increasing interest in developing and improving materials to meet the usage criteria of this technique. The process requires materials in powder format with specific properties to reach high consolidation and good performance. In this section, these requirements will be reviewed and contrasted with the limitations of material and powder production.

There is a limited number of technologies available to produce polymeric particles with desired LS properties. Table 2.4 describes the main methods. More recently, different technologies [85–88] were developed to improve polymer particles with inappropriate size and morphology; they will be discussed in Section 2.3.5.

The following sections will explore the main properties affecting powder performance in LS. Firstly, particle properties are explored. Then, these properties are associated with processing performance by investigating the bulk and processing environment; this is presented in the diagram of Fig. 2.8.

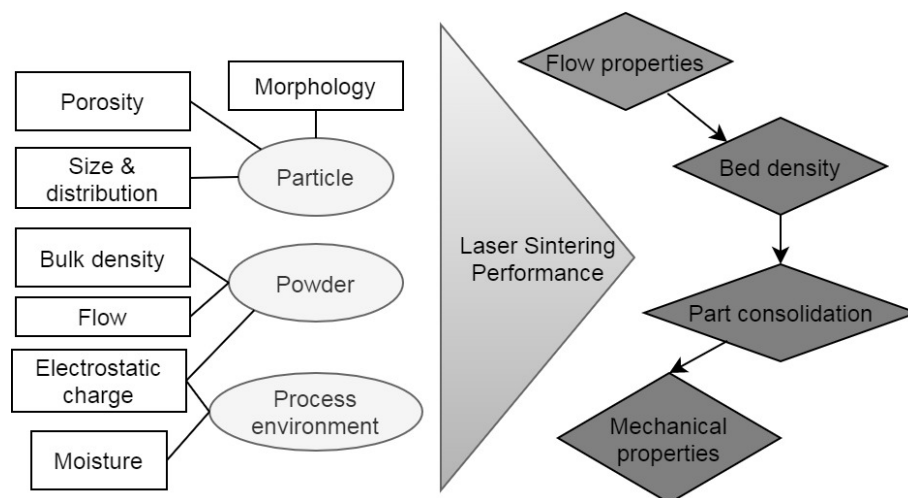


Fig. 2.8 Diagram illustrating the effect of particle and powder properties and environmental conditions in the final LS performance.

Table 2.4 Processes available to produce powder for LS.

Process	Description
Cryogenic milling	Popular technique to comminute polymer grains by mechanical impact. It is a simple, low-cost process and applicable to a wide range of polymer materials, including PAEKs [89]. However, the process is very energy consumptive, and post-milled particles often present irregular morphology with sharp edges, rough surface, and wide size distribution [90, 91]. TPE and thermoplastic polyurethanes (TPU) [92] are known as commonly comminuted by this technique.
Melt emulsification	The polymer matrix is dissolved in a dispersion phase under heat and pressure. The solution is stirred, and the temperature is gradually reduced to below T_m of the polymer until precipitation takes place [93]. This technique enables the production of almost spherical particles with low porosity and a narrow and controlled particle size distribution. Furthermore, the molecular weight can be controlled. The main limitation is the incorporation of additives, which are usually added in a later stage. The PA12 powders for LS are produced using this method [94].
Co-extrusion of non-miscible polymers	Two non-compatible polymers are dispersed in a piece of extrusion equipment set above T_m of the dispersed phase. The system is cooled down, and the microdroplet phase starts solidifying, which is separated from the dispersion medium by filtration. This method produces nearly perfect spheres with smooth surface roughness. The co-polypropylene polymer icoPP is produced using this process [95].
Spray drying	Polymer in a solution is atomised into spray droplets, which get in contact with hot air from a chamber to enable drying. This process results in spherical particles and is used to produce polyamide 6 powder and PP for LS [93, 96, 97].

2.3.1 Particle properties

Particle characteristics can significantly affect processing performance and final LS part properties. In the manufacturing of powders, these characteristics should be controlled to enhance flow and bulk density. The main particle characteristics will be discussed in the following sections.

2.3.1.1 Size and distribution

Producing powder for LS can be a challenging task. The first limitation is the layer thickness, as powders must have a lower diameter than the thickness specified during slicing to obtain parts with an accurate dimension. Furthermore, particle size distribution (PSD) [4] is strongly associated with the final consolidation of the sintered part [98].

Large particles prevent the achievement of homogeneous layers, which can result in part porosity. Fine particles are not desirable either as surface forces may cause agglomeration, which prevents free flow and affects the recoating process [4]. Several studies have analysed PSD for powders with application in LS [99–104]. Shi et al. [103] proposed an optimal PSD varying between 75 μm and 100 μm and was later contested by Goodridge et al. [102], who proposed a PSD between 45 μm and 90 μm for LS PA12 powder. According to Yang and Evans [101] and Amado et al. [100], however, ideal particle size for LS has a narrow distribution around 60 μm with a low amount of fine particles below 10 μm . For Lothar Fiedler et al. [105], particle size distribution must be between 1 and 100 μm with a mean diameter equal or larger than 10 μm .

Due to their surface volume, small particles tend to melt faster than large ones and fuse earlier on the powder bed. They also improve packing density by filling the interstitial gaps [104]. Vashishtha et al. [99] observed that small particles could partially eliminate warping and shrinkage of sintered parts. However, very fine powder leads to poor flow, agglomeration, undesired sintering [4, 106], fogging during LS, and difficulties in removing unsintered powder from the surface of LS parts at the post-sintering stage [107]. For these reasons, Schmid et al. [108] did not recommend large amounts of particles smaller than 20 μm . The only exception to having small particles is when surface treatment is applied to disrupt the Van der Waals forces dominating their surface, as shown for PBT powder [109].

According to Vasquez et al. [110], large polymer particles are less likely to melt entirely as a result of reduced thermal diffusivity, leading to porosity and rough surface of sintered parts. Hao et al. [111], however, could not identify any effect of larger PSD on the process and properties of final sintered parts.

Particle size also affect the density and surface roughness of the powder bed. As these parameters are difficult to assess, most measurements were performed through simulations. Parteli and Pöschel [112] applied a discrete element method (DEM) to understand the effect of particle size and shape when being spread using a roller as the recoating tool. They found that broader particle size distribution leads to a higher surface roughness of the bed due to the agglomeration of smaller particles, which leads to packing porosity.

For Xiang et al. [113], however, no correlation was obtained between particle distribution and bed density, but with layer thickness - the thicker the layer, the higher the packing density. Haeri et al. [114] concluded that segregation could occur in different layers of the powder bed if particle distribution is broader than ideal. Nonetheless, they stated that this phenomenon is a combination of particle size and morphology effect.

Currently, the most commonly employed method to measure PSD is laser diffraction technique; other techniques include sieving and microscopy/imaging analysis [115]. Laser diffraction is a precise technology when applicable to measure spherical particles. As described in Section 2.3, however, the processes available to produce LS powders often result in particles of irregular shape, therefore investigating morphology is crucial. Particle morphology will be discussed next.

2.3.1.2 Morphology

Morphology is highly associated with flow performance [116, 98, 117, 118, 100, 101] in LS. In addition to facilitating flow, spherical particles improve packing efficiency by reducing surface area to volume ratio [4].

Chan and Page [119] claim that angular shaped particles with irregular surface cause mechanical interlocking, reducing flow efficiency and increasing overall cohesive behaviour. Ziegelmeier et al. [98] noticed an increase in flow properties for denser particles of TPU and TPE with more spherical morphology; however, these particles presented a larger size. They concluded that the more spherical the particles, the higher the packing efficiency, whereas angular shaped particles showed a random bulk structure resulting from interparticle bridges and internal friction forces of particles with an irregular surface.

Verbelen et al. [120] were able to produce dense and smooth powder layers of TPU particles with irregular morphology. The parts produced, however, showed high porosity, which could be associated with the undesired shape of the particles in the study. Mielicki et al. [121] investigated the effect of LS processing time in PA12 powder exposed to bed temperature and found changes in surface roughness with ageing for particles larger than 100 μm . They concluded that PA12 powder reuse could lead to part surface roughness and porosity.

Morphology may affect bulk density; this is described in Fig. 2.9 in terms of relative roundness. The relative roundness is a shape descriptor defined as the ratio between the surface area of a sphere with the same volume as the test particle (S_s) and the actual surface area (S).

Methods to measure particle morphology

Several studies mention particle shape as a critical factor for successful powder processing in LS and claim that spherical particles are preferred [117]. However, due to the complexity of shapes and the difficulty of measuring it on a large scale, few studies were able to quantitatively associate morphology with LS processing and performance of final parts. Berretta et al. [117] analysed different powder grades for LS with the assistance of

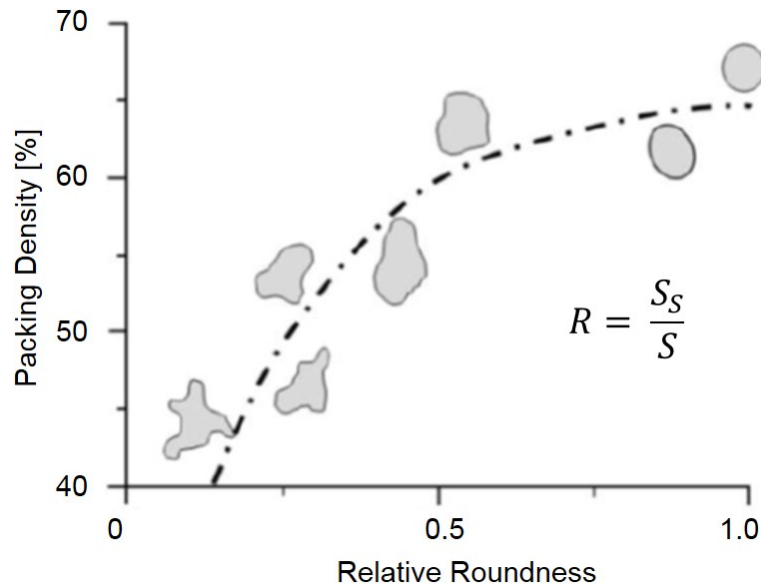


Fig. 2.9 Effect of particle morphology in powder bulk density [122]. Relative roundness R is defined as the ratio between the surface area of a sphere with the same volume as the test particle (S_s) and the actual surface area (S).

the ImageJ imaging technique. They found that commercially LS grades (PA12 and PEK) are round, circular, and show reasonably equiaxial shape, with high values of solidity but middle to low values of aspect ratio.

The method most commonly employed to measure particle shape is microscopy, followed by imaging analysis. This method is demanding if applied to a large scale of particles. Another alternative is the use of particle sorption techniques, which can measure the Brunauer-Emmett-Teller (BET) surface area [123].

More recently, different types of equipment were developed [124–126], offering automated and rapid morphological information of several particles. They usually involve a camera that captures pictures of particles in the static or dynamic condition. Then, the imaging software processes the captured images. Amongst the parameters used to measure particle morphology, area, perimeter, circularity, sphericity, roundness, convexity, and aspect ratio are commonly employed.

The area from imaging analysis is measured in square pixels and is calibrated to square units (μm^2 , mm^2 , etc.). The perimeter is assessed by the pixels in the outside boundary of the selection [127]. The ratio between area and perimeter square gives circularity, a direct measurement of particle morphology (Eq.(2.4)). This descriptor measures the proximity of a particle to a circle and varies between 0 to 1, being 1 a perfect circle [128].

$$\text{Circularity} = 4 \times \pi \times \frac{\text{Area}}{\text{Perimeter}^2} \quad (2.4)$$

Sphericity uses a similar approach to circularity to measure how close the morphology of a particle is to a circular geometry. This parameter is measured according to Eq.(2.5).

$$\text{Sphericity} = 4 \times \pi \times \frac{\text{Area}}{\text{Perimeter}} \quad (2.5)$$

Roundness is another shape descriptor that measures the proximity to a circle but is more sensitive to elongated deviations. This parameter is calculated using Eq.(2.6). Values closer to one are associated with rounder particles [128, 127].

$$\text{Roundness} = 4 \times \pi \times \frac{\text{Area}}{\pi \times (d_{max})^2} \quad (2.6)$$

Convexity is an indication of surface roughness and varies between 0 and 1. The closer to 1, the smoother is the particle. Convexity is calculated by Eq.(2.7), in which C_{Hull} corresponds to the perimeter of the convex hull, which describes the contour done by a rubber band placed around the particle in the image [128].

$$\text{Convexity} = \frac{C_{Hull} \text{ Perimeter}}{\text{Perimeter}} \quad (2.7)$$

The aspect ratio (AR) is a useful method to describe fibres as it measures the largest diameter against the smallest diameter, as shown in Eq.(2.8) [128, 127].

$$AR = \frac{d_{max}}{d_{min}} \quad (2.8)$$

Other parameters include solidity, concavity, and compactness [128]. Only few studies associated particle morphology to their effect during the LS process and in final part properties [115, 117, 121].

2.3.1.3 Porosity

Particle density is another critical factor in LS, as it affects processing and final part performance. According to Drummer et al. [6], high powder density leads to sintered parts with higher density, dimensional accuracy, and strength, but flowability may be compromised. The presence of pores inside particles decreases powder bulk density, which can result in porous LS sintered parts [98]. An example of particles with porous structure is presented in Fig.2.10.

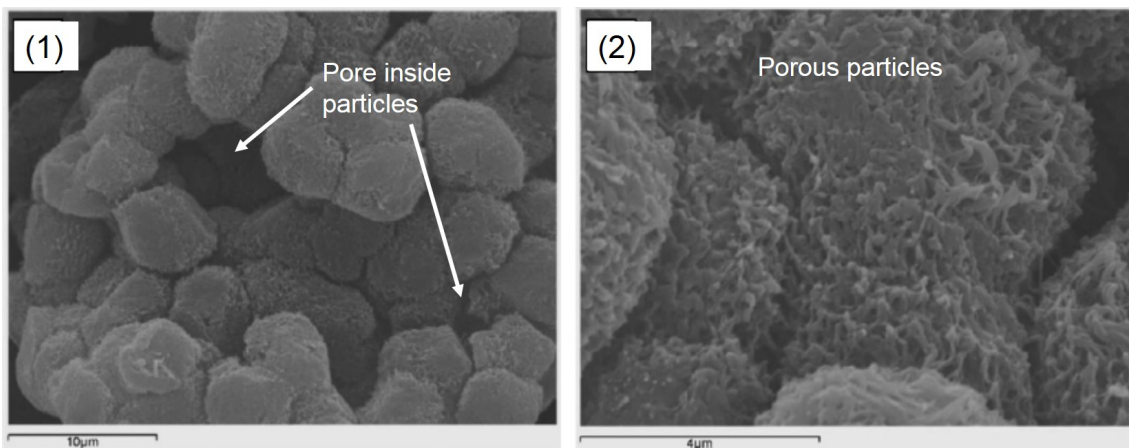


Fig. 2.10 SEM images of PEEK 150PF indicating (1) pores within the particle and (2) a porous particle structure. Adapted from [117].

By investigating lactose powder, Schweiger and Zimmermann [129] found that tensile strength between particles is higher for lower values of particle porosity, and cohesive forces are significantly reduced with porosity increase. In LS, most studies refer to bed porosity affecting part consolidation rather than the porosity of the feedstock [130–132]. However, the presence of pores in the particles' interstices can affect mechanical properties in LS, as it reduces powder bulk density. Low values of powder bed densities due to particle porosity can lead to porous structures, which compromise part elongation and may initiate/propagate cracks in the structure, accelerating part failure [2].

Nano-computed tomography (nano-CT) is the best alternative to measure porosity within the particles, but it is a relatively expensive technique. Therefore, studies often opt for microscopy analysis [117, 133], helium pycnometer [109, 123] and gas sorption techniques [134].

2.3.2 Powder flow: methods & properties

The ability of the powder to flow is key to guarantee successful LS processing and improve final part performance. Good powder flow allows consistent deposition of layers throughout manufacturing, increasing bed density, and, therefore, the consolidation of the sintered parts [4]. Several factors affect powders flow properties, from particle size distribution and morphology to processing temperature and the interparticle forces present in the system [135, 136]. The following sections will discuss different methods to assess flow and powder flow properties.

2.3.2.1 Methods to measure powder flow

One of the traditional methods employed to measure powder flow is known as the angle of repose (AoR) [137]. This method consists of quantifying the pile angle, which is the angle of a cone of bulk material over a flat surface. The powder is firstly dropped through a standard funnel to form the cone. The different angles formed with the surface are directly related to the flow properties of each powder grade, and the smaller the AoR, the higher is flowability [117]. Berretta et al. [117] measured the AoR of PA12, pure PEAK grades (commercially and non-commercially available), and filled PAEK powders with glass, hydroxyapatite, and calcium carbonate. They observed a slight improvement in the AoR for the grades with additives, according to their concentration and morphology. When additives in the nanometre size were included in the structure, a significant improvement in powder flow was achieved, decreasing up to 10° in the AoR with the inclusion of nano-particles of aerosil pharma. This improvement was attributed to the decrease in Van der Waals forces between a micrometric and a nanometric particle. From all the polymeric materials, PA12 showed the best flow performance (AoR of $38 \pm 1^\circ$), attributed to the particle shape of this grade - high values of roundness, circularity, and solidity - but also the physicochemical nature of the polymer.

Aside angle of repose, different techniques are used to characterise powder flow [138], mostly in the dynamic state, as it is shown to give more accurate results [100]. The most

traditional technique is described by ASTM D1895-17 [139] and consists of monitoring polymeric powder flow through a funnel. Although similar technique seems to work well for metallic powders, studies reported powder sticking to the walls of the funnel in the case of polymers [140]. Therefore, other techniques are employed to measure flow, as follows [138]:

1. **Bed expansion ratio:** Dynamic test to measure fluidized height versus upstream fluid flow under fluid drag load;
2. **Ring shear cell:** Measures shear force versus normal pressure/compression rate in a quasi-static test;
3. **Hausner ratio (HR):** Static test measuring the effect of powder weight by assessing loose and packed height with the number of taps.

The Hausner ratio is calculated by Eq.(2.9), in which HR is the Hausner Ratio, ρ_{tapped} is the density of the tapped powder and ρ_{bulk} is the density of the powder bulk. This test is used in literature to determine both powder flow and bed density in LS [138, 141].

$$HR = \frac{\rho_{tapped}}{\rho_{bulk}}. \quad (2.9)$$

Schmid et al. [138] assessed flow using HR and found it adequate to qualify and distinguish nine different LS powders. According to them, aired state condition seems to replicate more accurately the flow performance in LS, but powder compaction methods give some insights into static stability and compressibility of the powder bed.

Some studies found it challenging to relate powder flow in LS with the techniques listed above [142]. Up to date, there is not an established methodology to determine the ideal properties of LS powders, and most of the tests available explore individual characteristics, whilst several factors affect powder behaviour in LS simultaneously.

More recent technologies were developed to replicate the LS process, as the revolution powder analyser (RPA) [143] and the FT-4 powder rheometer [144]. The RPA uses a rotating drum and a digital camera system to describe powder flow in terms of the avalanche angle (Fig. 2.11(1)). The FT-4 powder rheometer consists of a blade rotating and translating simultaneously across a conditioned powder bulk and measuring the resistance to powder displacement regarding basic flowability energy (BFE) and specific energy (SE) [118] (Fig. 2.11(2)). Ziegelmeier et al. [98] performed the BFE test with the assistance of an FT-4 powder rheometer and found that packing density is inversely proportional to cohesivity. This cohesive behaviour was associated with particle size, as fine particles are more cohesive than coarse particles. In a different study [118], the same group assessed SE using an FT-4 powder rheometer and concluded the equipment is very accurate for predicting the flow of very fine particles, but could not differentiate two TPU powders with different particle size distribution.

The effect of holding polymer powder at bed temperature (T_{bed}) in LS, also known as processing temperature, is extensively mentioned in literature [146, 90, 147, 121,

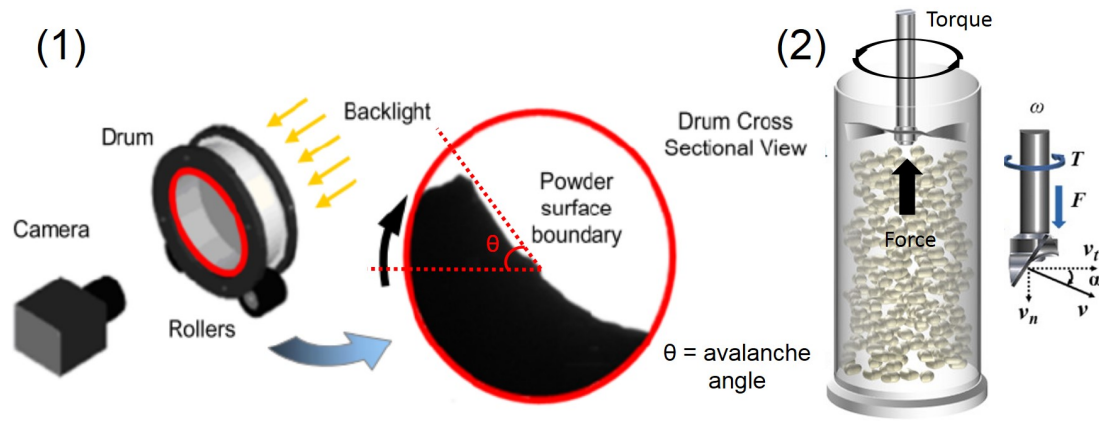


Fig. 2.11 Modern systems to assess powder flow. (1) Configuration of the revolution powder analyser indicating the avalanche angle (adapted from [145]) and (2) FT-4 powder rheometer indicating forces acting in the system and the angles of the blade (adapted from [144]).

148] and investigated when associated with powder recycling [149, 150]. Few studies attempted to assess particle and powder properties at high temperatures. Due to the lack of equipment available and the complexity of the measurement, the analysis remains challenging. Nonetheless, the application of heat can change particle and powder behaviour during LS and affect final part properties. These changes were reported by Mielicki et al. [121], who noticed an increase in the standard deviation of aspect ratio and sphericity values of particles larger than $100 \mu\text{m}$ exposed to T_{bed} of $174 \text{ }^\circ\text{C}$ at prolonged but different times.

Considering these thermal effects in LS, van den Eynde et al. [136] developed an in-house powder spread mechanism [151] coupled with IR ceramic heaters to replicate the heat input in LS. This system has a maximum operating temperature of $140 \text{ }^\circ\text{C}$, which is above the softening point of most commercially available polymers for LS but significantly below their processing temperatures. For high-temperature polymers like PAEKs, such a system would be of particular interest if able to operate at higher temperatures, since T_{bed} for these polymers is above their onset temperature of melting [152].

2.3.2.2 Flow properties

In LS, the powder must have suitable properties to produce uniform layers when spread across the powder bed. The desired behaviour would approach that of free-flow powders. According to Becker [115], however, free-flow is only achieved for particles larger than $250 \mu\text{m}$. As particles in LS range between 10 to $100 \mu\text{m}$, flow is disrupted by different interparticle forces [101, 100, 103], such as Van der Waals, friction and interlocking.

Van der Waals force is an electromagnetic force that is originated from the interaction of dipoles in the molecules [153]. In particles within the ideal range for LS, however, the main forces hindering flow are mostly mechanical, i.e., friction and interlocking, and are greatly affected by particle shape, size, and their surface roughness [98, 2].

Ziegelmeier et al. [98] investigated the effects of particle size distribution, packing, bulk density, and flow efficiency and correlated them with tensile strength, surface quality and consolidation of final laser sintered parts. They found an increase in part mechanical strength for powders with higher bulk density and flow properties, whilst surface quality was strongly linked to surface morphology affecting packing of the powder bulk. Good flow is also crucial to enable manufacturing - Koo et al. [154] reported difficulties in processing PA11 by LS, which they attributed to the poor flow performance of this powder.

Additives such as silica and carbon-black can be added to enhance powder flow, [4, 135, 6]. Verbelen et al. [142] assessed the powder flow of different polyamide grades of rough structure and sharp edges and found that the inclusion of additives significantly improved flow, therefore increasing bed density.

2.3.3 Powder bulk density: methods & properties

Bulk properties are highly dependent on particle characteristics and how the spreading mechanism compacts the particles. The interaction of these particles with each other may create interparticle forces that affect process performance and the final properties of LS parts. In addition to the forces generated as a result of particle interaction, there are also exterior forces resultant from the processing temperature and the interaction between the spreading tool and the powder, which may affect LS. The following sections will discuss methods to measure bulk density and the effect of processing in bulk properties.

2.3.3.1 Methods to measure bulk density

Bed density in LS can be measured by manufacturing hollow LS boxes, but full of powder inside, previously packed by the roller/blade, and weigh them before and after powder removal. This approach seems to be very accurate as it is able to monitor bulk density from *in situ* measurements [151, 155]. A similar method was conducted by Verbelen et al. [142], who developed a home-built setup in which a recoating blade spreads the powder, and the bed density is measured from the combined weight of 20 layers of polyamide powder.

The *in situ* measurements require the use of an LS system to assess bulk density, which can prolong the analysis. Hence, indirect measurements are commonly applied such as the Hausner ratio (Eq. (2.9)) [138], Carr index, consolidation test [123], conditioned bulk density (CBD) [144], and packing using RPA system [156]. The main issue with external systems is that they do not replicate the environment in LS, e.g., controlled atmosphere and temperature and the spreading mechanism of the recoater tool, which can affect powder density and flow behaviour. New systems have arrived to allow the measurement of flow at high temperatures, and other systems were modified to assess thermal effects in bulk density [136, 157]; this was explored in Section 2.3.2.1.

2.3.3.2 Bulk density properties

Powder bulk density is strongly associated with powder bed density in LS. This property is particularly important since the interaction between the laser and the powder is in the order of milliseconds [158]; hence initial powder packing has a remarkable effect in the consolidation of the final sintered parts and their mechanical performance [136, 138, 159]. Powder bulk density measures the unique characteristics of each particle (size, shape, etc.) interacting with each other in a static condition. Therefore, interparticle forces (friction, adhesion, and others) must be considered in addition to the intrinsic physical properties of the particles [123]. Furthermore, bed density is affected by processing characteristics that cannot be despised, e.g., the deposition mechanism and particle arrangement [160].

In respect to powder density, three main aspects may be considered: (1) the true density of polymer particles (particle porosity), (2) the densest packing arrangement for a particular grade with specific shape and size distribution (tapped density), and (3) the packing density generated from the spreading mechanism (bed density). These aspects are represented in Fig.2.12 for fully dense particles. From a process perspective, LS is best described by (3); typical values of bed density for PA12 powders range between 40 and 60% of the true density [161].

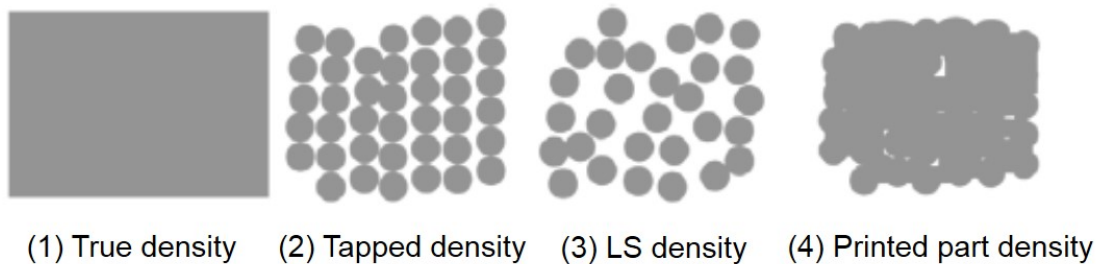


Fig. 2.12 Illustration of the different types of density measurements and their packing information [140].

In an ideal situation, one can achieve a maximum packing factor of 74% with face-centred cubic (FCC) structure of perfectly smooth and mono-sized particles with no interaction between them. In practice, particles are not spherical or smooth, and their random deposition on the powder bed leads to a heterogeneous particle arrangement. According to Becker [115] and Karapatis et al. [162], it is possible to optimise this density by filling the interstices with smaller particles, as shown in Fig.2.13, in which f_s is the solid fraction of small particles, f_L is the solid fraction of large particles and the maximum solid fraction f^* is achieved with a bi-modal distribution of small and larger particles. However, Ziegelmeier et al. [118] concluded that the presence of irregular particles substantially disrupt packing density, affecting the distribution of smaller particles filling the interstices of the bulk. This phenomenon was confirmed by Schmidt et al. [109], who successfully improved the morphology of PBT particles and therefore achieved higher bulk density and flow properties for this powder.

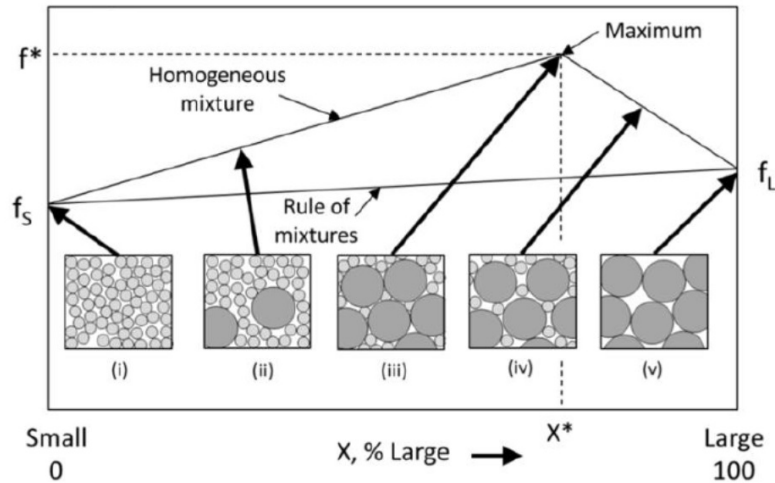


Fig. 2.13 Addition of small particles to enhance bulk density. f_s is the solid fraction of small particles, f_L is the solid fraction of large particles, and the maximum solid fraction f^* is achieved with a bi-modal distribution of small and larger particles [115].

Furthermore, particles have a variable diameter, whilst layer thickness in LS is constrained. For this reason, the top and bottom of the powder bed show lower powder compaction than the centre. In addition to size, particle shape seems to segregate throughout the powder bed [114]. Thakur et al. [163] mention that particles with higher aspect ratio lead to an increase of wall friction, i.e., the force generated between the particles and the lateral confining walls of the powder bed. Thus, a greater variation in density is found across the LS build. By applying a discrete element method simulation, Haeri et al. [114] confirmed this finding and showed that particles of $AR \geq 2.5$ tend to accumulate on the upper layers of the bed.

2.3.4 Other factors affecting powder flow

2.3.4.1 Electrostatic charge

Amongst other characteristics affecting powder behaviour is the electrostatic charge, which changes powder flow properties and hinders the achievement of uniform layers of powder [164]. Electrostatic forces are generated from the interaction of particle-charge and the transference of electrons between dissimilar materials [101]. It is proportional to the charge or surface charge density (q) and the contact distance between particles (r), as given by the relation:

$$F_{coulomb} = \frac{1}{4\pi\epsilon_0} \frac{q_1 q_2}{r^2}, \quad (2.10)$$

in which ϵ_0 refers to the permeability of the medium. According to Yang and Evans [101], particles can become electrostatically charged by the presence of crystalline defects, such as impurities or gas molecules in the structure, moisture, temperature, as a result of stress generated during milling, mixing or even by sieving and handling. Electrostatic charge directly affects powder flow and bulk density - Greiner et al. [165] attributed the

low powder bulk density of wet ground PBT to interparticle forces, including electrostatic charge.

The most popular method to assess electrostatic charge is using an electrostatic meter, which measures the electric field at a standardised distance. Zhang et al. [166], however, developed a new method to measure electrostatic charging in a free-fall test, which consists of two parallel copper plates connected to a high voltage power supply and a vibrating charging device.

The effect of electrostatic charge is particularly dominant in fine particles and can compromise powder flow [123]. A post-coating process can be used to cover the powder surface and limit such effect. There is also considerable interest in developing electrically conductive composites to ensure the dissipation of electrostatic charge [167].

2.3.4.2 Moisture

The dominant force resulting from the presence of moisture is capillary force, which creates moisture bridges inside the powder bulk [168]. However, moisture assumes different forms according to its concentration level and the material capability of absorption and reaction with water molecules. At low levels, moisture is present as adsorbed vapour, whilst above the critical value, liquid bridges are found [169]. Coelho and Harnby [169] defined the lower limit of humidity as H_{min} , which corresponds to the point at which one finds consistent and significant interaction resulting from the adsorbed layers. This parameter is dependent on Brunauer-Emmett-Teller (BET) constant as well as surface roughness. Hence, in a perfectly smooth surface, H_{min} depends on BET constant only, whereas the increase in surface roughness leads to an increase of H_{min} , and the effect of solid-vapour interaction approaches zero. When the critical value is achieved, H_{min} is equal or higher than the critical humidity H_c , and no adsorbed layer interaction will occur but condensation, leading to the formation of liquid bridges.

In a dry atmosphere, the following internal forces may exist: Van der Waals, friction and interlocking, electrostatics, chemical bonding, and for some materials, magnetic forces. The presence of adsorbed moisture affects these forces in different ways, as described in Table 2.5 [153].

Some studies [170, 153] reported the benefits of moisture in the bulk material, which in some cases can act as a lubricant and improve flow and powder bulk density. Seville et al. [168], however, claim that moisture prevents flow and packing efficiency as it creates bridges inside the bulk material. Batzer and Kreibich [171] and Goodridge et al. [172] claim that moisture can reduce T_g and affect the operating temperature of the material. In a different study, Coelho and Harnby [169] stress that it is not the moisture content of the powder that defines the effect of moisture (if adsorbed or in the form of liquid bridges) but relative humidity, temperature, pressure and atmosphere conditions. These factors were also stated by Kruth et al. [5] when assessing powder flow performance for LS [5].

Thakur et al. [163] experimentally assessed packing, compression, and cake behaviour of spray-dried detergent powders and found that samples with higher moisture showed

Table 2.5 Effect of humidity in interparticulate forces [153].

Interparticulate force	Definition	Moisture effect
Van der Waals	Interaction of dipoles in the molecules. Very sensitive to surface roughness, more significant for fine powders.	Decrease the distance between particles as adsorbed layers are considered part of the particles, and increase Van der Waals forces.
Friction and interlocking	Mechanical forces acting in the presence of particles' movement. Significantly increased with surface roughness	Moisture acts as a lubricant and reduces friction and interlocking.
Electrostatics	Generation of electrostatic charges on the particles, mutually attracting or repelling them	Particles discharge may occur as the air becomes conductive in the presence of moisture
Chemical bonding	Forces originated from a chemical reaction or hydrogen bonding	Hydrogen bonding may occur only when critical humidity H_c is reached.

a higher degree of compressibility, lower bulk porosity, and higher cake strength. They attributed this behaviour to the intraparticle porosity of the samples with lower moisture content, which masked the higher interparticle porosity found for the samples with higher moisture content.

PEEK is highly resistant to water absorption, which is maintained even at temperatures of 288 °C [167, 17]. As opposed to PAEKs, LS PA12 shows a critical moisture uptake due to its hydrophilic nature. Vasquez [173] reports a moisture range between 0.2-0.3% for a non-dried sample of PA 2200; this is enough to create hydrogen bonding and decrease intermolecular attraction, modifying viscosity [174, 175]. Furthermore, the absorption of moisture by recycled PA12 powder may reduce powder flow efficiency and can form cracks and aggravate surface finish of LS parts [176]. For this reason, most powders are subjected to drying before processing by LS. It is essential to highlight, however, that moisture evaporation can occur during the prolonged pre-heating stage in LS, which is usually above 100 °C [177].

Powders are usually vacuum dried to prevent moisture absorption affecting LS performance [178, 142, 179]. Different methods can be employed to measure moisture content, from moisture balance [163] to Karl Fischer titration [132]. However, the most popular methods are TGA [173, 180] or moisture analyser equipment [98, 148] as they are relatively simple methods which give accurate results.

2.3.5 Methods for improving particle and powder properties for LS

This section will focus on different methods to improve powder properties by modifying particle porosity and shape. This concerns specifically powders that are difficult to achieve a spherical morphology from the polymerisation process, and are usually subjected to a second or even a third stage to control PSD, reduce porosity, and improve morphology.

In 2010, EOS GmbH released a patent [88] on a method to improve the bulk density of PAEKs. This method consists of tempering the powder at temperatures between T_g and T_m , preferably at 250 °C for different periods, but ideally 15 h. After this treatment, not only bulk density increased from ~ 0.4 to ~ 0.45 g cm⁻³, but the surface area of small particles was reduced, suggesting particle smoothness.

Arkema also developed a method to improve the bulk density of PEKK [85], which consists of mixing the powder in a rapid commercial mixer with a rotary stirrer and at least one blade. The mixing is carried out for usual periods varying between 30 and 60 minutes at blade tip speeds from 30 m s⁻¹ to 70 m s⁻¹. This method resulted in a 56% increase in the tapped density of PEKK, from 0.32 to 0.5 g cm⁻³, when no thermal regulation is applied. The non-regulation of temperature led to a maximum temperature rise of 100 °C, which is still significantly below T_g of PEKK and far from being considered a thermal treatment.

The Institute of Particle Technology in Erlangen-Nuremberg University developed a route to improve particle shape of thermoplastic polymers using a downer reactor. This system comprises multiple heating bands, the first being well above T_m , followed by subsequently lower temperatures to reach solidification [181]. The atmosphere is controlled with nitrogen gas. This gas is used as a sheath gas, and to carry and disperse the particles inside the downer reactor. An illustration of the downer reactor setup is shown in Fig.2.14 [181].

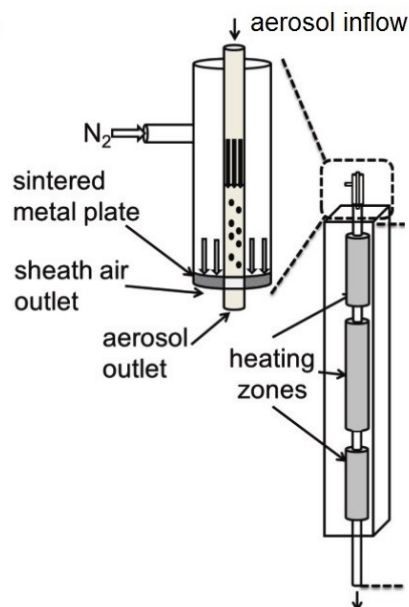


Fig. 2.14 Illustration of the downer reactor configuration to round polymer particles for LS application [181].

The residence time in the downer reactor was calculated using Kirchoff Equation [182]:

$$t_{sintering} = \frac{\sigma}{\eta x_f}, \quad (2.11)$$

in which x_f is the particle diameter, σ is the surface tension, and η is the viscosity of the polymer melt. Sachs et al. [86] calculated a maximum time of sintering equals to 2.6 s for a particle size of 10 μm and successfully achieved round PS particles with no agglomeration or changes in PSD. For the rounding of PBT particles [109], the first and second heating zones were set above melting, in where PBT remained for 7.7 s. The third zone was set to 150 °C, followed by a cold zone to guarantee solidification. The rounding process successfully enabled obtaining perfectly spherical PBT particles.

Although a promising technology, the route to rounding particles using a downer reactor is still not applicable to PAEKs due to their high melting point, which would require additional and longer heating bands to increase the residence time of such particles.

2.4 Particle Coalescence of Polymers

2.4.1 Fundamentals of coalescence

The mechanisms to consolidate polymers by LS induce different physical phenomena than what observed with sintering of metal or ceramic powders, in which atom diffusion is the main factor binding particles and promoting consolidation. The coalescence of polymer particles, however, is mostly driven by viscous flow. Understanding coalescence is, therefore, fundamental to achieve good consolidation in LS of polymers.

The coalescence behaviour of polymers is highly dependent on their intrinsic properties such as molecular weight (M_w) and degree of crystallinity because they affect viscosity. A classic example is PA12, the most popular polymer for LS. Due to the low viscosity $\eta \approx 100 \text{ Pa}\cdot\text{s}$ and a surface tension of $\gamma \approx 30 \text{ mN m}^{-1}$, consolidation is easily achieved. On the other hand, PC presents similar surface tension than PA12 but cannot be fully consolidated by LS due to the critical viscosity of $\eta \approx 5000 \text{ Pa}\cdot\text{s}$ [5].

The presence of crystalline structure directs viscous flow to a preferential orientation, as crystals constrain vacant sites to a fixed space in the lattice [183]. In amorphous materials, viscous flow is triggered by the diffusion of lattice sites or migration of atoms on the surface, which leads to motion in the direction of the shearing stress with the increase of temperature [184].

Intrinsic material properties also affect the dominant mechanism of consolidation. According to Kruth et al. [185], five primary mechanisms are present in LS: solid-state sintering (SSS), liquid phase sintering (LPS), partial melting, full melting, and chemically induced binding (CIB). The consolidation of polymers mostly occurs at LPS, in which the primary transport mechanism is viscous sintering. Organic molecules like polymers require extremely high activation energy for diffusion to occur at solid-state; the fast scan

speed of the laser does not allow sufficient time to transfer this energy [4]. Therefore, LS of polymers must occur in the presence of a liquid phase (above T_m).

Depending on the material and parameters selected, full melting or partial melting can occur. Full melting promotes almost full dense parts in a single step, whereas partial melting induces a series of binding mechanisms in which part of the powder is melted, and the rest remains solid. Partial melting can occur when the heat supplied is insufficient, the temperature is below melting, but above T_g for semi-crystalline polymers, smaller particles can melt, but larger ones cannot, or when chain rearrangement or cross-linking occurs, for the case of thermoset polymers [185].

The coalescence of two micron-sized polymer particles driven by viscous sintering consists of two different phases, neck growth, and equilibration. According to Mazur [186], these phases occur in three main steps represented in Fig.2.15:

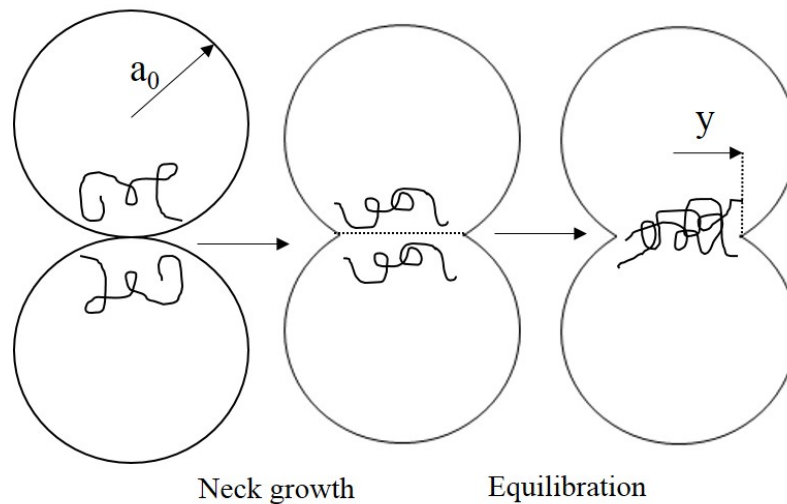


Fig. 2.15 The different stages of micron-sized polymer particles under coalescence, adapted from [186].

1. Contact between particles surface, forming 'necks';
2. Neck growth, leading to changes in particle morphology, but internal boundaries remain intact;
3. Equilibration achieved with the organisation of molecules due to chain relaxation and diffusion across interparticle interfaces.

When a system of more than two particles is studied, a final stage is observed, known as densification [187, 188]. This stage consists of material shrinkage and pores elimination, and it is crucial to determine final consolidation achieved with the coalescence process.

Particle coalescence and growth are key information to determine the success of LS [176, 90, 189, 133], as in this process no external forces are present in the system but consolidation occurs as a result of heating effects, gravity, and capillary forces [4, 185]. One must also account for the layer's thermal characteristics, since the time in which the

laser provides energy is significantly lower than in conventional sintering, in the order of milliseconds [190, 5]. Furthermore, coalescence is mostly driven within seconds after laser exposure, whilst consolidation is achieved in a significantly longer time when the polymer is under the influence of T_{bed} , hence the importance of controlling temperature throughout the process [191, 192, 185]. The following section will explore multiple studies developed to predict coalescence using different approaches, such as analytical and numerical solutions, and experimental analysis.

2.4.2 Mechanisms of coalescence

The first attempt to understand particle coalescence driven by viscous sintering was proposed by Frenkel [183] and soon modified by Eshelby, Mackenzie & Shuttleworth in 1949 [193]. Frenkel aimed to model sintering by considering viscous flow under the action of surface tension. This model is represented by Eq.(2.12), which assumes an isolated system constituted of two equal spheres of incompressible and viscous newtonian flow with no thermal gradient within them [175].

$$\frac{y}{a} = \left(\frac{\gamma t}{\eta_0} \right)^{1/2}, \quad (2.12)$$

in which y is the neck radius, a is the particle radius, γ is the surface tension, η_0 is the zero-shear viscosity, and t is time [194]. Following the Frenkel model, Kingery and Berg [195] and Exner and Petzow [196] described the rate of approach of the centres of two spheres at the initial stage of sintering by considering neck curvature as a tangent circle model. According to them, the approach of particles is a result of shrinkage rate and is linearly dependent on time, even for later stages of sintering. Exner and Petzow [196], however, highlight the effect of irregular packing and morphology on shrinkage rate, which also leads to asymmetric neck growth, particle rearrangement, and the formation of new contacts during sintering.

So far, all the models presented constrain particle volume; such assumption is accepted at the early stages of sintering but significantly differ at the later stages as particles are driven by viscous flow rather than surface tension alone [197]. Hence, for the later stages of viscous sintering, the models of Mackenzie & Shuttleworth [184] and Cosgrove et al. [198] are generally accepted. Mackenzie & Shuttleworth [184] analysed the effect of gas in the pores and on the final density of sintered metal particles and concluded that it is vital to consider the interaction of one pore with its neighbours, as isolated pores do not close at the end of coalescence but pores in powder compacts do. Cosgrove et al. [198] developed a model to predict the sintering of a linear array of rods based on Navier-Stokes equations. They found an utterly non-linear character at the later stages of sintering, which results in a neck growth rate significantly lower at this stage when compared with the earlier stages of sintering.

Hopper [199] proposed a coalescence model for two equal cylinders instead, driven by capillary forces. He used Navier-Stokes equations for two-dimensional viscous flow to

model the coalescence at the early stage, with the shape of the cylinders varying with time, involving a mapping function. This mapping function was originally guessed; later Hopper [200] showed the difficulties on finding it, he was only able to solve it for a circular disk with a circular hole centred at the origin.

More recent studies developed different numerical solutions to predict viscous sintering [201–204]. The first genuine attempt was performed by Ross et al. [204], who considered viscoelastic effects. Kuczynski et al. [205] and Mazur & Plazek [206] identified viscoelastic effect while monitoring coalescence of acrylic resins, which makes newtonian sintering models not applicable to determine the rate of coalescence for polymers. The model proposed by Ross et al. [204] employed the finite element method (FEM) to solve the Navier-Stokes equation of an infinite line of cylinders with their morphology and neck being monitored with time. This model, however, fixed the distance between the centre of the cylinders, as if no shrinkage was present [204].

Jagota et al. [207] separated the viscoelastic behaviour of particles into initial elastic adhesion and viscous sintering. They mention two different modes of contact growth driven by surface forces: the first is known as initial elastic contact, it is predominant in the early stage of sintering and is dominated by van der waals attraction forces acting in a zipping mode contact closure across the gap ahead of the contact edge (Fig.2.16(1)). In the later stage, curvature-based tractions normal to the surface of the sphere drive viscous sintering, and the contact grows in a stretching mode (Fig.2.16(2)). The transition between both modes is therefore viscoelastic and dependent on the contact radius, hence dependent on particle radius.

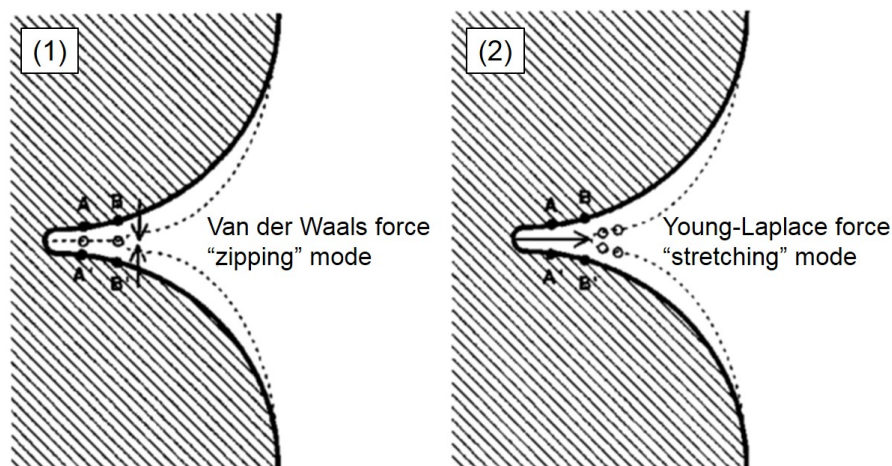


Fig. 2.16 Schematic illustration of contact growth modes adapted from Jagota et al. [208]. (1) Elastic adhesion driving contact growth in a zipping mode; (2) tractions viscous sintering driving contact growth in a stretching mode.

Jagota and Dawson [209, 210] then developed an FEM to predict coalescence of two equal spheres and an infinite line of equal spheres under viscous flow. They modeled the particle packing as a framework of links between any pair of spheres touching each other, whereas the neck growth is described considering each pair of spheres coalescing separately [210]. This model shows a good description of coalescence when compared with

experimental data of two-dimensional packing of mono-sized glass spheres. Nevertheless, coalescence for polymers is delayed. Mazur & Plazek [206] attributed such delay to the diffusion of chains across the interface and the establishment of the equilibrium distribution of chain entanglements. They found out that stress relaxation occurs regardless of particle size for acrylic particles. Therefore, time for chain relaxation must be taken into account to obtain bulk mechanical properties.

Van de Vorst [203] modeled the coalescence and densification of particles using the boundary element method (BEM) and evaluating different contact shapes between two particles. Martínez-Herrera and Derby [211] employed FEM to study a two-particle system. Both studies showed good agreement with Hopper's model predictions. In a later study, Martínez-Herrera and Derby [212] simulated the coalescence of three particles from several initial configurations by employing the FEM method to find a numerical solution. They concluded that shrinkage occurs at a faster rate for a three-particle system than for a two-particle one, and they confirmed the independence of different particle contacts on the initial stage of sintering, previously suggested by Jagota and Dawson [209].

Bellehumeur et al. [197] applied Frenkel-Eshelby and Hopper model to compare the effect of coalescence on different grades of polyethylene. They concluded that the model proposed by Hopper represents better the coalescence process than the Frenkel-Eshelby model, although both showed higher values of coalescence rate if compared to their experimental data for polyethylene grades. They also claim that the Frenkel model considers particle radius constant with temperature, and this assumption is only satisfactory for y/a lower than 0.3.

Hence, Pokluda et al. [194] proposed a different model that accounts for the variation of particle radius with time during the coalescence process, using Runge-Kutta-Fehlberg numerical integration. They studied the coalescence behaviour of two equal spherical droplets of a newtonian fluid. According to them, coalescence is completed at y/a_0 close to 1.26 using the Frenkel-Eshelby model, whilst if Hopper model is chosen, y/a_0 is equal to 1.41. Their model approaches Frenkel-Eshelby and Hopper models at the early stages of sintering, but present a lower coalescence rate at later stages, assuming a quite similar behaviour to Jagota and Dawson [209, 210, 207] model throughout the coalescence process. When compared with the experimental data of Bellehumeur using polyethylene grades, the values differ at the late stage of coalescence. Pokluda et al. [194] attributed such deviation to the destruction of particle sphericity as they spread on the surface.

Kandis and Bergman [213] and Tarafdar and Bergman [214] used Pokluda's approach [194] and considered the effect of conductive heat transfer in a column of particles subjected to sintering. In doing so, they were able to predict physical and thermal responses for different sizes of particles. Zhou and Derby [202] used a parallel FEM code for numerical solution to investigate the sintering of three particles in 3D. They found similar results to Herrera and Derby [211], proving the different and anisotropic shrinkage of a three-particles system when compared with two.

Bellehumeur et al. model [215] used Frenkel's and Pokluda's approaches but also considering viscoelastic effects to predict sintering of different grades of polyethylene

and propylene-ethylene copolymers. They concluded that sintering is slower for more elastic polymers as well as the action of surface tension is best described when using the Maxwell model in Frenkel's equation. Even so, they successfully fitted the model to their experimental data if high values of relaxation time are considered. These values, however, are not visible in the data, and the model was not consistent with Mazur and Plazek [206] experimental tests for PTFE particles.

Kirchhof et al. [182] performed a three-dimensional simulation using the fractional volume of fluid (VoF) method to study the neck growth of two spheres of different sizes driven by viscous flow. They concluded that the smaller particle dominates the kinetics of neck growth in the system, and that speed increases for more significant differences in particle size. By using the same approach in a later study, Kirchhof et al. [216] investigated the sintering of vitreous nanoparticles and concluded that van der Waals interactions are acting as additional driving forces to viscous flow when the particle diameter is below 200 - 300 nm.

Wakai et al. [201] investigated the forces acting in viscous sintering using FEM simulation to predict the coalescence of two identical spheres. The driving force for neck growth and shrinkage was defined as the difference between the average pressure on the contact area and the surface tension along its circumference. They concluded that sintering forces are indeed the main driving forces, and they were able to predict two-dimensional viscous sintering. Other models attempted to describe the coalescence process driven by viscous flow. Most of them can be found in Table A.1 available in Appendix A.

2.4.3 Coalescence under hot stage microscopy (HSM) and in laser sintering

Currently, the most employed method to track particle coalescence is HSM [176, 116, 110, 175], which monitors neck growth with time/temperature by capturing several successive images under an optical microscope. Rosenzweig and Narkis [217, 218] were the first to monitor neck growth under HSM for PMMA [217] and polystyrene (PS) [218]; they obtained similar slope than what proposed by Frenkel model, of 0.53 and 0.57, respectively. Hornsby and Maxwell [219] found a slope between 0.45 and 0.48 by assessing the neck growth of polypropylene beads of different sizes and melt viscosities.

Interesting studies used HSM to assess neck growth and morphology of ultra-high molecular weight polyethylene (UHMWPE). Truss et al. [220] investigated five grades of UHMWPE with two different morphologies, fibrous and nodular. The fibrous morphology showed a significant increase in compaction over the nodular structure; they attributed that to the multiple points of contact between the fibres and the penetration of them into other particles, which allows a closer packing structure. Siegmann et al. [221] investigated the effect of particle morphology on the sintering of PMMA, PS, regular molecular weight polyethylene (RMWPE), high molecular weight polyethylene (HMWPE), and UHMWPE. Although the study confirmed the dependence of coalescence on polymer viscosity and particle size for amorphous polymers, it highlights the effect of particle morphology

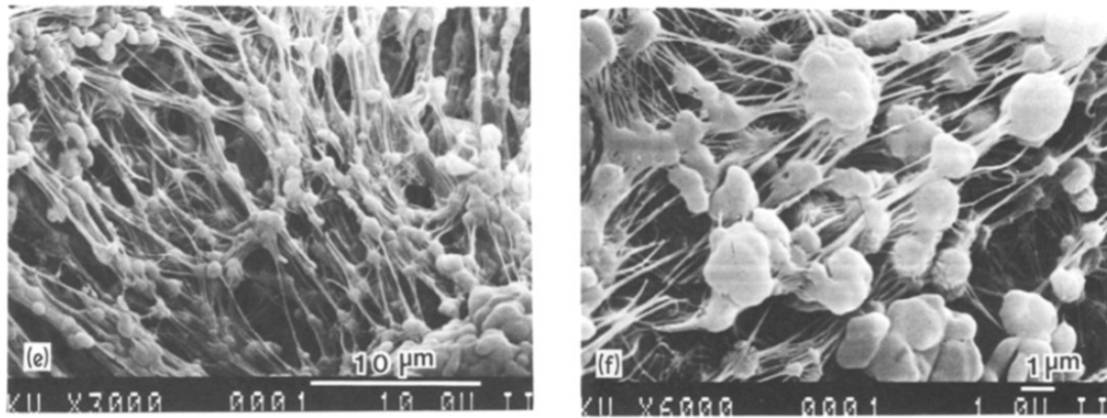


Fig. 2.17 SEM micrographs of UHMWPE particles showing nodular structures aggregated into larger structure units [221].

in semi-crystalline polyethylenes, which showed an increase in surface energy. In the particular case of UHMWPE, nodules of less than $1 \mu\text{m}$ aggregated into larger structure units (Fig.2.17), as reported by Truss et al. [220]. These structures allow the sintering of UHMWPE whilst unprocessable by other manufacturing techniques.

Aid et al. [222] investigated the coalescence of particles from different materials, polyvinylidene fluoride (PVDF) and PMMA, their particle size, and isotherm temperatures. Their model was based on the Bellehumeur model, which states coalescence is driven by viscosity, surface tension, and relaxation time. In their study, however, Aid et al. [222] found that relaxation time does not influence coalescence, but surface tension, viscosity, and particle size do.

With the consolidation of powder bed fusion technology, recent investigations on powder for AM were developed. Haworth et al. [175] studied the coalescence of PA12 under dynamic HSM at $10 \text{ }^\circ\text{C min}^{-1}$. Their conclusions, however, were quite uncertain. Dadbakhsh et al. [176] performed HSM to compare the coalescence of virgin and used PA12 at the same rate of $10 \text{ }^\circ\text{C min}^{-1}$. They concluded that powder reuse delays coalescence by around $10 \text{ }^\circ\text{C}$, but neck growth was not monitored.

Vasquez et al. [110] investigated the coalescence of TPU powder at dynamic rates of $10 \text{ }^\circ\text{C min}^{-1}$. They found a slower consolidation rate than for PA12, possibly a result of the elastic recovery of this material, which increases relaxation time. A later study [223] monitored coalescence of cryogenically milled polybutene-1 at faster rates of $30 \text{ }^\circ\text{C min}^{-1}$ and achieved a fast coalescence, which was attributed to the low viscosity of this material. Indeed, the rate of coalescence is crucial and must be adjusted to the application. In LS, the heat transfer from the laser to the polymer bed seems to occur in milliseconds at an extremely high heating rate above $22000 \text{ }^\circ\text{C min}^{-1}$ [158]. Therefore, Berretta et al. [116] opted to use the maximum heating rate available in the hot stage setup, of $120 \text{ }^\circ\text{C min}^{-1}$, to assess the coalescence for three different grades of PAEKs in a two-particle system. They concluded that viscosity was the most influential parameter in coalescence.

There are, however, a few limitations of the HSM technique. Barnetson and Hornsby, [224] mention the substrate, which can act as a barrier to heat transfer in different degrees

depending on the contact surface of the particle to the substrate, and the difficulty in visualising whether the particles are only touching or overlapping each other.

Therefore, Hejmady et al. [225] developed a novel setup to investigate *in situ* coalescence in the LS process. Their experimental setup contains side and top cameras inside a system in which several parameters can be controlled, including laser power, scan speed, scan spacing, spot size, and chamber temperature. The study investigated different combinations of parameters to monitor the coalescence of PS particles with equal size and round morphology. The authors concluded that sintering kinetics is very complicated as several factors affect transient rheology, like finite relaxation time and the time-dependant temperature profile. Since the heating stage is not homogeneous, it may slow down and even halt the laser-induced particle sintering due to an increase in viscosity at later stages, when relaxation time takes place. As the temperature profile is not uniform either, complex flow fields may exist, which makes the study even more complicated.

2.5 Process: Additive Manufacturing (AM)

This section provides a brief description of AM and focuses on the study of high-temperature laser sintering (HT-LS), the most commonly used technique to manufacture PEKK parts. The literature review then compares the first HT-LS system, the EOS P 800, with conventional LS systems and the ThermoMELT process concerning configuration and parameters.

According to ASTM F42, additive manufacturing is the “process of joining materials to make objects from 3D model data, usually layer upon layer, as opposed to subtractive manufacturing methodologies” [226]. The basic principle of this technology consists of building a part, layer-by-layer, from a 3D Computer-Aided Design (CAD) model [227], either from a liquid, powder, or solid supply. When the material is supplied in the form of powder and a laser/electron beam or a thermal print head is used to melt/sinter the particles together and form a 3D part, this process is classified as powder bed fusion (PBF). The most commonly employed technologies within PBF are Selective Laser Melting (SLM), Direct Metal Laser Sintering (DMLS), and Selective Laser Sintering (SLS). In SLM, metal particles are fully melted to form a 3D part, whilst in DMLS, only sintering takes place [228]. The SLS technique is usually employed to process polymers, but this term is often misemployed as melt rather than sintering occurs for semi-crystalline polymers. However, SLS was first used to process acrylonitrile butadiene styrene (ABS), an amorphous polymer, thus with an undefined melting point but a gradual softening of the chains until a viscous liquid state is achieved. The term ‘laser sintering’ was already well established when semi-crystalline polymers became the most popular polymers to be processed by this technique [229].

2.5.1 High temperature laser sintering (HT-LS)

The LS process dated back to the 1980s and was developed by Carl Deckard at the University of Texas, Austin [229]. The LS technology is one of the most versatile technologies within AM [230], as it enables serial production with reproducible part properties. It also offers cost reduction potential, increased surface resistance to wear and fatigue, extended part/tool life, and promising reduction of energy intensity and environmental impacts [231, 232]. Fig.2.18 illustrates a standard laser sintering system and its main components.

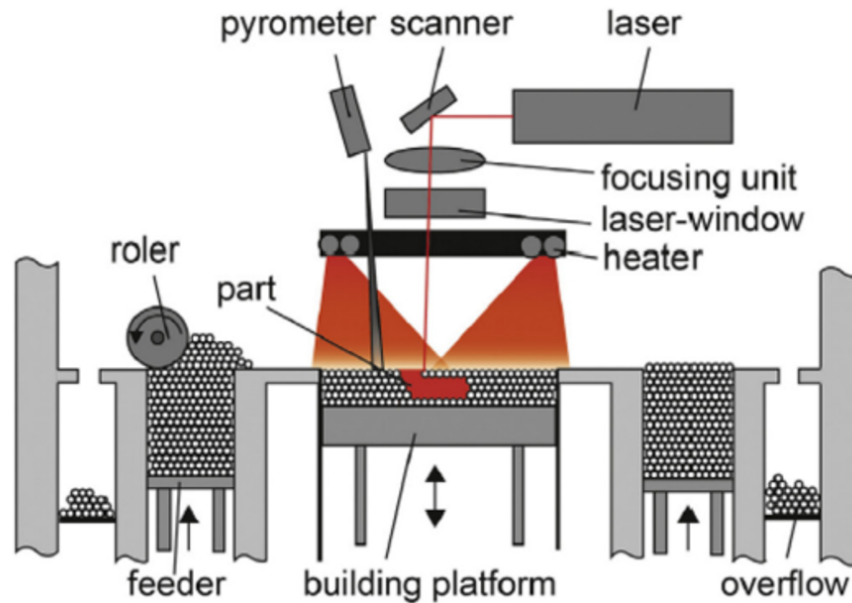


Fig. 2.18 Illustration of the LS process and the main components in the system [233].

According to Kruth et al. [5], LS is the most promising technique to produce polymer parts of high performance. As opposed to commodity thermoplastics, high-performance polymers usually require high processing temperatures often not achieved with conventional LS systems. For this reason, EOS released the P 800 high-temperature LS system in 2008 [11]. An image of the system is available in Fig.2.19.

The EOS P 800 HT-LS platform is able to process polymers up to temperatures of 385 °C [11], being the first commercially available system operating at temperatures above 250 °C [9]. With the rapid growth of AM and the desire for processing different materials with increased performance, two other high-temperature LS systems are now commercialised by EOS: the P 500 and the P 810.

According to EOS [235], the process in P 800 follows the same sequential steps of conventional LS machines:

1. Model of a CAD representation;
2. Conversion of the CAD into thin layers (slicing process);
3. Powder spread and heat over the manufacturing region (powder bed);



Fig. 2.19 The EOS P 800 HT-LS system [234].

4. Application of laser heat to scan the predefined cross-sectional area of the CAD geometry on the powder bed;
5. Downward movement of the piston equivalent to one layer thickness;
6. Recoating of a new layer of powder;
7. Cycle repeat (from no. 4) until the part is completed;
8. Part removal and post-processing.

Unlike the stereolithography (SLA) technology employed for polyamides, LS does not require post-curing and offers excellent mechanical and temperature resistance performance regardless of moisture content, and a higher rate of fabrication [236, 237]. The LS of polymers is also beneficial over SLM of metals as it does not require support structures, reducing material waste and time of post-processing [238, 236]. Nevertheless, the LS technology is reliant on many physical parameters: flow properties, the rate of absorption of laser energy to reach a fully melted state, particle shape, particle size distribution, suitable polymer viscosity – low enough to fill the inter-particle gaps but high enough to prevent the molten material from sinking into the supporting powder bed - interparticle porosity, and degree of crystallinity [2].

Bourell et al. [2] attributed the high strength results of LS parts to a higher degree of crystallinity achieved with the slow cooling cycle of the process. The low values of elongation at break, typically an order of magnitude smaller than IM, were justified by the little or no entanglement between neighbouring spherulites crystals, the increase in spherulite size due to a prolonged cooling cycle, and the presence of porosity resultant from partial melting.

The success of the LS process also depends on the following factors:

- The maximum polymer particle size must be limited by the layer thickness selected for the process;
- The process chamber must be heated to avoid curling, warping, or any thermal distortion. Heat is also required to promote adhesion between layers. The heating temperature varies with the polymer, but is usually closer to the melt temperature of semi-crystalline thermoplastics or the glass transition temperature of amorphous thermoplastics;
- The process chamber must be inert to prevent material oxidation.

As a viable solution to process high-temperature polymers without HT-LS, the ThermoMELT process can be used. This technique consists of creating a substrate structure to be fixed just above the build platform and before the application of the first layer of powder. The laser is firstly applied on the substrate, melting its surface and promoting adherence between the first layers of powder and the substrate. A support structure is built between the parts and the substrate, which enables stress transference. Therefore, the accumulation of residual thermal stress from cooling is mitigated [239].

According to Meyer [239], the main advantage of ThermoMELT is powder recyclability, since T_{bed} is slightly above T_g . As for drawbacks, higher laser energy is required to melt the powder fully, and more material, as well as long post-processing, is needed to remove the support structures. Furthermore, the objects must be built in the horizontal direction, since unacceptable distortion may occur as a result of the temperature gradient.

2.5.2 Configuration

The main components of the LS system directly affecting the process include the CO₂ laser, the heated and inert chamber, and the coating tool. In this section, the configuration of HT-LS systems will be discussed with respect to laser type, build size, deposition mechanisms, i.e., recoater, and heating system/time.

2.5.2.1 Laser type

As opposed to metal machines, the laser used to process polymers in LS operates in a carbon-dioxide (CO₂) gas medium, which generates infrared output wavelength from 9.0 to 11.0 μm ; the most popular in LS being 10.6 μm . Despite the relatively short life of CO₂ lasers, the wavelength emitted is ideal for processing polymers, as the absorption of light by organic molecules is maximum at around 10.6 μm , and can be higher than 90% of the total laser emission for polymers like polyamides [232]. Due to the large manufacturing area, the EOS P 800 system has two CO₂ lasers operating simultaneously in different locations of the build area. Each laser has a maximum power output of 50 W [235].

2.5.2.2 Build size

The EOS P 800 system comprises one of the largest build size volumes available for part production in LS, of $700 \times 380 \times 560 \text{ mm}^3$ [240]. In other conventional polymer systems, such as the Formiga P 100, the build dimensions are of $200 \times 250 \times 330 \text{ mm}^3$ [241]. For some applications, however, large production areas are undesirable as the ratio of used powder to part production may increase. Therefore, the P 800 system offers two reduced build configurations; their dimensions can be compared with the maximum volumetric capacity in Fig.2.20. The reduced configurations do not require any additional support as PAEEKs are self-supporting powders and do not flow to non-manufactured regions. In the maximum reduction configuration, however, the recoater needs to be slightly adapted to displace powder only from the back of the manufacturing area.

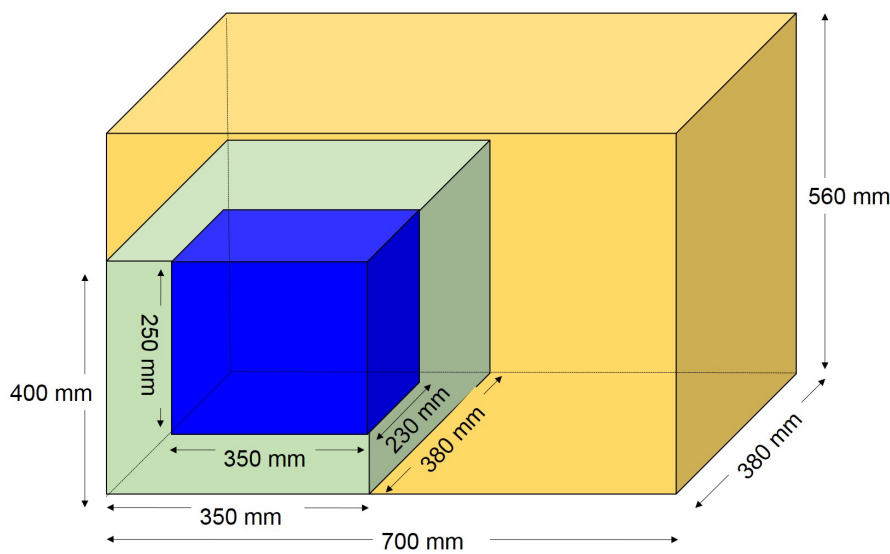


Fig. 2.20 Build dimensions of EOS P 8000 HT-LS system in the maximum capacity (yellow) compared to the two reduced configuration options (green and blue).

In Berretta et al. study [9] on optimising the processability of PEEK for HT-LS, the system configuration did not seem to affect tensile testing data of PEEK 450PF, which showed repeatable properties regardless of the build configuration chosen for manufacturing.

2.5.2.3 Deposition mechanisms

A deposition mechanism is used to transport the powder, i.e., recoater, which attempts to spread successive layers of powder with homogeneous thickness and high packing density. There are currently two commercially available spreading tools, the counter-rotation roller from 3D Systems and the translational blade system available in the EOS machines; they are illustrated in Fig.2.21.

In the counter-rotation roller system, the feed zones are located parallel to the powder bed, and powder is supplied from below the part bed plane in the exact amount required to complete one layer thickness. In this system setup, preheating is available in the feed zones, which helps to prevent undercooling. This is particularly important when processing

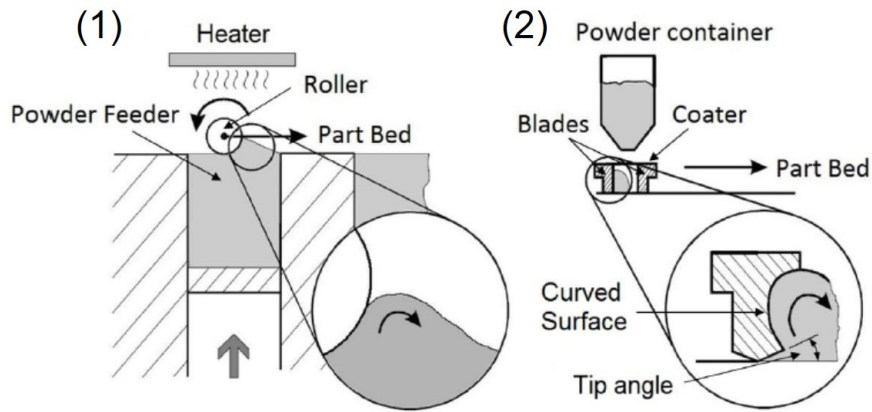


Fig. 2.21 Illustration of the deposition systems commercially available for LS; (1) counter-rotation roller and (2) translational blade system [115].

high-temperature polymers such as PAEKs. The pressure applied by the roller was studied [114] and proved to result in better powder bed quality than the blade system. The results obtained by Schmid et al. [138] revealed similar packing density for this system than what obtained with the tapped powder of PA2200 grade. However, excessive pressure of the roller on the powder bed may result in a heterogeneous bed with powder sticking to the surface of the roller [155].

In the translational blade systems, the powder is supplied from a hopper located above the powder bed and is delivered in front of the blade or in between blades for the double-blade systems. The hopper dispenses more material than required to complete one layer thickness. The extra powder can generate more pressure and induce shear stresses on the powder bed, which may shift the sintered layer below [242]. This system is highly sensitive to collisions and imperfections in the powder bed, and according to Budding and Vaneker [159], achieve a lower packing density than the roller. However, by changing the blade profile in the region of contact with the powder bed can significantly improve spreading with the blade system. Haeri [242] found that shorter and wider profiles generate higher volume fractions, and better powder spread is achieved with a super-elliptic edge blade design. In the EOS P 800 system, the translational double-blade system is used and sold with the standard blade profile.

2.5.2.4 Heating system & heating time

Section 2.5.1 discussed the LS of polymers and the main difference between polymer and metal systems, i.e., the use of a heated chamber for polymer machines. Goodridge et al. [4] mention the need for pre-heating just below T_m of semi-crystalline polymers and close or at T_g for amorphous polymers. The pre-heating minimises the amount of energy required by the laser for consolidation, promotes a lower thermal gradient between the sintered powder and the surrounding powder, and provides a more controlled thermal expansion [243]. A heated chamber is also required to prevent processing errors such as curling, warping, and shrinkage [244]. Furthermore, time for coalescence and then adhesion between layers is extended with a heated chamber.

The selection of appropriate T_{bed} for semi-crystalline thermoplastics is based on the sintering window of the polymer, known as the area between the onset of the melting peak and the onset of crystallisation peak [110, 5]. Section 2.5.3.3 further describes this selection.

The most important difference between HT-LS systems and conventional polymer LS machines is that HT-LS supports processing at higher temperatures. The processing at high temperatures requires the maintenance of T_{bed} across the manufacturing area, as well as uniform heating-up and cooling-down, which is parametric in the EOS P 800 system.

Ceramic heaters supply the heating of conventional LS systems and are usually located on the top of the powder bed. The EOS P 800 HT-LS uses infrared (IR) heaters to heat the top of the powder bed, in addition to two other ceramic heaters around the building chamber, to minimise temperature distortions and uneven part properties. One of the ceramic heaters is located on the side frames of the system, whilst an additional heater is found between the piston and the powder bed, as shown in the schematic illustration of Fig.2.22. The temperature provided by the IR heaters on the top is known as the process chamber temperature (T_{bed}) (a), the temperature of the walls is known as exchangeable build frame temperature (T_{ebf}) (b) and the temperature of the ceramic heaters in contact with the piston is known as building platform temperature (T_{bp}).

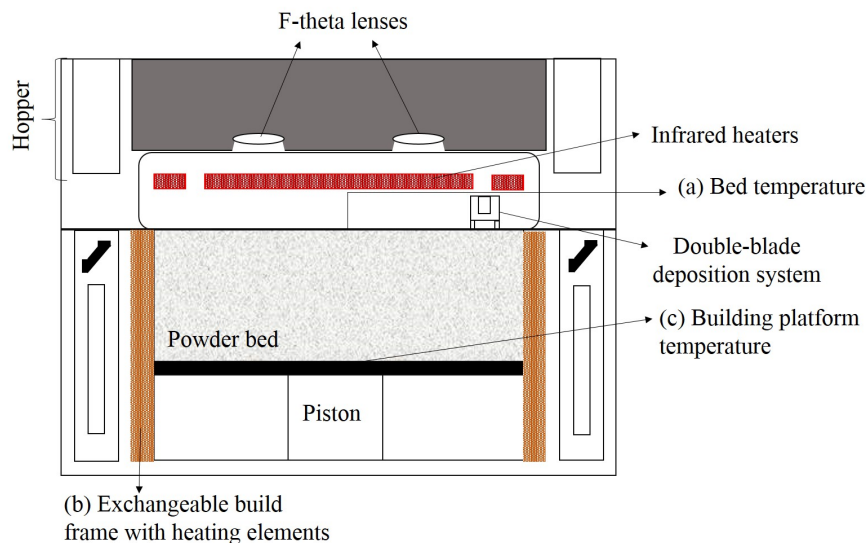


Fig. 2.22 Schematic illustration of the EOS P 800 system showing (a) process chamber temperature; (b) exchangeable build frame temperature and (c) building platform temperature.

Another particular feature of HT-LS systems is the post-sintering time, known as the additional heating phase applied to each layer after the laser application. This heating is provided by the IR heaters during a specific time determined by the operator and aims to guarantee uniform melt between the initial and final areas subjected to laser exposure in the same layer.

The post-sintering time feature was investigated by Berretta et al. [9], which evaluated potential changes in tensile behaviour, surface topography, and DMA values. They consid-

ered four different post-sintering times: 6 s, 9 s, 12 s, and 15 s. No significant changes were observed in tensile testing or dynamic-mechanical analysis (DMA) results, but different topography values were obtained, in which PEEK showed irregular surface with cavities of different sizes. These irregularities, however, seemed to be more dependent on the powder grade than on post-sintering time. The conclusions of this work revealed that the standard post-sintering time of 12 s is the most suitable as the surface of the specimens seemed to be less irregular, and the processing time shorter than 15 s of post-sintering time.

2.5.3 Parameters

This section will focus on the main processing parameters directly associated with material properties. As processing parameters, energy absorption, and the corresponding laser parameters - power, scan speed, and scan spacing - will be discussed in addition to shrinkage and sintering window. As this thesis aims to investigate the effect of material and process interaction, the design and production of complex features will not be explored.

2.5.3.1 Energy absorption

LS systems are sensitive to several build parameters. Some of them directly influence part density and mechanical behaviour of laser sintered parts; they are energy density (ED), bed temperature, and part orientation [2, 152, 133, 6]. The appropriate combination of laser parameters provides the energy density to obtain solid parts with desired properties. Amongst the laser parameters, laser power, scan speed, and hatching distance are the main ones as they directly affect the energy density applied to the parts, as shown in Eq.(2.13). Other parameters also include beam offset, angle of exposure, number of exposures, path strategy, and contour parameters.

$$ED = \frac{P_L}{v_s h_s}, \quad (2.13)$$

in which, ED is the energy density (J mm^{-2}); P_L is the laser power (W); v_s is the scan speed (mm s^{-1}) and h_s is the scan spacing (mm). Eq. (2.13) is very general and only considers the energy carried by the laser beam, regardless of T_{bed} or the capability of the material to absorb the laser energy. Indeed, the coefficient of laser energy absorption is highly dependent on material intrinsic properties, and the wavelength of the laser. Therefore, the light will always be absorbed, reflected, and transmitted in different amounts [90]. For a generic PA powder, the absorption coefficient at CO_2 wavelength is reported to as great as 0.9, which means that 90% of the energy carried by the laser beam is absorbed. Eq.(2.14) summarises this phenomenon [232].

$$E_{abs} + E_{ref} + E_{tr} = 1. \quad (2.14)$$

E_{abs} corresponds to the energy absorbed by the material, E_{ref} is referred to as the energy reflected by the material, and E_{tr} is the energy transmitted through the material. Note that

the last equation neglects the absorption of laser energy by vapour and plasma generated during prolonged irradiation emissions.

Considering the losses with laser reflection and transmission, Keshavamurthy et al. [245] proposed an equation relating the energy applied to the energy absorbed by the material:

$$E_{abs} = \alpha_{abs} \times P_L \times \frac{2B}{v_s}, \quad (2.15)$$

in which E_{abs} is the energy absorbed per unit area (J mm^{-2}), α_{abs} is the absorptivity of the powder, P_L is the laser power (W), B is the laser beam incident radius on the powder bed (mm) and v_s is the scanning speed (mm s^{-1}).

Several researchers mentioned laser absorption as a critical parameter to understand the behaviour of polymers during the LS process [90, 246, 247, 5, 185]. According to Kruth et al. [185], the microstructure of LS parts is strongly dependant on the thermal conduction and temperature gradient induced by the laser absorption. They also related material absorption with laser wavelength - the higher the laser absorption of the material, the narrower is the variation in absorption during the build and the easier to control the process.

Wang et al. [247] investigated PEEK reinforced with graphite platelet processed by HT-LS. They concluded that the addition of graphite improved laser absorption as a result of its higher coefficient of absorption; this also assisted heat transference to PEEK particles. On the other hand, graphite compromised overall flowability.

Laumer et al. [246] considered the influence of PA and polyethylene (PE) molecular structure on the absorption mechanism of laser radiation. They concluded that different molecular structures result in distinct vibrational excitation energies, therefore different absorption spectra. They also identified a different absorption behaviour for PE in powder format when compared to bulk polyethylene - the powder format resulted in a lower transmittance than bulk polyethylene. This result was explained by the multiple reflections occurring in the gaps between particles, leading to higher absorption but also an increase in the probability of single rays being reflected towards the powder surface.

Berretta et al. [152] reported difficulties in achieving a high consolidation with PEEK processed by HT-LS. They listed poor absorption of the laser energy and other intrinsic properties of PEEK material (high onset degradation temperature, low specific heat capacity, low enthalpy of melt, and low packing fraction) as factors preventing the achievement of good processability.

Vasquez et al. [110] performed tensile tests in thermoplastic polyurethanes and achieved a linear relationship between energy density, ultimate tensile strength (UTS), and tensile modulus. They found an increase from 3 to 6 MPa in UTS and from 50.2 to 122.2 MPa in tensile modulus when the ED changed from approximately 0.0175 J mm^{-2} to 0.03 J mm^{-2} .

Starr et al. [248] studied the effect of laser parameters on the mechanical performance of PA12 manufactured by LS. They found that strength and elastic modulus reach their

limit when the energy applied is enough to melt the powder fully. For the elongation at break, however, they did not observe a maximum until the energy given exceeded by three times the energy necessary to melt the powder fully.

Athreya et al. [133] claimed that excessive laser energy could result in extremely high temperatures, which can cause pyrolysis and lead to part porosity. This effect is aggravated when carbon black is added to the polymer, as it increases the absorption of CO₂ laser radiation and lead to localised heating. A couple of studies have compared polymer grades with and without the addition of carbon black pigment [142, 6]. Verbelen et al. [142] used PA11 with black pigment and found a laser absorption improvement. Drummer et al. [6] added 0.4% wt. of carbon black in high-density polyethylene and reported a higher degree of absorption and better flowability.

Schmid et al. [108] reported absorption as the least critical of the intrinsic polymer properties, since an increase in laser energy power can compensate the polymer low absorption capability. In future research, however, Schmid and Wegener [90] mention that an increase in laser power must be limited to prevent degradation. According to Berretta [240], an exceeding application of laser power can also lead to curling and part distortion significantly below degradation, as higher laser power reduces viscous flow, thus increasing shear stresses between layers.

A few studies claim that each laser parameter contributing to ED can have their own effect in final mechanical properties, consolidation, and even shrinkage of LS thermo-plastics [249, 250]. Drexler et al. [250] found an increase in the elongation at break by maintaining ED but reducing scanning speed, which also seemed to slightly increase tensile strength and reduce the surface roughness of PA2200 parts. When investigating the effect of processing parameters on shrinkage of PA 3200GF parts, Negi and Sharma [249] found that scan speed, scan spacing, and T_{bed} are the dominant parameters in LS.

Hofland et al. [251] investigated the effect of pre-heating, laser parameters - power, scan spacing, and scan speed - and layer thickness on mechanical properties and density of PA2200 parts fabricated using the EOSINT P395 system. They found that energy density is a suitable parameter to control mechanical properties, but scan spacing and layer thickness seem to be the process factors that affect these properties the most, followed by scan speed and then pre-heating temperature, and laser power.

The effect of laser parameters was also investigated for PEEK. Schmidt et al. [252] found similar values of consolidation of PEEK 150PF when maintaining ED but varying scan spacing and laser power. These values diverge when the ED is insufficient to promote a consolidation higher than 95%; in this case, laser power seems to have a more significant effect.

2.5.3.2 Shrinkage factors

Shrinkage is extensively mentioned in the literature as one of the major causes of dimensional instability and poor performance in laser sintering. As opposed to conventional processes, e.g., IM, in which dimensional inaccuracy is mostly a result of high cooling rates

[253, 254], other sources in addition to cooling may be causing a dimensional mismatch in LS, such as the slicing process [249, 255] and even the configuration of the deposition mechanism. Drummer et al. [256] found higher part densities for powder spread using the blade rather than the roller, which led to a lower overall part shrinkage. Shrinkage during cooling, however, is the fundamental aspect preventing dimensional accuracy and part reproducibility in LS, in some cases leading to curling and warping [257–260]. For this reason, an optimal shrinkage factor is applied.

In IM, the retraction factor of PA12 varies from 0.7% to 2% [261]. In the case of PEEK, such values vary between 1.2% and 1.5%. Interestingly, the retraction factor is significantly lower for IM PEKK, from 0.004 to 0.005%, due to its low degree of crystallinity [261, 262]. In LS, scaling factors used to compensate shrinkage are highly dependent on the grade but also on the system. The recommended scaling factors for EOS PA2200 powder manufactured using a Formiga P100 system are 3.2%, 3.2%, and 2.2%, in X, Y, and Z direction, respectively. The scaling factors to manufacture PEK HP3 parts in an EOS P 800 system is of 4.5% in all directions but reduces to 3% in the Z direction from 200 mm high [263]. In the case of PEKK, the scaling factors are not yet available, but the prolonged time for cooling in LS leads to a complete crystalline structure, as opposed to the amorphous structure obtained with IM of PEKK.

The melting promoted in LS is also different from other conventional processing techniques as it is constrained by the spot size of the laser, therefore focused on a punctual region of the powder bed. The cooling of LS parts is subdivided into a millisecond cooling once the laser scan is finished [115], followed by a slow cooling, which starts during manufacturing and takes several hours. In IM, consolidation occurs from a polymer in the liquid phase, which solidifies in seconds due to the high cooling rates applied. The effect of cooling rate in the crystalline structure is therefore significant: larger crystals for IM and finer ones for LS, which affect final properties [8].

Few studies attempted to explore the main causes of shrinkage in LS; Shi et al. [103] mentioned the change in temperature, process characteristics, and crystallisation. Thermal shrinkage (β_T) is the shrinkage associated with the change in temperature when no phase transformation is observed. This value is an intrinsic property of the material and is assessed through a linear expansion/retraction coefficient. According to Shi et al. [260], such shrinkage is insignificant when compared with the change in dimensions due to crystallisation.

Shrinkage due to process refers to the retraction associated with the parameters of manufacturing and the process selection. The parameters in LS include laser parameters - power, scan spacing, scanning speed, beam offset, scanned path, spot diameter - and machine parameters, such as layer thickness, temperatures, and the recoating process. Negi and Sharma [249] studied the effect of laser power, scan speed, scan spacing, and scan length in shrinkage of LS PA 32000GF. By varying the scan speed from 2500 mm s⁻¹ to 4500 mm s⁻¹, the extreme speed values tested, shrinkage increased by 4.75%. When varying laser power from 28 W to 36 W, the extreme values of power selected, shrinkage increased by 1.38% only. The values of shrinkage are intermediate when changing part bed

temperature and scan spacing. They attributed the more significant effect of scan speed in shrinkage to the temperature difference caused by the shorter time interval between the sintered and non-sintered region when applying a high scan speed; this leads to an expansion of the heat exchange area due to less time of exposure to the laser.

Kumar et al. [15] stressed the importance of maintaining a uniform bed temperature throughout manufacturing to avoid curling. Indeed, temperature control throughout the bed is an issue reported by several studies. Nonetheless, shrinkage due to the LS process can be significantly reduced on parts with similar geometry placed in the same system using the same combination of laser parameters [260].

Another particularity of AM hence LS is the layer-by-layer nature of the process; this leads to part anisotropy, especially in the Z direction, which does not seem to be linear throughout manufacturing [258, 255]. Soe et al. [258] investigated the non-linearity of PA12 shrinkage in Z direction using an EOS P 700 equipment. They concluded that optimal part placement, parameter control, and management of material improve part accuracy; however, the elimination of non-uniform shrinkage in Z remains a challenge. A few studies also associate dimensional inaccuracy in LS with the rough surface of the parts resulting from the adhesion of extra layers in the bottom and on the top of the LS object [264–266], known as downskin and upskin effect.

Crystallisation influence on shrinkage

Crystallisation is extensively mentioned as the dominant material factor causing shrinkage and leading to dimension inaccuracy in LS [223, 257, 142, 4, 6, 260]. This parameter is not present in amorphous polymers as they do not have a specific melting temperature but show a progressive change in volume with temperature. Nevertheless, other limitations are found when processing amorphous materials, as poor consolidation achieved in the final part and the challenge on identifying the sintering window for successful processing [4, 5]. A schematic representation of the change in volume for amorphous and semi-crystalline polymers is shown in Fig. 2.23.

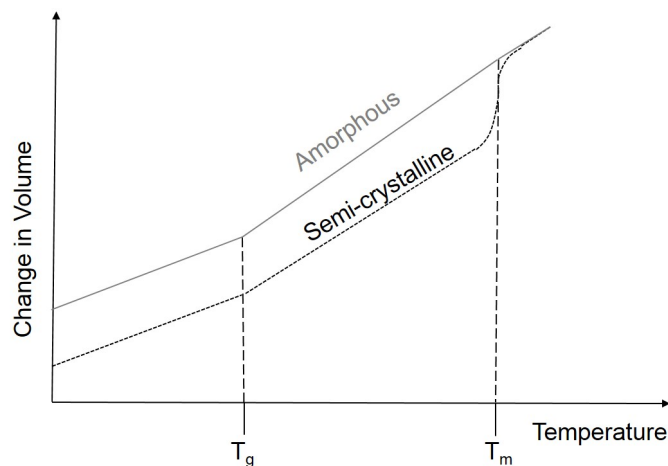


Fig. 2.23 Comparison of the change in volume between amorphous and semi-crystalline polymers.

Crystallisation is the rearrangement of the chains into an organised structure of a lower volume. Therefore, higher levels of crystallinity are expected to increase shrinkage, whilst different crystalline structures result in different volumes and degrees of shrinkage. Van den Eynde et al. [223] found an overall shrinkage of 2.9% for LS polybutene-1 in the tetragonal structure, whilst the hexagonal structure of this polymorph, observed a few days after sintering, shrank approximately 5.8%. Verbelen et al. [142] assessed the shrinkage of EOS PA2200 and Arkema Orgasol PA12 and obtained shrinkage values of, respectively, 4.7% and 4.6%. For PAEK polymers, crystallisation can vary from 0% to 42% [76, 75], depending on the process, cooling rate and time.

The chosen manufacturing process displays a fundamental role in the morphology and degree of crystallinity achieved in the final part. For LS, crystallisation can be significantly different due to its prolonged cooling-annealing stage. The more extended cooling avoids distortion caused by abrupt changes in temperature and promotes highly ordered crystal structures, hence shrinkage [257, 5].

2.5.3.3 Sintering window

LS materials are often selected according to their sintering window. The sintering window is commonly defined as the area between the melting endotherm peak and the exothermic crystallisation peak in the DSC analysis. The bed temperature of LS systems is usually set within this range for semi-crystalline polymers because it allows effective part consolidation by avoiding premature crystallisation on cooling [110, 5]. In order to achieve effective sintering, a wide sintering window is desired with neither double melting peaks nor overlapping melting and re-crystallisation peaks.

Despite not presenting an operation window (Fig.2.24(1)), PAEKs are successfully processed by HT-LS at temperatures within the melting peak [152, 149]. The processing temperature of PAEKs was investigated by Berretta et al. [152], who observed that T_{bed} matches with the minimum of the first derivative of the heating segment in the DSC. This behaviour can be observed in Fig.2.24(2) and (3), respectively, for PEK HP3 and PEEK 450PF.

PAEKs processed at these temperatures can achieve full consolidation, excellent mechanical properties, and avoid premature crystallisation [149]. Despite the high temperature, minimum signs of degradation are observed, which do not prevent the reuse of PAEK powders.

Understanding and controlling processing parameters - laser power, laser scan speed, scan spacing, part bed temperature, and shrinkage factors - are vital to achieving suitable mechanical properties and consolidation in LS [2]. The mechanical properties will be discussed in the following section.

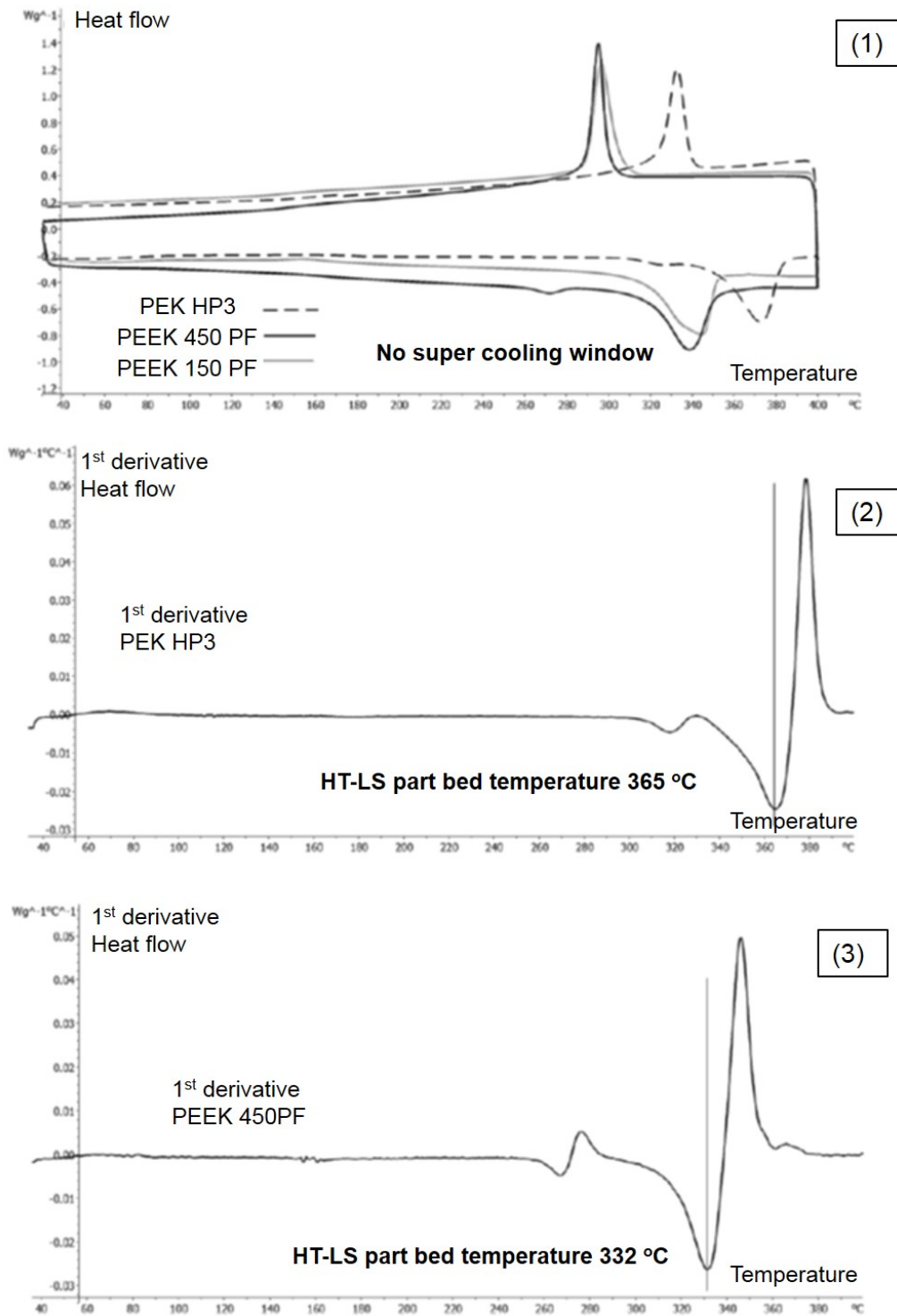


Fig. 2.24 (1) DSC of different PEEK grades showing no operating window. The processing temperature is set within the melting peak and corresponds to the minimum of the first derivative of the heating curve in the DSC. These curves are shown for (2) PEK HP3 and (3) PEEK 450PF [152].

2.6 Properties: Mechanical Behaviour

This section will explore the mechanical properties obtained with LS, especially of PAEKs. The polymer structure and the process properties highly influence the mechanical properties of semicrystalline polymers. In polymer structure, some factors can greatly affect performance, as molecular weight, configuration, arrangement, degree of crystallinity, and crystal morphology. For process properties, some examples include laser parameters, layer interfaces, particle-to-particle interfaces [267], porosity and partial coalescence [268, 5]. The interfaces and porosity are not homogeneous across the build, but highly dependent on the orientation of manufacturing, a key factor to be taken into account when using AM technologies [268, 10].

The thermal processing conditions of LS differs from conventional techniques as the melt is punctual (controlled by the laser spot size) and gradual (layer-by-layer), whilst cooling is slow, therefore increasing the level of crystallinity, the size of the spherulites and even modifying the crystal structure.

2.6.1 Influence of crystallisation in mechanical performance

The crystallisation kinetics and crystalline structure of semi-crystalline polymers processed by LS were recently investigated and compared with IM for PA12 [269–271], PA11 [267], PP [272], PBT [8] and PAEKs [76]. All the studies revealed different structures varying with the process, which directly affected final mechanical properties. The degree of crystallinity in LS is usually high and the crystal structure, i.e., spherulites, smaller [273]. Smaller spherulites are preferred as crack propagation is delayed. The number of nuclei and the cooling rate must be high to obtain small spherulites [50]. Regarding mechanical properties, the increase in the percentage of crystallinity results in higher strength and modulus but significantly lower elongation [272].

In some cases, however, strength is still below the obtained with IM. Arai et al. [8] found lower mechanical performance for LS PBT despite the finer spherulites and higher degree of crystallinity (36.4% against 26.9% for IM). They concluded that the effect of porosity ($\sim 1.7\%$) was dominant over crystallisation in the mechanical properties of LS PBT.

Drummer et al. [6] achieved higher tensile modulus, UTS, and elongation at break for PA12 manufactured by LS when compared to IM. For high-density PE processed by LS and IM, similar properties were obtained, but poly(oxymethylene) (POM), PEK, and PP processed by LS showed a significantly lower mechanical performance. According to Kruth et al. [185], the slow cooling in LS should allow time for full particle coalescence and bonding as well as chain rearrangement for crystal formation and growth. For polymers with high kinetics of crystallisation, bonding can be compromised if the preceding layers do not remain in the molten state. This is the case of POM polymer, which due to the high kinetics of crystallisation, failed in a brittle fashion despite successfully consolidated [6].

From all the mechanical properties, elongation at break seems to be the most affected in parts produced by LS [274, 2, 267, 271]. To illustrate the brittle behaviour resulting from LS, Duraform polyamide 12 (PA12), a widely used LS grade, has the elongation reduced from 200 - 300% when processed by IM to 14% when processed by LS [2]. When subjected to compression, the strain of LS parts is improved but still lower than in IM. Ajoku et al. [271] found a compression strain of 15% for LS PA12 against 17% when PA12 is processed by IM. The lower ductility of LS specimens was associated with process properties - part porosity and incomplete melting - and material structure, such as the increase in the level of crystallinity, the spherulites growth obtained with the slow cooling in LS, but mainly the little or no entanglement between the spherulite crystals [2].

For PEK HP3, Ghita et al. [10] achieved an elongation at break of 3% in LS against the almost 100% obtained with IM. Leigh [267] attributed the low elongation of LS specimens to the poor layer-to-layer adhesion resulting from the existence of micro-cracks or voids in the consolidated structure, the increase in crystallinity and the insufficient cross-linking between particles in the melt pool.

Wang et al. [76] observed a significant increase in the level of crystallinity of PEEK and PEK powder subjected to LS. The LS specimens revealed three different crystal morphologies within the spherulites, following a hierarchical structure. In the primary structure, the size of crystal blocks varies from 20 to 30 nm. A secondary structure bonds the crystal structure together in a less ordered arrangement. Then, a third structure of granular crystal blocks is identified, which is formed by the combination of primary crystal blocks and secondary structure with size varying between 75 and 145 nm.

2.6.2 Influence of molecular weight in mechanical performance

Some studies found an increase in the elongation at break for polymers with higher molecular weight (M_w) [185, 260]. Zarringhalam et al. [270] compared the elongation at break of two different PA12, EOS PA2200, and Duraform PA12 under three different conditions: virgin, refreshed (67% used powder and 33% virgin powder) and used (100% used powder). They found an increase in M_w from 70,000 g mol⁻¹ for virgin to 170,000 g mol⁻¹ for used PA2200 powder. The elongation at break followed a similar trend, and the specimens built with refreshed and used powder showed higher values of elongation, which were attributed to the M_w increase. When investigating the microstructure, the spherulites of both PA12 grades processed by LS are significantly larger than IM and showed unmolten particle cores from which crystals are formed. The unmolten cores matched the DSC analysis in which the particle cores presented a higher melting peak.

Garcia-Leiner et al. [275] found key differences in the crystallisation rate and degree of crystallinity amongst other properties of PEEK with different molecular weight and molecular weight distribution. The degree of crystallinity was approximately 8% higher for the grades with lower molecular weight, whilst their crystallite size increased by 1 nm. Interestingly, the grades with lower M_w showed higher mechanical strength (~ 98.8 MPa) and elongation at break ($>55\%$) than the grades with higher M_w processed by IM.

These results contradict Zarringhalam et al. [270] findings, in which elongation of PA12 was higher the higher the M_w . Garcia-Leiner et al., however, justified their results by the increase in the degree of crystallinity of IM specimens with lower M_w .

2.6.3 Effect of part orientation in mechanical performance

Besides the polymer structure, powder properties (Section 2.3), laser parameters (Section 2.5.3), and part orientation have shown to affect consolidation and mechanical performance significantly. In this section, the effect of orientation will be discussed.

Part anisotropy is one of the main limitations of the LS process, as the lack of adhesion between layers can significantly compromise final performance [268, 10]. It is mostly originated from the weak layer bonding resulting from incomplete fusion of particles in the interlayer area [274]. According to Dupin [135, 191] and Zarringhalam [276], pores and partially-melted particles in the interlayer can be reduced by applying higher energy densities. For Bourell et al. [2], however, partially-melted particles are difficult to control due to heat inconsistency in the LS chamber. Therefore, cold spots lead to porosity and particle coring, whilst hot spots can cause degradation. They also mention inconsistent powder deposition as another factor preventing strong adhesion between layers. These factors lead to up to 50% deviation in elongation between specimens manufactured at different orientations [274].

The orientation of manufacturing significantly affects the mechanical properties of the LS PAEKs. Whilst PEK HP3 manufactured in X orientation showed a tensile strength of 90 MPa, the strength reduced by 12% in Y orientation and by 50% in Z orientation. Regarding elongation, specimens produced in Y orientation achieved strains at break of 3.8% against 2.7% in X orientation and only 1.5% in Z orientation [10].

Anisotropy effect remains a challenge in LS and cannot be completely mitigated [268]. Wegner and Witt [274], however, were able to achieve almost isotropic characteristics for specimens of EOS PA2200 subjected to double laser exposure. The application of two laser exposures in each layer also increased the elongation at break to more than 20% in the specimens built in the same orientation of manufacture.

Optimising mechanical properties in LS is vital for multiple applications, especially in the aerospace field. Current researches, however, are still not able to achieve comparable mechanical properties to IM PEEK using the LS process. Table 2.6 presents some of the mechanical properties of PEK HP3, IM PEEK 450G and the LS PA2200 [277, 10, 278–280].

2.7 Applications

This section will explore the main fields of LS and PAEKs application. As this study focuses on developing PEKK for aerospace applications, a separate section will be dedicated to this industry.

Table 2.6 Some of the mechanical properties of LS PEK HP3, IM PEEK 450 and LS PA2200 [277, 10, 278–280].

Material	PEK HP3 [10, 280]	PEEK 450G [278]	PA2200 [277, 279]
Tensile modulus (GPa) [ISO 527]	X: 4.25 ± 0.15	X: 4	1.7 ± 0.15
	–	–	1.7
	–	–	1.7
Tensile strength (MPa) [ISO 527]	X: 90 ± 5	X: 98	X: 50
	Y: 79.3 ± 5.5	–	Y: 50
	Z: 44.3 ± 3.1	–	Z: 50
Elongation at break (%) [ISO 527]	X: 2.8 ± 0.2	X: 45	X: 20
	Y: 3.8	–	Y: 20
	Z: 1.5	–	Z: 10
Flexural modulus (GPa) [ISO 178]	3.26 ± 0.7	3.8	1.5
Compressive strength (MPa) [ISO 604]	184 ± 15	125	53 ± 15

2.7.1 Aerospace Industry

The rapid development of AM technology has broadened the possibilities of design and structure fabrication for the aerospace industry. AM can, in addition to manufacturing complex and unique parts, be applied to considerably reduce weight by building internal cavities and lattice structures without compromising the mechanical performance, and improve system integration for lightweight or space-limited structures [281, 282].

The aerospace industry is highly affected by the development of AM techniques. Firstly, the small scale production required for aerospace, limited to a maximum of several thousand parts, raises the cost for tooling and mould production in conventional manufacturing. Furthermore, the aerospace industry can take advantage of the complex geometry designs to reduce weight and maintain the structural elements [283].

AM produces less waste material than traditional processes, a determining factor when using expensive aerospace materials such as titanium. As a result, the aerospace and defense industry contributed to about 10.2% of AM's \$2.2 billion global revenues in 2012. In Table 2.7, Coykendall [282] summarises the advantages of AM over traditional processes in the aerospace and defence industry.

Some examples of AM's extensive use in the aerospace industry include wind turbine blades, rotor blades, metallic and composite structures, interconnects, heaters, sensors, transducers, antennas, coatings, schim, and many other multifunctional aerospace parts [281].

Table 2.7 The advantages of using AM to manufacture aerospace and defence parts compared to conventional processes [282].

Part cost down	50%
Scrap down	10%
Time-to market down	64%
Part weight down	64%
Buy-to-fly ratio	1:1

Furthermore, millions of parts go into building a commercial airplane but, when they break, the process of transporting, setting up, and manufacturing a different mould every time a replacement part is needed is time-consuming. With LS, the cost of moulds, transportation, storage, and corrosion can be eliminated. All the data needed to produce parts can be stored in one place and accessed when needed [229].

PAEK polymers show an extensive application in the automotive and aerospace industry. Firstly, they are suitable for automated fibre placement, one of the most advanced methods for fabricating composite structures [284]. PAEK polymers are also suitable for autoclave consolidation [285], resulting in similar mechanical properties as thermosets yet with no need for curing and the benefit of being reshaped and reused.

PEEK is well-suited for parts both in the interior and exterior of the aircraft. In the interior, it can be used when durability, flammability, and low smoke toxicity properties are required. In the exterior, PEEK lightweight and chemical resistance enable the contact with atmospheric particulates and chemicals without damaging the structure [16]. Examples of parts able to be manufactured in PEEK include blades [286] and structural components in contact with hydraulic fluids and synthetic lubricants [17]. Furthermore, the use of PAEK polymers can significantly increase the aircraft rate of production, a critical issue for aircraft manufacturers [27].

2.7.2 Other fields

The market for AM users is continuously increasing, with major brands from varied areas such as Boeing, BMW, Nike, and Johnson & Johnson adopting 3D printing as a technique to produce custom parts [287]. Vashishtha et al. [99] reported that 31.7% of the market production is destined to the motor vehicles industry, in which 18.4% is present as a consumer product. This sector is followed by medical and aerospace industries, which account for 8.8% and 8.6% of the whole production, respectively. Other fields include government/military use, academics, electric home appliance, and jewellery production [15].

Gao et al. [288] classified the applications of AM from nano to large-scale and outlined bio-fabrication, electronics, personal products, automotive, architecture/construction, and aerospace/defense as the main applications of AM in engineering. Wendel et al. [289] mention several applications of polymers in a wide range of sectors, including medical,

aerospace, and mechatronics, in which thermal conductive parts can be used to dissipate heat. Other studies report the use of neat and reinforced fibre polymers manufactured by LS [90, 290, 177, 291, 245], especially PEEK [152, 23, 9, 149, 10, 292].

In the medical field, biocompatibility combined with the overall excellent performance of PAEKs make these polymers highly desired for medical applications such as implants [252]. Panayotov [293] reports three grades of PEEK with biocompatible properties - PEEK-LT1, PEEK-LT2, and PEEK-LT3 - and showed a varied range of successful surgeries in which they were applied, from spine surgery to orthopedic and maxillofacial surgeries. Other biomedical applications include prosthetics, scaffolds, tissue regeneration (bone, cartilage, and tendon), biodegradable platforms, and hearing aids [14, 15].

Chapter 3

Materials and Methods

3.1 Summary

This chapter comprises a description of the material grades and characterisation procedures performed to investigate PEKK properties in powder or specimen format, according to the objective of each experiment. Assessing general material and particle characteristics is crucial to understand and proceed with the other topics explored in the following chapters of this thesis. Understanding the effect of the LS process in mechanical properties, consolidation, surface quality, and intrinsic material behaviour is vital for the successful development and completion of this research. Therefore, different characterisation methodologies were employed to study the items listed as follows:

1. Particle and powder characteristics: scanning electron microscopy (SEM), particle size distribution (PSD), shape analysis and hot stage microscopy (HSM);
2. Powder bulk density and flow: powder rheometry;
3. Thermal properties: differential scanning calorimetry (DSC), dynamic mechanical analysis (DMA) and thermomechanical analysis (TMA);
4. Crystallisation: DSC, wide-angle x-ray diffraction (WXR), transmission electron microscopy (TEM) and TMA;
5. Mechanical properties: tensile testing, flexural testing, and compressive testing.
6. Consolidation: micro-computer tomography (micro-CT), SEM;
7. Surface analysis: surface topology;
8. Powder recyclability analysis: optical microscopy (OM) of the cake, *in situ* bulk density, thermogravimetric analysis (TGA), powder rheometry, SEM, DSC, and WXR.

A schematic representation of the fields of characterisation and their respective experimental methodologies are described in Fig.3.1.

3.2 Materials

This thesis comprises the study of different PEKK grades supplied by Arkema. The grades are identified as Kepstan 6002 PEKK [12]. All Kepstan 6002 PEKK grades of this study are prepared at a concentration of 60/ 40 T/I of terephthalic acid (T) with para phenyl links and isophthalic acid (I) with meta phenyl links. The differences between them concern viscosity and particle characteristics. The PEKK grades were compared with two other commercially available LS grades, known as PEEK HP3 [280] and Orgasol PA12 [294]. Table 3.1 provides some general properties of each grade within the Kepstan 6002 PEKK. Despite the commercial name, PEEK HP3 does not have the same chemical structure

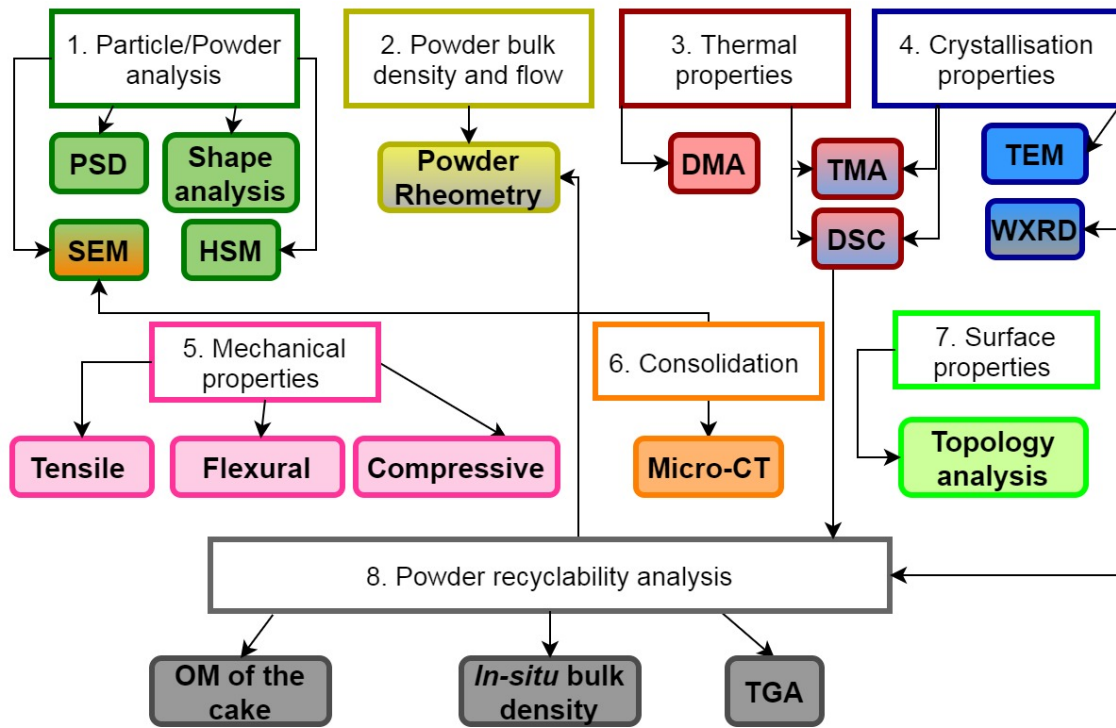


Fig. 3.1 Schematic illustration of the characterisation methodologies performed to describe general properties of PEKK in powder and specimen format.

of PEEKs, but a PEK structure, as shown by the thermal analysis results performed by Berretta et al. [152]. In order to avoid any misunderstanding, this thesis will refer to PEEK HP3 as PEK HP3.

Table 3.1 General properties of different grades investigated in this study. Three grades referred as Kepstan 6002 PEKK were compared with the LS PEK HP3 [280] and Orgasol PA12 [295] grades.

Supplier	Commercial name	Grade	T_g (°C)	T_m (°C)	Viscosity (Pa.s)	D_{50} (μm)
Arkema	Kepstan 6002 PEKK	HL1327	160	297	500*	50.5
		P12S959a	160	300	500*	87.5
		HL1320	160	296	400*	55.6
EOS	PEK HP3	–	164	372	200** [296]	60
Arkema	Orgasol PA12	ES4 NAT3	55	177	–	40

* Conditions of test: 380°C and 1Hz; ** Viscosity measured at 400 °C according to ISO 11443, values of frequency not provided.

All the PAEK grades studied in this work come out of the polymerisation process in the form of flakes, which are broken apart by milling. The resulting milled particles are usually porous and not ideal for LS application, in which high bulk density is desired [85, 88]. Some powders go through a secondary process to eliminate the porous structure, which involves melting to achieve fully dense particles. The molten material is usually extruded and then comminuted to the size range applicable to be processed by LS. This secondary stage is time-demanding and significantly increases the final material cost,

therefore undesirable for large-scale applications. The HL1327 PEKK grade subjected to this secondary comminution process is referred to as P12S959a. Therefore, these grades, i.e., HL1327 and P12S959a, are initially the same material, but the resulting powder structure is different.

The LS PEKK currently being commercialised by Arkema, the PEKK HPS1, is a Kepstan 6002 PEKK grade with the same properties to HL1327 PEKK. Therefore, HL1327 grade will often be referred to as Kepstan 6002 PEKK, unless when compared with the other two PEKK grades, P12S959a and HL1320. The information provided in Table 3.1 was used as a start point to characterise and understand further the most important properties required in LS.

3.3 Experimental Methods

3.3.1 Scanning electron microscopy (SEM)

SEM is a widely applied imaging technique that uses a focused electron beam to interact with the atoms of the sample and produce images with high resolution. Most of the analyses of this thesis used a TESCAN VEGA3 microscope, which contains a secondary electron detector and a back-scattered electron detector, enabling image capture at large magnifications. For the analysis of some powders reported in this thesis, a Hitachi S-3200N scanning electron microscope was used. The samples in powder or specimen form were coated from 7 to 10 nm thick of gold or 10 to 20 nm of chromium to reduce surface charging. The analysis was conducted at a current of 0.13 nA and an accelerating voltage varying from 5 to 20 kV depending on the sample/equipment. Several images were captured at magnifications varying from 30 \times to 15,000 \times .

3.3.2 Particle size distribution (PSD) and shape analysis

The laser diffraction technique is the most commonly employed method to measure particle size and span size. It consists of applying a laser beam through a dispersed particulate sample and measure the angular variation in the intensity of scattered light. A detector capable of acquiring the scattered light computes PSD by applying Mie or Fraunhofer theory, which attribute small angles of scattered light to large particles, whilst small particles scatter light at large angles [297].

The analysis of PSD and shape were performed using a Microtrac TurboSync equipment [124]. This equipment couples red and blue laser diffraction technique with a high-speed camera which captures pictures of particles on focus to describe their morphology. The combination of both lasers allows precise measurement of particles ranging from 0.01 to 4000 μm , according to ISO 13320.

As shape cannot be assessed using laser diffraction, Microtrac developed a dual system, in which 5.2-megapixel camera with a resolution of 22 frames per second can measure particle shape of thousands of particles in the same analysis. The results are assessed by

applying a range of shape descriptors to the data. They will be described in Section 3.3.3 [124].

The Microtrac Turbosync system used in this research operates in a dry mode and uses compressed air and flow conditions settings to disperse the particles. Multiple tests were performed, and PSD was monitored across them to select the appropriate suction pressure and sample dispersion pressure. Their analysis is completed once the pressures were sufficient to break the agglomerates apart but insufficient to break smaller structures within the particles. This difference is identified by a plateau in the PSD, which then shifts to smaller sizes when small structures are pulled out from the particles' core. The suction pressure of 0.5 psi (~ 3.45 kPa) and sample dispersion of 5.0 psi (~ 34.47 kPa) were ideal for performing PSD measurements.

The reflective mode was selected to measure PSD. For each grade, five repeats were performed at a standard background collection time of 10 s and a run time of 20 s. The data was processed using a Microtrac Flex 12.0 software, in which the morphology of at least 1,500 particles was investigated for each condition. Several shape descriptors were applied to assess morphology with either Microtrac Flex 12.0 or alternative imaging processing software such as ImageJ.

3.3.3 Particle size and shape descriptors

The most commonly employed parameter to describe particle size is the diameter. Therefore, span size considers particle size distribution in terms of diameter; this parameter can be calculated according to Eq.(3.1):

$$\text{Span size} = \frac{D(90) - D(10)}{D(50)}, \quad (3.1)$$

in which $D(90)$ corresponds to the diameter which contains 90% of the total volume of particles, $D(50)$ is the diameter which contains 50% of the total volume of particles, and following the same logic, $D(10)$ is the diameter which contains only 10% of the total volume of particles. Therefore, the span size is an indication of how far apart are the 10 and 90 percentage points, normalised with the midpoint, $D(50)$. By analysing particles' images, other measurements of size can be used, such as feret diameter and perimeter. The feret diameter is the longest distance between any two points along the selection boundary, whilst perimeter is the length of the outside boundary of the selection [127].

Several parameters are available to describe particle morphology, as shown in Section 2.3.1.2. They consider different aspects of particle shape and are suitable for distinct applications and analyses. The shape descriptors used in this study are circularity, roundness, aspect ratio (AR), and convexity; their equations are repeated below [127]:

$$\text{Circularity} = 4 \times \pi \times \frac{\text{Area}}{\text{Perimeter}^2}, \quad (3.2)$$

$$\text{Roundness} = 4 \times \pi \times \frac{\text{Area}}{\pi \times (d_{\max})^2}, \quad (3.3)$$

$$AR = \frac{d_{max}}{d_{min}}, \quad (3.4)$$

$$Convexity = \frac{C_{Hull} Perimeter}{Perimeter}, \quad (3.5)$$

in which $C_{Hull} Perimeter$ corresponds to the perimeter of the convex hull, which describes the contour done by a rubber band placed around the image. The shape was investigated in terms of circularity because it is a good surface descriptor and is able to quantify particle roughness. The roundness and aspect ratio are useful parameters to monitor sharp edges and fibre-like shape. Finally, convexity is the default parameter used by Microtrac to investigate particle morphology.

3.3.4 Hot stage microscopy (HSM)

HSM analysis was performed to investigate three different aspects of particle behaviour:

- Particle change in size and shape at dynamic conditions during the melt;
- Coalescence and rate of neck growth during the melt;
- Particle change in size and shape at isothermal conditions.

For all the experiments, a Linkam THMS600 microscope stage was coupled with a Bruker IRScope II microscope operating in reflection mode and on the range of the visual spectrum. A DinoEye eyepiece camera was connected to the system, and images were captured at a magnification of $400\times$ with the assistance of DinoCapture 2.0 software. The sample size of each study consisted of ten individual particles or ten pairs of particles for the coalescence analysis. The image processing was conducted using ImageJ software and following the method described in Fig.3.2.

After capturing the picture (1), the scale of the image is converted to pixels (2), the particles are manually contoured (3), the image is converted to binary (4) and the threshold which matches best the original particles is applied (5). The neck is measured to investigate coalescence, and final dimensions are displayed in Table (6a) of Fig.3.2. The analysis includes a series of size and shape descriptors such as feret diameter, perimeter, circularity, and roundness. These parameters were discussed in Section 3.3.3.

The individual particles and coalescence in dynamic condition used the same methodology to monitor particle change and neck growth; they will be described in Section 3.3.4.1. The HSM in the isothermal condition will be described in Section 3.3.4.2.

3.3.4.1 HSM under dynamic condition

Particle characteristics may affect the coalescence process and consolidation in LS. For this reason, the behaviour of pairs of particles was investigated in dynamic conditions. This experiment attempts to explore the effect of the laser on coalescence, from before to

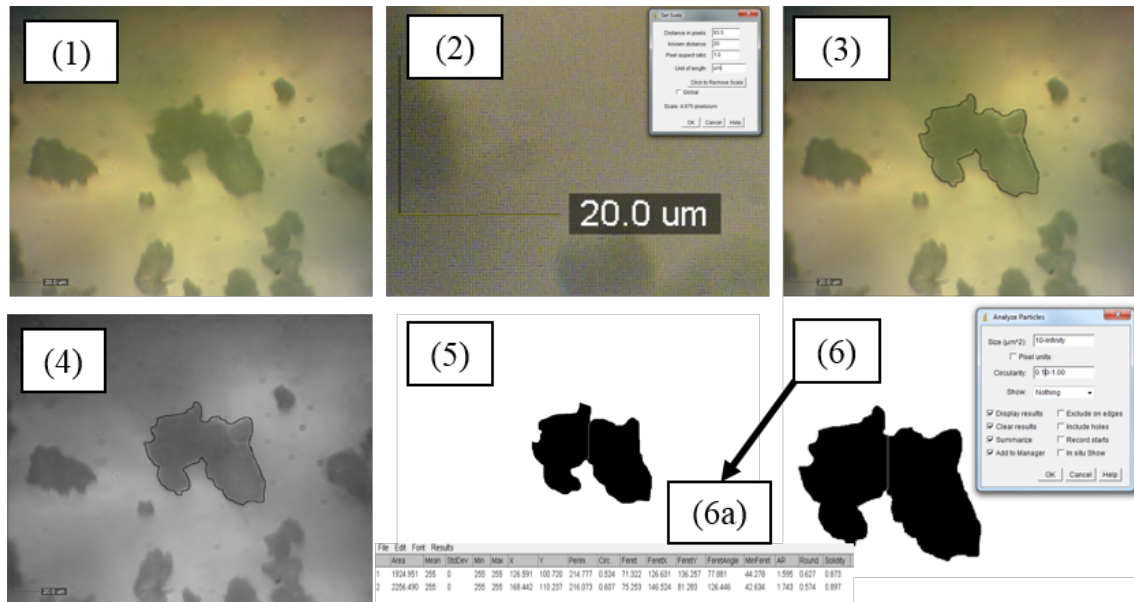


Fig. 3.2 Stages performed in ImageJ software to describe particles under HSM. (1) Image capture, (2) scale conversion, (3) manual contour, (4) binary conversion, (5) threshold application, and (6) measurement of the neck and/or particle size and morphology.

after melt. The size and shape of individual particles were monitored during the melt to complement this study, also at dynamic conditions.

The investigation of particle change and coalescence from before melt until the melt is completed was performed using an HSM. The tests were conducted from room temperature to a maximum of 450 °C, at 120 °C min⁻¹. The high heating rate was used to simulate the melt promoted by the laser, which interacts with the powder in the order of milliseconds [158]. The pictures were captured every 2 s, hence in an interval of 4 °C per picture. A total of 20 pictures were selected for each trial, starting from the image in which the neck is formed. The selection of this image was based on the change in the brightness of the particles and is referred to as T . Images above and below T (°C) were selected for analysis according to Table 3.2. The stages described in Fig.3.2 were applied to process these images.

Three substrates were investigated: glass slides, glass slides coated with silicone, and PEKK films on glass slides. Glass is the standard substrate used to perform HSM [110, 149, 173, 192], therefore chosen for analysis. A silicone-based separator spray was used as a coating to prevent particles from wetting on the glass surface. A fine layer was gently sprayed on the glass slides, and they stayed drying in atmospheric conditions for at least one day. By mitigating the contact between the surface, the size and shape of particles varying with temperature can be more accurately described. Finally, coalescence was monitored on top of 100 μm thick film of Kepstan 6002 PEKK. The film was placed between the glass slide and the particles to replicate coalescence in LS by promoting polymer to polymer contact. As part of monitoring particle coalescence, different methods were applied. They will be described in Section 5.2 and Section 5.3.

Table 3.2 Criteria used to select the images for ImageJ analysis.

1	Room temperature
2	At 200 °C
3	(T-36) °C
4	(T-32) °C
5	(T-28) °C
6	(T-24) °C
7	(T-20) °C
8	(T-16) °C
9	(T-12) °C
10	(T-8) °C
11	(T-4) °C
12	(T) °C, at neck formation
13	(T+4) °C
14	(T+8) °C
15	(T+12) °C
16	(T+16) °C
17	(T+20) °C
18	(T+24) °C
19	At maximum experimental temperature
20	At 200 °C, after cooling

3.3.4.2 HSM under isothermal condition

In LS of polymers, the chamber is heated to avoid material warping. When assessing particle size and shape, however, most studies neglect the effect of processing temperatures, especially the bed temperature (T_{bed}), and analyse these properties at room temperature [121]. As process conditions, the temperature, in particular, can affect particle size and shape, these changes were monitored using HSM.

The isothermal tests were performed on glass slides. The method to select the isotherm temperature was based on the study of Berretta et al. [152] on the minimum of the first derivative of the heating and applied to HL1327 grade. This temperature corresponds to 292 °C. The PEKK particles were monitored for 6 hours at 292 °C, with images captured every 30 minutes.

3.3.5 Powder rheometry

Powder rheometry properties were assessed using a Freeman FT4 powder rheometer [144], which measures stability and flow, bulk density, compressibility, aeration, permeability, shear behaviour amongst other powder properties. The tests of focus in this study concern stability, flow, bulk density, and compressibility behaviour. They were performed for the different PEKK grades subjected to different environmental conditions (Section 3.3.5.1). The tests are described in Sections 3.3.5.2 and 3.3.5.3.

3.3.5.1 Environment conditions

As discussed in Section 2.3.2, moisture has a significant impact on powder properties since it creates bridges in the bulk material and changes the effect of the internal forces in the system [168]. Moisture is particularly strong in hydrophilic materials, e.g., PA12, but should not interact with PAEKs as this family is highly resistant to moisture absorption. Nonetheless, the increase in the surface area of micron-size LS particles can shift such behaviour and affect final powder properties; this was the main motivation for this study. The powder properties were assessed at three different environment conditions:

- **Dry:** powders were sieved at 212 μm , heated in an industrial oven at 100 °C for 8 h and then sieved again at 212 μm ;
- **As received:** powders were tested as received, in standard atmospheric conditions with relative humidity varying from 30 to 60 %;
- **Humid:** the powders were placed in a humid chamber with relative humidity above 90% for at least 48 h;

The powders exposed to different conditions from 'as received' were quickly removed from their own environment and placed in the FT-4 powder rheometer system for the analysis of stability, flow rate, and compressibility behaviour.

3.3.5.2 Stability and flow rate test

The stability and flow rate test measures the effect of particle characteristics (size, distribution, and morphology) in powder flow properties. A standard split vessel of 25 mm \times 25 ml of volume is filled with powder. A conditioning cycle is performed to loosen and slightly aerate the powder bulk, therefore removing any pre-compaction or excess of air from the system. Then, the vessel is split into two parts to monitor the weight in a constrained volume, and to measure bulk density. Following the conditioning stage, a metal blade moves downwards while rotating counter-clockwise at 100 mm s⁻¹. The standard methodology consists of repeating this cycle seven times to obtain the stability index (SI), calculated from the ratio between the average energy required to perform the last cycle and the average energy required to perform the first cycle. The SI value is, therefore, an indication of how powder behaviour is preserved throughout the cycles and should achieve a plateau as the cycles progress.

Highly unstable powders do not achieve a plateau by the end of seven cycles. Therefore, the test needs to be adapted, usually by increasing the number of cycles until achieving a plateau. A few powders analysed in this research project have their standard tests modified to find the stable region.

The energy required to displace the powder from its original position in the last cycle at 100 mm s⁻¹ is referred to as the basic flowability energy (BFE). Specific energy (SE) is calculated from the average energy applied to lift the blade by rotating it clockwise at

the last and second last cycle at 100 mm s^{-1} . The average energy is divided by the mass contained in the vessel so that the effect of powder packing is negligible [144].

The blade tip speed is reduced to 70 mm s^{-1} , 40 mm s^{-1} and then 10 mm s^{-1} , performing one cycle at each of these speeds. The speed reduction aims to monitor the sensitivity of the powder to changes in flow rate. Thus, the flow rate index (FRI) is calculated by dividing the energy required to displace the powder at 10 mm s^{-1} by the energy required to displace the powder at 100 mm s^{-1} . The higher the values of FRI, the more sensitive the powder is to flowing. Each of these parameters refers to a specific property of particles and their interaction. A description is provided in Table 3.3.

Table 3.3 Description of the parameters measured with stability and flow rate test [144].

Parameter	Description
Conditioned Bulk Density (CBD)	Measures the ability of the powder to fill the voids in the structure without the application of a force. It is an indication of packing efficiency and is directly associated with particle configuration, morphology, and flowability.
Stability Index (SI)	Measures how powder behaviour is preserved through different test conditions. It is an indication of powder uniformity and the presence or not of segregation in the structure.
Basic Flowability Energy (BFE)	Measures how difficult to displace the powder using the blade in a confined state. It is an indication of powder cohesivity, morphology, and packing.
Specific Energy (SE)	Measures how difficult to lift the blade through the powder in an unconfined state. It is an indication of particle size, shape, surface texture, friction, and mechanical interlocking.
Flow Rate Index (FRI)	Measures how powder flow is preserved through different test conditions. It gives information about powder uniformity, cohesivity, and segregation.

The test was repeated three times for each grade/condition. A free flow powder has SI value as close to 1 as possible, high BFE, low SE, and FRI values below 1, characteristic of Newtonian flow.

3.3.5.3 Compressibility test

The compressibility test determines the change in density as a function of applied normal stress. A standard split vessel of $25 \text{ mm} \times 10 \text{ ml}$ of volume is filled with powder. The test is preceded by a conditioning cycle as described to measure stability and flow rate. Then, the vessel is split into two parts, and pressure is applied by a vented piston onto the bottom split cylinder, from 0 to 15 kPa, whilst monitoring the percentage change in volume. The variation in the curve is associated with cohesivity and particle size; the

larger the cohesive behaviour and the smaller the particle size, the higher is compressibility. Therefore, low compressibility is preferred as it suggests higher packing efficiency and free flow. An irregular morphology, however, can prevent higher compressibility but may not indicate good flowability. Therefore, this test must be analysed in combination with stability and flow rate test results. The compressibility test was repeated three times for each grade and condition.

3.3.6 Differential scanning calorimetry (DSC)

DSC analysis is a powerful technique to measure material phase transformation. The data is acquired by monitoring heat flux against time or temperature of a crucible containing the sample under analysis and a reference crucible. The test is performed in a controlled atmosphere and follows the methodology created regarding temperatures, heating, and cooling rates.

DSC experiments were performed using a Mettler Toledo 821e/700 [298] with a nitrogen flow rate of 50 ml min⁻¹. Samples with a weight varying between 5 mg to 10 mg were placed in aluminium crucibles with a volume of 40 μL or 100 μL. The data were analysed with the assistance of Star^e SW 12.10 software.

The heat of fusion for 100% crystalline polymer was applied to assess the degree of crystallinity. The values are shown in Table 3.4. The degree of crystallinity was measured according to Eq.(3.6),

Table 3.4 Enthalpy of fusion of the fully crystallised PEKK, PEEK and PA12 polymers at the equilibrium temperature [299, 66, 300].

Material	ΔH_f^0 (J/g)
PEKK	150 [80]
PEEK	130 [66]
PA12	209.2 [300]

$$X_c = \frac{\Delta H_f}{\Delta H_f^0}, \quad (3.6)$$

in which X_c is the fractional crystallinity (%), ΔH_f is the heat of fusion, and ΔH_f^0 corresponds to the heat of fusion of the fully crystalline polymer.

Different methods were applied to measure the melting peak, sintering window, crystallisation kinetics, and degree of crystallinity of PEKK, in isothermal or dynamic conditions. They are described in the following sections.

3.3.6.1 Dynamic DSC

The standard dynamic condition applied to PAEKs consisted of heating the sample from room temperature to 400 °C at 10 °C min⁻¹ rate, and then cooling it back to room

temperature at the same rate. Different heating and cooling rates were also explored, varying from $1\text{ }^{\circ}\text{C min}^{-1}$ to $50\text{ }^{\circ}\text{C min}^{-1}$ between room temperature to $400\text{ }^{\circ}\text{C}$.

3.3.6.2 Isothermal DSC

The slow kinetics of crystallisation of Kepstan 6002 PEKK hinders crystallisation analysis in dynamic condition. Hence, isothermal tests were performed to investigate PEKK crystallisation at different temperatures.

The methodology used for isotherm measurements are as follows: powder was heated at $20\text{ }^{\circ}\text{C min}^{-1}$ from $25\text{ }^{\circ}\text{C}$ to $380\text{ }^{\circ}\text{C}$, then quickly cooled at $80\text{ }^{\circ}\text{C min}^{-1}$ until the isotherm temperature. The isotherm was maintained for 120 min followed by cooling until $25\text{ }^{\circ}\text{C}$, at $20\text{ }^{\circ}\text{C min}^{-1}$. Finally, the sample was heated up to $380\text{ }^{\circ}\text{C}$ at $20\text{ }^{\circ}\text{C min}^{-1}$ to measure T_g , T_m and the melting enthalpy induced by the crystallisation cycle.

The isotherm temperatures chosen varied from $200\text{ }^{\circ}\text{C}$ to $270\text{ }^{\circ}\text{C}$ at an interval of $10\text{ }^{\circ}\text{C}$. The data were analysed with the assistance of Star^e SW 12.10 software, and the time to achieve half of the maximum crystallinity was measured for each isotherm. The isothermal DSC experiments were performed in $100\text{ }\mu\text{L}$ aluminium crucibles to increase peak intensity and facilitate the analysis.

3.3.7 Dynamic mechanical analysis (DMA)

A Mettler Toledo DMA STARe System was used in the compression sample holder configuration to enable thermomechanical analysis. This test aims to measure the material retraction during cooling due to changes in temperature rather than phase transformation. For this reason, no melting was conducted. Two cubic samples with a volume of $2 \times 2 \times 2\text{ mm}^3$ of Kepstan 6002 PEKK (HL1L327 grade) were tested and compared with Orgasol PA12 samples.

The cubes of Kepstan 6002 PEKK were produced by IM in order to obtain a fully amorphous structure, therefore enabling a more accurate analysis of shrinkage by separating shrinkage due to temperature from shrinkage due to crystallisation. The cubes were heated at $1.5\text{ }^{\circ}\text{C min}^{-1}$ from $25\text{ }^{\circ}\text{C}$ to $292\text{ }^{\circ}\text{C}$ and remained at $292\text{ }^{\circ}\text{C}$ for 10 min. This temperature corresponds to the T_{bed} used to manufacture PEKK in the EOS P 800 HT-LS system (Section 7.2.2). The cooling stage was carried out from $292\text{ }^{\circ}\text{C}$ to $25\text{ }^{\circ}\text{C}$. Liquid nitrogen was dispersed around the chamber to maintain the amorphous structure during cooling. The cooling with nitrogen reached a rate of approximately $-5\text{ }^{\circ}\text{C min}^{-1}$, and the full cooling profile was used to measure the coefficient of thermal retraction.

The cubes of Orgasol PA12 were manufactured by LS using an ED of 42 mJ mm^{-2} , T_{bed} of $168\text{ }^{\circ}\text{C}$ and $100\text{ }\mu\text{m}$ of layer thickness. These parameters were the same parameters used to produce the parallelepipeds of Orgasol PA12 and evaluate shrinkage behaviour in LS (Section 8.2.1). The cubes were heated at $1.5\text{ }^{\circ}\text{C min}^{-1}$ from $25\text{ }^{\circ}\text{C}$ to $168\text{ }^{\circ}\text{C}$ and remained at $168\text{ }^{\circ}\text{C}$ for 10 min. This temperature was chosen as it corresponds to the recommended T_{bed} of Orgasol PA12 when processed by the EOS Formiga P100 LS system. The cooling stage was performed at the same rate, $1.5\text{ }^{\circ}\text{C min}^{-1}$ (30% of the cooling rate

used for PEKK), from 168 °C to 25 °C as fully amorphous structure is not easily achieved with Orgasol PA12. The full cooling profile was selected to measure the coefficient of thermal retraction.

3.3.8 Thermomechanical analysis (TMA)

TMA test was performed to assess full retraction at cooling from the melt, but particularly the shrinkage resulting from crystallisation. A TA Instruments Q400 TMA was used in the compression mode with a flat-tipped dilatometer probe of 3 mm in diameter. Two different methods were chosen, a rapid cooling method and a slow cooling method. They are described in Table 3.5.

Table 3.5 Methods for dilatometry analysis.

Grade	Slow cooling	Rapid cooling
Kepstan 6002 PEKK (HL1327)	<ul style="list-style-type: none"> • 25 °C to 292 °C at 20 °C min⁻¹ • 292 °C to 303 °C at 0.5 °C min⁻¹ 	<ul style="list-style-type: none"> • 25 °C to 380 °C at 20 °C min⁻¹ • 380 °C to 25 °C at quick liquid nitrogen cooling
	<ul style="list-style-type: none"> • Remain at 303 °C for 5 min • 303 °C to 25 °C at 0.5 °C min⁻¹ 	

During the cooling stage of the rapid cooling method, liquid nitrogen was dispersed around the furnace, resulting in an approximate cooling rate of 55 °C min⁻¹. The maximum temperature for the rapid cooling method is higher than for the slow cooling method to compensate for any possible thermal lags. The samples of Kepstan 6002 PEKK (HL1327 grade) were produced using a cubic iron mould of 5 × 5 × 5 cm³. The mould was half-filled with powder and then compressed with the assistance of a universal Shimadzu AGS-X series tensile tester. The force selected was close to 20 kN, and the powder remained under compression for 12 h. After removal, the samples were cut from the block into cubes of 5 × 5 × 5 mm³. Three repeats were performed for each method.

The samples were weighed and accurately measured using a micro-computer tomography (micro-CT) (Section 3.3.14). Once the TMA test was completed, the cooling profile was extracted, and the region of crystallisation was selected to measure shrinkage due to crystallisation. This region of crystallisation was determined as between 292 °C and 200 °C.

3.3.9 Wide angle X-ray diffraction (WXR)

WXR is used to characterise crystalline materials concerning their structure, phase, crystal orientation, degree of crystallinity, grain size, and other parameters. A monochromatic beam of X-ray light interacts with the lattice planes from a sample and is scattered at specific angles, according to the lattice plane in contact [301]. The multiple scattered

lights leaving the crystals interfere with each other, and the constructive interactions are collected to create the X-ray diffraction spectrum.

The WXR D analysis was performed using a Bruker D8 Advanced X-Ray Diffractometer with Cu K α ($\lambda = 0.1542$ nm) radiation and a LynxEye detector operating at a voltage of 40 kV and a current of 40 mA. The data was collected in a fixed time mode (1 s) with a step size of 0.05° and run from $2\theta = 4$ to 65° . Crystallinity was measured by firstly selecting the background baseline using DIFFRAC V6.0 software. Then, the total area of the crystalline peaks was divided by the total area of the WXR D spectrum to measure the degree of crystallinity.

LS specimens and samples in powder format were investigated under WXR D. The powder samples were placed on glass slides and compressed/spread with the assistance of another glass slide to obtain a flat and homogeneous surface.

3.3.10 Transmission electron microscopy (TEM)

TEM is a technique that uses a high energy beam of electrons to investigate material structure. The electron beam interacts with the atoms of a very thin sample in the order of nanometres and enables visualising features as crystal morphology, grain boundaries, membrane materials, and others. The TEM technique shares the same principle of optical microscopy, but the use of an electron beam allows enhanced resolution even in high orders of magnitude, revealing details at the atomic level [302].

A JEOL JEM-1400 electron microscope was used in the transmission mode to investigate the crystal structure of Kepstan 6002 PEKK, HL1327 grade, manufactured at different LS conditions. The LS specimens were cut into thin sections of approximately 90 nm with the assistance of an RMC POWERTOME PC Ultracut. The sections taken for analysis were removed from the middle of the specimens.

The imaging analysis was conducted at a voltage of 120 kV and $77.2 \mu\text{A}$ using an ES 100 W CCD digital camera (Gatan, Abingdon, UK). Images were captured at different magnifications varying from $3,000\times$ to $25,000\times$.

3.3.11 Tensile testing

Tensile testing was performed using a Shimadzu AGX-plus equipment with a maximum force of 2 tonnes. A sample size of ten specimens was chosen to investigate each combination of laser parameters, different processing temperatures, and orientation of manufacture. The specimens were tested at 1 mm min^{-1} following ISO 527-2-1BA guidelines. The standard consists of specimens with an approximate length of 80 mm, a testing width of 5 mm, and 4 mm of thickness. The orientations of manufacturing - X, Y, and Z - are described in Fig.3.3.

The calculation of elastic modulus considered a deformation of 0.2% in the elastic region. The elongation was monitored using a TRViewX non-contact digital video extensometer coupled to the universal testing equipment.

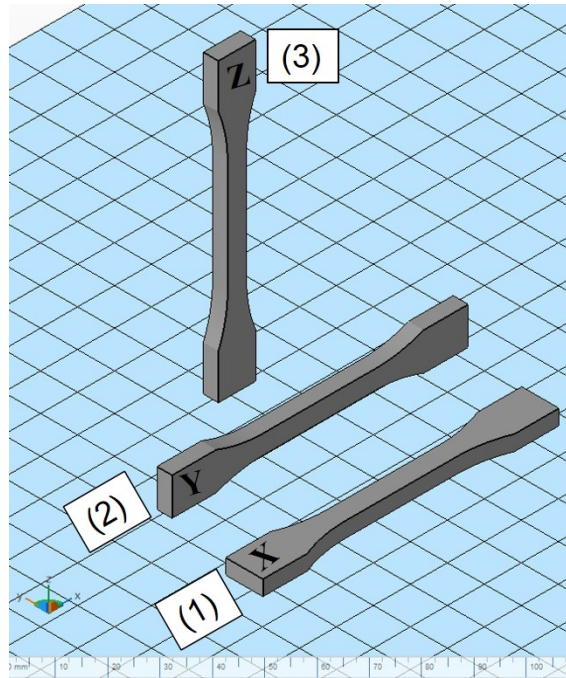


Fig. 3.3 Illustration of the different orientations of manufacturing, (1) X, (2) Y, and (3) Z. The specimens manufactured in X and Y orientation were placed at 0° in relation to the powder deposition direction, whilst Z specimens were manufactured at 0° and 90° rotation in relation to the direction of powder deposition.

3.3.12 Flexural testing

Flexural behaviour was investigated using a Lloyd EZ20 equipment with a load cell of 500 N at a three-point bending configuration, according to ISO 178 for plastics. The standard specimen has the shape of a parallelepiped with an approximate length of 80 mm, a width of 10 mm, and a thickness of 4 mm. Test speed of 1 mm min^{-1} was chosen, and ten specimens for each orientation (X, Y, and Z, see Fig.3.3) were tested at the best combination of laser parameters and processing temperatures.

3.3.13 Compressive testing

Compressive testing was performed following ISO 604 guidelines. Cylindrical specimens of approximately $10 \times 10 \times 4 \text{ mm}^3$ were manufactured to measure strength and elongation, whilst parallelepipeds of $50 \times 10 \times 4 \text{ mm}^3$ were used to measure compressive modulus, according to the ISO standard mentioned above. The test used a Lloyd LR 300K equipment operating at 5 mm min^{-1} . The sample size consisted of ten specimens for each orientation, X and Z, at the best combination of laser parameters and processing temperatures. The chosen limit for compressibility was 75% of the specimens' height regardless of apparent failure or not.

3.3.14 Micro-computer tomography (Micro-CT)

Micro-CT was used to map the porosity of laser sintered parts manufactured at different conditions, as well as to measure the dimensions of TMA cubic samples. The test was conducted using an X-Tek benchtop CT 160 Xi System with a resolution of $3\ \mu\text{m}$. The samples were examined at 360° rotation using a current of $65\ \mu\text{A}$ and a voltage of $65\ \text{kV}$.

The micro-CT test virtually divides each specimen in a series of 2D slices, which are irradiated with X-rays. The 2D images are reconstructed into a 3D image with the assistance of VGStudio MAX software. The reconstruction enables the analysis of different morphological characteristics, including damage or defect analysis, porosity percentage, and pore size. This study only investigated porosity percentage.

3.3.15 Surface analysis

Surface topology was investigated using a Taylor-Hobson Talyscan 150 surface profiler. This technology uses a laser probe with a deflection range of $6.29\ \text{mm}$ and a resolution of $162\ \mu\text{m}$ to measure surface roughness. The parameters used to analyse surface topography included the arithmetical mean height of an area (S_a) and a line (R_a) and the average difference between the absolute peak and pit height (S_t and R_t).

The quality of the surface was assessed on specimens manufactured in X, Y, and Z orientations, in the regions described in Fig.3.4. LS films were also produced to monitor differences in the surface topology of PEKK manufactured with a different combination of laser parameters. This analysis was extended to study the effect of multiple exposures. The production of films consists of regular sintering followed by the interruption of the build straight after the sintering of the last layer to avoid further deposition of non-sintered powder on the top. This method is more accurate when investigating the effect of laser parameters on part surface quality as it avoids upskin effect [265]. For both types of samples, specimens and films, areas of $3 \times 3\ \text{mm}^2$ were selected and scanned at $750\ \mu\text{m}\ \text{s}^{-1}$ with a spacing of $3\ \mu\text{m}$ in X and $5\ \mu\text{m}$ in Y. The test was repeated three times for each set of parameters/orientation.

3.3.16 ANOVA statistical analysis

ANOVA statistical analysis was used to investigate the statistical significance of the mechanical testing results, porosity analysis, surface roughness data, and degree of crystallinity of LS PEKK specimens. The comparison was developed for specimens manufactured in different orientations (see Fig.3.3), with different processing temperatures and cooled for different times. The software package IBM SPSS Statistics 26 [303] has been employed to perform the analysis. One-way and two-way ANOVA were used depending on the test comparison. The experiments were analysed at a confidence level of 95% using the Tukey method for the post-hoc test. The level of significance was explored regarding 'P-values', with values below 0.05 being statistically significant, therefore confirming the significant difference resulting from the condition to which each data was generated.

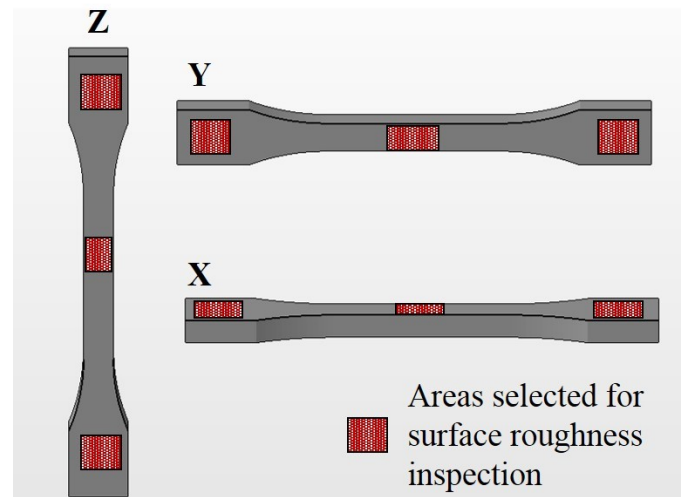


Fig. 3.4 Areas selected for the inspection of surface roughness on specimens manufactured in different orientations.

3.3.17 Cake analysis under optical microscopy

A visual inspection was conducted to investigate the non-sintered powder within the build chamber in LS, also referred as part cake. This test used a standard optical microscope coupled with a DinoEye eyepiece camera at $60\times$ magnification. Several images were captured with the assistance of a DinoCapture 2.0 software and analysed using ImageJ software. The analysis consisted of filtering voids and porosity present in the cake images from the solid structure of the powder by converting them into binary colour. The ratio between the area of the voids against the total area of the image was calculated for at least 15 images of each part cake. This inspection aims to compare cakes processed at different temperatures regarding overall porosity, density, and particle size. A typical image captured with the optical microscope is shown in Fig.3.5(1). The resulting binary conversion of the same image is shown in Fig.3.5(2).

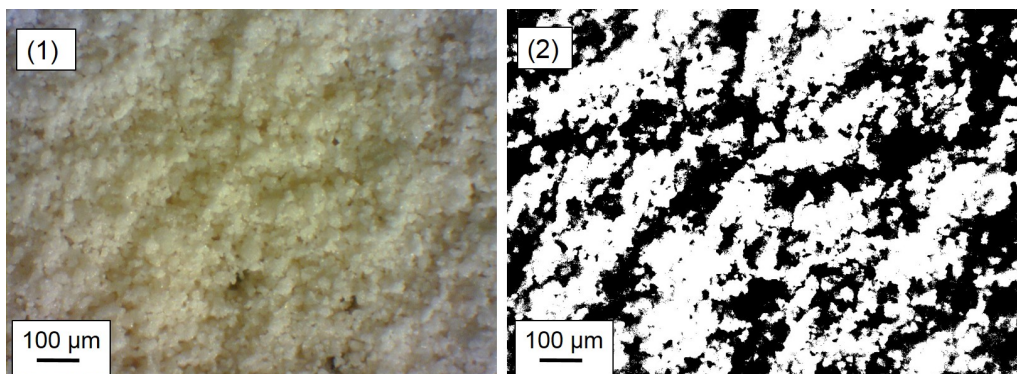


Fig. 3.5 (1) Optical image of the cake and (2) conversion of the image into binary colours.

3.3.18 *In situ* bulk density

Measuring bulk density inside the LS system is the most accurate method to monitor bed density of the process. This test was performed inside a EOS P 800 HT-LS system operating at T_{bed} of 292 °C and T_{bp} of 265 °C. Six boxes with a wall thickness of 2 mm and an empty volume of 25 cm³ were manufactured using HL1327 PEKK grade. Once the boxes were completed, the production was interrupted, and no subsequent layers were applied on the top. As Kepstan 6002 PEKK powder has the ability to self-support itself at the end of each layer-by-layer spreading, the boxes were easily removed from the powder bed with the unsintered powder inside them. They were weighed before and after the removal of the powder to calculate powder bulk density, as illustrated in Fig.3.6.

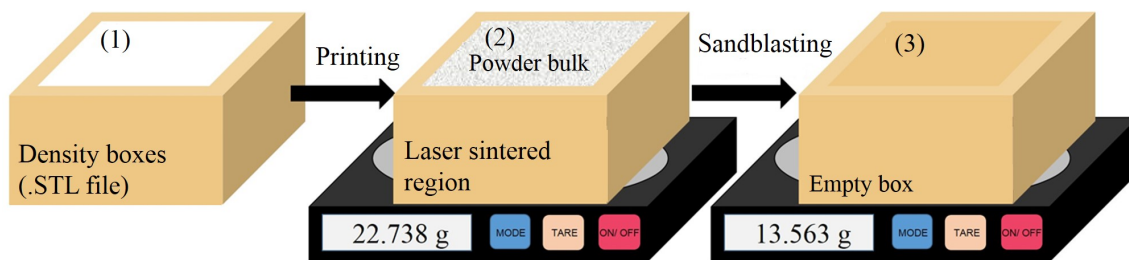


Fig. 3.6 Laser sintered boxes manufactured to assess powder bulk density of Kepstan 6002 PEKK. (1) .STL file, (2) manufactured boxes filled with powder after removal from the LS system; (3) empty boxes (after sandblasting and cleaning).

3.3.19 Thermogravimetric analysis (TGA)

TGA is one of the most commonly employed techniques to measure thermal stability and degradation. This test monitors mass loss over temperature or time under a controlled atmosphere, whilst the temperature is constant (isothermal) or linearly increasing with time (dynamic). TGA tests were performed using a horizontal Mettler Toledo TGA/DSC 1-1100 °C system [180]. Samples of approximately 10 mg of virgin and processed powder were placed into alumina crucibles of 70 μ L of volume and heated at 10 °C min⁻¹ from room temperature to 900 °C using a nitrogen flow rate of 50 ml min⁻¹. The data were analysed with the assistance of Star^e SW 12.10 software.

Chapter 4

Powder Characterisation

4.1 Summary

The three PEKK powders described in Section 3.2, Table 3.1, were characterised regarding particle and powder properties. The flaky structure resultant from the polymerisation process of PAEKs is comminuted into porous particles of heterogeneous shape. Such a structure can be disrupted by melting, extrusion, and subsequent milling, which were the steps applied to produce P12S959a particles.

Particle and powder properties were investigated under SEM, PSD, and powder rheometry. PEK HP3 and Orgasol PA12 grades were used for comparison and benchmarking. The effect of environment condition was explored to powder samples of PAEKs regarding flow and bulk density. Moisture effect was also considered as pre-drying is usually required for LS powders such as PA12, but currently not performed in PAEK powders.

The screening of different powder properties revealed HL1327 and P12S959a PEKK as suitable grades for LS, although HL1327 powder shows more similar behaviour to PEK HP3. HL1327 powder has ideal size distribution, whilst P12S959a particles are solid and closer to a spherical shape. In comparison to HL1320, these grades present higher viscosity, which is usually associated with an increase in the mechanical properties of the final LS part. The investigation of different environmental conditions confirms the high resistance of PAEKs to moisture uptake due to the high chemical stability of the monomer [304, 149, 63, 252]. However, particles with a rough surface and internal porosity had their flow performance improved when subjected to a humid environment. This behaviour is supported by Coelho and Harnby [153], who claim that water acts as a lubricant and reduces friction and interlocking forces between particles. The HL1327 powder subjected to humid condition, however, does not interact with the powder bulk by creating capillary forces, which means that PAEK particles can be used in LS without the need of drying before processing.

4.2 Particle Characteristics

4.2.1 Scanning electron microscopy (SEM) analysis

The three grades of Kepstan 6002 PEKK - HL1327, P12S959a, and HL1320 - were analysed using the SEM technique. Images of the particles were captured at different magnifications, varying from 500 \times to 2,000 \times , as shown in Fig.4.1. P12S959a and HL1320 particles are shown in Figs.4.2 and 4.3, respectively. The images were used for general screening of powder morphology, size, distribution, and porosity evaluation. They were compared with commercial and well-established LS grades, Orgasol PA12 (Fig.4.4), and PEK HP3 (Fig.4.5).

Following a qualitative SEM evaluation, the particles of HL1327 grade seem to range within the appropriate size distribution for LS, and they mostly show similar morphology (Fig.4.1(1)), except for the few particles with elongated shape, e.g., Fig.4.1(2). However, the surface of HL1327 particles is rough, and they present a porous structure. HL1320

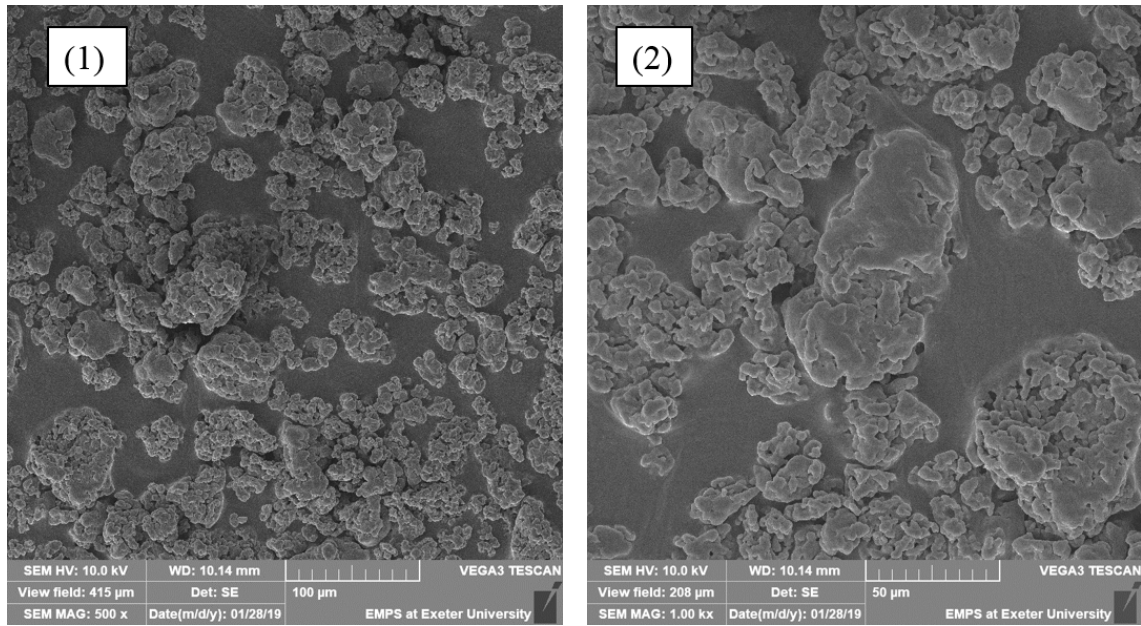


Fig. 4.1 Typical SEM images of HL1327 powder (Kepstan 6002 PEKK) at increasing magnification. Note the scale bars of (1) 100 μm and (2) 50 μm .

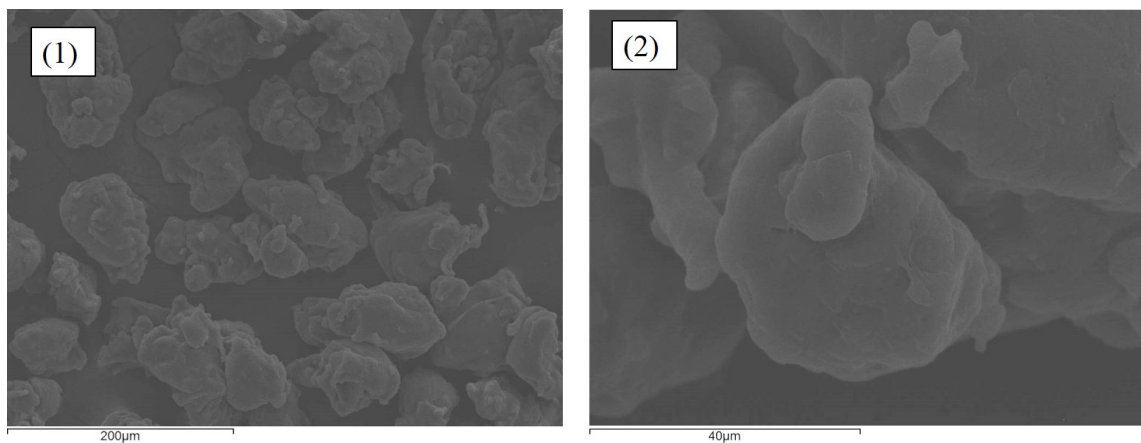


Fig. 4.2 Typical SEM images of P12S959a powder at different magnifications. Note the scale bars of (1) 200 μm and (2) 40 μm .

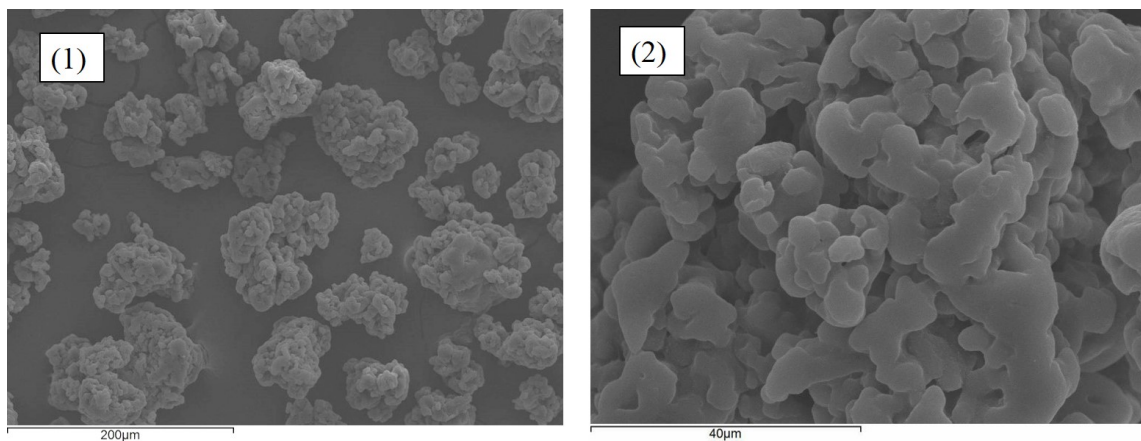


Fig. 4.3 Typical SEM images of HL1320 powder at different magnifications. Note the scale bars of (1) 200 μm and (2) 40 μm .

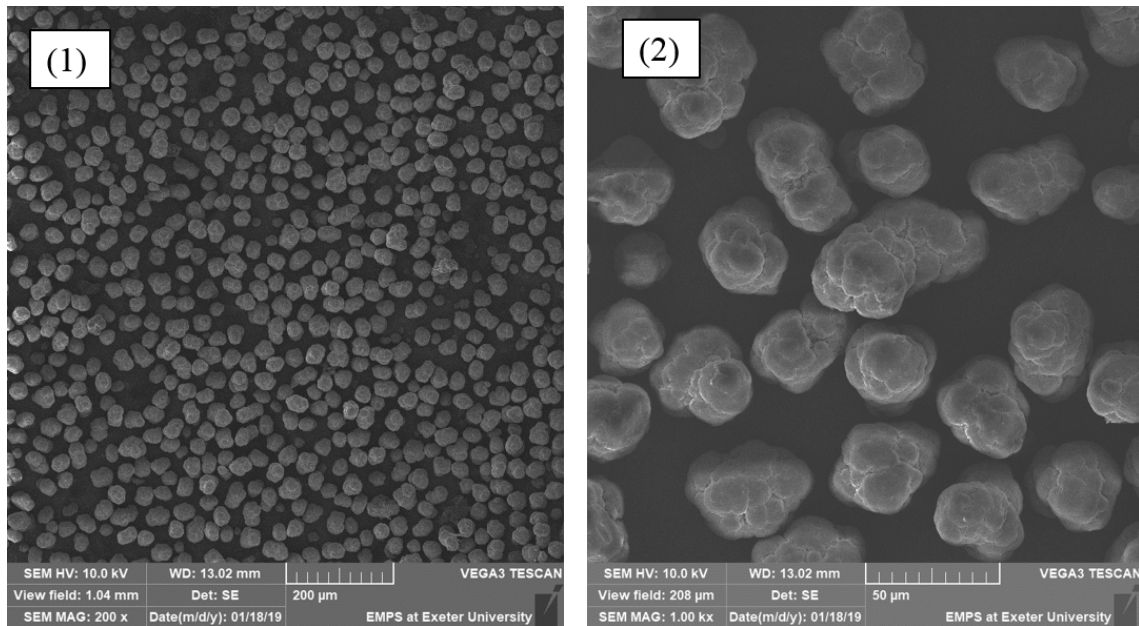


Fig. 4.4 Typical SEM images of Orgasol PA12 powder at different magnifications. Note the scale bars of (1) 200 μm and (2) 50 μm .

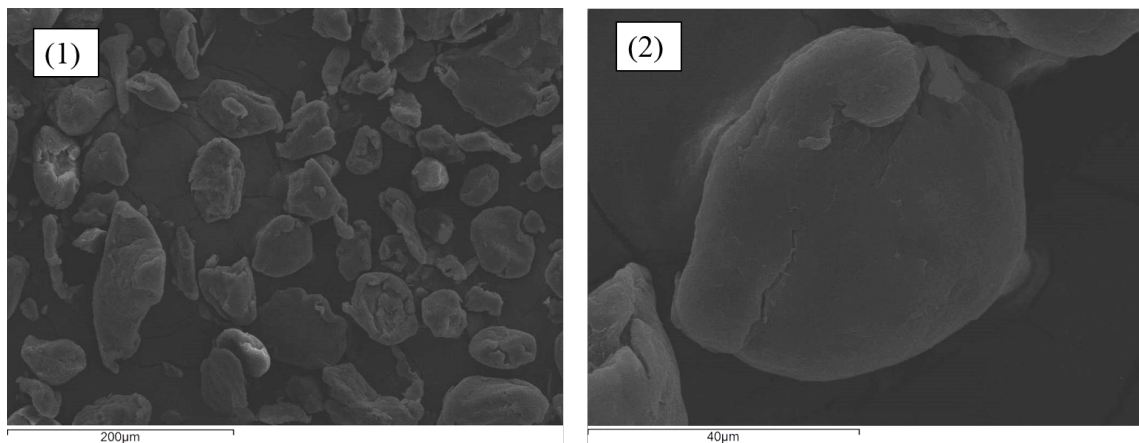


Fig. 4.5 Typical SEM images of PEK HP3 powder at different magnifications. Note the scale bars of (1) 200 μm and (2) 40 μm .

particles (Fig.4.3) share a similar size, morphology, and porous interior with HL1327 grade. As opposed to HL1327 and HL1320, P12S959a particles (Fig.4.2) are solid with no visible porosity in the interstices. These characteristics are supported by the additional step on particle production, which disrupts the flake and porous structure by melting, extruding, and milling the solid PEKK into particles. The cryogenic milling process leads to potato-shaped geometries and sharp edges, as observed for some of the P12S959a particles. However, this morphology is still preferred over HL1327 powder.

Amongst all grades taken to SEM analysis, Orgasol PA12 approaches the most desired size and morphology for LS application. The particles show uniform diameter (Fig.4.4(1)), almost spherical shape, and a solid interior (Fig.4.4(2)). Furthermore, the surface seems very smooth, despite some protuberances in localised regions of the particles. Likewise Orgasol PA12, the PEK HP3 particles shown in Fig.4.5 look very dense and smooth. Their shape, however, seems to vary significantly, with several elongated particles, some of them

approaching the shape of fibres. The morphology distribution looks quite broad too - the smaller the particles, the rounder they look, whilst the increase in size leads to particles resembling the potato geometry. Nonetheless, the sample size of the SEM images is quite narrow. Therefore, particle size distribution and morphology analysis were performed; the results are discussed in Section 4.2.2 and Section 4.2.3.

4.2.2 Particle size distribution analysis

PSD was performed using a piece of Microtrac TurboSync equipment, as reported in Section 3.3.2. The (1) volumetric and (2) cumulative distribution results are reported in Fig.4.6. A summary of particle size distribution analysis is shown in Table 4.1, in which span size is calculated by Eq.(3.1).

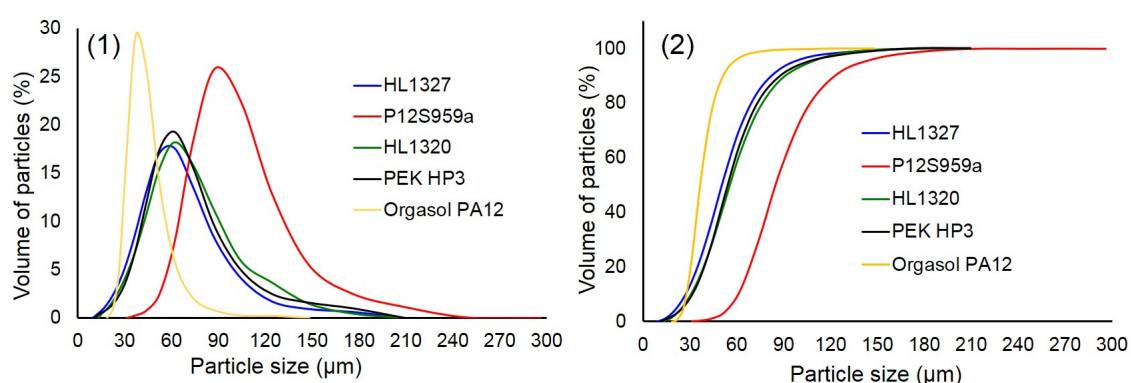


Fig. 4.6 Particle size distribution results of different PEKK grades. PEK HP3 and Orgasol PA12 were added for comparison. (1) Volumetric distribution and (2) cumulative distribution of particle size.

Table 4.1 Summary of particle size distribution analysis of PEK HP3, Orgasol PA12, and different PEKK grades.

Volumetric parameter	HL1327	P12S959a	HL120	PEK HP3	Orgasol PA12
D(10) (μm)	27.4	60.8	30.83	31.8	27.8
D(50) (μm)	50.6	84.7	55.6	54.3	36.6
D(90) (μm)	82.1	122.6	91	87.9	51.3
Span size	1.1	0.7	1.1	1	0.6

From graph (1) of Fig.4.6, HL1327 and HL1320 powders have a similar distribution to PEK HP3. If compared to Orgasol PA12, however, these grades present larger particle size, broader distribution (span provided in Table 4.1), and less spherical shape. P12S959a grade shows a clear shift to larger particle size in comparison to the other PEKK grades. Whilst most PEKK grades have an average D(50) between 50 and 56 μm , P12S959a shows a D(50) approximately 30 μm above the D(50) of PEK HP3. This size distribution is outside the expected range for LS and is a result of the method employed for the fabrication of P12S959a powder.

For the following sections of this chapter, HL1320 PEKK will be excluded from the analyses due to presenting very similar properties to HL1327 PEKK powder. This resemblance is not surprising since these powders were produced using the same methodology. However, because they differ in viscosity, HL1320 will be introduced again in Chapter 5 to discuss coalescence behaviour.

4.2.3 Shape analysis

The analysis of shape calculated from Microtrac TurboSync consisted of firstly comparing the HL1327 and P12S959a PEKK grades and then benchmarking HL1327 grade with PEK HP3 and Orgasol PA12, as shown in Fig.4.7. The HL1327 grade was selected for comparison due to its particular shape. The morphology was evaluated regarding perimeter, circularity, roundness, and convexity; they were described in Section 3.3.3.

The graphs on the left (Fig.4.7(a)) highlight the apparent difference in the diameter of P12S959a particles, as shown by the PSD analysis. Regarding perimeter, P12S959a and HL1327 grades present an almost linear trend, which suggests that the same shape is maintained across the particle size scatter. At diameters above 120 μm , however, a broader scatter is observed, especially for P12S959a particles. The scattered values of circularity and convexity are slightly narrower for P12S959a than for HL1327 grade, justified by the smoother surface of P12S959a particles as presented in the SEM images of Fig.4.2.

The shape comparison performed in the graphs of Fig.4.7(b) (HL1327 against PEK HP3 and Orgasol PA12) presents similar particles scattering for PEK HP3 and HL1327 grade, which above 100 μm are scattered to wider shape distribution and less spherical morphology (lower values of circularity, roundness, and convexity). As opposed to the PAEK grades, Orgasol PA12 has a narrow particle size distribution with circularity and roundness values mostly varying between and 0.5 and 0.9, whilst convexity is mainly above 0.8. The controlled spherical shape of Orgasol PA12 grade comes from the method employed to manufacture polyamide powders, which cannot be applied to PAEKs. However, PEK HP3 is a widely established grade for LS, and the similar trends in shape achieved with HL1327 and P12S959a are very promising for the same application.

4.3 Powder Properties

4.3.1 Powder rheometry results

Table 4.2 provides a general summary of the results achieved with the powder rheometry tests described in Section 3.3.5, Chapter 3.

The stability test consists of repeated measurements of the energy required to displace the powder from its original position. A powder becomes stable when the total energy applied by the blade to displace the particles from their original position reaches a plateau. As explained in Section 3.3.5.2, the tests were modified to achieve a stable condition for each grade in the 'as received' condition.

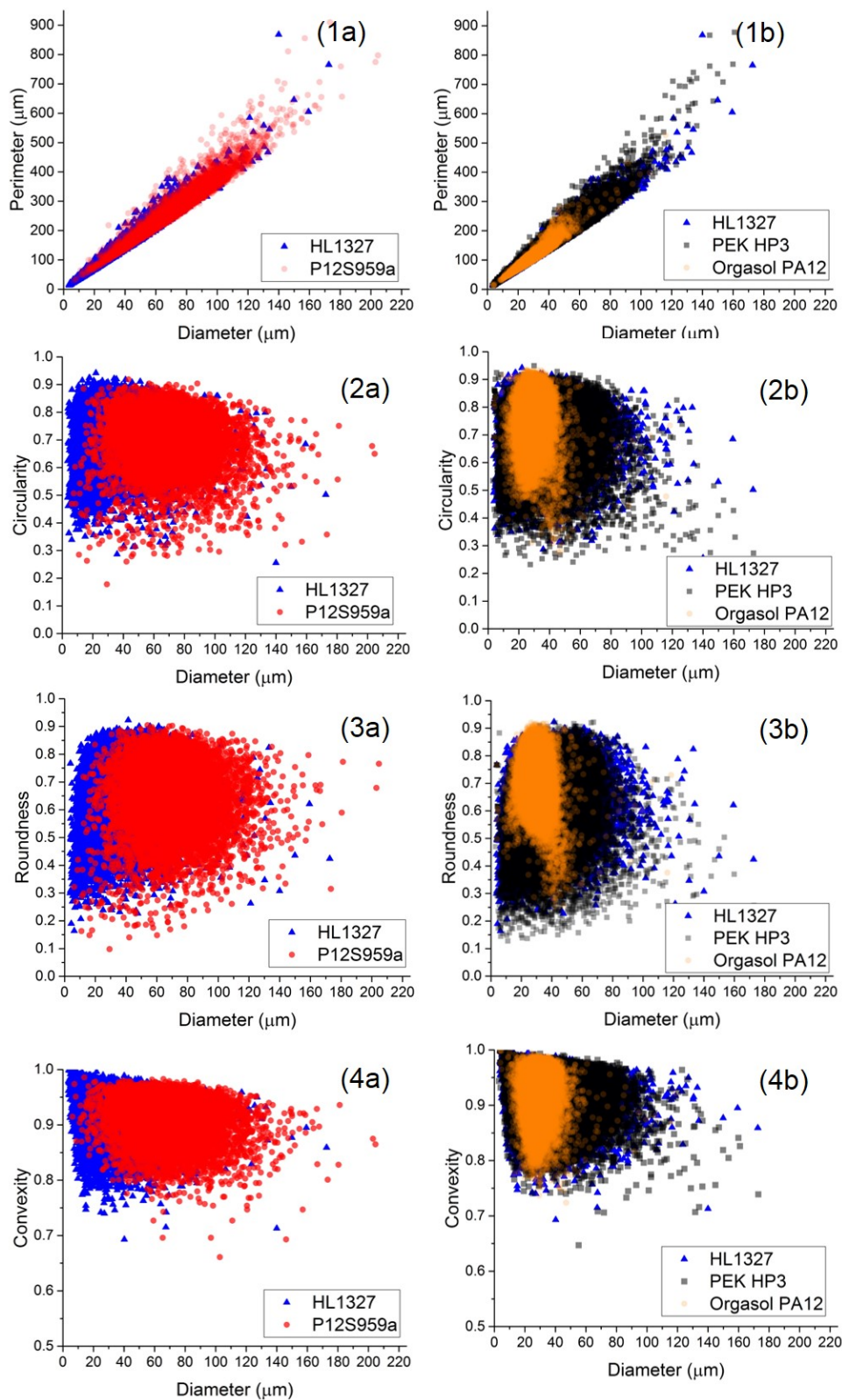


Fig. 4.7 Shape descriptor results for (a) different PEKK grades and (b) Kepstan 6002 PEKK compared with well-established LS grades. The shape was described in terms of particle diameter against (1) perimeter, (2) circularity, (3) roundness, and (4) convexity.

Table 4.2 Summary of powder rheology results for different PEKK grades. PEK HP3 and Orgasol PA12 were included for comparison.

Parameter	HL1327	P12S959a	PEK HP3	Orgasol PA12
CBD (g/ml)	0.36 ± 0	0.5 ± 0	0.47 ± 0	0.54 ± 0
SI	1.47 ± 0.2	2.09 ± 0.5	1.57 ± 0.1	0.97 ± 0
BFE (mJ)	173 ± 11.2	389.3 ± 31	240.4 ± 1.8	126.3 ± 3.5
SE (mJ/g)	19.3 ± 1.3	31.4 ± 2.4	20.5 ± 0.3	2.92 ± 0
FRI	1.48 ± 0	1.15 ± 0	1.55 ± 0	1.23 ± 0
Compressibility (%)	10.2 ± 0.5	7.7 ± 0.4	11.9 ± 0.4	1.5 ± 0.2

Hence, a total of 20 and 40 cycles were used, respectively, for HL1327 and P12S959a PEKK. For the benchmarked grades PEK HP3 and Orgasol PA12, 20, and 7 cycles were required to achieve a stable level. The curves are reported in Fig.4.8.

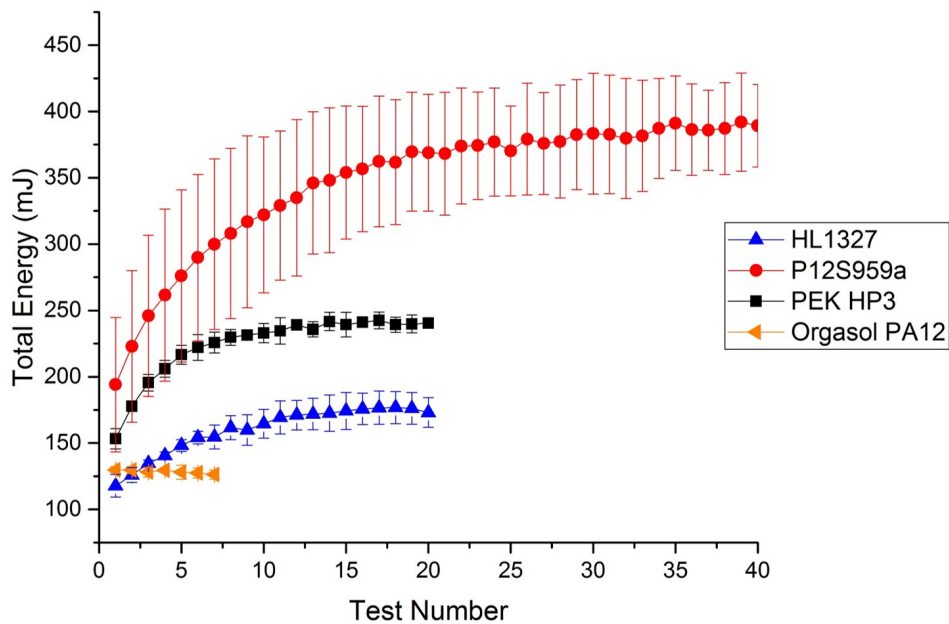


Fig. 4.8 Stability test curves for PEKK grades. PEK HP3 and Orgasol PA12 were introduced for comparison.

P12S959a shows a clear discrepancy from the other grades in analysis and took the longest to stabilise, a total of 26 cycles. HL1327 achieved a plateau after 11 cycles, followed by PEK HP3, which took ten cycles to stabilise. On the contrary, Orgasol PA12 shows a very stable behaviour from the first cycle due to its narrow distribution and uniform particle shape. The stability indexes in Table 4.2 support the results of Fig.4.8, in which Orgasol PA12 has the closest value to 1.0 (0.97, from Table 4.2), suggesting a stable behaviour, and P12S959a is the least stable grade, with an SI of 2.09. The high instability

of P12S959a might indicate segregation in the powder bulk. This phenomenon can be inferred from the large particle size (Table 4.2), which may have led to different particle arrangements with the rotation and translation movement of the blade across the bulk. In the case of HL1327, stability values can be justified by the irregular morphology and high surface roughness.

Fig.4.9 presents the flow curves of PAEKs and Orgasol PA12 with decreasing blade tip speed. Except for Orgasol PA12, all grades require more energy to displace the particles from their original position when tip speed is reduced. This behaviour is particularly evident for PEK HP3 and HL1327, in which interlocking may be affecting flow. P12S959a grade seems to be the least affected by tip speed; this may be a result of high particle density, large particle size, and a smoother surface. Once again, Orgasol PA12 shows the best flow properties as less energy is required to promote flow. The BFE row in Table 4.2 supports this discussion, in which P12S959a powder requires three times more energy to be displaced than Orgasol PA12. The values of bulk density (first row) are higher for the powders with denser particles and smoother surface.

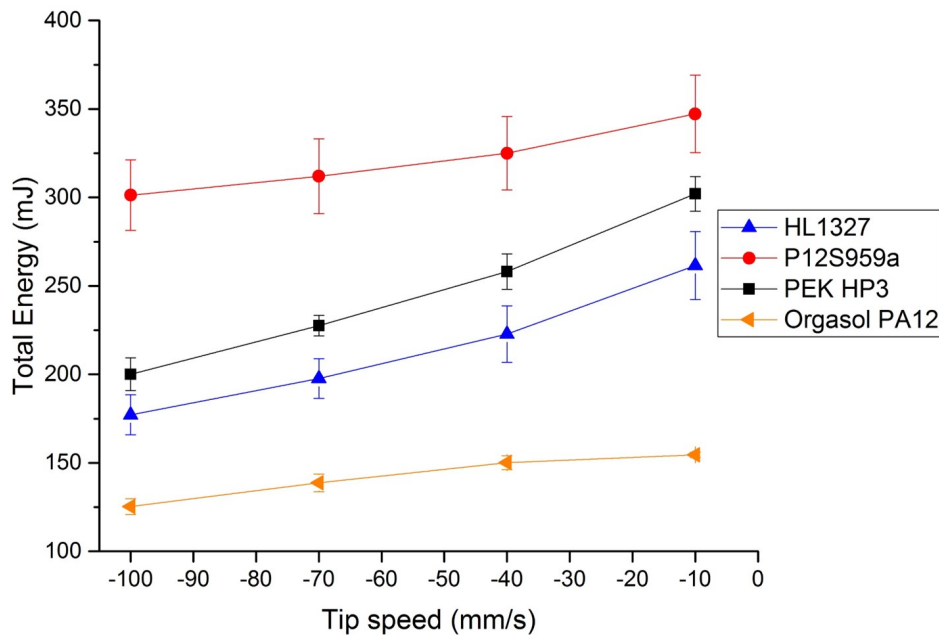


Fig. 4.9 Flow rate curves of PAEKs and Orgasol PA12 varying with tip speed.

The compressibility curves of PAEKs are shown in Fig.4.10. PEK HP3 has the highest degree of compressibility, of 20.2%. Nonetheless, the initial structure of PEK HP3 at 1 kPa of normal stress is also the highest, of approximately 8%. High levels of compressibility are attributed to low powder compact but also suggests that it is possible to rearrange the powder structure by applying an external force to the bulk. On the contrary, P12S959a is less compact and less compressible, a possible effect of fully dense particles of large size. For LS application, Orgasol PA12 shows the ideal compressibility behaviour as particles are already in a compact arrangement regardless of applying any external force to the system.

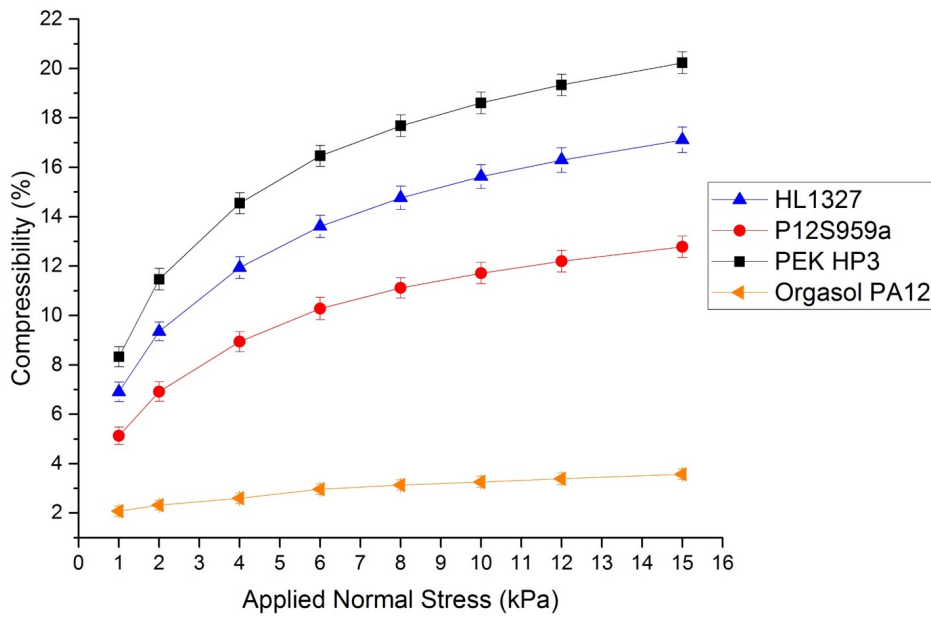


Fig. 4.10 Compressibility behaviour of PAEKs and Orgasol PA12.

4.3.2 The effect of moisture on powder flow

The effect of moisture on the flow of PEKK powders was assessed using the FT-4 powder rheometer and then compared with the commercially available PEK HP3 grade. The summary of the powder rheology data is shown in Table 4.3. Firstly, stability and flow rate tests were performed; the results are shown in Fig.4.11 (Stability) and Fig.4.12 (Flow rate). The standard stability test was selected since clear differences were already observed for different environmental conditions.

The HL1327 powder shows very unstable behaviour, as reported in Fig.4.11(1). The instability is especially remarkable for dried HL1327 powder, in which the energy to perform a cycle increases linearly with the number of cycles. It is likely that drying HL1327 powder creates external forces to the particles, e.g., electrostatic charge, and increases interlocking behaviour. The humid condition follows a similar trend to 'as received', with SI values being the closest to 1. The presence of moisture in the bulk of HL1327 powder is separating the particles and improving their morphology by filling the interstices of the rough regions and reducing cohesion and interlocking behaviour of adjacent particles [153]. For rounder and denser PAEK particles, such as the ones from P12S959a grade (Fig.4.11(2)), moisture is possibly leading to voids formation within the structure, therefore facilitating the displacement of these particles from their original position, as supported by the lower but similar energy trend to 'as received' condition. The PEK HP3 (Fig.4.11(3)) exposed to a humid environment showed a different trend from the other environmental conditions. Whilst 'as received' and 'dry' condition behave similarly and require more energy as the number of cycles progress, the presence of moisture is leading to a decrease in the total energy, supported by the lower BFE values. It seems moisture is facilitating flow, as observed for the PEKK grades.

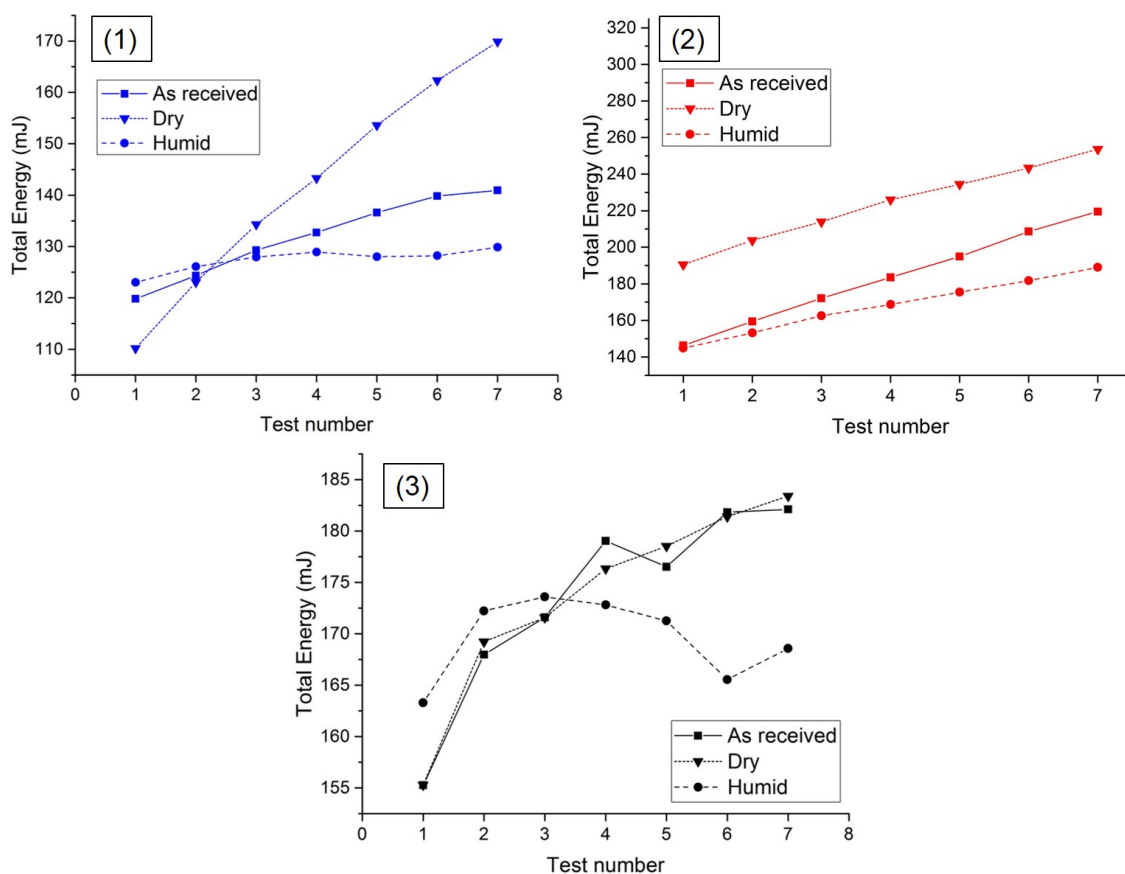


Fig. 4.11 Stability test results for (1) HL1327, (2) P12S959a, and (3) PEK HP3 at different environmental conditions. Note that the standard stability test was used.

The flow curves for the HL1327 powder present the humid condition as being the most susceptible to flow, supported by its lower SE and BFE values shown in Table 4.3. The 'as received' condition shows intermediate energy for powder flow, whilst dry HL1327 particles require the highest energy to flow. Interestingly, CBD is not affected by environmental conditions; this can be explained by moisture molecules filling the gaps caused by the irregular surface morphology of HL1327 particles only, rather than increasing the distance between particles in the bulk. Similar flow behaviour is observed for P12S959a (Fig.4.12(2)), although at significantly higher energy. The higher energy is justified by the larger and denser particles of P12S959a grade, which are more difficult to displace. For this grade, 'as received' condition shows an intermediate trend between humid and dry conditions. The CBD value of the humid condition is not decreasing either, despite significantly improving flow. The large particles of P12S959a PEKK are possibly leaving empty voids for water molecules to fill, therefore not disrupting the original powder bulk structure. A similar phenomenon is found for PEK HP3, in which particles show an irregular morphology, leaving space for water to fill the voids. For this grade, however, the 'as received' condition behaves in a very similar fashion to the dry condition, supporting the hydrophobic behaviour of PAEKs.

To summarise, PEKK grades in as 'as received' condition behaves very similarly to 'humid' condition. The presence of moisture slightly assists flow as the molecules can fill

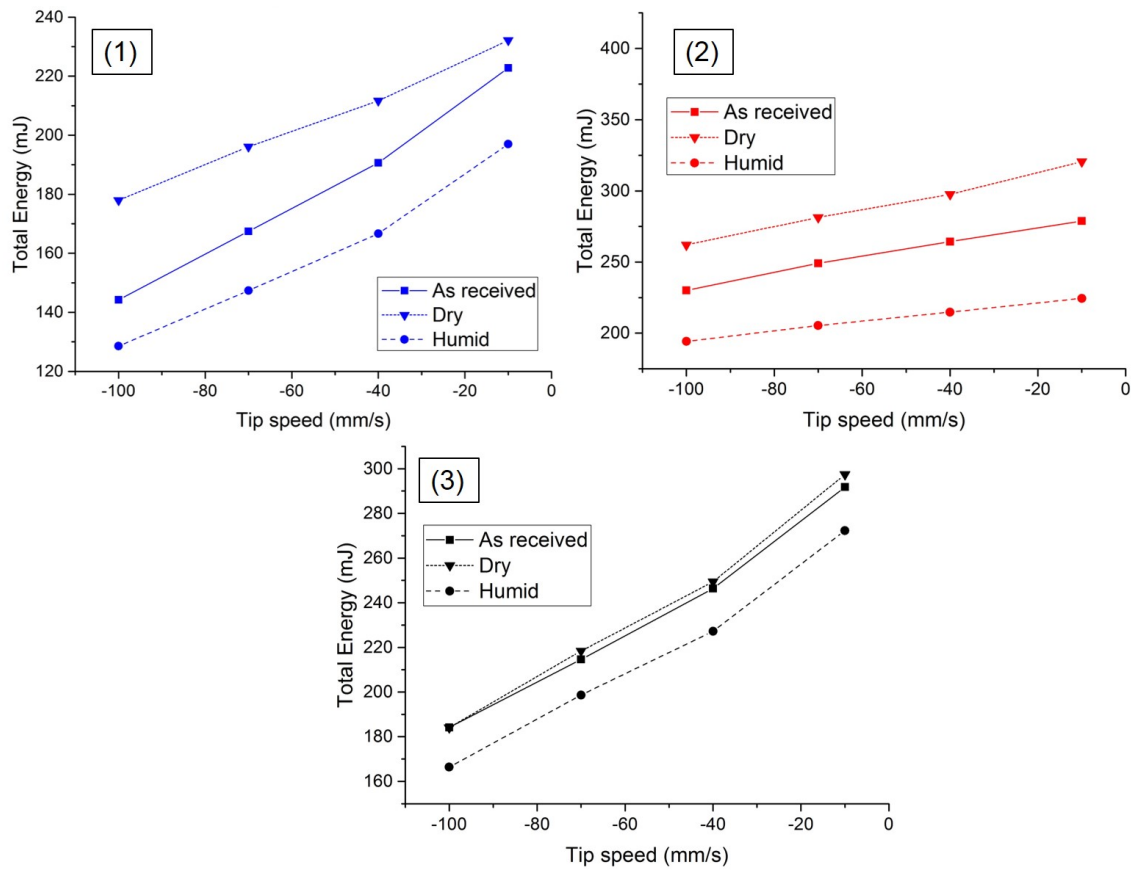


Fig. 4.12 Flow rate test results of (1) HL1327, (2) P12S959a, and (3) PEK HP3 subjected to different environmental conditions.

the voids resultant from a rough surface, sharp edges, and large particle size, therefore reducing cohesive behaviour.

Compressibility was assessed for all the grades in the analysis. The results are shown in Fig.4.13. As expected, the dry HL1327 powder showed the highest degree of compressibility, since the absence of moisture in the powder bulk enables a more compact structure. The 'as received' condition, however, follows a similar trend to the humid condition.

Similar behaviour is observed for P12S959a grade, in which compressibility increases for the dry condition. This increase can be explained by more space for compaction when moisture is removed from the bulk, and a normal force is applied to the system. For this grade, 'as received' condition shows an intermediate value of compressibility. By comparing to the particle morphology of HL1327 grade, moisture occupying the voids created by the rough surface structure (HL1327 grade) may be harder to be removed than moisture present in the voids between large particles (P12S959a grade).

The compressibility of PEK HP3 exposed to different environmental conditions behaves slightly differently, and the humid PEK HP3 powder showed an intermediate degree of compressibility. This behaviour is justified by moisture partially evaporating from the powder bulk. This result supports that drying PAEK powder increases compressibility. However, the bulk density values highlight that such changes are observed only when normal stress is applied to the powder bulk. In LS, the recoater mechanism does not compress

the powder but carries it. Therefore, the changes obtained with the compressibility test is not applicable to replicate powder bed density in LS.

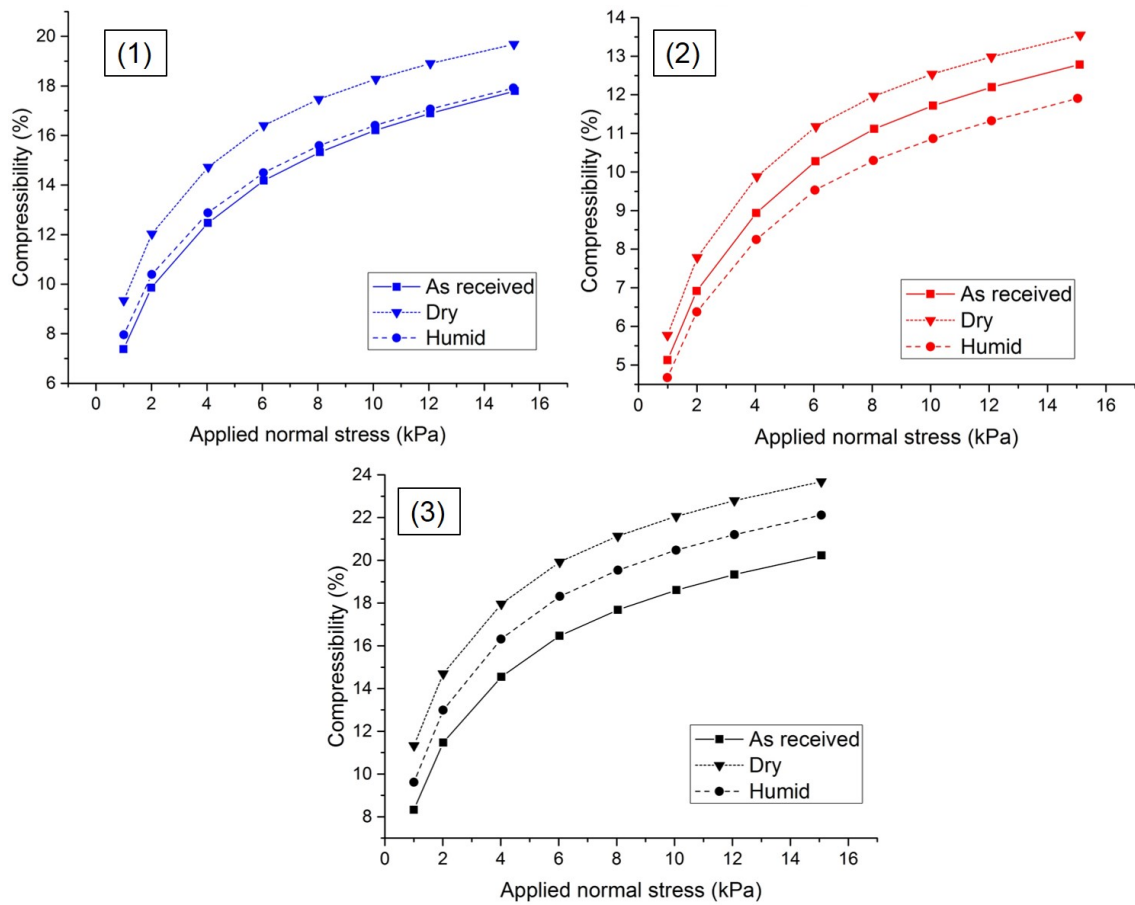


Fig. 4.13 Flow rate test results of (1) HL1327, (2) P12S959a, and (3) PEK HP3 subjected to different environmental conditions.

Table 4.3 Summary of FT-4 powder rheometry results of PAEK grades subjected to different environmental conditions.

Parameters	HL1327			P12S959a			PEK HP3		
	Humid	As received	Dry	Humid	As received	Dry	Humid	As received	Dry
CBD (g/ml)	0.36 ± 0	0.36 ± 0	0.36 ± 0	0.49 ± 0	0.48 ± 0	0.49 ± 0	0.46 ± 0	0.46 ± 0	0.45 ± 0
SI	1.1 ± 0	1.2 ± 0.1	1.1 ± 0	1.3 ± 0.1	1.5 ± 0.1	1.3 ± 0.1	1 ± 0.1	1.2 ± 0.1	1.2 ± 0
BFE (mJ)	130 ± 2.7	141 ± 2.4	132 ± 4.7	189 ± 25.9	220 ± 20.4	254 ± 18	169 ± 8.6	182 ± 0.8	183 ± 6.3
SE (mJ/g)	5.6 ± 0.2	6.2 ± 0.2	5.9 ± 0.2	5.4 ± 0.5	5.6 ± 0.3	6.7 ± 0.4	6.2 ± 0.3	7.2 ± 0.2	7.2 ± 0.2
CPS (%)	18 ± 0.9	18 ± 0.4	20 ± 0.8	12 ± 0.9	12 ± 1.4	14 ± 0.3	22 ± 0.5	20 ± 0.4	24 ± 0.9

4.4 Conclusions

The first part of this chapter characterised different PEKK grades supplied by Arkema. It showed that, amongst the PEKK grades, HL1327 presents ideal particle size distribution, but irregular morphology, whilst P12S959a particles are large but with solid interior and more spherical morphology. These particle properties affect powder stability, flow, and compressibility behaviour in different ways: P12S959a presents a highly unstable behaviour, requires more energy to flow, but is less affected at lower tip speeds, possibly due to larger particle size and smoother surface. As opposed to this grade, HL1327 seems to have similar stability, flow, and compressibility behaviour to the commercially available PEK HP3, despite presenting a completely different powder structure. The effect of irregular particle morphology seems less pronounced than particle size when assessing powder rheometry; for this reason, HL1327 was preferred over P12S959a grade. This grade is also more suitable than HL1320 due to the higher viscosity reported in Table 3.1. If able to be processed, more viscous polymers improve the mechanical performance of final sintered parts.

The effect of different environmental conditions on powder properties was monitored for HL1327 and P12S959a grades. It was shown that moisture has a minimum effect on PEKK grades due to their highly hydrophobic behaviour. Nonetheless, moisture can still be present in the powder bulk, filling the voids between particles, as was observed for P12S959a, or acting as a lubricant and reducing friction and interlocking forces between them HL1327 particles. This effect improved powder flow but compromised compressibility. Therefore, a spherical shape is preferred to guarantee homogeneous performance in LS.

To final characterise the effect of particles' structure in LS, coalescence is investigated. This topic will be discussed in Chapter 5.

Chapter 5

An experimental Investigation of PAEKs Behaviour at High-Temperature

5.1 Summary

The LS process requires heating from two different sources - the laser and the heated chamber - to complete manufacturing. The first promotes binding of the particles, and the other guarantees a smooth process; both are vital and may be assessed to understand the physical phenomena taking place during manufacturing. This chapter comprises a series of experimental studies to investigate the 1) coalescence/melting (laser effect) and 2) the effect of processing temperatures in LS (heated chamber).

Coalescence is crucial to understand the consolidation of polymers as the heat emitted by the laser beam during LS triggers different coalescence mechanisms, which affect consolidation. Monitoring changes at processing temperatures is also necessary as particles may behave differently at room temperature than when exposed to high temperatures.

The study of coalescence started by monitoring individual particles during the melt at dynamic conditions. Three different methods of assessing such changes were investigated, and three types of substrates were tested: glass, glass-coated silicone, and PEKK films. The experiment was performed for the three grades in the study, HL1327, P12S959a, and HL1320, and then compared with PEK HP3. The second stage of the analysis consisted of evaluating particle coalescence of pairs of particles in dynamic conditions. The coalescence behaviour was monitored using three different methods, the three PEKK grades and PEK HP3, and the substrates mentioned above. Finally, to assess the effect of processing temperatures in particle change, individual particles were investigated at isothermal conditions. Changes in the perimeter of HL1327 particles placed on a glass substrate were monitored throughout the time of the experiment. A schematic representation of this chapter is shown in Fig.5.1.

All individual particles shrunk prior to melting, achieving up to 30% reduction in the perimeter at temperatures just above T_m . This shrinkage is followed by an increase in size driven by viscous flow. Shrinkage is expected to affect neck growth by delaying coalescence, as particles are pulled away whilst neck increases. This theory is a plausible explanation for why neck growth occurs at a lower rate than predicted by most coalescence models. The use of different substrates does not seem to affect particle interaction below melt (T), but slight changes are observed after (T). Viscosity and particle size influence overall particle behaviour at melting, whilst the impact of morphology and porosity is significantly lower in particle coalescence. This study concluded the characterisation of different PEKK grades by selecting HL1327 as the most suitable grade for LS.

The particles of HL1327 grade exposed for prolonged times at processing temperatures did not seem to change in size or morphology, and very random behaviour was observed. In addition to other characterisation techniques, a larger sample size is needed to support the stagnation of particle size and shape throughout time at T_{bed} .

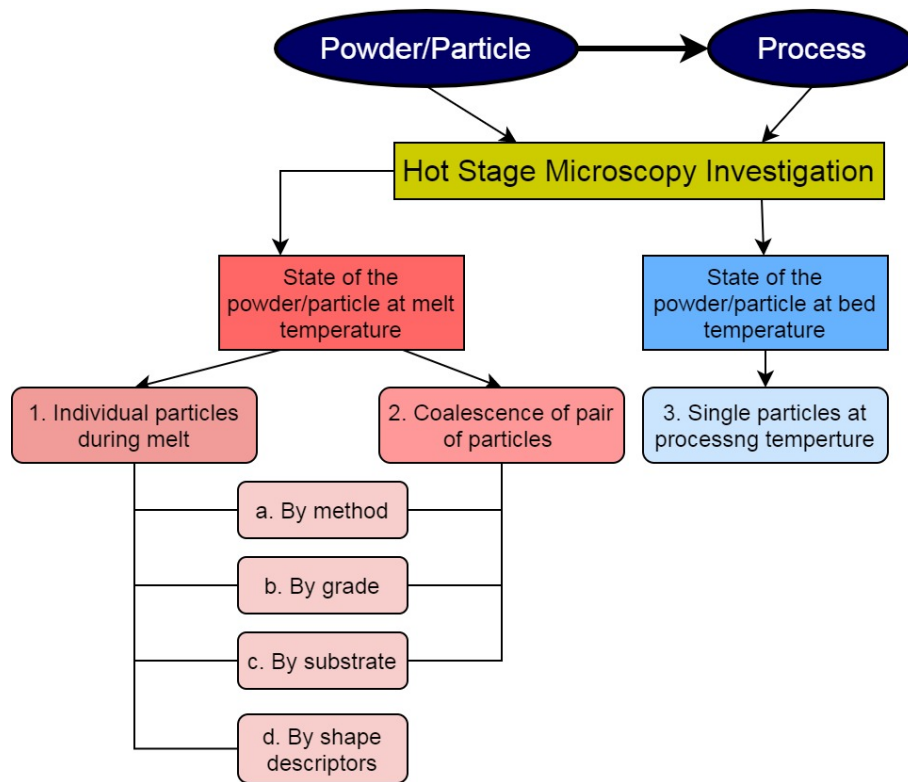


Fig. 5.1 Schematic illustration of Chapter 5.

5.2 Methods of Evaluating Individual Particles Behaviour with Temperature

All previous studies identified in literature focused on monitoring particle coalescence and neck growth with time/temperature [194, 197, 199], but none considered the behaviour of individual particles during the melt. By investigating the behaviour of single particles during melt enables separating physical properties from the sintering process and its mechanisms of diffusion and viscous flow through which consolidation is achieved. Three different methods for measuring dimension change of individual particles with temperature were considered; they will be referred to as methods S1, S2, and S3.

5.2.1 Method S1

The first approach considered the average feret diameter (d_{fx}) and perimeter (p_x) of individual particles, which were monitored along the temperatures shown in Table 3.2.

5.2.2 Method S2

The second method consisted of normalising the values of d_{fx} by the feret diameter measured at room temperature (d_{fi}). This is described by Eq.(5.1),

$$D = \frac{d_{fx}}{d_{fi}}, \quad (5.1)$$

in which d_{fx} is the feret diameter at a temperature x and d_{fi} is the feret diameter at room temperature.

5.2.3 Method S3

The third approach normalises particle size in terms of perimeter. This method is described by Eq.(5.2).

$$D = \frac{p_x}{p_i} \quad (5.2)$$

The variable p_x corresponds to the perimeter at a temperature x and p_i is the perimeter at room temperature.

5.3 Methods of Assessing Neck Growth with Temperature

The second part of this study evaluates neck formation and growth during coalescence and correlate them with material properties (viscosity, surface tension) and particle characteristics (size, porosity, morphology, roughness). The methods developed will be referred to as N. Three different approaches were considered to assess neck growth - method N1, N2, and N3.

5.3.1 Method N1

The first approach consists of measuring the contact length between the particles with the assistance of the segmented line tool (ImageJ analysis, see Section 3.3.4 for more information), and then dividing it by the average feret diameter or perimeter of both particles at room temperature. This approach is described in Eq.(5.3). The analysis of feret diameter enables an experimental comparison with the Frenkel-Eshelby model [193, 183], whilst perimeter considers the effect of morphology in the analysis.

$$Y = \frac{y_x}{\frac{d_{1fi} + d_{2fi}}{2}} \quad \text{or} \quad Y = \frac{y_x}{\frac{p_{1i} + p_{2i}}{2}}, \quad (5.3)$$

in which y_x corresponds to the contact length between two particles at a specific temperature x , d_{1fi} and d_{2fi} are the feret diameter at room temperature of particles 1 and 2, respectively, and p_{1i} and p_{2i} are the perimeter at room temperature of particles 1 and 2, respectively.

5.3.2 Method N2

The second approach divides the contact length between the particles by the average feret diameter of them at a respective temperature x , according to Eq.(5.4). This method

was based on Pokluda et al. [194] findings, which show that coalescence is better described when it accounts for the variation of particle radius with time at isothermal conditions. As this study is performed at dynamic conditions to simulate the effect of the laser during LS, particle diameter was monitored over temperature rather than time.

$$Y = \frac{y_x}{\frac{d_{1fx} + d_{2fx}}{2}}, \quad (5.4)$$

in which d_{1fx} corresponds to feret diameter of particle 1 at a temperature x and d_{2fx} is the feret diameter of particle 2 at a temperature x .

5.3.3 Method N3

The third approach evaluates the length of contact between two particles in terms of the average perimeter between them, varying with temperature. This approach is described in Eq.(5.5):

$$Y = \frac{y_x}{\frac{p_{1x} + p_{2x}}{2}}, \quad (5.5)$$

in which p_{1x} corresponds to the perimeter of particle 1 at a specific temperature x and p_{2x} is the perimeter of particle 2 at the same temperature x .

5.4 Individual Particles Changes with Temperature

Each method described in Section 5.2 was firstly compared for particles of HL1327 grade, following the methodology described in Section 5.2. Fig.5.2 shows two individual particles of HL1327 monitored with temperature increase.

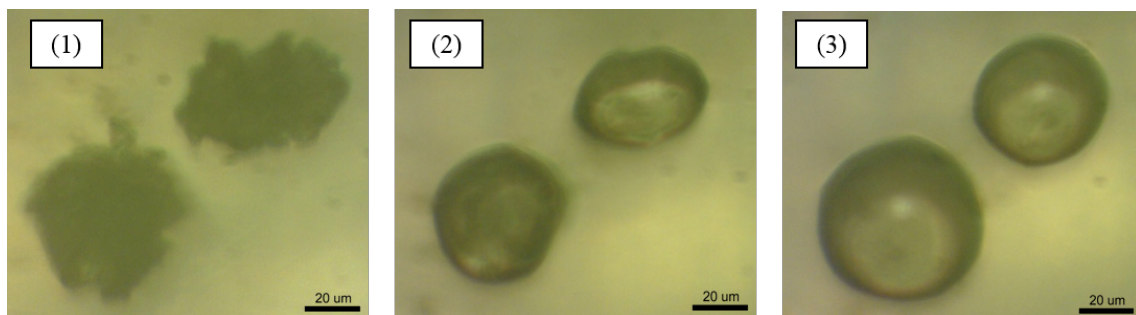


Fig. 5.2 Particles of HL1327 at (1) room temperature, (2) sintering temperature (T), and (3) maximum test temperature of 96 °C above (T).

5.4.1 By method

The changes in particle size were firstly assessed using method S1, which consists of monitoring the particles in terms of feret diameter and perimeter. The average feret

diameter and perimeter of ten individual particles were monitored with temperature, as shown in Fig.5.3(1). The particles go through an almost identical trend, however at different scales, since the order of magnitude of the perimeter is higher than the feret diameter. Size significantly decreases from (T-12), followed by an expansion from (T+4). The high standard deviation values are justified by the small sample size but mostly the broad differences between particles, which are heterogeneous in size and shape. For this reason, the following methods opted for a normalised approach of feret diameter (method S2) and perimeter (method S3) to monitor particle change with temperature. The results are shown in Fig.5.3(2).

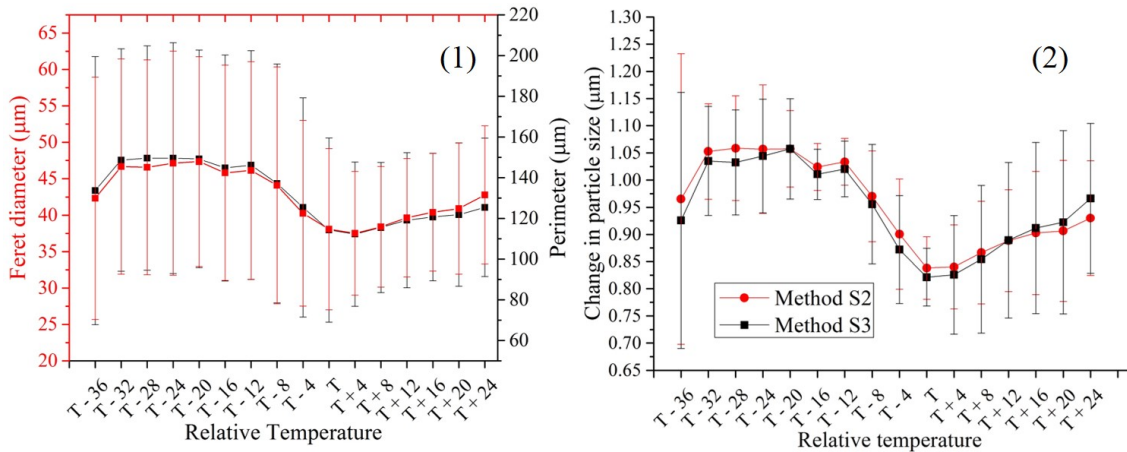


Fig. 5.3 Change in particle size of HL1327 PEKK grade with temperature increase. (1) Method S1 and (2) methods S2 and S3.

The curves for methods S2 and S3 show particles with a slightly smaller size at (T-36) than at room temperature. At (T-32), a small increase in size is observed, and the particles maintain a similar diameter and perimeter until they reach (T-16). From this point, shrinkage takes place, and the particles have their size reduced by approximately 20% until the complete melt is achieved at (T). The melt induces expansion, and the particles recover from 10 to 15% of their size at (T+24) despite being smaller than at room temperature. The shrinkage just below melt comes from the tendency of the particles to reach their lowest state of energy, which is achieved with the spherical shape. By increasing temperature, material transfer occurs from the region of maximum diameter to the region of minimum diameter, and irregularities in shape, size, and in the surface of the particles are reduced if not completely mitigated. Furthermore, eventual pores in the interstices disappear. As a result, the particles experience a reduction in size observed by the curves of Fig.5.3(2).

5.4.2 By PAEK grade

The comparison between different PAEK grades was performed using method S3 (normalised change in perimeter), because it monitors the effect of temperature increase in particle size and morphology. In this study, morphology is a property of particular interest given the irregular surface texture of HL1327 and HL1320 grades when compared with PEK HP3 and P12S959a. Furthermore, this is the first experimental study that assesses

melt and coalescence in terms of perimeter, providing valuable insights into the effect of particle morphology on their melt. The results are shown in Fig.5.4.

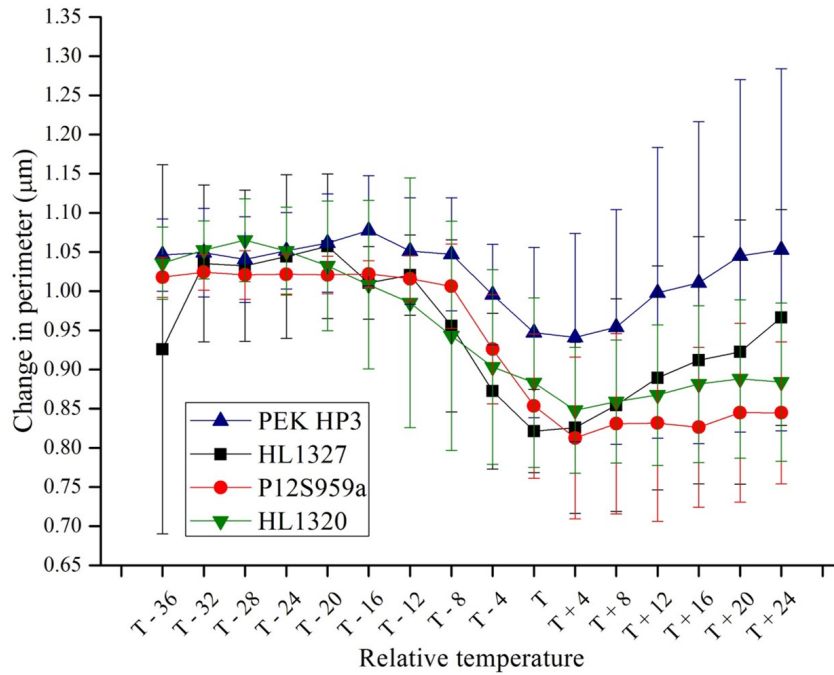


Fig. 5.4 Change in normalised perimeter (method S3) of different PAEK grades.

All PAEK particles shrunk before melting until 4 °C above (T). As opposed to the evident expansion of particles from HL1327 and PEK HP3, P12S959a and HL1320 showed just a slight increase in particle size after (T), of less than 5%. A plausible explanation for the low expansion of P12S959a is the particle size, which is approximately 30 μm (50%) larger than the other grades. This size increase delays melt as more energy is required to disrupt the surface area of larger particles and reach a viscous state. Furthermore, SEM images (Section 4.2.1, Fig.4.2) of these particles show a dense structure, which means that more material needs to be melted. HL1320 particles, on the other hand, are about 4 μm (7%) larger than HL1327 particles, but less viscous. The effect of viscosity is clear before the melt, in which particles of HL1320 gradually shrunk until they reach (T+4), whilst the slope for the other grades is steeper before (T). This result supports Frenkel and more recent models developed to predict coalescence. From (T+4), however, HL1320 particles do not expand as HL1327 ones, despite the similar morphology and size. This behaviour can be explained by a simultaneous shrinkage and expansion of HL1320, the first being a combination of high internal porosity and a gradual decrease in size with temperature, and the second being a result of temperature increase and low viscosity.

All PEKK grades particles did not reach their original size at (T+24), but PEK HP3 grade does, having its size slightly increased. This difference may be a result of the smaller particle size, viscosity, and more circular morphology of this grade at room temperature. Furthermore, PEK HP3 has a T_m of at least 64 °C above the other PEKK grades (see Section 6.2 for further information), which might be affecting expansion after melting. Table 5.1 provides the values of (T) for all the grades in the analysis. Note that (T) is

Table 5.1 Corresponding (T) values for each PAEK grade in the analysis.

Grade	(T) [°C]
PEK HP3	395
HL1327	318
P12S959a	331
HL1320	325

slightly above T_m for all the grades (see Section 6.2 for comparison with DSC values). This behaviour can be justified by the thermal lag resulting from the high heating rates applied in HSM.

Fig.5.5 presents different stages of particle growth with temperature for all the grades. The same particle had its images overlapped at different temperatures to compare the change in size and morphology. As shown by Fig.5.4, PEK HP3 particles maintain their size and morphology at the end of the test as particles of this grade are initially more circular. For PEKK grades, a definite change in morphology is observed, and HL1327 and HL1320 particles approach a spherical shape at the maximum temperature, T_{max} . The changes in size are not apparent from room temperature to maximum experimental temperature for any of the grades in the study.



Fig. 5.5 Particle change with temperature. The darkest image corresponds to the particle at room temperature, followed by the image at (T), whilst the lightest colour corresponds to the particle at the maximum experimental temperature.

5.4.3 By substrate

The effect of different substrates was investigated for particles of HL1327 grade. The changes in normalised perimeter (method S3) achieved on top of glass slides were compared with glass-coated silicone, which aims to prevent particle wettability with the glass surface. The results are presented in Fig.5.6.

The particles show a similar trend from (T-36) to (T+4), and shrinkage of HL1327 PEKK takes place from approximately 12 °C below melt for both substrates. From (T+4), a clear change in slope is observed. The particles on glass substrate start expanding,

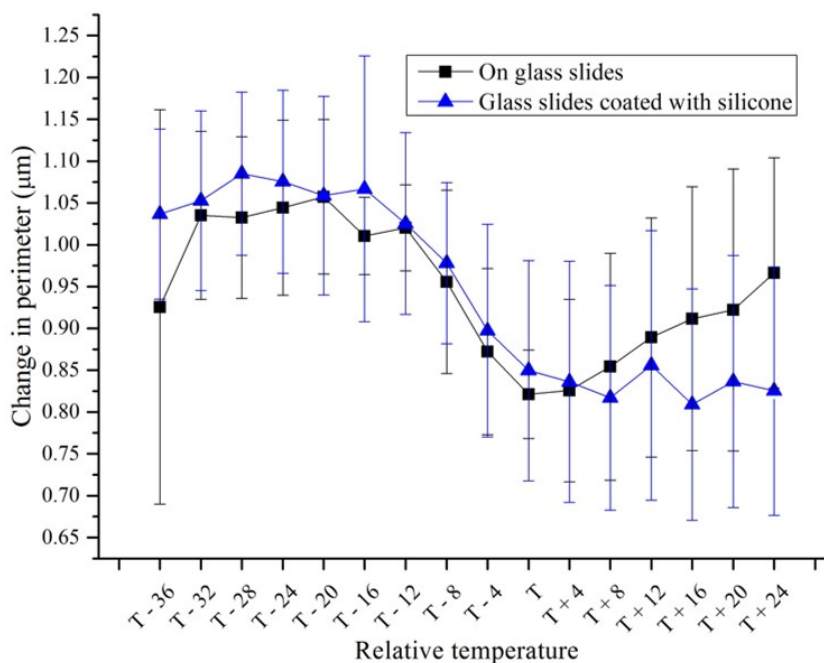


Fig. 5.6 Change in normalised perimeter of HL1327 particles on different substrates.

whilst the particles on top of glass coated silicone remain with similar size than at (T), approximately 15% lower in perimeter than at room temperature. Expansion is likely delayed due to a lower contact area of the particles on glass coated silicone substrate, in addition to an extra barrier preventing the transference of heat from the hot stage platform to the particles.

The particles on top of the silicone coated substrate, however, are difficult to track as they continuously move on the hot stage platform rather than anchoring to the glass surface. For this reason, the glass substrate was preferred when comparing particle change with temperature for different PAEK grades.

5.4.4 Shape comparison

Change in particle shape was monitored regarding circularity and roundness; these shape descriptors are calculated as described in Section 3.3.3. The results for the different PAEK grades are shown in Fig.5.7.

The PEK HP3 particles show values of circularity 9% above the PEKK grades at the beginning of the recording, at (T-36). Nevertheless, the rate of changes is more significant for all the PEKK grades in comparison to PEK HP3 (See Fig.5.7(1)). The values of circularity at (T) are similar for the PEKK grades, as opposed to PEK HP3, in which circularity is of 0.78. Different properties can be associated with this behaviour, including internal particle porosity, viscosity, and particle size.

Regarding roundness (Fig.5.7(2)), a similar trend is observed: PEK HP3 grade shows a rounder morphology at (T-36), which gradually increases with temperature. At (T+24), however, the values of roundness for the PEKK grades are reasonably higher than for PEK HP3, of 0.92 against 0.86. The trend of roundness for the PEKK grades is not as abrupt

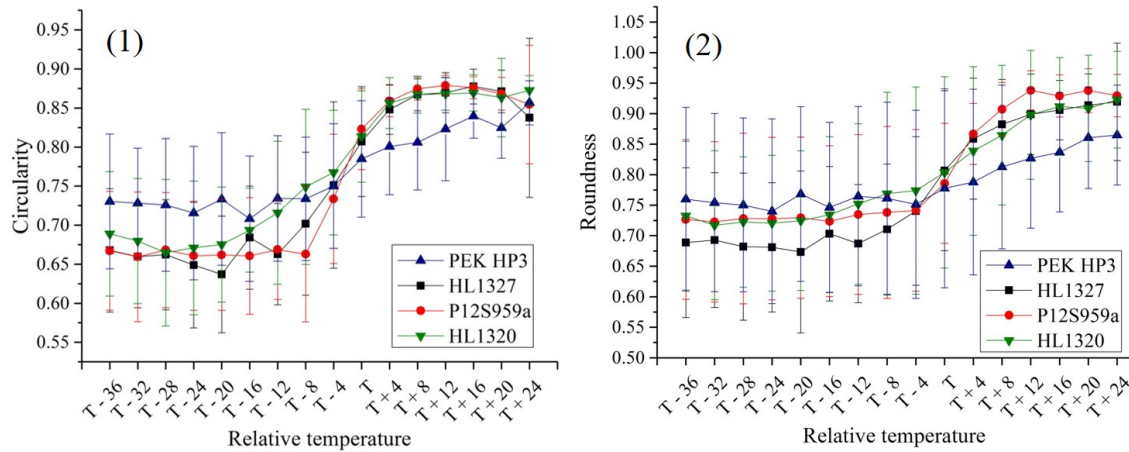


Fig. 5.7 Change in particle shape of different PAEK grades. The shape was described in terms of (1) circularity and (2) roundness.

as for circularity but remains much steeper than for PEK HP3. At (T) , similar values of roundness are found for all the grades in analysis, of 0.78.

The monitoring of shape reveals similar values of circularity and roundness at $(T-36)$, which are increased in the same proportion until (T) . For PEK HP3, the proportion of circularity and roundness is maintained until $(T+24)$. On the other hand, the PEKK grades show an increase in roundness, which reaches ~ 0.92 at $(T+24)$ as opposed to ~ 0.85 for circularity. When analysing the state of PEKK particles at (T) , however, circularity is higher than roundness. These results suggest that, before the melting, temperature increase contributes more to smooth the surface of the particle, whilst from (T) to $(T + 24)$, the material is transferred to achieve a uniform diameter throughout the particle.

5.5 Hot Stage Microscopy Analysis for Neck Growth

The neck formation and growth were monitored according to the different methodologies described in Section 5.3. These methods were first applied to measure the coalescence of HL1327 particles on a glass substrate. The most suitable method was selected to compare the coalescence behaviour of different PAEK grades. Then, the effect of three different substrates was evaluated: glass slides, glass slides coated with silicone, and PEKK films. Fig.5.8 shows two particles initially in contact with each other at room temperature, and coalescence taking place as temperature increases.

5.5.1 By method

By studying the behaviour of single particles during the melt, neck growth is better understood, and the effects associated with the physical behaviour of particles can be separated from the coalescence process. Neck growth was monitored for ten pairs of particles of HL1327 PEKK on glass substrate using the different methodologies presented in Section 5.3. The results are shown in Fig.5.9.

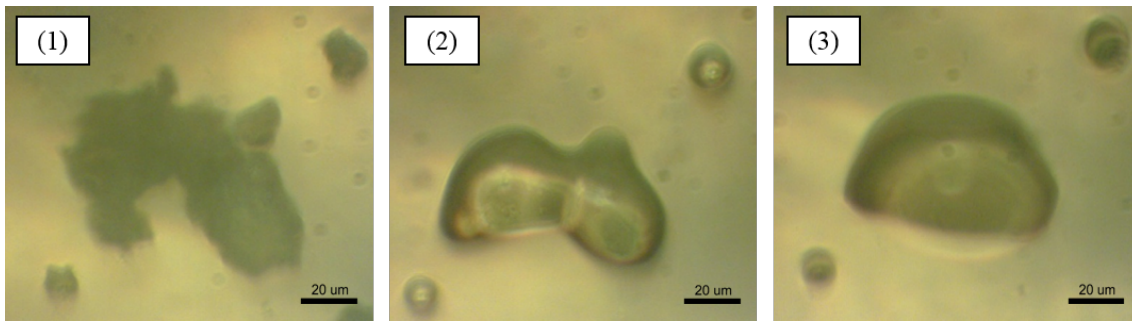


Fig. 5.8 A pair of particles of HL1327 grade under coalescence at (1) room temperature, (2) neck formation temperature (T), and (3) maximum test temperature of $88\text{ }^{\circ}\text{C}$ above (T).

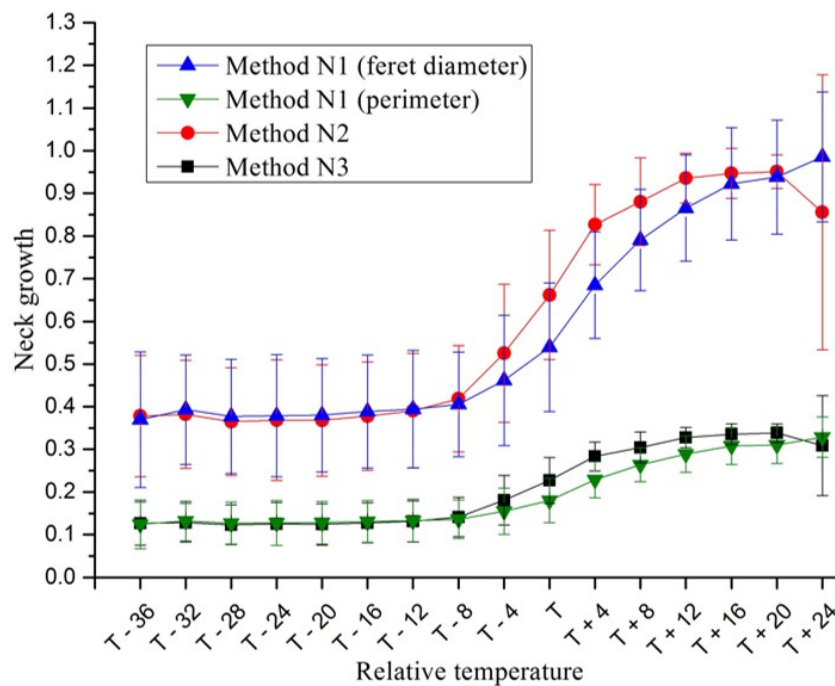


Fig. 5.9 Evaluation of different methods to monitor neck growth of HL1327 particles on a glass substrate.

The study of neck growth in combination with assessing changes in the size of individual particles shows that the neck starts to form when particles begin to shrink, indicating a movement of material to the region of contact in between them. These phenomena are combined in Fig.5.10, in which the average change in normalised perimeter of HL1327 particles can be compared with neck formation and growth, also normalised by the perimeter, for the same grade. In Fig.5.10, the neck has notably increased with temperature whilst particles are slightly smaller at (T) than at room temperature. For polymers, coalescence occurs near the T_m ; this is also observed for HL1327 PEKK. Therefore, viscous sintering is the dominant mechanism of transportation and enables the neck to grow simultaneously to changes in particle size and morphology [305, 5].

Regardless of the method selected for neck growth analysis, the curves of Fig.5.9 approach a logistic shape. The methods normalised by perimeter showed a less pronounced neck growth, as expected. From ($T-4$), a change in the slope is noticed when comparing

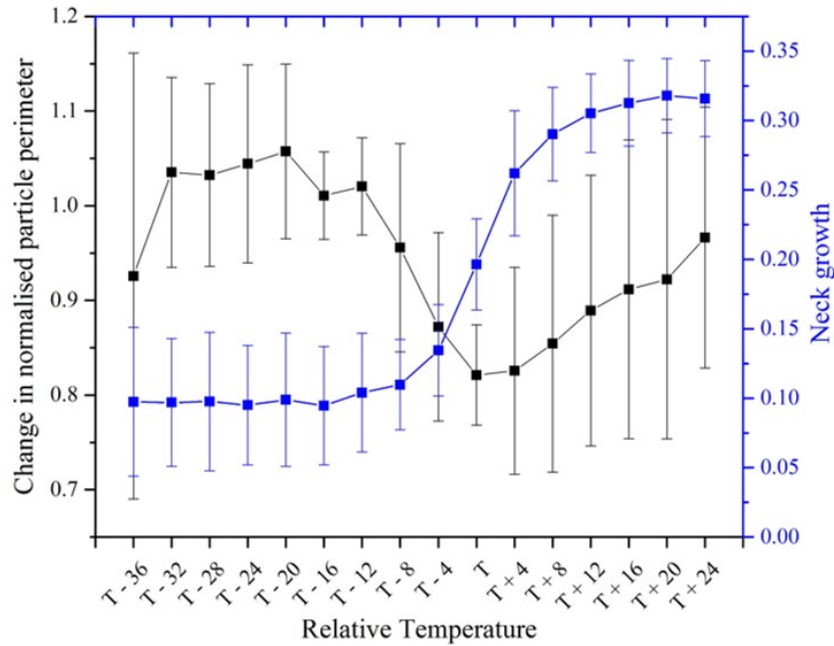


Fig. 5.10 Neck growth and change in normalised particle perimeter with temperature for HL1327 grade.

method N1 (neck normalised by feret diameter or perimeter of the particles measured at room temperature) to method N2 (neck normalised by feret diameter of the particles as temperature increases) or N3 (neck normalised by the perimeter of the particles as temperature increases). By normalising neck growth with the average particle size at each relative temperature, the rate increases as particle shrinkage takes place close to sintering temperature (Section 5.4). As neck growth is not proportional to particle shrinkage, a change in slope is observed. This change becomes clearer when either of the approaches using feret diameter is selected. The reduction of neck growth at (T+24) is possibly a result of particle expansion as the temperature is well above (T).

The monitoring of size and shape in terms of feret diameter or perimeter are two different but reliable approaches. However, they must be assessed with temperature, as highlighted by Pokluda et al. [194]. For the case of particles with a very heterogeneous and rough surface, perimeter gives a more consistent description of particle behaviour and coalescence as standard deviation is reduced. Furthermore, by measuring neck growth normalised by particle perimeter, morphology can be taken into account, which may change the coalescence rate. Mielicki et al. [121] support this argument. They observed changes in morphology whilst size remained the same for LS PA12 particles. To guarantee the reliability of the test and the consistency with the method used for assessing individual particles (in terms of perimeter change), method N3 was preferred.

5.5.2 By PAEK grade

The coalescence process was monitored for all the PAEK grades on glass substrate, according to method N3; the results are reported in Fig.5.11. All the PEKK grades showed

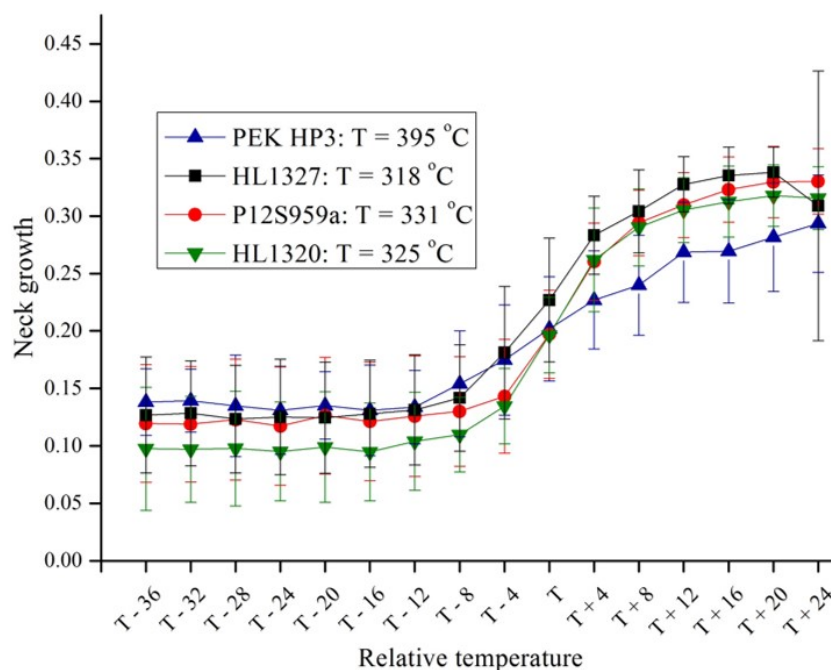


Fig. 5.11 Coalescence of different PAEK grades on a glass substrate according to method N3 (neck growth normalised by the average perimeter of the particles).

similar trend and the neck significantly started to increase from (T-8). These grades also achieved similar neck growth at (T+24), of 0.32. The slope of PEK HP3 is similar to a logistic curve, but changes are more subtle and neck did not seem to complete by (T+24). The high T_m of this grade in combination to operating the hot stage platform close to its temperature limit may be affecting these results. The lower rate of coalescence of PEK HP3 can also be explained by the more circular morphology of the particles at lower temperatures.

Several studies mention the slow coalescence of polymer particles when compared with the predicted rate of mathematical models (Frenkel, Frenkel-Eshelby, Hopper models). This phenomenon, however, was not monitored experimentally for individual particles, but only when assessing neck growth [197]. In this study, it seems that shrinkage of individual particles observed in Section 5.4 is delaying the process of coalescence shown in this section, as it draws particles apart at a temperature just below the start of neck growth, continuously acting as a barrier whilst neck is being formed. As mentioned by previous studies [208, 206, 205], this shrinkage is possibly caused by the recovery of elastic deformation at the early stages of neck growth. This phenomenon delays neck formation in the later stages of coalescence due to the prolonged time for chain diffusion across the interface and the establishment of an equilibrium distribution of chain entanglements [206].

For all the grades, (T) is at least 20 °C above T_m , a likely effect of the high heating rates applied. For P12S959a, however, this difference increases to more than 30 °C, which is attributed to the larger particle size. Fig.5.12 shows a schematic representation of the progress of coalescence for all the grades in the analysis. Three images of particle pairs were overlapped at different temperatures to compare the change in morphology, size, and

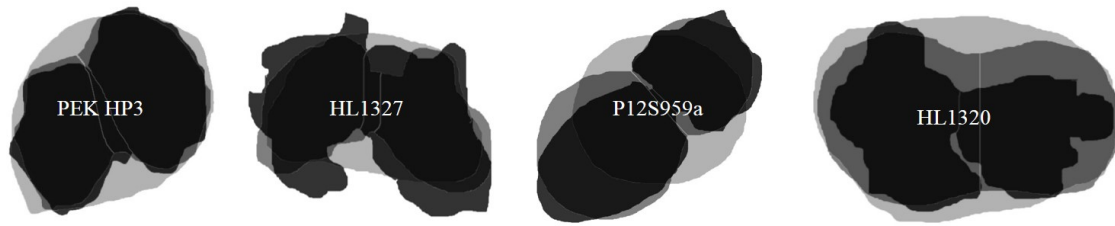


Fig. 5.12 Progress of particle coalescence. The darkest images correspond to the particles at room temperature, followed by the particles at (T), and the lightest colour images correspond to the particles at maximum experimental temperature.

the progress of coalescence. The pairs of particles of all grades approach a spherical shape at T_{max} , but the shapes are more circular for P12S959a and PEK HP3 as no porosity is found in their interstices, and the particles are initially more regular. The coalescence of HL1327 draws particles closer; however, no expansion is visible at T_{max} as observed for HL1320 particles. The increase in temperature is sufficient to maintain the initial size of HL1327 particles by eliminating porosity and surface roughness. For HL1320 grade, the lower viscosity enables a quicker viscous flow followed by an apparent expansion at T_{max} (Fig.5.12).

This section concludes the characterisation analysis of different PEKK grades supplied by Arkema. The investigation of particle size distribution, morphology, powder flow, and bulk density was supported by the study of coalescence and the additional information on powder production methods. The results obtained led to the selection of HL1327 as the most suitable grade for LS, given the ideal particle size and the ability to flow regardless of interlocking and friction forces present in the powder bulk. The porous interior and rough morphology do not seem to affect coalescence, as the melt disrupts such undesired properties.

5.5.3 By substrate

The process of coalescence was evaluated under three different substrates: glass, glass-coated silicone, and PEKK film. The film is made of the same Kepstan 6002 PEKK grade and aims to replicate the LS process by having a layer of the same material melted under the particles ready to coalesce. Particles of HL1327 grade were monitored according to method N3 (neck normalised by perimeter as temperature increases). The results are presented in Fig.5.13.

Similar trends are obtained for the coalescence of HL1327 particles on different substrates. When on top of glass coated silicone, the curve starts differing from the glass substrate at (T+16). This difference is a result of particle contact with the glass, which is significantly reduced for the particles on silicone, as shown in Fig.5.6. Therefore, the values of neck growth are the highest for particles on silicone. The particles monitored on top of PEKK film suddenly started to sink and disappeared in seconds. This is observed right after (T), and at (T+4), the particles are already sinking, as shown in Fig.5.14.

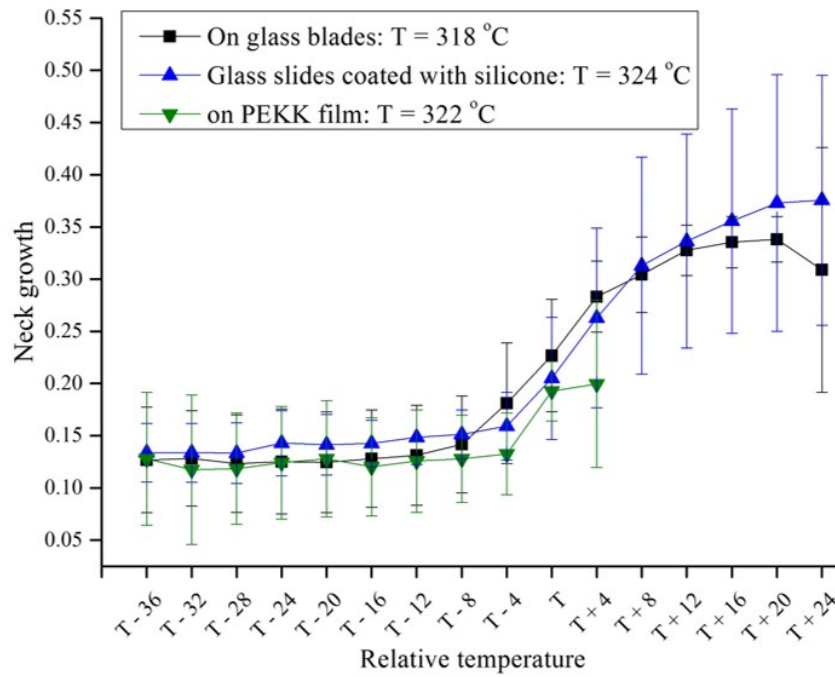


Fig. 5.13 Average neck growth of HL1327 grade on different substrates using method N3 (neck normalised by perimeter as temperature increases).

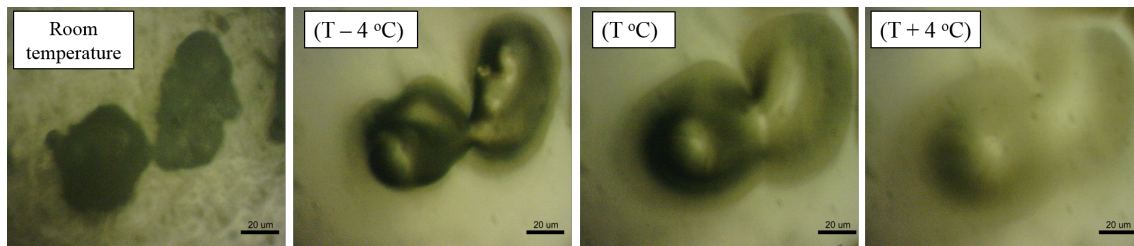


Fig. 5.14 Progress of coalescence of HL1327 particles on PEKK film.

The change in substrate also delays neck formation at (T): for the pair of particles monitored on top of glass slides, coalescence occurs 6 °C below the particles monitored on glass coated silicone and 4 °C below the particles on PEKK film substrate. The addition of silicone or PEKK film to the system is possibly creating an extra barrier for heat transfer. In the case of glass slides coated silicone, the increase in surface tension can also be a plausible explanation for coalescence delay.

From (T-36) to (T), the effect of different substrates on neck growth can be neglected due to similar behaviour. After (T), monitoring particle coalescence on the PEKK film becomes difficult as the film starts to melt, and the particles suddenly sink in. The standard deviation on the glass-coated silicone substrate is significantly higher than for particles on the glass due to the constant movement of the particles on the hot plate, although the trend only differs in the three last points.

This chapter is the first step to experimentally measure particles growth of different shapes and levels of porosity and the effect of different substrates on particle coalescence. For the first time in literature, feret diameter and perimeter were used to monitor and assess neck growth as well as particle growth, and these methods proved to be more effective

and reliable. Particle size and morphology affect coalescence, but they are significantly reduced at higher temperatures, i.e., above T . Such effect is equally unnoticeable when particles are investigated on PEKK film, the substrate added to this study to replicate the coalescence behaviour in the LS process.

5.6 Particles Behaviour at Processing Temperature: Isothermal Investigation

Particles of HL1327 grade were subjected to isothermal HSM to replicate the effect of processing temperature in LS, i.e., the effect of heating provided by the infrared heaters. The chamber is heated below the melting temperature of the particles at a temperature known as T_{bed} . According to Berretta et al. [152], the T_{bed} to process PAEKs by HT-LS corresponds to the minimum of the first derivative of the heating curve in the DSC. For Kepstan 6002 PEKK, this temperature is equal to 292 °C (further explored in Chapter 6, Section 6.2). The hot stage platform was set to 292 °C, and ten individual particles of HL1327 were monitored for six hours. This time corresponds to an average time of exposure of the particles to LS processing. In Fig.5.15(1), the average perimeter was plotted against time of exposure at 292 °C, whilst Fig.5.15(2) shows the normalised curves of perimeter achieved for all individual particles under analysis. The perimeter values were normalised against P_0 , which corresponds to the perimeter of the particles at the start of the isotherm at 292 °C.

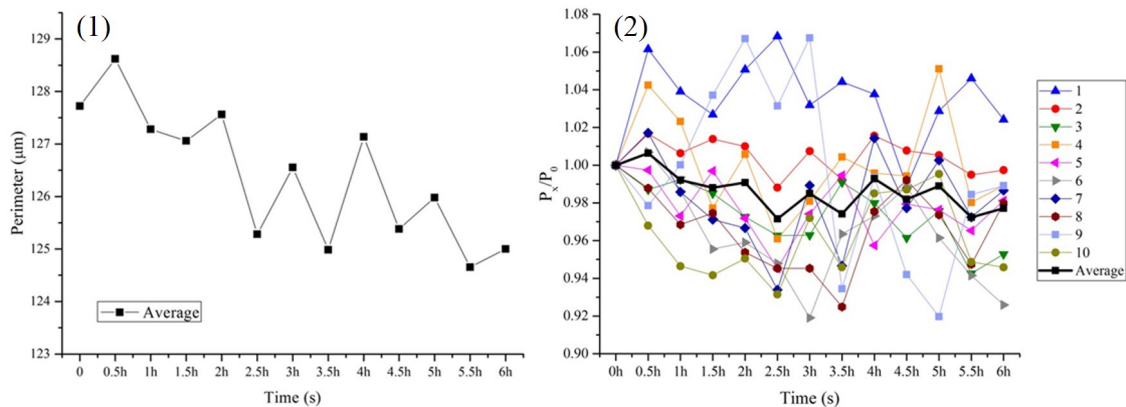


Fig. 5.15 PEKK particles exposed to HSM under the isothermal condition at 292 °C for six hours. The results were monitored in terms of (1) average perimeter, (2) normalised perimeter for each individual particle.

The analysis revealed a non-linear decrease in average perimeter with the time of exposure at T_{bed} . However, such a decrease is equivalent to only 2% of the total perimeter of the particles. Fig.5.15(2) clarifies the insignificant changes observed in the perimeter of the particles with the time of exposure at T_{bed} . The individual curves show the random pattern of perimeter change with time; this supports the fact that particles are different, and the morphology, porosity content, and size reflect on the changes in the perimeter with exposure to processing temperatures.

In the study of the melt of individual particles, shrinkage is representative due to phase transformation, from solid to liquid state, of the polymer subjected to heating. In this isothermal study, no phase transformation occurs since the particles are subjected to temperatures below T_m , therefore remaining in their solid-state. This explains the insignificant changes in perimeter registered for the PEKK particles.

5.7 Conclusions

In this chapter, coalescence of PAEKs was successfully measured and correlated with LS by evaluating different substrates and considering the effect of particle morphology in the process. The investigation of coalescence was complemented with the analysis of individual particles of the PAEK grades, which shrunk from prior to melting until (T+4) °C. This phenomenon does not seem to be a result of porosity within the particles but was attributed to the recovery of elastic deformation before the melt. As a result of shrinkage, coalescence is delayed as the first draws particles apart at a temperature just below the start of neck growth, continuously acting as a barrier whilst the neck is being formed.

Regarding the different methodologies developed in this study, measuring size and shape in terms of feret diameter and perimeter are two reliable approaches when monitored with temperature. For the case of particles with a very heterogeneous and rough surface, perimeter gives a more consistent description, as morphology is taken into account.

The perimeter methods (S3 and N3) were selected to compare different PAEK grades. Viscosity affects coalescence as HL1320 particles started to shrink before the other grades. Particles with more spherical shape resulted in a more spherical coalescence; less porous particles expanded at a slower rate as more heat is necessary to promote viscous flow, and the contact area between particles seems to affect coalescence and growth. Nevertheless, the combination of these characteristics does not result in significant changes in neck growth or particle melting, as the trend is quite similar for the different grades in the analysis.

From the three substrates investigated in this study, glass slides and glass coated silicone showed very similar particle behaviour. However, a delay in particle growth was observed in the later stages of coalescence for the particles on top of glass slides coated with silicone. This delay is possibly a result of the lack of wettability with the surface, which mitigates the contact points between the particles. The particles on the PEKK film substrate showed a sudden melt after (T) and 'sunk' in the substrate, preventing further analysis from (T+4). Glass slides were preferred over PEKK film and glass coated silicone as they result in clearer images and allow more accurate measurements during image processing. Furthermore, the particles on top of glass coated silicone were difficult to monitor as they were constantly moving on the glass slides.

The isothermal investigation at LS processing temperature (292 °C) resulted in minimal changes in the dimension and morphology of individual HL1327 particles, which presented an utterly random behaviour (Fig.5.15(2)). Therefore, the shrinkage seems to be directly associated with the melting process (solid to viscous-liquid transformation).

This chapter is the first step to experimentally measure the growth of particles with different shapes and levels of porosity, and the effect of different substrates on their coalescence. For the first time in the literature, feret diameter and perimeter were used to monitor neck growth as well as particle growth; these methods proved to be more effective and reliable. Particle size and morphology affect coalescence, but their effect is significantly reduced at higher temperatures, i.e., above (T). The same behaviour is observed for the the particles placed on top of glass coated silicone and PEKK film, the substrate added to this study to replicate the coalescence behaviour in the LS process.

Chapter 6

Thermal and Crystallisation Properties of PEKK

6.1 Summary

This chapter presents some relevant information on the thermal behaviour and crystallisation properties of PEKK. When compared to other PAEK grades, Kesptan 6002 PEKK is known to have a low T_m and a very slow kinetics of crystallisation due to the 60/40 T/I moieties concentration. The slow crystallisation becomes evident by the amorphous behaviour of this material when processed by conventional techniques, like IM. This chapter will investigate crystallisation using DSC in dynamic and isothermal conditions. This study attempts to understand and then correlate kinetics of crystallisation of PEKK with the LS process. The DSC in dynamic condition will also be used to determine appropriate T_{bed} of PEKK for LS. WXRd was conducted to support DSC analysis, measure the degree of crystallinity, and investigate the crystal structure of PEKKs in comparison to PEK HP3.

The melting of Kesptan 6002 PEKK is ~ 70 °C below PEK HP3. Such lower T_m is beneficial as it decreases the processing temperature of this material to below 300 °C (292 °C). The dynamic DSC analysis reveals significantly slow kinetics of crystallisation for the Kesptan 6002 PEKK grades, which can crystallise only at cooling rates below 2 °C min⁻¹. The very shallow crystallisation peak obtained with this rate is of complicated analysis; therefore, an isothermal investigation was conducted.

The isothermal DSC thermograms support the slow crystallisation of PEKK, which is maximum at ~ 230 °C, as shown by Choupin et al. study [27]. At this temperature, PEKK takes approximately 7 min to crystallise half of its maximum relative crystallisation. These results are promising for application in LS, as slow kinetics of crystallisation avoids curling/warping, but also increases the time for layer bonding in Z orientation. Furthermore, the significantly slow kinetics of crystallisation of PEKK at temperatures near T_g and T_m might enable tailoring of mechanical properties of PEKK parts processed by LS.

The WXRd analysis reveals two different crystal structures present in PEKKs. As opposed to PEK HP3, which only crystallises into the most stable PAEK form, the form I, PEKK powders present a secondary form, form II, identified by the 2θ peak at 15.6° [13]. These powders are also less crystalline than PEK HP3. The results of this chapter will serve as a basis to develop the studies discussed in Chapter 9.

6.2 Dynamic Differential Scanning Calorimetry (DSC)

Melting and crystallisation behaviour were firstly studied using DSC. Fig.6.1 shows the heating and cooling curves of different PAEK grades at the standard rate of 10 °C min⁻¹.

The T_g can be noticed at ~ 160 °C for the PEKKs. A clear difference of ~ 70 °C is observed in the T_m of PEKKs when compared to PEK HP3. This decrease in T_m highlights the structure difference between PEK and Kesptan 6002 PEKKs. The small difference in T_m between HL1327 (297 °C) and P12S959a (300 °C) is attributed to the dense and large particles of the latter, as shown in Chapter 4. Kesptan 6002 PEKKs are semi-crystalline polymers; the presence of a softening point and a melting point in the DSC curves of Fig.6.1 support this behaviour. However, no crystallisation peak is identified in the cooling

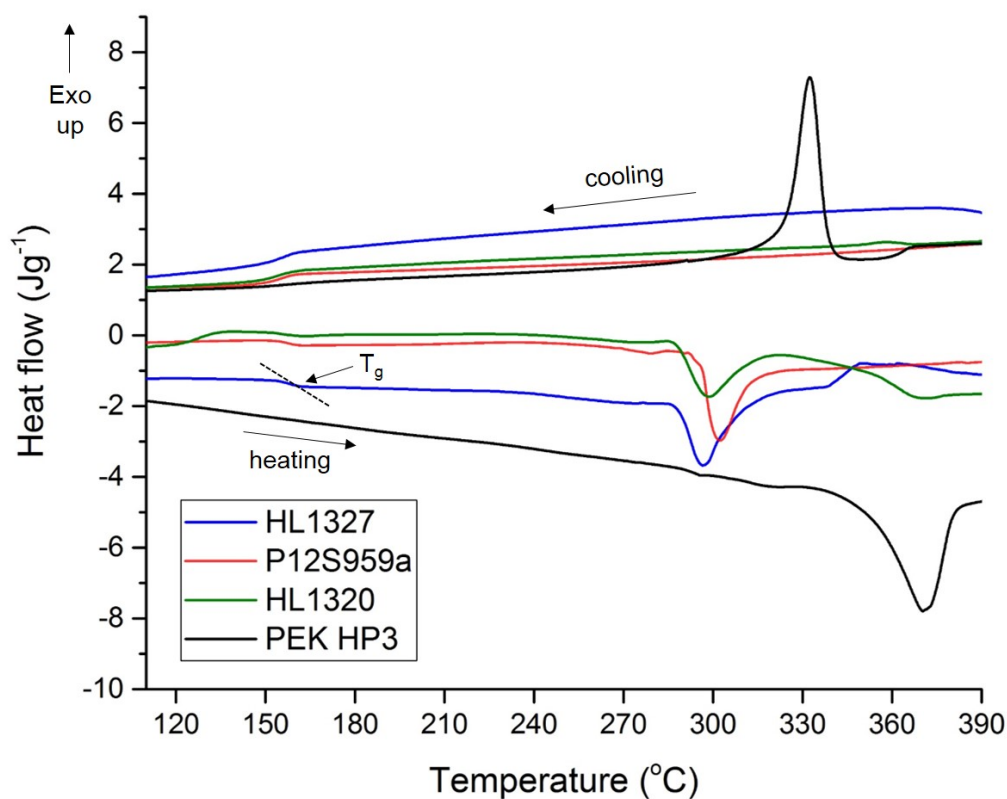


Fig. 6.1 Heating and cooling profiles of standard DSC runs for the three different PEKK grades compared with PEK HP3. The melting peak is visible for all the grades, but no sign of crystallisation is found except for PEK HP3.

profile of these grades, as opposed to PEK HP3, which at $-10\text{ }^{\circ}\text{C min}^{-1}$ shows a clear peak at $332\text{ }^{\circ}\text{C}$. The cooling rate affects the kinetics of crystallisation, and at $10\text{ }^{\circ}\text{C min}^{-1}$ PEKK chains are not able to organise into a crystalline structure.

Following the absence of a crystallisation peak for PEKKs (Fig.6.1), low heating and cooling rates were applied to HL1327 grade. The results are shown in Fig.6.2. The reduction in the heating rate significantly broadens the melting peak of HL1327 (Fig.6.2(1)), which at 2 and $1\text{ }^{\circ}\text{C min}^{-1}$ resemble the slight decline observed at the softening point of HL1327 (Fig.6.1). Furthermore, the melting point of HL1327 seems to shift to higher temperatures at $1\text{ }^{\circ}\text{C min}^{-1}$. In Fig.6.2(2), no clear crystallisation peak is observed for HL1327, regardless of the cooling rate employed. Therefore, these curves were further magnified and are shown once more in Fig.6.3.

HL1327 PEKK has a very shallow crystallisation peak when cooled at slow rates, as shown in Fig.6.3. The integration of the peak obtained with $1.5\text{ }^{\circ}\text{C min}^{-1}$ of cooling reveals a degree of crystallinity of 13%. In Section 6.4, the degree of crystallinity obtained for HL1327 powder using WXR is higher than that. Therefore, to further investigate the crystallisation of PEKK using DSC, the isothermal approach was employed. This approach will be discussed in Section 6.3.

The PEK HP3 grade was also subjected to different heating and cooling rates. The results can be seen in Fig.6.4. As opposed to PEKKs, PEK HP3 shows a clear crystallisation peak regardless of the cooling rate. Lower cooling rates, however, lead to shallower melting

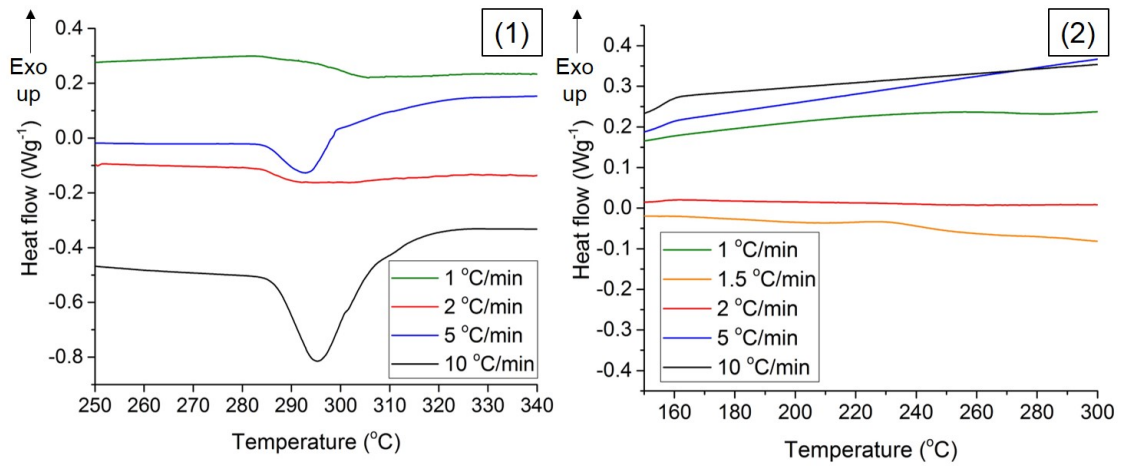


Fig. 6.2 DSC profiles for HL1327 grade at different (1) heating and (2) cooling rates.

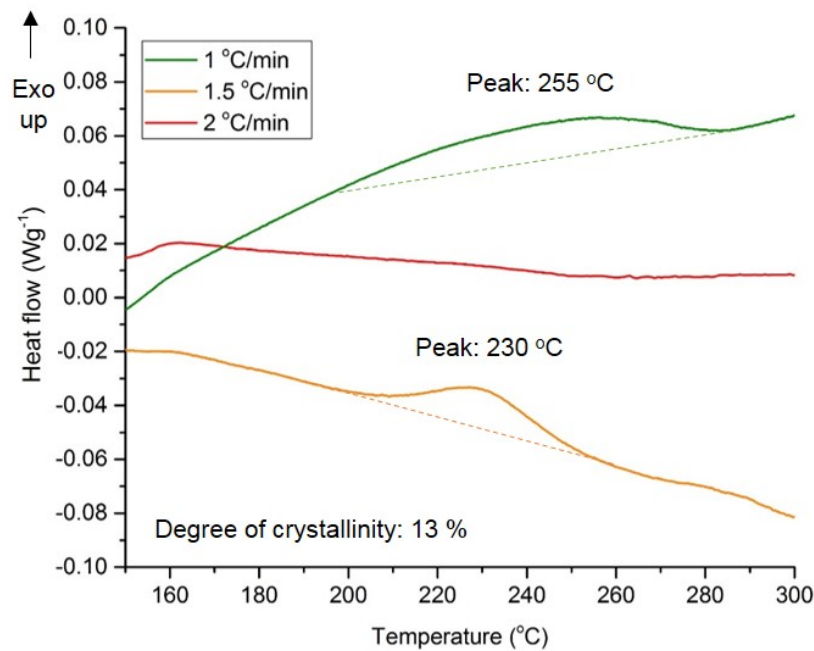


Fig. 6.3 Magnified DSC cooling curves of HL1327 PEKK. Crystallisation peaks are found for PEKK cooled at 1.5 °C min⁻¹ and 1 °C min⁻¹.

and crystallisation peaks, although maintaining the degree of crystallinity. The same degree of crystallinity suggests that sufficient time is provided for chain arrangement in all the cooling rates performed.

As discussed in Section 2.5.3.3, PAEKs are not laser sintered in the region commonly known as the sintering window, but the processing temperature (T_{bed}) of these materials is usually within their melting peak. Berretta et al. [152] developed a method to find T_{bed} of PAEKs using DSC. This method defines the ideal T_{bed} as the minimum point of the first derivative curve of the heating segment obtained with DSC. The method was employed for HL1327 grade as shown in Fig.6.5. The onset of the melt of HL1327 is 286 °C, whilst the first derivative of the heating thermoscan, indicated by the red curve, has a minimum at approximately 292 °C. This temperature will be selected to process PEKKs by HT-LS in Chapter 7.

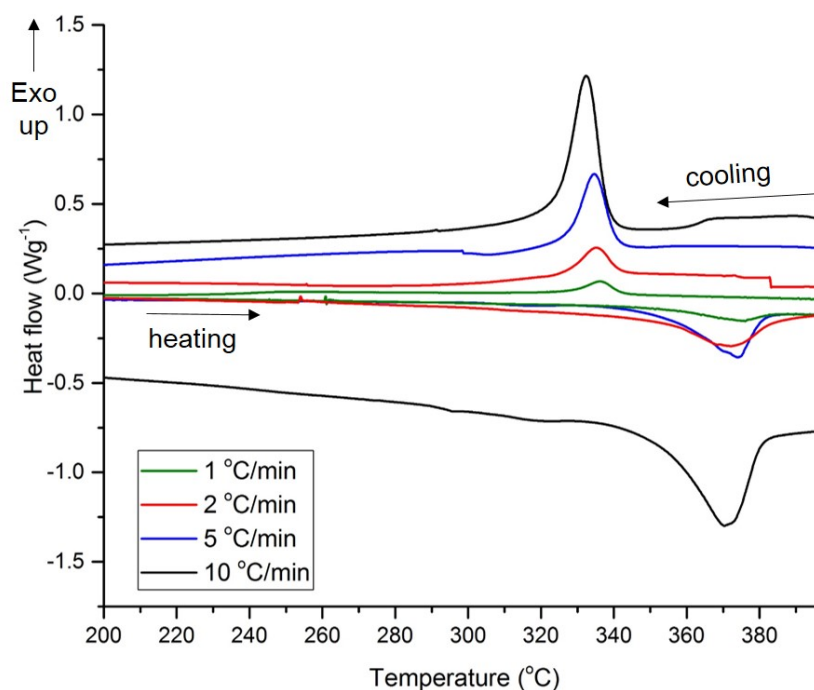


Fig. 6.4 Heating and cooling DSC profiles for PEK HP3. Melting and crystallisation peaks are observed despite the test rate selected.

6.3 Isothermal Crystallisation of PEKK

As shown in Section 6.2, PEKK is completely amorphous at standard DSC rates, and a crystalline peak is only observed below 2 °C min⁻¹. Therefore, crystallisation was measured isothermally, as described in Section 3.3.6.2 for temperatures varying from 200 °C to 270 °C at an interval of 10 °C. The relative volumetric crystallinity of each isotherm from HL1327 grade is presented as a function of time in Fig.6.6.

The HL1327 PEKK grade subjected to isothermal crystallisation at 220 °C, 230 °C and 240 °C is fully crystalline in less than 30 minutes. The rate of crystallisation is gradually lowered for isotherm temperatures below and above these temperatures and is the longest at 270 °C, the temperature in which chain mobility is high, but nuclei formation is the lowest. In Fig.6.7, these results are presented as a function of time versus temperature to crystallise half of the maximum relative crystallinity.

The resulting U-shape curve has a minimum time near 230 °C, which corresponds to the temperature in which PEKK crystallises the fastest (~7 min). This curve agrees with the results obtained by Choupin et al. [27]. The data for each isotherm is presented as a function of enthalpy of fusion in Fig.6.8.

The enthalpy of fusion follows a similar trend to Fig.6.7, in which enthalpy is minimum in the edges (~ 9 J g⁻¹), but achieves a maximum at 240 °C, of 17.8 J g⁻¹.

The curves presented in this section will serve as a basis to investigate the crystallisation of PEKK when processed by LS (Chapter 9).

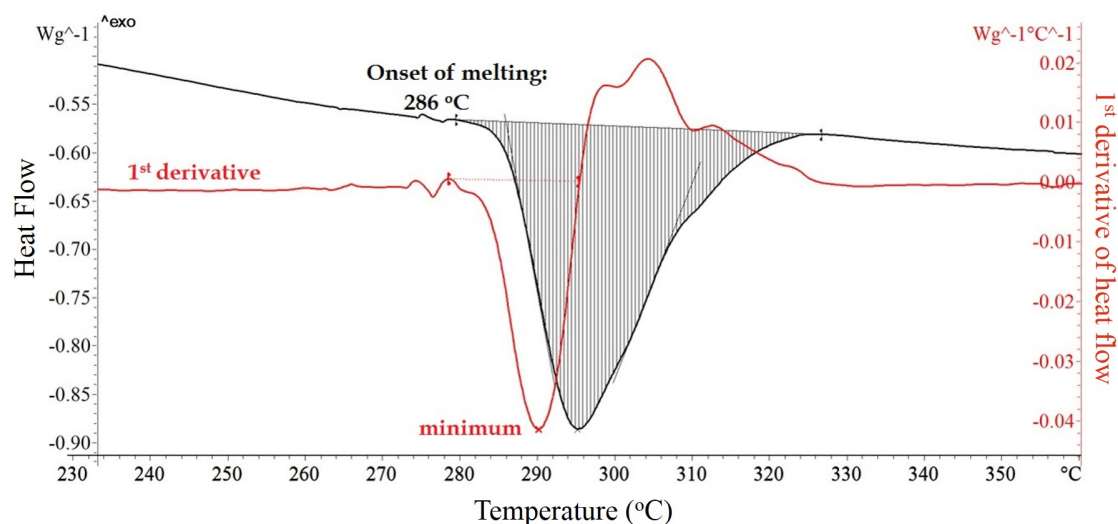


Fig. 6.5 DSC heating thermoscan of Kepstan 6002 PEKK indicating melting and the first derivative of the melt (in red).

6.4 Wide Angle X-ray Diffraction (WXR) Results

The PAEK grades in powder format were tested using WXR, following the methodology presented in Section 3.3.9. Their spectra are shown in Fig.6.9.

All the PAEK grades crystallise in an orthorhombic lattice structure, supported by the spectra of Fig.6.9. Interestingly, the PEKK powders present a peak at $2\theta = 15.6^\circ$, which is not observed in the spectrum of PEK HP3. This peak was associated with the form II of the orthorhombic unit cell ($a = 0.393$ nm, $b = 0.575$ nm and $c = 1.016$ nm) of PEKKs [13] (see Section 2.3.1.2). Zimmermann and Könnecke [306] were able to relate the crystallographic parameters with the chemical composition of PAEKs. They found that the intensity ratio of (200) to (110) peaks increases linearly with the increase of ketone content in the monomer structure - the spectra of Fig. 6.9 support this finding as the PEKK grades show a higher ratio between (200) and (110) peaks than PEK HP3.

Table 6.1 presents the degree of crystallinity resulting from the WXR analysis. All the PEKK grades have a similar degree of crystallinity. The slight shift to a lower degree of crystallinity of P12S959a grade can be explained by the secondary process used to mill these particles, which involves melting and cooling at different conditions from HL1327 and HL1320 particles. PEK HP3 presents a degree of crystallinity about 6% higher than PEKKs. PEK HP3 is a different polymer and is produced by a different polymerisation method; this may be the reason for the difference observed in the crystallisation properties.

6.5 Conclusions

This chapter provides general insights into the thermal and crystallisation properties of Kesptan 6002 PEKK. When compared to PEK HP3, the PEKK grades in this study show a melting peak of approximately 70 °C below, which significantly decreases the temperature required to process such powders by LS. By applying the methodology developed by

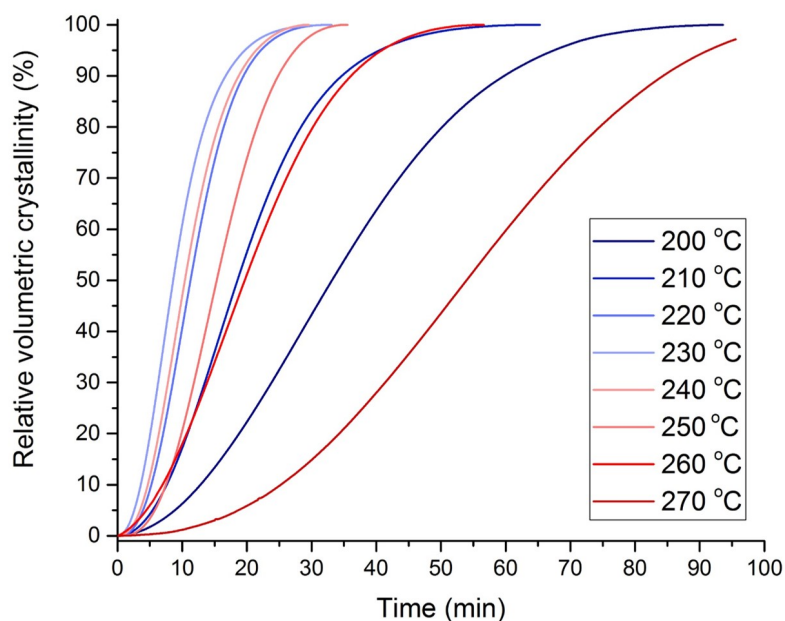


Fig. 6.6 Relative volumetric crystallinity of Kesptan 6002 PEKK, HL1327 grade, at different isotherms.

Table 6.1 Degree of crystallinity for different PAEK grades using the WXR D technique.

Grade	Degree of crystallinity (%)
HL1327	32.8
P12S959a	30.2
HL1320	32.4
PEK HP3	38.5

Berretta et al. [152], the minimum of the first derivative of the heating of Kesptan 6002 PEKK is of 292 °C. This temperature was selected as the LS processing temperature (T_{bed}) of this polymer in the following chapters.

As opposed to PEK HP3, which presents a defined crystallisation peak at standard DSC rates (10 °C min⁻¹), PEKK has an amorphous behaviour at cooling rates above 1.5 °C min⁻¹. This structure is also obtained when processing PEKK by conventional techniques, such as IM. The slow kinetics of crystallisation of PEKK hinders the investigation at dynamic conditions. Therefore, isothermal DSC was conducted.

PEKK can crystallise between 200 °C to 270 °C, with a minimum time of ~7 min to achieve half of its relative crystallinity at 230 °C. This time gradually increases the farther from 230 °C; the enthalpy of fusion follows a similar trend. The slow kinetics of crystallisation of PEKKs is very promising for LS application, as it mitigates curling/warping, but also prolongs the time for adhesion between layers in Z orientation. Furthermore, the slow cooling rate in LS combined with the slow crystallisation of PEKK may enable tailoring of the mechanical properties of this material; this will be discussed in Chapter 9.

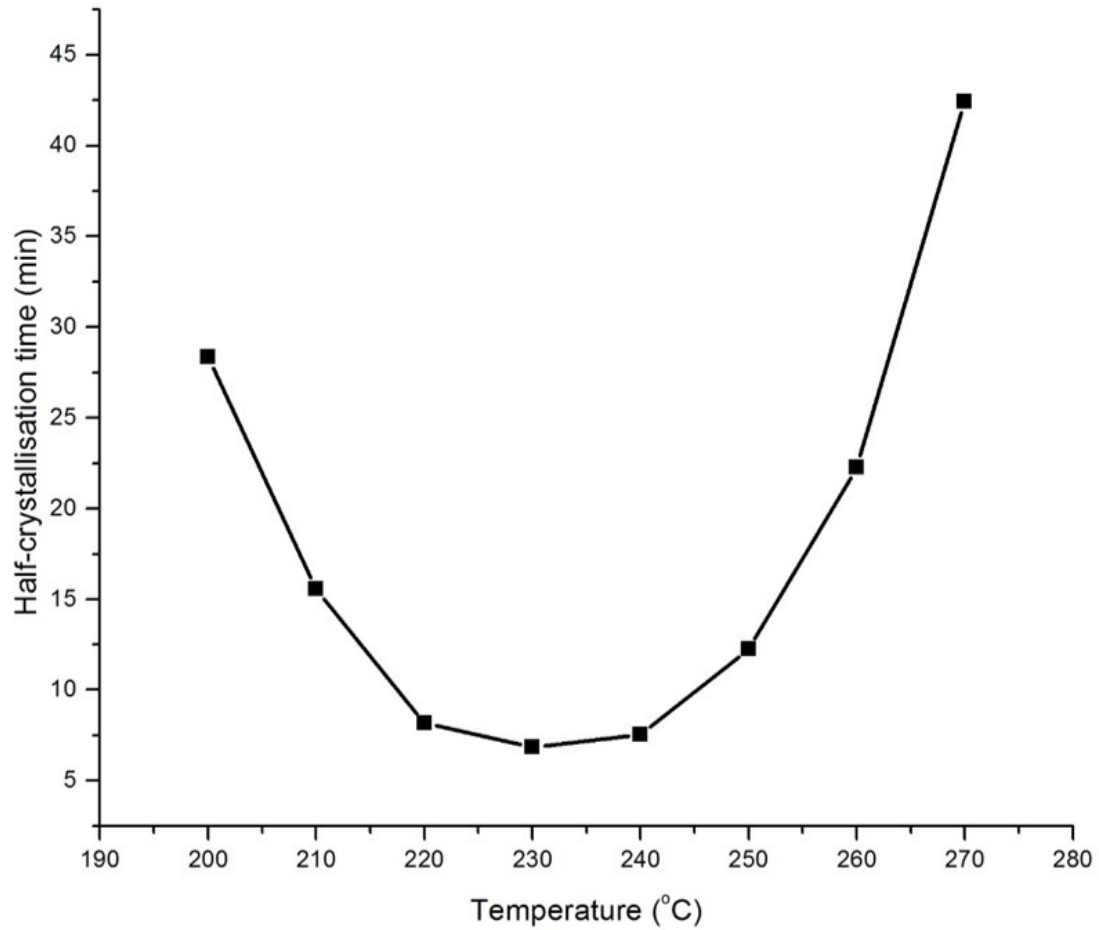


Fig. 6.7 Time taken to crystallise half of the maximum crystallisation of Kesptan 6002 PEKK, HL1327 grade, at different isotherms, also known as the half-time crystallisation curve.

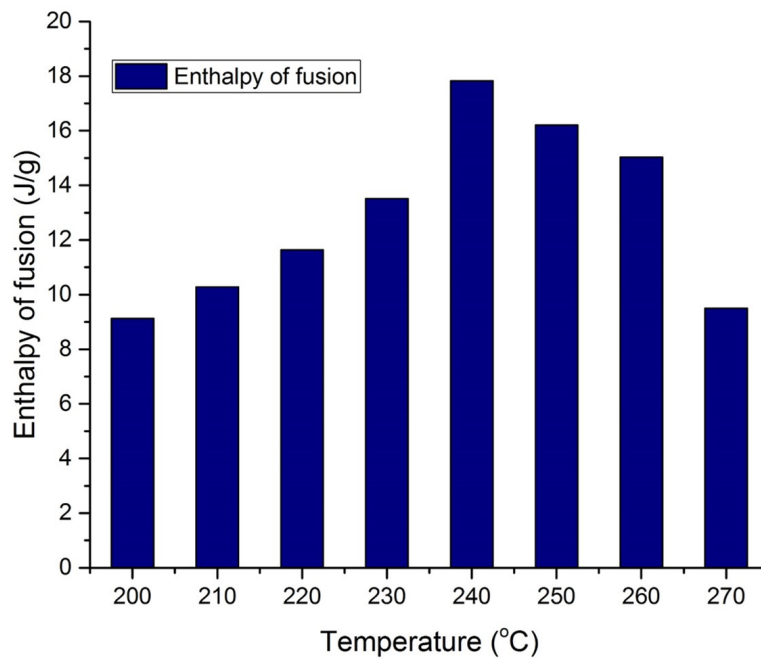


Fig. 6.8 Enthalpy of fusion of HL1327 PEKK at different isotherms. Note the maximum enthalpy at 240 °C.

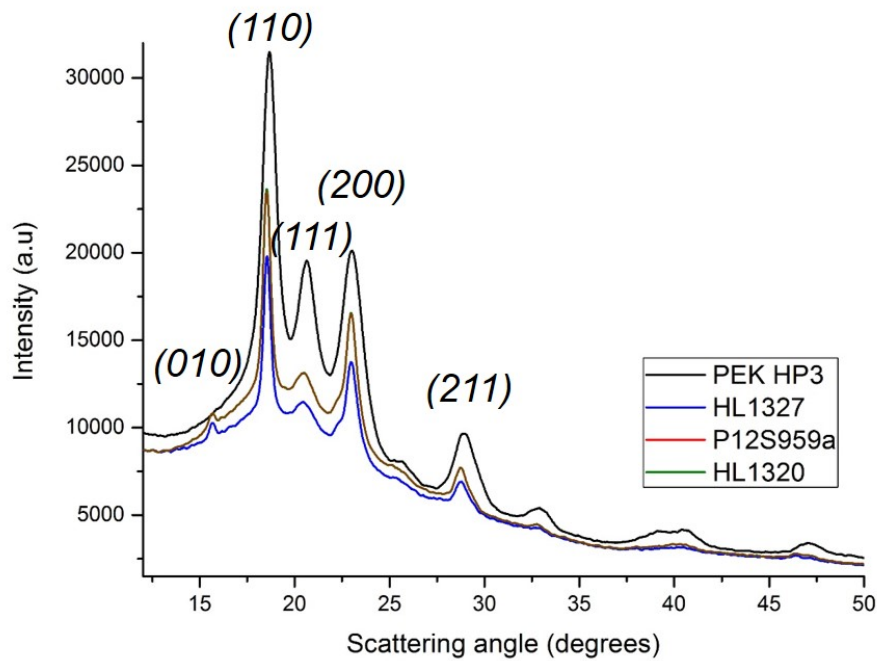


Fig. 6.9 WXR D spectra for different PAEK grades.

The WXR D analysis reveals two crystal structures for PEKK, whilst PEK HP3 only shows the stable form I. The secondary crystallisation, form II, can be identified by the shallow peak at 2θ of 15.6° in the spectra of all the PEKK powders. The degree of crystallinity varies between $\sim 32\%$ for PEKKs to 38.5% for PEK HP3 and is affected by the polymerisation process as well as the thermal history of the polymer.

Chapter 7

Process Optimisation

7.1 Summary

This chapter is the first to explore the effect of LS in the process and properties of Kepstan 6000 PEKK. The process must be tailored to the material in use to achieve the best performance in LS; this will be conducted by firstly performing a screening of the laser parameters, followed by the analysis of manufacturing orientation, processing temperatures, and the effect of multiple laser exposures. These factors were assessed regarding mechanical properties, consolidation, and surface quality. The diagram of Fig.7.1 illustrates the fields of study in this chapter.

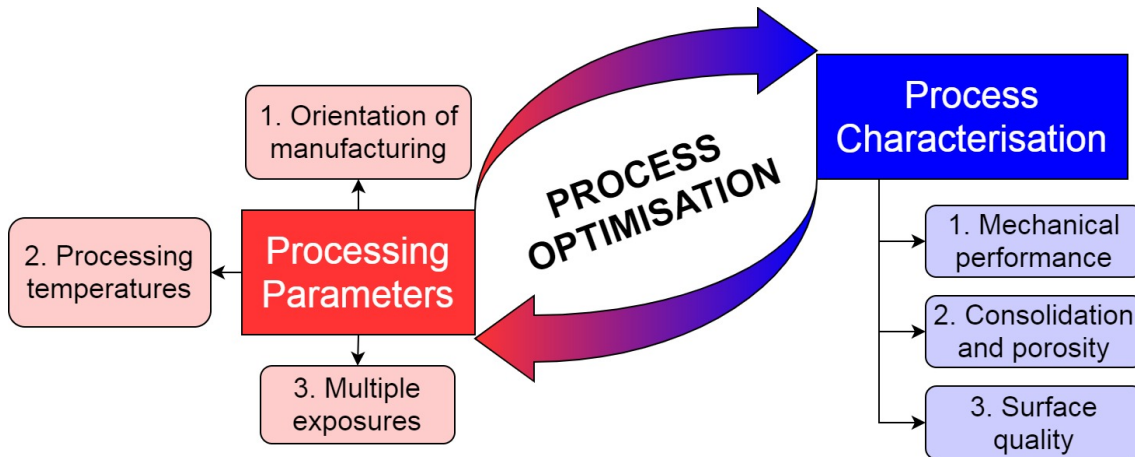


Fig. 7.1 Schematic representation of processing parameters and characterisation methods employed to assess LS quality of PEKK.

The optimisation involved a cyclic process of manufacturing and properties investigation. The main interest consisted of improving the mechanical properties of PEKK, which were measured through tensile, flexural, and compressive testing. The list below specifies the techniques used to determine the properties illustrated in the diagram of Fig.7.1:

1. **Mechanical performance:** tensile testing, flexural testing, compression testing;
2. **Consolidation and porosity:** SEM, micro-computer tomography (micro-CT);
3. **Surface quality:** surface roughness, SEM.

Tensile strength of almost 91 MPa was achieved for specimens built in X orientation with the best combination of laser parameters - 12 W of laser power, 2550 mm s⁻¹ of scan speed and 0.2 mm of scan distance. For these specimens, T_{bed} of 292 °C and building platform temperature (T_{bp}) of 265 °C were selected. Despite the comparable mechanical properties to PEK HP3 grade, the elongation at break remains low, of 2.6%, justified by the usual brittle behaviour of LS specimens. The flexural testing supported the tensile testing results, whilst compressive testing revealed plastic deformations of up to 75% without layer delamination or shattering of the specimens. As opposed to X orientation, the failure of specimens manufactured along Y and Z orientation seemed to have started from the

surface; this is supported by the surface topology results and fracture images analysis. Porosity also changed with the orientation of manufacturing.

Despite less porous, the increase of T_{bp} resulted in worse mechanical performance due to semi-sintered particles adhering to the surface of the sintered layers and leading to failure. For higher T_{bp} , crystallinity is slightly increased, whilst the spherulites are larger in diameter due to the prolonged time for growth.

The multiple laser exposures study showed that energy density (ED) is the main factor affecting mechanical properties, but three laser exposures with the same ED resulted in significantly worse performance. Double exposure decreased mechanical strength and maintained elongation at break and surface topology in comparison to a single scan with the same ED .

7.2 Processing Parameters & Optimisation

7.2.1 Laser parameters

Laser parameters are key for LS processing as they enable fusion between particles in the selected areas of the powder bed. The main parameters are laser power (P_L), scan speed (v_s) and scan spacing (h_s); they are usually described in terms of energy density (ED) as shown by Eq.(7.1):

$$ED = \frac{P_L}{v_s h_s}. \quad (7.1)$$

In the EOS P 800 system, the maximum P_L is 50 W, v_s operates in a range between 2000 and 6000 mm s⁻¹ and h_s is fixed at 0.2 mm [235]. Layer thickness must be included in Eq.(7.1) to calculate volumetric ED , which is fixed to 120 μm in the EOS P 800 system. The recommended laser parameters to process PEK HP3 powder are available in Table 7.1. These parameters will be used as a reference to determine the first laser screening parameters to process Kepstan 6000 PEKK.

Table 7.1 Standard laser sintering parameters for PEK HP3 [263].

Parameters	PEK HP3
Fill laser power (contour)	8.5 W
Fill laser power (hatching)	15 W
Scan spacing	0.2 mm
Scan speed (contour)	1000 mm s ⁻¹
Scan speed (hatching)	2550 mm s ⁻¹
Beam offset	0.39 mm
Energy density (hatching)	29.4 mJ mm ⁻²

7.2.2 Processing temperatures

In the LS process of polymers, the presence of a heated chamber allows full coalescence and adhesion between layers, controls consolidation, and prevents warping, distortion, and any additional stress which may compromise polymer manufacturing [237]. The heated chamber replaces support structures often used in metals [307], therefore reducing post-processing time and material waste.

The temperatures selected for processing are dependent on material thermal properties but are often in between the crystallisation and melting peak of polymers, also known as the sintering window [110, 5]. In the case of high-temperature polymers such as PAEKs, the bed temperature (T_{bed}) is above the onset of melting and corresponds to the minimum of the first derivative of the heating segment in the DSC, as shown by Berretta et al. [152].

The first derivative of the melt was applied to Kepstan 6000 PEKK in Section 6.2. The average of the minimum point of three runs is equal to 292 °C, which was the temperature chosen as T_{bed} throughout this work. Indeed, change in powder colour was observed at higher temperatures than 292 °C, whilst at lower temperatures, curling was noticed in the cold spots of the LS powder bed. More accurate control of heat fluctuations would be required to avoid curling and warping at lower T_{bed} , or as an alternative, the use of support structures, as shown when describing the ThermoMELT process (Section 2.5.1).

Besides the laser heat and T_{bed} , the EOS P 800 HT-LS system has two other sources of heat, as described in Section 2.5.2.4. They are the exchangeable build frame temperature (T_{ebf}) and building platform temperature (T_{bp}). The T_{bp} was selected within the usual sintering window. Choupin et al. [27] showed that the maximum rate of crystallisation of Kepstan 6002 PEKK is at 230 °C; this was confirmed in Section 6.3. Therefore, the initial attempt consisted of applying the average between the maximum rate of crystallisation temperature (230 °C) and the melting peak (~ 300 °C) of PEKK, which corresponds to ~ 265 °C. In Section 7.4, the T_{bp} was increased to the onset of melting, which is of 286 °C for Kepstan 6002 PEKK. By raising the T_{bp} from 265 °C to 286 °C, the cooling rate is reduced, and more time is allowed for coalescence, therefore possibly decreasing the porosity of the final part. These temperatures are illustrated in Fig.7.2 along with the minimum of the first derivative of heating.

T_{ebf} was selected the same as T_{bp} to guarantee a homogeneous heat distribution across the chamber. Table 7.2 summarises the set of temperatures used in each of the sections of this chapter.

7.2.3 Screening of laser parameters

All the trials performed in this chapter used the reduced build configuration with minimum dimensions, as shown in Fig.2.20. Previous literature [9] proved that no significant change is observed in the properties of parts manufactured at the different build configurations available in the EOS P 800 system. The layer thickness and scan spacing are fixed at 120 μm and 0.2 mm, respectively.

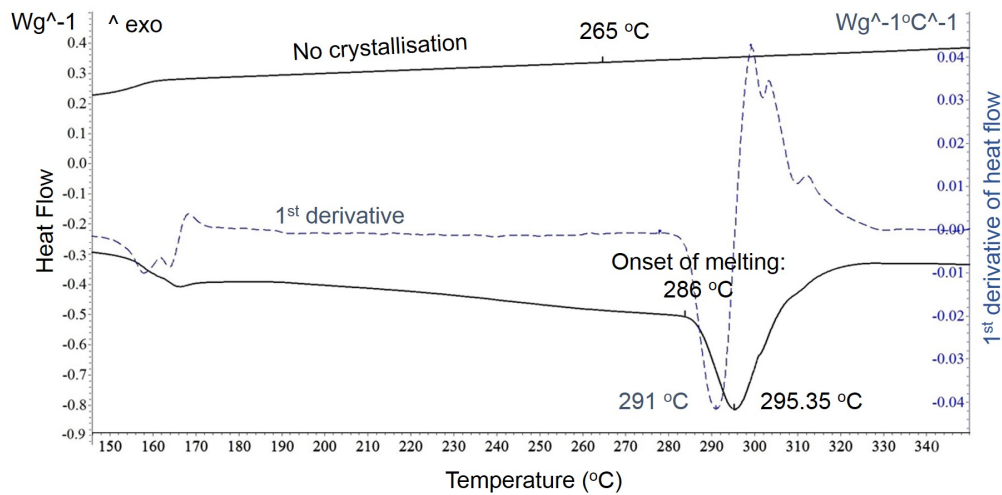


Fig. 7.2 DSC profile of Kepstan 6002 PEKK indicating melting and the first derivative of the heating (dashed curve). The T_{bed} (292 °C) and T_{bp} (265 °C) were extracted from the DSC curves.

Table 7.2 Processing temperatures selected to perform LS trials according to each section of this chapter.

Section	T_{bed} (°C)	T_{bp} (°C)	T_{ebf} (°C)
7.3	292	265	265
7.4	292	286	286
7.5	292	265	265

The effect of P_L was investigated for Kepstan 6002 PEKK powder, HL1327 grade, by maintaining the laser parameters set of Table 7.1, but varying the laser power from 2 to 20 W. The specimens were manufactured in X orientation following ISO 527-2-1BA guidelines. Each group set contained ten specimens arranged in two columns in the XY plane, as shown in Fig.7.3. The more parameters tested, the higher the stacking in Z orientation. This configuration (two columns in XY plane, and groups of specimens stacked in Z orientation) is the standard applied to most of the trials in this chapter (Section 7.4 and Section 7.5), unless when build orientation was investigated.

The results were assessed regarding ultimate tensile strength (UTS), as shown in Fig.7.4. The curve reaches a plateau from 10 W of laser power (energy density ~ 19.6 MJ mm^{-2}). The maximum UTS was achieved by applying a P_L of 12 W, which corresponds to approximately 23.5 MJ mm^{-2} of ED per manufactured layer. This energy produced specimens with a tensile strength of almost 91 MPa, similar to the tensile strength values obtained for LS PEK HP3 [280]. Therefore, the laser power was fixed to 12 W to perform the screening of scan speed. The results are shown in Fig.7.5.

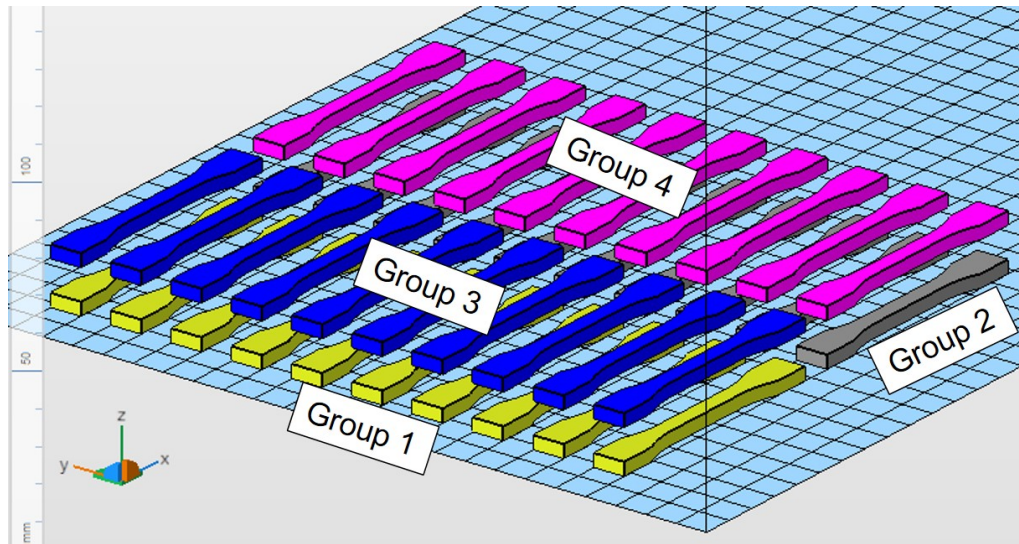


Fig. 7.3 Usual build configuration for specimens manufactured in the X orientation.

The maximum tensile strength was still 16 MPa below the strength achieved with 2550 mm s^{-1} and a laser power of 12 W. Fig.7.6 provides a comparison of the tensile strength (1) and elongation at break (2) data obtained by varying power and speed.

The results of Fig.7.6(1) support that ED is not sufficient to predict the mechanical behaviour of Kepstan 6002 PEKK, and different combinations of laser power and scan speed affect strength and elongation at break. The scan speed of 2550 mm s^{-1} is the optimum value, which, in combination with 12 W of laser power, gives the best tensile strength and elongation at break (Fig.7.6(2)) for LS Kepstan 6002 PEKK. The elongation obtained with LS PEKK (2.6%), however, is still minimal, being an order of magnitude lower than IM PEKK specimens, which present an elongation above 80% [12]. The leading cause for this drastic reduction in elongation can be attributed to the poor layer bonding resulting from the incomplete fusion of particles in the interlayer area [274]. Furthermore, porosity and particle-to-particle interfaces compromise elongation at break [267]. In the case of PEKK, the amorphous structure obtained by IM against the semi-crystalline LS parts is an essential factor which leads to reduced elongation; this will be explored in Chapter 9.

Films were manufactured using different laser powers to complete the screening of laser parameters. Their production is interrupted once the top layer is completed to avoid any addition of powder to the top layer. By doing so, the effect of laser parameters on surface quality can be isolated from powder properties and the mechanism of deposition. The films were taken to SEM and surface topology analyses. Fig.7.7 presents the SEM images of the films produced with 3W(1), 6W(2), and 12W(3) at 2550 mm s^{-1} of scan speed. The results infer that a laser power of 6 W and below is insufficient to create a robust structure, and the specimens are mostly porous.

This porosity and irregular surface topology were quantified in terms of R_a values, as shown in Fig.7.8. The surface significantly improves from 4 W to 6 W of P_L , supporting the SEM images of Fig.7.7. It seems that the pores observed in the films of 3 W (Fig.7.7(1)) are deeper than one sintered layer, whilst the pores in the films produced with 6 W (Fig.7.7(2))

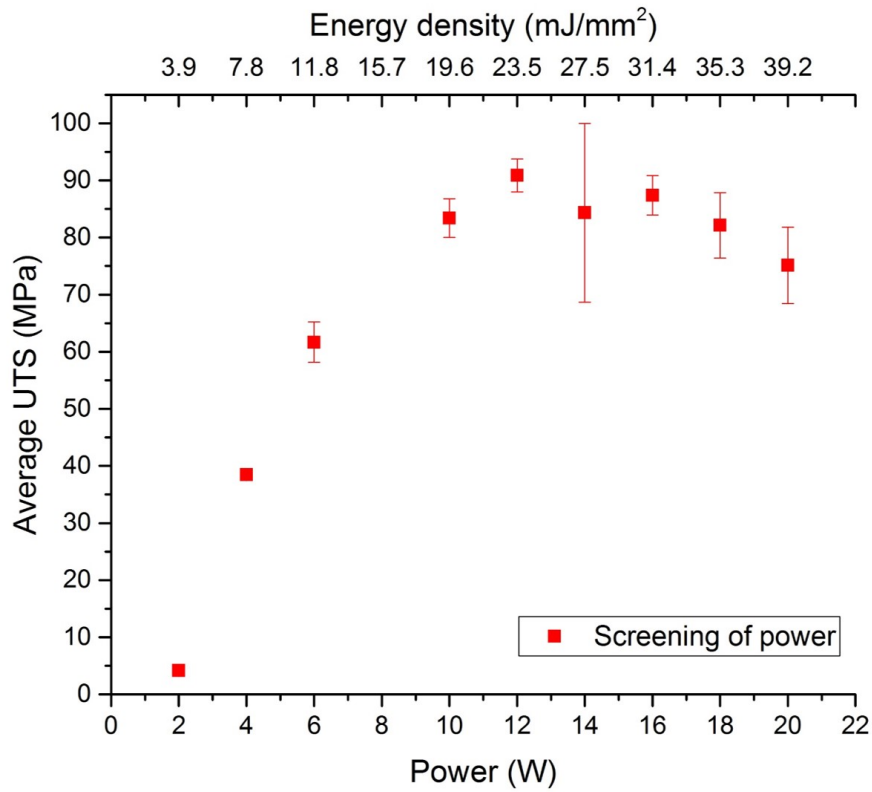


Fig. 7.4 Average UTS of LS HL1327 PEKK specimens manufactured at different laser powers.

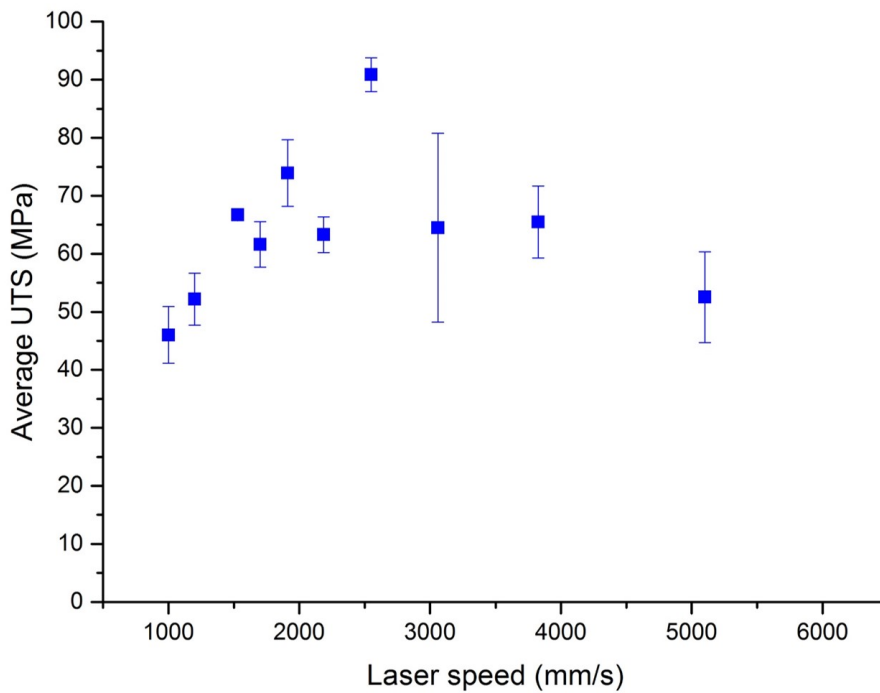


Fig. 7.5 Average UTS of LS HL1327 PEKK specimens manufactured at different laser scan speeds.

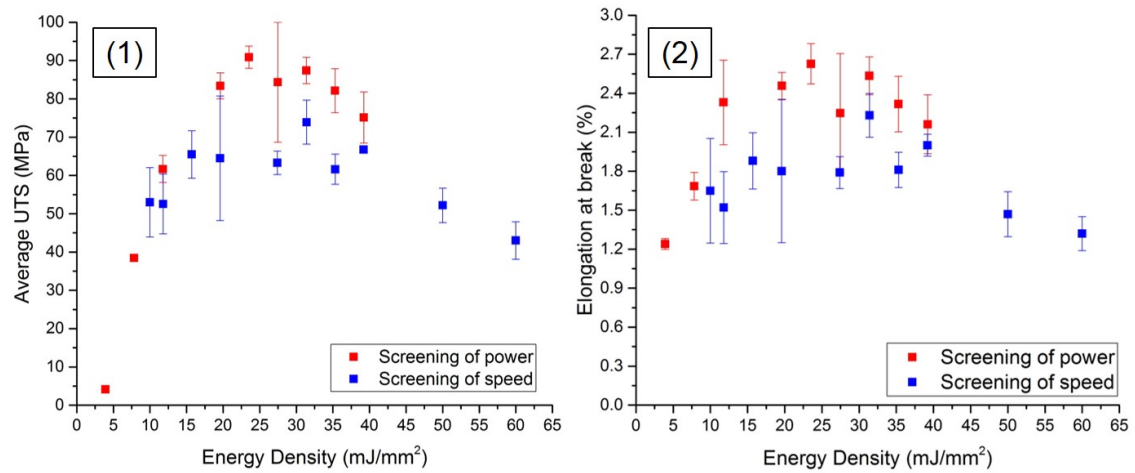


Fig. 7.6 Average UTS (1) and elongation at break (2) of LS HL1327 PEKK manufactured using different energy densities.

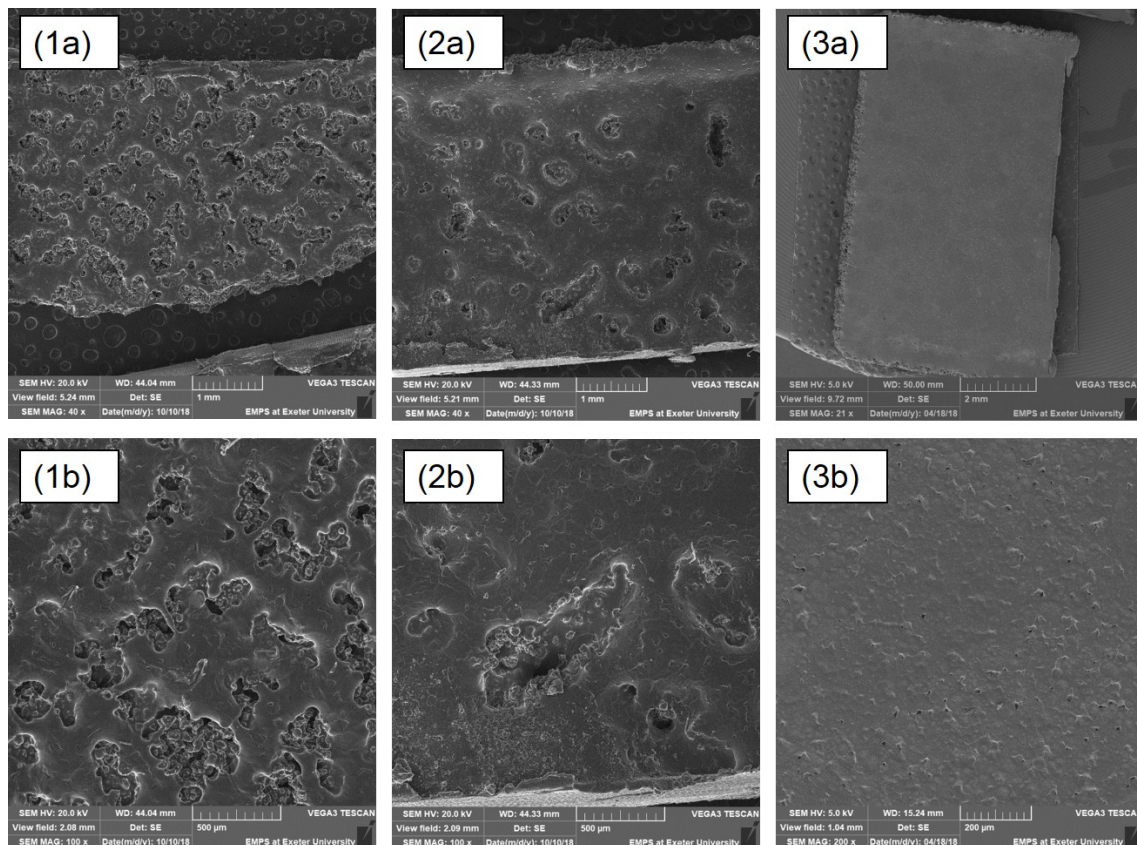


Fig. 7.7 SEM images of films produced using different laser powers and energy densities. (1) 3 W and 5.9 mJ mm⁻², (2) 6 W and 11.8 mJ mm⁻², and (3) 12 W and 23.5 mJ mm⁻². Note the different scale bars of (a) 1 and 2 mm and (b) 500 μ m and 200 μ m.

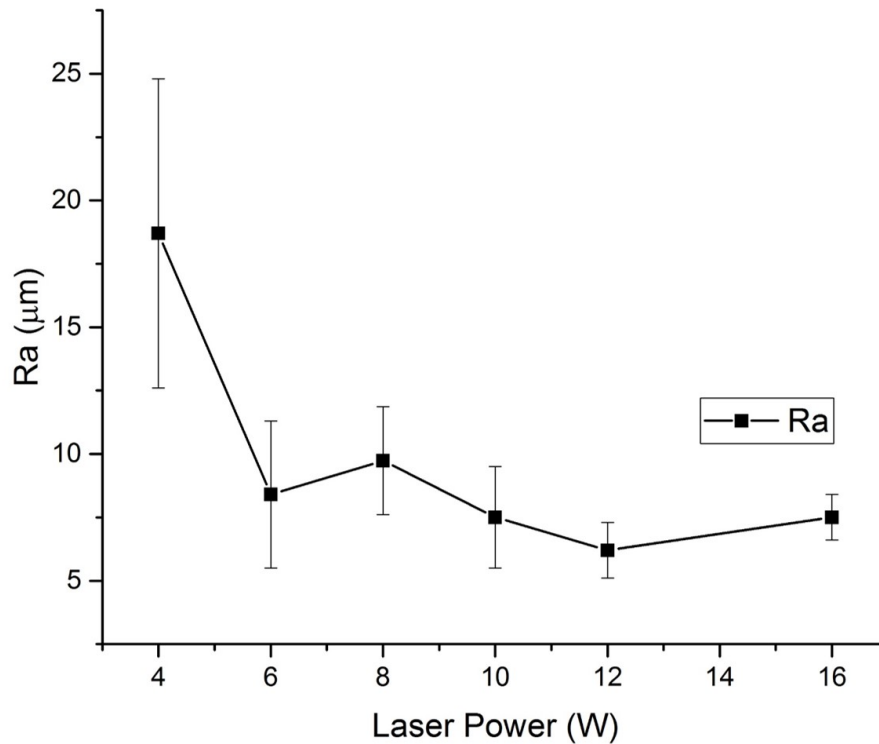


Fig. 7.8 Relation between laser power and surface topology (S_a) of PEKK films.

are, if not one layer deep, less deep than the films manufactured with 4 W of P_L . The R_a values continuously decrease from 8 W until 12 W, point at which best surface quality is achieved. Such a result is supported by Fig.7.7(3), which shows tiny pores on the top layer of the films produced with 12 W of P_L .

7.3 Effect of Building Orientation

From the screening of laser parameters, specimens produced with an ED of 23.5 mJ mm^{-2} (12 W, 2550 mm s^{-1} and 0.2 mm) were selected to evaluate the effect of building orientation. The orientation of manufacturing was assessed using tensile testing, flexural testing, and compressive testing. A sample size of 10 specimens was used for each orientation. Fig.7.9 presents the build configuration of tensile specimens manufactured in Y and Z orientation. Fig.7.10 shows the results of tensile strength and elongation at break under tensile conditions.

Similar to other materials processed by LS, Kepstan 6002 PEKK specimens were greatly affected by anisotropy. The difference in UTS between groups is statistically significant, with $P \leq E^{-7}$ for any group comparison, e.g., specimens manufactured in X orientation against the ones produced in Y orientation. The results of elongation at break are also statistically different, with $P \leq 0.01$ regardless of the groups in comparison. The specimens built in X performed significantly better. This orientation gives the best UTS and elongation at break, with an average of, respectively, 90 MPa and 2.6%. The worst performance is in Z orientation as a result of the poor adhesion between layers, supported by a flat failure, i.e., failure throughout only one layer of manufacture, and low

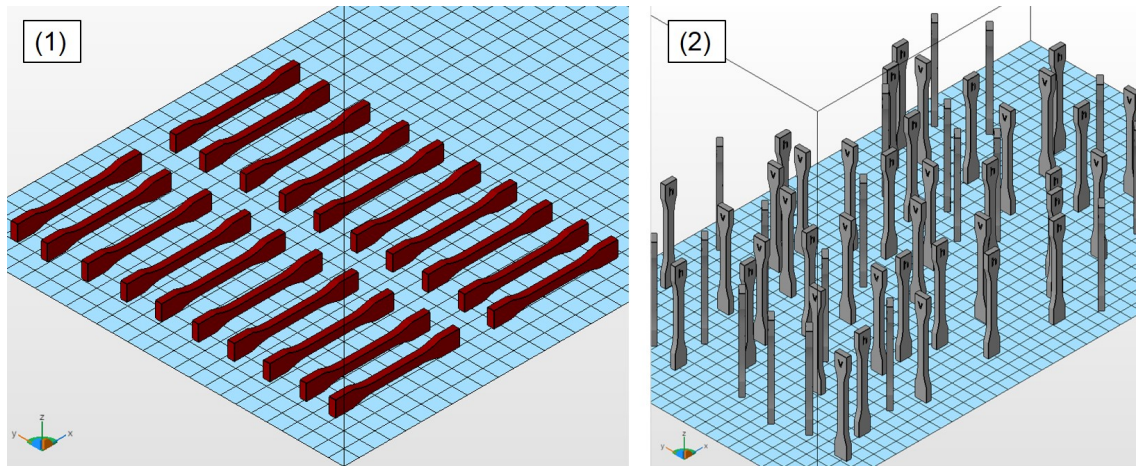


Fig. 7.9 Build configuration of specimens manufactured in (1) Y, and (2) Z orientation.

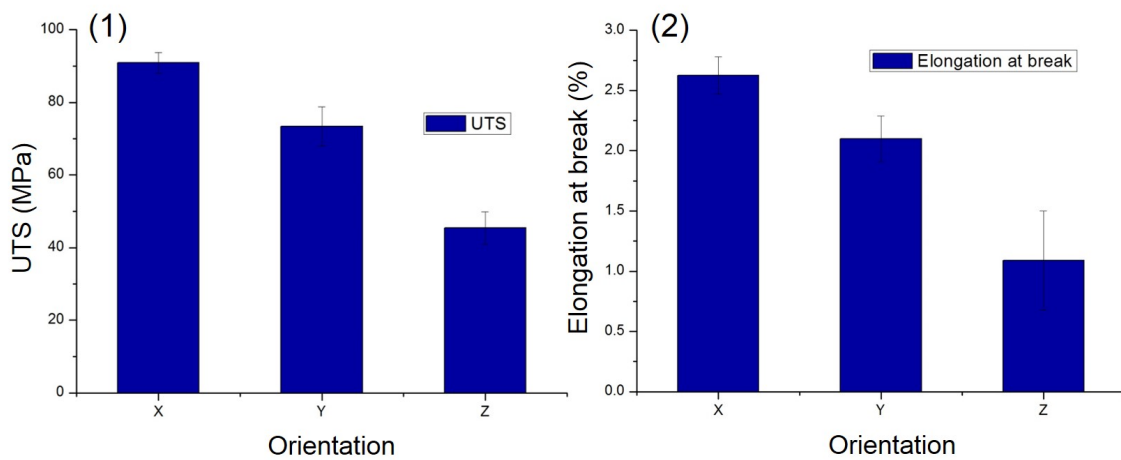


Fig. 7.10 (1) Ultimate tensile strength and (2) elongation at break of Kepstan 6002 PEKK manufactured in different orientations.

elongation. For these specimens, the average UTS was 50% lower than the values achieved in X orientation, whilst elongation was reduced by almost 60%.

The results of flexural strength are summarised in Fig.7.11. The flexural testing data support the results obtained with tensile testing, with the difference between groups being statistically significant ($P \leq 0.05$), despite the specimens produced in X and Y orientation having a more similar performance than the tensile testing specimens produced in the same orientation. The specimens in the Z orientation showed a significant drop in strength in comparison to X and Y orientation. This difference in strength with orientation suggests heterogeneity in the structure caused by the low adhesion between layers in Z direction [274].

Compressive properties were assessed in X and Z direction; the results are shown in Fig.7.12. PEKK showed outstanding plastic behaviour and most specimens remained unbroken even at 70% of deformation, as observed in Fig.7.12(2). Due to the high deformation, strength can be challenging to assess. Therefore the curves were separated in three regions: (i) elastic region (from 0 to ~20%), (ii) plastic deformation up to 50% and (iii) plastic deformation between 50% and 75%. The compressive strength achieved in the

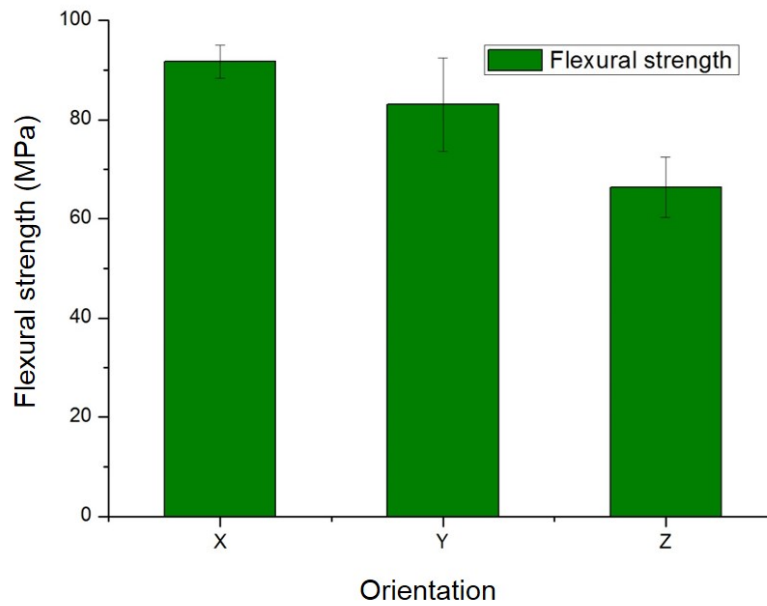


Fig. 7.11 Flexural strength of Kepstan 6002 PEKK specimens manufactured in different orientations.

elastic region, at 20% deformation, was of 168 ± 10 MPa, comparable to what reported by Hoskins [277] for PEK HP3. However, Kepstan 6002 PEKK does not break at the end of the elastic region, but shows an outstanding plastic behaviour, deforming up to 75% of the original thickness with no signs of delamination. At this compression, the average stress in Z orientation is of 557 MPa, whilst the specimens in X orientation reached 734 MPa of compressive strength. This behaviour has never been observed for LS PAEKs before.

The fracture of the specimens manufactured at different orientations was investigated using SEM; they are shown in Fig.7.13. Whilst the fractures of images (1) and (4) of Fig.7.13 show an uneven surface resulting from the fibrils oriented towards the fracture region, image (7) presents a very flat failure characteristic of the poor layer adhesion in Z orientation. In Fig.7.13(4), the fracture was originated near the upper left corner and might be a result of poor surface properties. In the case of image (1), however, the fracture is not as evident, as supported by the fibrils of image (2) being less aligned than the fibrils of image (5). The fracture in X orientation investigated at higher magnification reveals localised ductile zones not observed with the specimens built in the other orientations. Although concentrated in specific regions of the fracture, these ductile regions are possibly holding the structure before failure.

The volumetric porosity was assessed using micro-CT. The experiment was conducted in three different samples at each orientation of manufacturing; therefore, nine specimens in total. Fig.7.14 presents a micro-CT scan section of a specimen manufactured in X orientation (1) and the reconstructed 3D scan (2). Fig.7.15 summarises the results of volumetric porosity.

The volumetric porosity changes with the orientation of manufacturing and specimens produced in Z orientation show almost 44% more porosity than specimens manufactured in X orientation. Despite the statistical difference between the porosity percentage of X

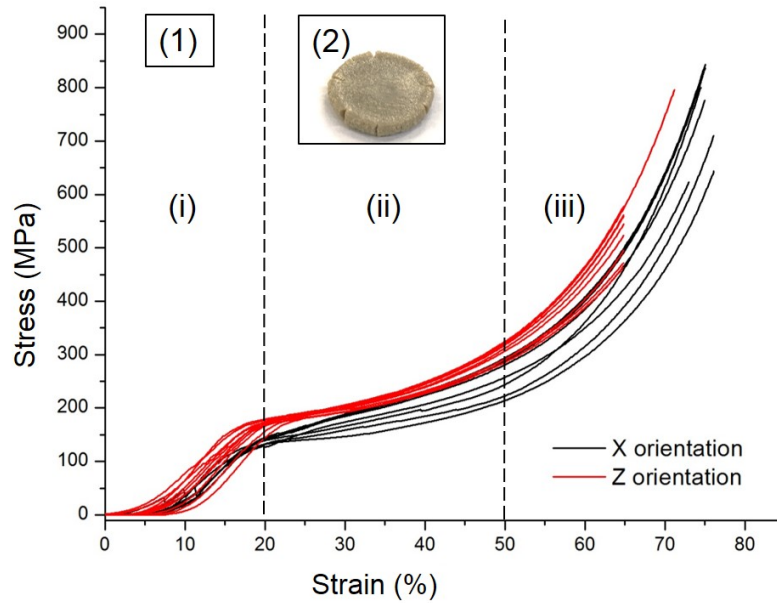


Fig. 7.12 (1) Compressive strength of PEKK specimens manufactured in different orientations. The curves were separated into (i) elastic region, (ii) plastic region up to 50%, and (iii) plastic region $>50\%$; (2) example of a specimen after being subjected to compressive testing.

and Z specimens ($P = 0.04$), and Y and Z specimens ($P = 0.018$), such a difference is not significant when comparing specimens built in X orientation with the specimens built in Y orientation ($P = 0.187$). Wegner and Witt [274] mentioned that porosity is higher in the interlayer area due to incomplete particle fusion. The number of layers increases with orientation, in the order $X < Y < Z$. Therefore, the results herein support Wegner and Witt [274] claim and can be associated with the mechanical performance shown in Fig.7.10, in which more layers resulted in lower mechanical strength and elongation at break.

Besides porosity, failure can be a result of poor surface properties [308, 309]. Flodberg et al. [308] identified non-melted or fused particles on the surface of PA12 tubes. They associated this lack of fusion to the large pores observed near the surface, with a diameter above $100\ \mu\text{m}$. According to them, these pores were likely to initiate fatigue cracks and lead to mechanical failure. Damon et al. [309] confirm the critical effect of porosity on the mechanical properties, and highlight that pores close to the surface often lead to the initiation of fatigue cracks regardless of stress or loading conditions.

For this reason, the surface roughness of the specimens was investigated in respect to S_a , S_t and R_a in the areas reported in Fig.3.4. The average results of three measurements in each orientation are presented in Table 7.3.

Specimens built in X orientation showed statistically different S_a values when compared with the specimens built in both Y ($P = 0.01$) and Z ($P = 0.07$) orientation. However, the difference in S_a values between specimens in Y and Z orientation are not significant ($P = 0.275$); this is supported by the manufacturing on the side walls (Y and Z specimens) not being as accurate as of the top (X specimens). The poor layer adhesion increases surface roughness and is possibly causing earlier mechanical failure and lower elongation

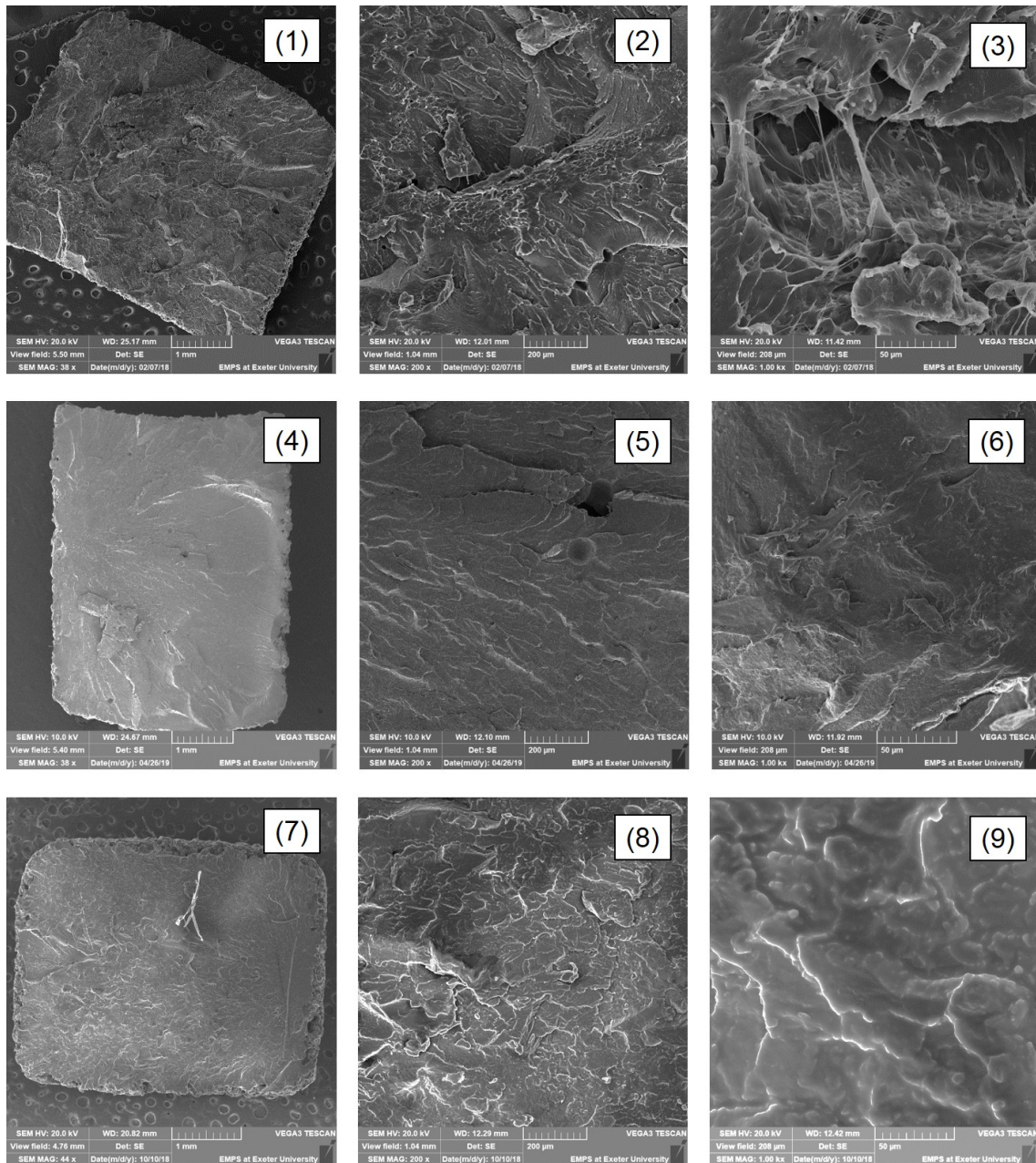


Fig. 7.13 Tensile testing fracture of LS Kepstan 6002 PEKK specimens produced at (1-3) X, (4-6) Y, and (7-9) Z orientation. Note the scale bars of 1 mm (left column), 200 μm (centre) and 50 μm (right column).

Table 7.3 Average surface roughness of Kepstan 6002 PEKK specimens manufactured at different orientations.

Orientation	S_a (μm)	S_t (μm)	R_a (μm)
X	19 ± 3.4	199 ± 18.8	123 ± 15.9
Y	30 ± 0.4	692 ± 725.8	177 ± 7.6
Z	27 ± 1.2	2803 ± 107	863 ± 227

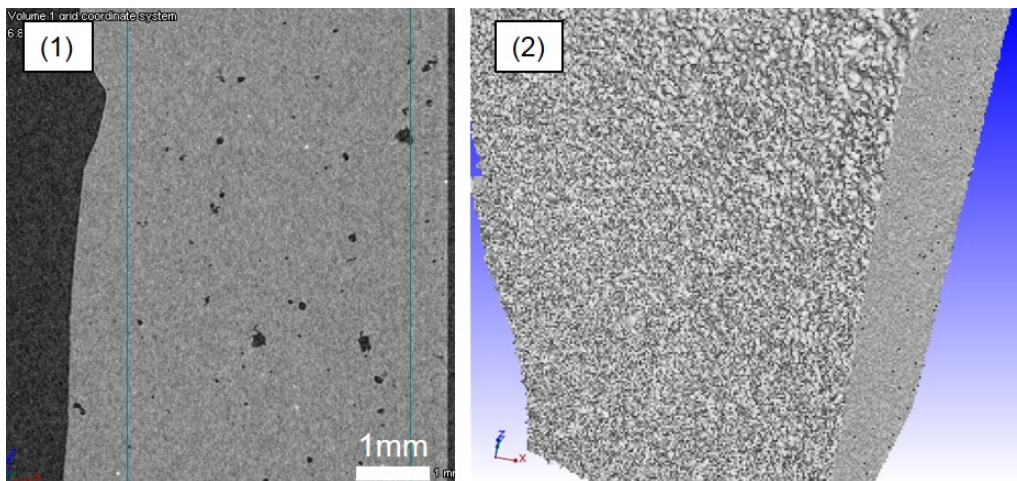


Fig. 7.14 Micro-CT scan of a specimen manufactured in X orientation. (1) Section showing internal porosity and (2) volumetric reconstruction of the scan.

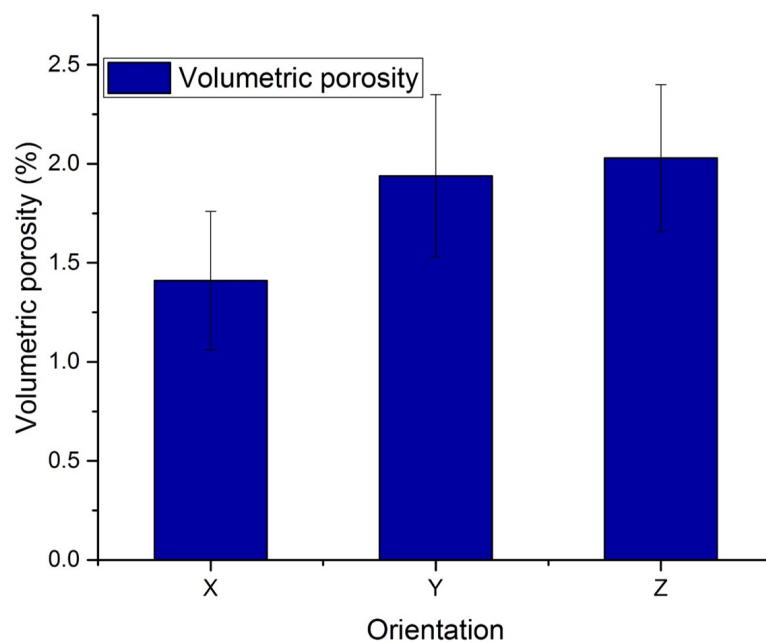


Fig. 7.15 Volumetric porosity of Kepstan 6002 PEKK specimens measured using a Micro-CT scan.

as shown in Fig.7.10. The high standard deviation of S_t and R_a values for the specimens built in Y and Z orientation are likely to be a result of porosity in the structure, as observed in Fig.7.13(5) and supported by the micro-CT analysis of Fig.7.15. Porosity is also present in the specimens produced in X orientation but at a significantly lower level. The presence of pores in the structure leads to highly different S_t and R_a values performed in specimens produced in the same orientation. Therefore, S_a was preferred to measure surface roughness due to the more reliable results.

From the surface analysis, it is possible to conclude that surface roughness does impact mechanical performance, and it is recommended to polish the specimens before use to avoid failure due to high surface topology, especially for specimens manufactured along Y and Z orientation.

7.4 Effect of Different Processing Temperatures

Following the screening of laser parameters (Section 7.2.3) and the effect of building orientation (Section 7.3) on mechanical properties, final part consolidation, and surface roughness, the effect of different processing temperatures was explored. As mentioned in Section 2.5.2.4, the EOS P 800 HT-LS system has three sources of heat applied to the powder bed aside from the laser; they are controlled by bed temperature (T_{bed}), exchangeable build frame temperature (T_{ebf}), and building platform temperature (T_{bp}).

Section 7.3 associates the volume of porosity with final mechanical properties. By increasing T_{bp} and T_{ebf} to the onset of the melting of PEKK (Fig.7.2), porosity will possibly reduce due to a prolonged time given for coalescence to occur. The increase in consolidation will hopefully improve the final mechanical performance of PEKK parts. Specimens with the best combination of laser parameters ($ED \sim 23.5 \text{ mJ mm}^{-2}$) were manufactured in X and Y orientation using a T_{bp} and T_{ebf} of 286°C . Fig.7.16 compares the mechanical properties (UTS and elongation at break) with the specimens built using a T_{bp} of 265°C .

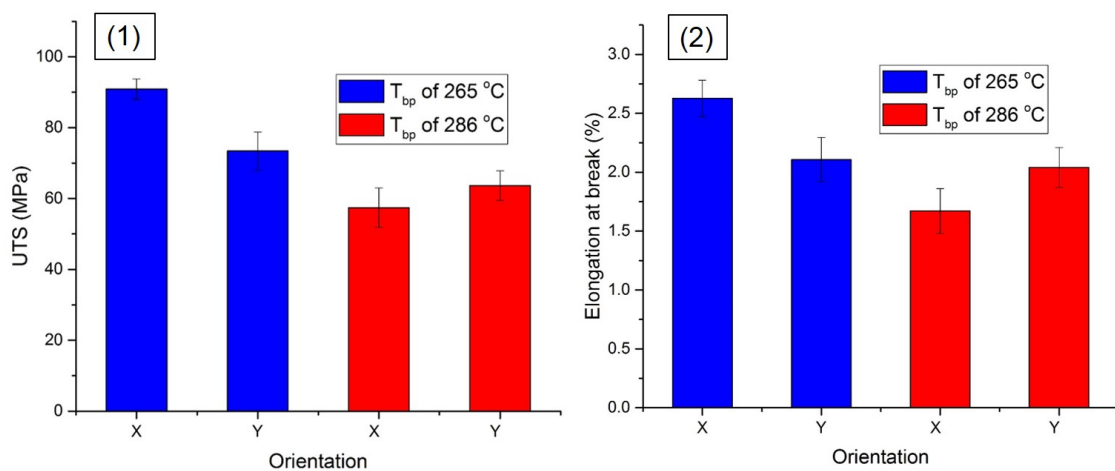


Fig. 7.16 Comparison of the (1) ultimate tensile strength and (2) elongation at break of Kepstan 6002 PEKK specimens processed at different building platform temperatures.

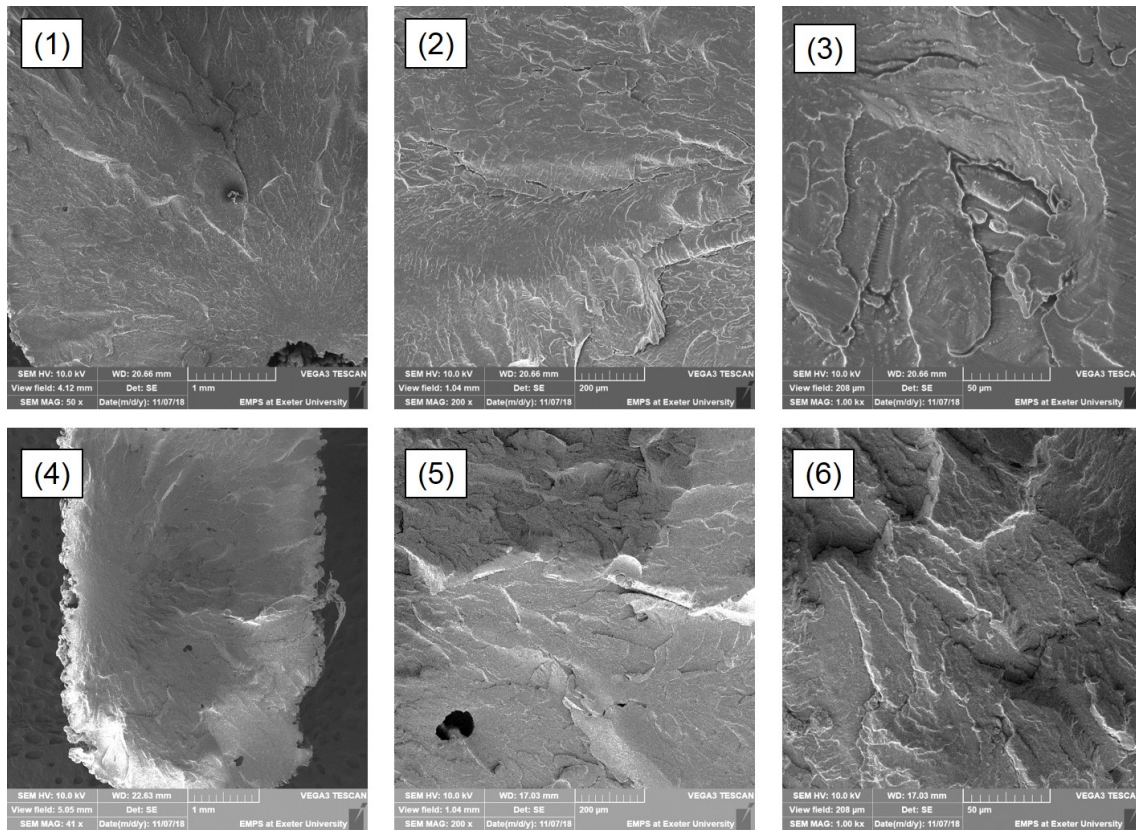


Fig. 7.17 Tensile strength fracture of LS Kepstan 6002 PEKK specimens manufactured using T_{bp} of 286 °C at (1-3) X and (4-6) Y orientation. Note the scale bars of 1 mm (left column), 200 μm (centre) and 50 μm (right column).

One-way and two-way ANOVA were used to compare the mechanical properties of specimens manufactured in different orientations (one-way ANOVA) in combination with varying T_{bp} (two-way ANOVA). Firstly, there is a significant difference with $P = 0.017$ in the UTS of specimens built with T_{bp} of 286 °C and different orientations (X and Y). As opposed to the T_{bp} of 265 °C, the specimens produced in Y orientation performed best, with a higher UTS and elongation at break. The difference is, however, smaller than what obtained with a lower T_{bp} of 265 °C and different orientation, as supported by the P value of $3.21E^{-8}$. The increase of T_{bp} reduced mechanical strength and elongation at break to about $\sim 36\%$ in X orientation. By prolonging the time for coalescence, the layers are better adhered to each other, therefore reducing interlayer failure; this explains the higher performance of Y oriented specimens. There is, however, secondary factors lowering the performance of specimens produced at 286 °C of T_{bp} when compared with 265 °C. They include surface smoothness, which will be discussed later in this section.

The fracture of the specimens produced at T_{bp} of 286 °C was investigated under SEM. Images at different magnifications are shown in Fig.7.17.

Fig.7.17(1) and (4) present an apparent failure starting from the surface of the specimens. The more brittle behaviour supported by the lower elongation at break of Fig.7.16(2) can also be identified by the less amount of fibrils trying to hold the structure together. In Fig.7.17, a few pores are observed in the structure (Fig.7.17(5)), but most of them are concentrated on the surface. No localised plastic zones are found, even at higher

magnifications, as shown by Fig.7.17(3) and (6). The brittle behaviour supports the poorer elongation at break of the specimens manufactured using a T_{bp} of 286 °C.

Porosity, surface roughness, and crystallisation can explain the lower mechanical performance observed for the specimens manufactured at higher T_{bp} . These factors were investigated using micro-CT, surface profiler, and WXR, respectively. The results of volumetric porosity varying with T_{bp} are shown in Table 7.4.

Table 7.4 Volumetric porosity of Kepstan 6002 PEKK specimens processed at different T_{bp} .

T_{bp} (°C)	Orientation	Average volumetric porosity (%)
265	X	1.41 ± 0.35
265	Y	1.94 ± 0.41
286	X	1.15 ± 0.33
286	Y	1.55 ± 0.44

The level of porosity is significantly affected by orientation - X or Y - with $P = 0.018$, and temperature - 265 °C or 286 °C - with $P = 0.009$. The specimens in X orientation showed a lower level of porosity, possibly because of the lower number of layers, therefore fewer interlayer regions. With the increase of T_{bp} , porosity was reduced due to the prolonged time given for coalescence. A less porous specimen, however, did not result in better mechanical performance, but worse. This result led to the investigation of surface roughness. The data were compared with the specimens manufactured at T_{bp} of 265 °C; they are presented in Table 7.5.

Table 7.5 Surface roughness of Kepstan 6002 PEKK specimens manufactured at different orientations.

T_{bp} (°C)	Orientation	S_a (µm)	S_t (µm)	R_t (µm)
265	X	19 ± 3.4	199 ± 18.8	135 ± 15.9
265	Y	30 ± 0.4	692 ± 725.8	177 ± 7.6
286	X	27 ± 0.8	252 ± 86.6	183 ± 19.0
286	Y	39 ± 7.8	2710 ± 541.5	674 ± 781.0

The parameter S_a was chosen for comparison for the same reasons explained in Section 7.3. Once again, there are significant difference between building orientation, X and Y ($P = 3.85 \times 10^{-4}$) and T_{bp} , 265 °C and 286 °C ($P = 5 \times 10^{-3}$). The difference in surface roughness explains the lower mechanical performance obtained for the specimens manufactured at T_{bp} of 286 °C. The specimens produced in X orientation with T_{bp} of 286 °C presented almost the same roughness as the specimens built in Y orientation but at a

lower T_{bp} of 265 °C. The side walls also showed an increase in roughness for both T_{bp} . The high standard deviation can be explained by the semi-sintered particles and the potential pores on the surface, which may have triggered overall failure during tensile testing. The overall increase in surface roughness with increasing T_{bp} is possibly associated with the partial-sintering of the particles before the laser scan. A T_{bp} of 286 °C is already on the onset of the melting of PEKK, and temperature fluctuations are observed in the powder bed.

The spectra of Kepstan 6002 PEKK powder was compared with the LS specimens manufactured in X orientation at T_{bp} of 265 °C and 286 °C; they are shown in Fig.7.18. The degree of crystallinity was assessed using WXR and is presented in Fig.7.19.

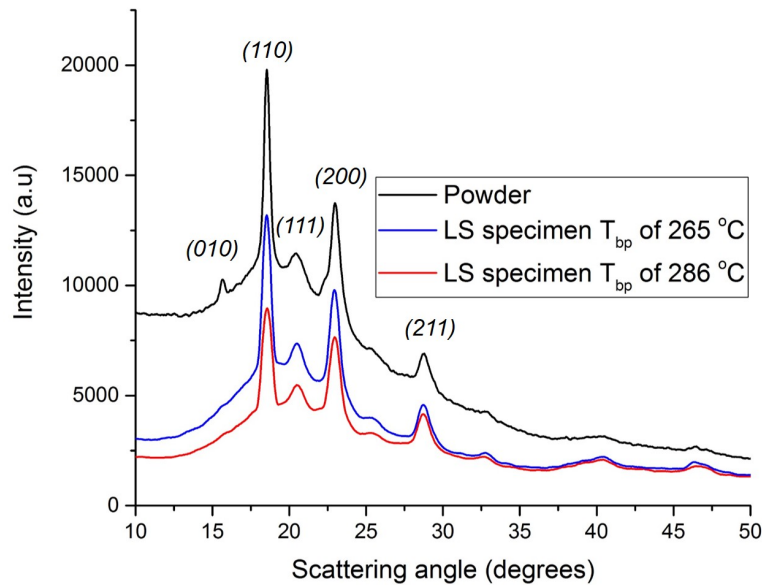


Fig. 7.18 WXR spectra of LS specimens of Kepstan 6002 PEKK manufactured at different T_{bp} and compared with the virgin PEKK powder.

The spectra of both LS specimens are very similar, however different from the powder, in which an additional peak at 15.6° is observed. This peak was previously associated with form II of the orthorhombic unit cell of PEKK [13] but seems to disappear when processed by LS.

The degree of crystallinity seems to have slightly increased with a T_{bp} of 286 °C. This difference, however, is not statistically significant ($P = 0.209$). Therefore, as far as the temperatures are above or within the crystallisation range of PEKK during the LS process, and this process follows the standard cooling methodology, the given time will be sufficient to crystallise PEKK fully. The crystal morphology, however, can vary according to the parameters selected. Thus, the size and morphology of PEKK spherulites were investigated under TEM analysis. The specimens taken to TEM were manufactured in X orientation. Images with different magnifications are shown in Fig.7.20(1) for T_{bp} of 265 °C and Fig.7.20(2) for T_{bp} of 286 °C.

The average diameter of the spherulites exposed to T_{bp} of 265 °C varies from 2.8 to 5.8 μm , whilst at T_{bp} of 286 °C their average diameter increases to between 3.7 and 7.5 μm .

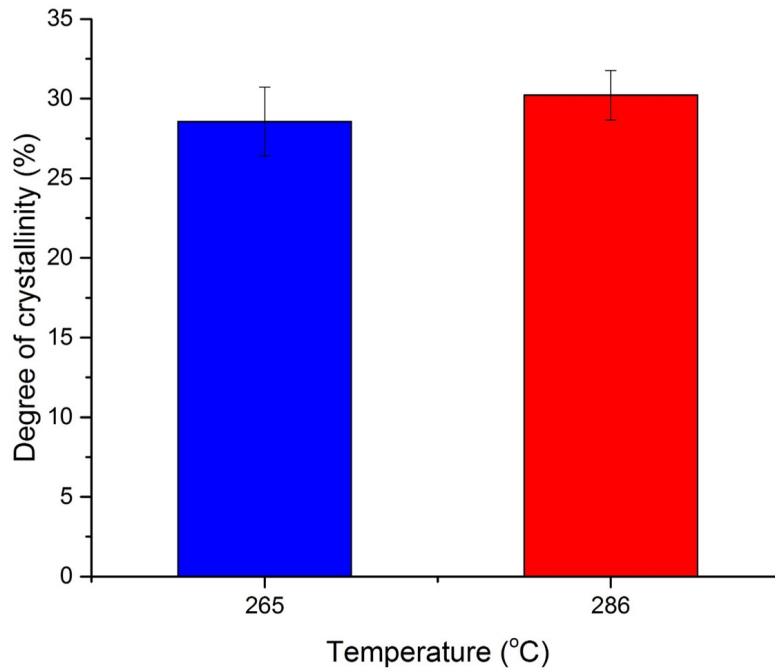


Fig. 7.19 The average degree of crystallinity obtained with WXRd for specimens manufactured in X orientation at different T_{bp} .

These findings are in agreement with the theory of crystallisation, in which more nuclei are stabilised at temperatures near the maximum rate of crystallisation. Therefore, less space is left for growth as they collide with each other. On the other hand, fewer nuclei are stable at higher temperatures (T_{bp} of 286 °C), the chains are freer to move, and the spherulites achieve a larger diameter [50]. The larger diameter of the spherulites leads to an earlier mechanical failure due to less disruption for crack propagation. This phenomenon supports the values of mechanical strength presented in this section.

The increase of T_{bp} does improve the consolidation of LS parts but decrease overall mechanical performance. By applying temperatures near the melt of PEKK, semi-sintered particles adhere to the surface of the specimens creating a rougher topology from which failure starts. This justifies the significantly lower mechanical strength obtained with T_{bp} of 286 °C when compared to 265 °C. The increase in temperature increases the size of the spherulites, which can, therefore, compromise mechanical performance. These findings highlight the need for polishing the surface of LS specimens, which, unlike IM surfaces, are still quite rough for multiple applications. Furthermore, powder recyclability must be considered as different processing temperatures may change powder behaviour; this will be explored in Chapter 10.

7.5 Effect of Multiple Laser Exposures

A few studies identified the application of multiple laser exposures as a solution to improve the consolidation and mechanical performance of LS parts [274, 310]. Laumer et al. [246] studied the absorption of CO₂ laser wavelength ($\lambda = 10.6 \mu\text{m}$) by PA12 and

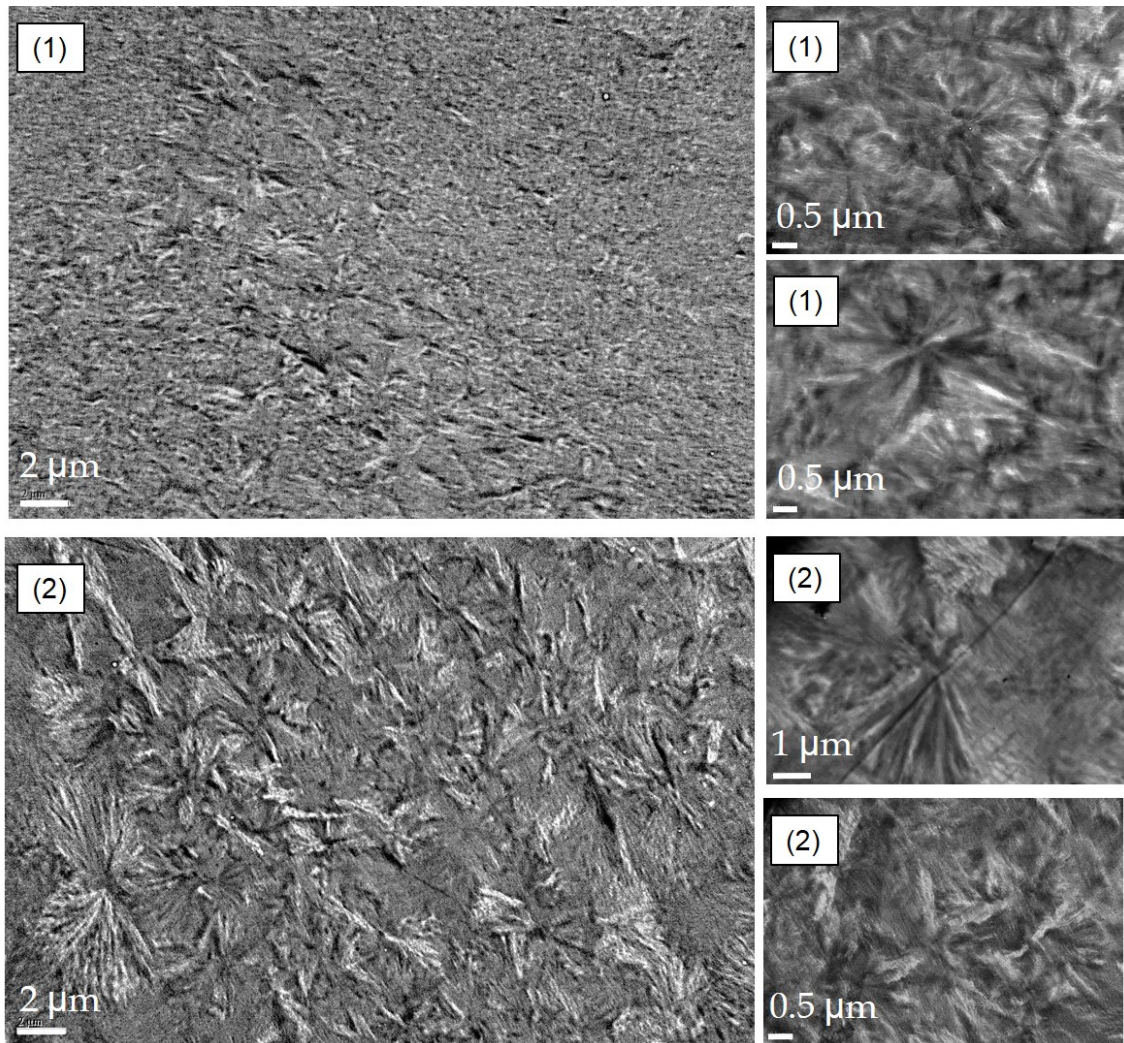


Fig. 7.20 TEM images of LS specimens manufactured at T_{bp} of (1) 265 °C and (2) 286 °C at different magnifications, as shown by the scale bars. The spherulites obtained at T_{bp} of 265 °C are overall smaller and vary between 2.8 and 5.8 μm in diameter, whilst the spherulites resulting from a T_{bp} of 286 °C are larger and vary between 3.7 and 7.5 μm in diameter.

polyethylene polymers, and found a striking increase in the absorption for the powder in comparison to the solid material. The authors explained that the light is transmitted multiple times in a layer of powder. The transmitted light is absorbed by other particles successively, resulting in increased power absorption. Such a phenomenon does not occur for the fully solid material.

Considering this difference in absorption, and knowing that low P_L is insufficient to melt the powder into an entirely solid structure, this study aims to explore the effect of multiple laser exposures of different P_L on the properties of LS PEKK. The slow crystallisation kinetics of PEKK in combination with the multiple laser exposures can potentially contribute to achieving improved final properties, as a successive application of power could take place before complete solidification. The properties investigated in this study concern tensile strength, elongation at break, and surface topology.

The mechanical properties were assessed by producing PEKK specimens under ISO 527-2-1BA guidelines; surface topology was measured on films of 10 sintered layers and $50 \times 20 \text{ mm}^2$. The films were produced with the laser power of the intermediate steps to investigate multiple laser exposures thoroughly. As an example, films exposed firstly to 4 W and then 8 W were assessed by building two sets of films, the first using 4 W and the second using (4+8) W of P_L . For the case of tensile specimens, only the final step, e.g., (4+8) W, was produced.

In addition to double laser exposures, two combinations of three laser exposures were evaluated. Table 7.6 summarises the combinations of tested powers, and the scanning strategies applied. For all these combinations, a scan speed of 2550 mm s^{-1} and a scan spacing of 0.2 mm were used according to described in Section 7.2.1.

Table 7.6 Design of experiment showing different laser power combinations used to study the effect of multiple laser exposures.

		First exposure					
		Power (W)	3	4	6	8	12
Second exposure	0			X	X		X
	3		X				
	4					X	
	6				X		
	8			X			
	9		X				
+ Third exposure	3 + 3				X		
	3 + 6		X				

Table 7.7 shows the average mechanical strength for each combination of laser exposures. As shown in Fig.7.4, optimum tensile strength is achieved at ED of 23.53 mJ mm^{-2} and 12 W of P_L . These laser parameters are taken forward in this section and compared with multiple laser exposures to investigate whether properties can be further improved. The strength of the specimens produced with different combinations of double exposure is always above 80 MPa, but below the resulting mechanical strength of one exposure at 12 W of P_L . For three exposures, strength was further reduced by maintaining the energy density the same as one exposure of 12 W ($\sim 23.5 \text{ mJ mm}^{-2}$).

Elongation at break was also assessed; Table 7.8 presents the results. The elongation at break remains very similar, if not the same, with two exposures than what achieved with one exposure at 12 W of P_L . Fig.7.21 compares tensile strength and elongation at break for different scan strategies. The standard deviation of the elongation at break overlaps the potential difference between the scan strategies. This overlapping is true for most of the cases, except for the triple exposure with (6 + 3 + 3) W. The trend of mechanical strength seems to decrease with three exposures, whilst elongation seems to follow a plateau except

Table 7.7 Average mechanical strength of specimens produced with different laser powers and laser exposure strategies.

		Tensile strength (MPa)				
		1 st exposure				
	Power (W)	3	4	6	8	12
2 nd exposure	0					91 ± 2.9
	3					
	4				83 ± 2.8	
	6			83 ± 5.1		
	8		83 ± 5.6			
	9	86 ± 2.7				
+ 3 rd exposure	3 + 3			67 ± 6.2		
	3 + 6	78 ± 7.4				

for (6 + 3 + 3) W. Zarringhalam [276] studied the effect of multiple laser exposures in the crystallinity of PA12, which was then associated with part strength and elongation at break. He found higher elongation for parts produced using double exposure, which was correlated with the lower degree of crystallinity. In the case of Kepstan 6002 PEKK, the insignificant differences in the elongation at break achieved with multiple laser exposures can be attributed to the slow kinetics of crystallisation [27], in which the time between exposures is insufficient to change the final degree of crystallinity.

The SEM images of the films produced with two exposures are shown in Fig.7.22. The images infer that low laser power in the first laser exposure cannot fully sinter the particles into a solid structure; therefore, porosity remains, as shown in Fig.7.22(1). By the time of the second laser scan, the part is already solidified, and the structure can be hard to disrupt. The different patterns observed on the surface of the film from Fig.7.22(3b) can be associated with shrinkage from the first exposure taking place at the same time as the second melt exposure.

The experiments with three laser exposures have a laser power of 3 W or 6 W in the first scan, which creates a primarily porous structure. The semi-sintered layer solidifies before the next exposure and can disrupt further melting. This structure is particularly visible for the strategy using (3 + 3 + 6) W of laser power.

The surface topology of the films presented in the SEM analysis was investigated in terms of the arithmetical mean height of a line (R_a). The results are presented in Table 7.9. For most of the scan strategies, the application of two exposures maintains the surface roughness obtained with one exposure. As a general statement, it seems that the last exposure is dominant over surface topology. Three scans do not seem to improve surface topology; this is supported by the SEM images (Fig.7.23) and the R_a values achieved with (6 + 3 + 3) W films.

Table 7.8 Average elongation at break of specimens produced with different laser powers and laser exposure strategies.

		Elongation at break (%)				
		1 st exposure				
Power (W)		3	4	6	8	12
2 nd exposure	0					2.6 ± 0.2
	3					
	4				2.4 ± 0.1	
	6			2.3 ± 0.2		
	8		2.4 ± 0.3			
	9	2.5 ± 0.2				
+ 3 rd exposure	3 + 3			1.7 ± 0.4		
	3 + 6	2.2 ± 0.3				

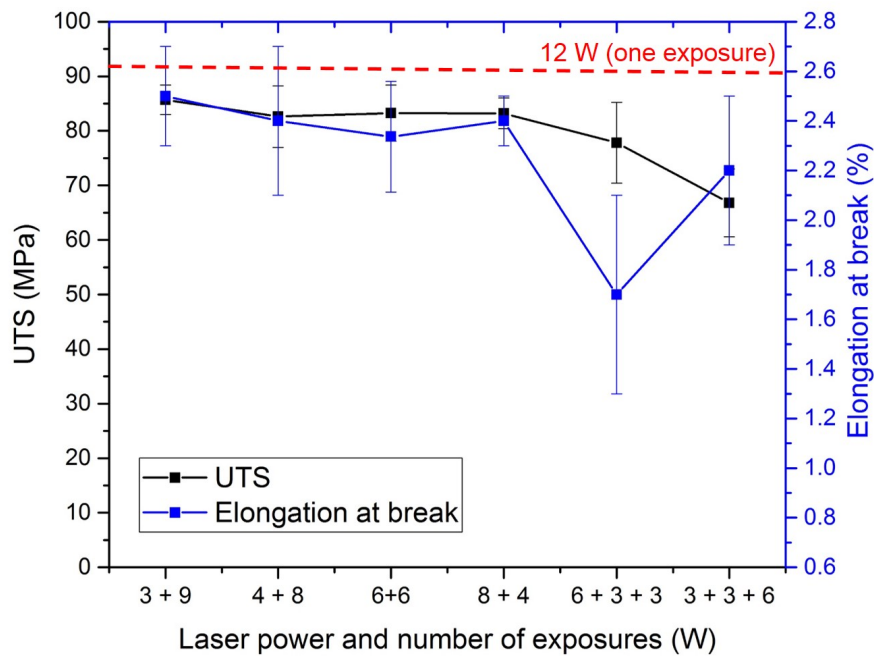


Fig. 7.21 Relation between scan strategy, tensile strength, and elongation at break of PEKK specimens produced with different ED and laser exposures.

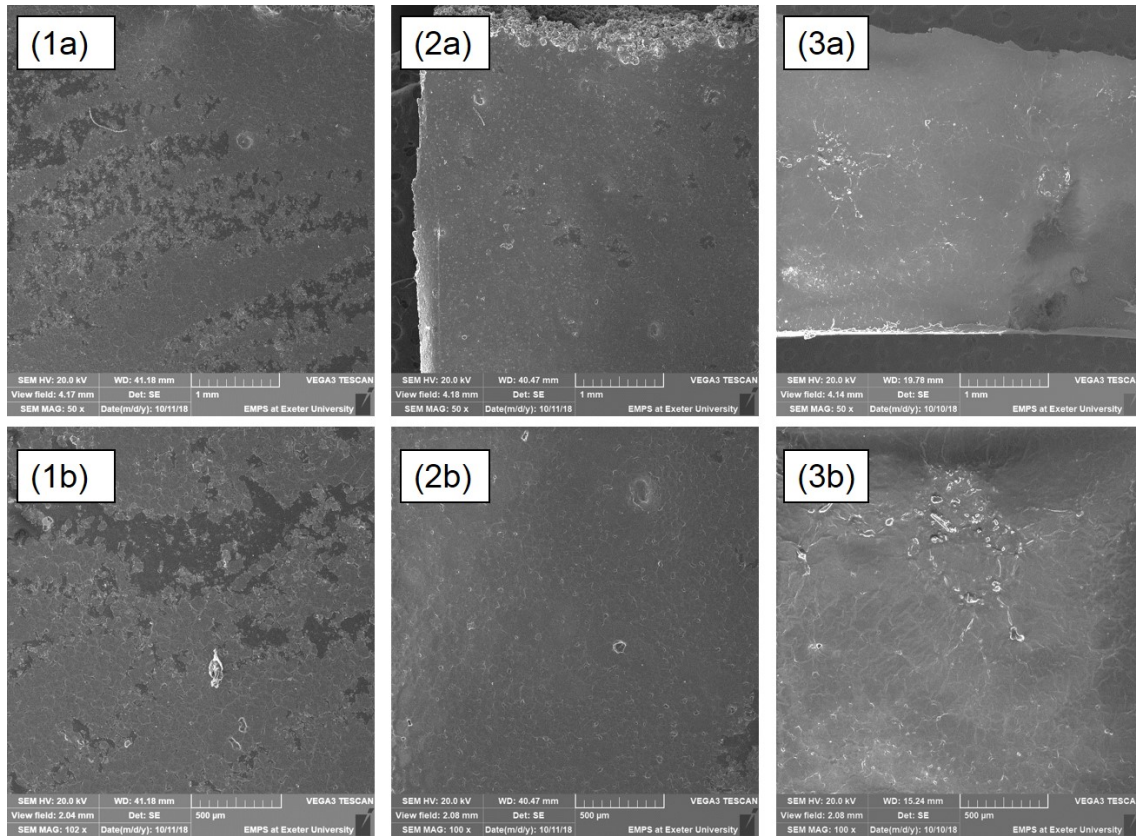


Fig. 7.22 SEM images of films produced with double laser exposure and the same ED (23.5 mJ mm^{-2}). (1) 3 + 9 W, (2) 4 + 8 W and (3) 8 + 4 W. Note the different scale bars of (a) 1 mm and (b) $500 \mu\text{m}$.

Table 7.9 Average R_a values of films produced with different laser powers and laser exposure strategies.

		Arithmetical mean height of a line (R_a) (μm)				
		1 st exposure				
Power (W)		3	4	6	8	12
2 nd exposure	0	23 ± 11.9	19 ± 6.1	8 ± 2.9	10 ± 2.1	6 ± 1.1
	3	23 ± 17.8		8 ± 1.4		
	4				6 ± 2	
	6					
	8		6 ± 1.4			
+ 3 rd exposure	9	6 ± 1.0				
	3 + 3			8 ± 1.1		
	3 + 6	7 ± 0.8				

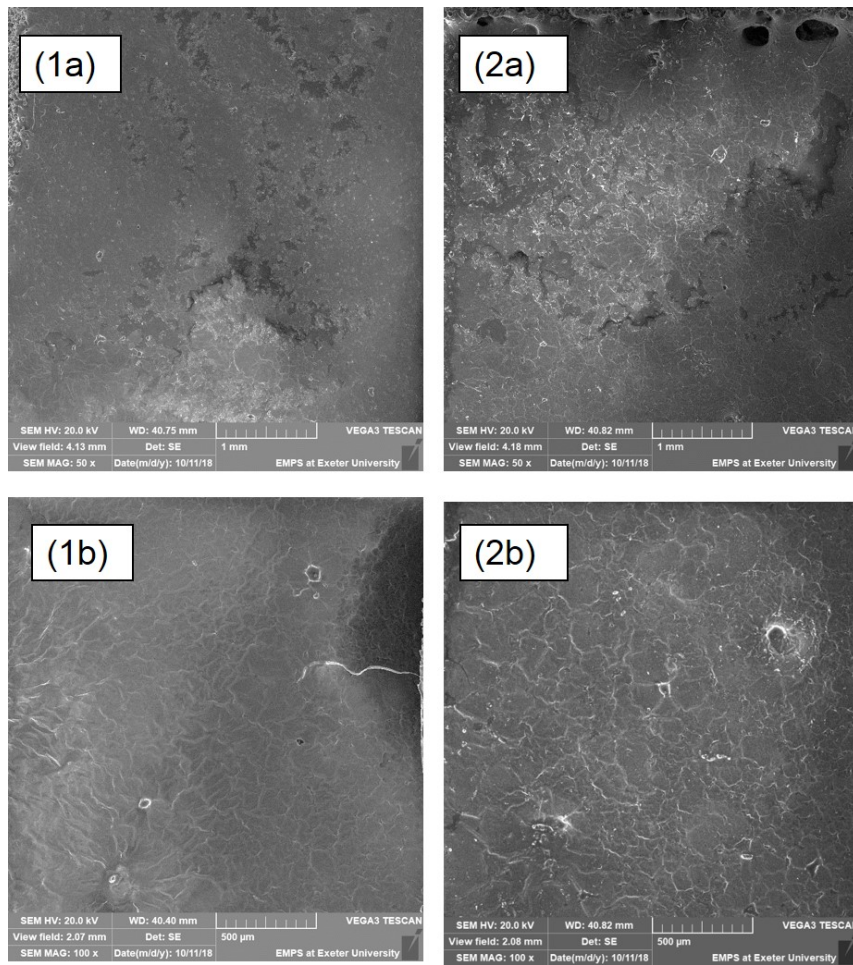


Fig. 7.23 SEM images of films produced with three laser exposures and the same ED (23.5 mJ mm^{-2}). (1) 3 + 3 + 6 W and (2) 6 + 3 + 3 W. Note the different scale bars of (a) 1 mm and (b) $500 \mu\text{m}$.

Surface topology was plotted against tensile strength and scan strategy in Fig.7.24. There is a clear inverse correlation of almost -0.9 between tensile strength and R_a values. As observed in Table 7.7 and Fig.7.23, triple exposure does not improve mechanical performance or surface quality. The poor results achieved with three laser scans are possibly caused by partial sintering, which leads to internal porosity, but can be a result of combining different levels of shrinkage in each exposure. The application of two exposures slightly decreases mechanical strength but does not affect surface topology or elongation. Different orders of power applications slightly change surface quality, but most of the time, the standard deviation is overlapped.

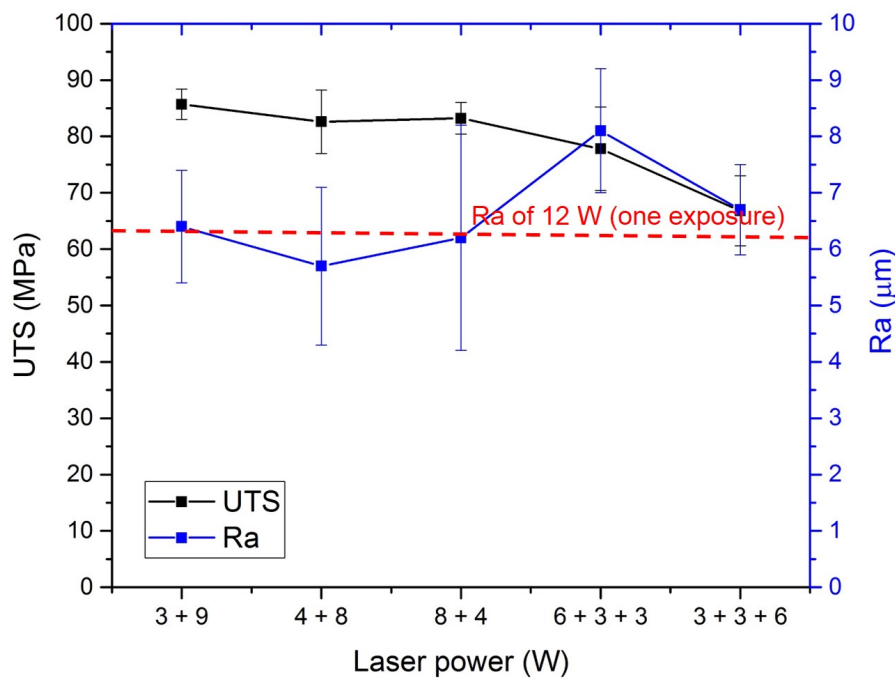


Fig. 7.24 Relation between scan strategy, tensile strength, and surface topology of PEKK specimens produced with different ED and laser exposures.

Wegner and Witt [274] mentioned that the application of two laser exposures reduces temperature gradients during the manufacturing of EOS PA2200 parts using a Formiga P100 system. In the case of high-temperature systems, such as the EOS P800, the temperature gradient does not seem to act differently for a different number of exposures. However, it is important to highlight the high T_{bed} used in this study, which is very close to the T_m of PEKK, and part orientation, as all the specimens were produced in the X direction. Soe et al. [310] achieved a remarkable increase in tensile strength and elongation at break of Duraform Flex exposed to four scans if compared to a single exposure. As opposed to the results shown with PEKK in this section, the scanning strategy selected consisted of applying the same laser power in all exposures [258] rather than maintaining the balanced ED as in this study. The high ED would likely degrade PEKK instead of improving mechanical properties. Therefore, a successful optimisation of part properties is highly dependent on material properties.

7.6 Conclusions

This chapter presented the first results of optimising Kepstan 6002 PEKK (HL1327 grade) for LS. The optimisation consisted of varying laser parameters, building orientation, processing temperatures, and the number of laser exposures. The optimisation was assessed regarding mechanical performance, internal porosity, surface topology, fracture analysis, and crystallisation. The following conclusions were drawn from this chapter:

1. Different combinations of laser power and scanning speed lead to different mechanical performance despite maintaining the same ED . Such difference, however, is significantly lower than when varying ED ;
2. The best performance of PEKK specimens is obtained with 12 W of laser power, 2550 mm s⁻¹ of scan speed, 0.2 mm of scan spacing ($ED \sim 23.5$ mJ mm⁻²), T_{bed} of 292 °C and T_{bp} of 265 °C;
3. The orientation of manufacturing has a crucial effect in the final performance, and specimens manufactured with T_{bp} of 265 °C and in Z orientation showed half of the UTS obtained with the specimens manufactured in X orientation and same T_{bp} . The order of performance according to orientation is X>Y>Z;
4. PEKK is extremely resistant to shattering failure under compression and can deform up to 70% regardless of the orientation of manufacturing;
5. Ductile zones in the fracture can be associated with higher elongation at break and higher UTS. These zones work as a stress relieve regions and can hold the structure together for longer periods of intense stress;
6. Porosity is concentrated in the interlayer area [274], therefore the more layers in a specimen, the higher the chances for poorer mechanical strength and elongation. However, this is not applicable if particle coalescence is fully achieved, e.g., selecting a T_{bp} of 286 °C;
7. Side walls present a significantly higher surface roughness than the roughness obtained on the top surface, and can lead to failure starting from the surface;
8. The increase of T_{bp} to 286 °C improves consolidation but significantly reduces mechanical performance and surface smoothness. Such results can be explained by partial-sintering occurring before the laser exposure, caused by temperature fluctuations during manufacturing and the high T_{bp} of 286 °C, which matches the onset of the melt of PEKK;
9. The increase of T_{bp} to 286 °C leads to an increase in the average diameter of the spherulites;
10. The application of ED in two steps (double laser exposure) reduces mechanical strength but does not compromise elongation at break or surface roughness;

11. Three laser exposures neither improves mechanical properties nor surface topology.

Chapter 8

Shrinkage Behaviour of PEKK in High-Temperature Laser Sintering

8.1 Summary

Shrinkage is extensively mentioned in the literature as one of the leading causes of dimensional instability or poor performance in LS. This chapter proposes and examines a methodology to describe shrinkage in cooling from a material perspective. The methodology was applied to Kepstan 6002 PEKK and compared with Orgasol PA12, a widespread LS grade. Thermal behaviour and crystallisation effects were measured to determine the influence of powder structure and density on overall LS shrinkage.

The shrinkage parameter associated with powder bulk properties has the most significant impact in PEKK, contributing to 57% of the total shrinkage observed in cooling for this material. This shrinkage is supported by the low values of bulk density, irregular morphology, and internal porosity observed in PEKK particles. The main cause of shrinkage in PA12 is crystallisation, which corresponds to 60% of the overall shrinkage. When producing parts with simple geometry using LS, PEKK shows an overall shrinkage approximately 30% lower than PA12, which makes it a promising material for part dimension accuracy.

8.2 Shrinkage Factors

In literature, the shrinkage effect is investigated when associated with processing parameters or location/orientation in the LS system [258, 255]. Nevertheless, the intrinsic properties of materials can significantly affect shrinkage. A fully solid semi-crystalline thermoplastic polymer exposed to heating will expand; if the same material is subjected to cooling, retraction is observed. Most of the time, however, semi-crystalline polymers do not come back to their original dimension as they are affected by the kinetics of crystallisation. In LS, the degree of crystallinity after cooling can be higher than before the melt due to the prolonged time of cooling, leading to the rearrangement of the molecules. This behaviour is illustrated in Fig.8.1.

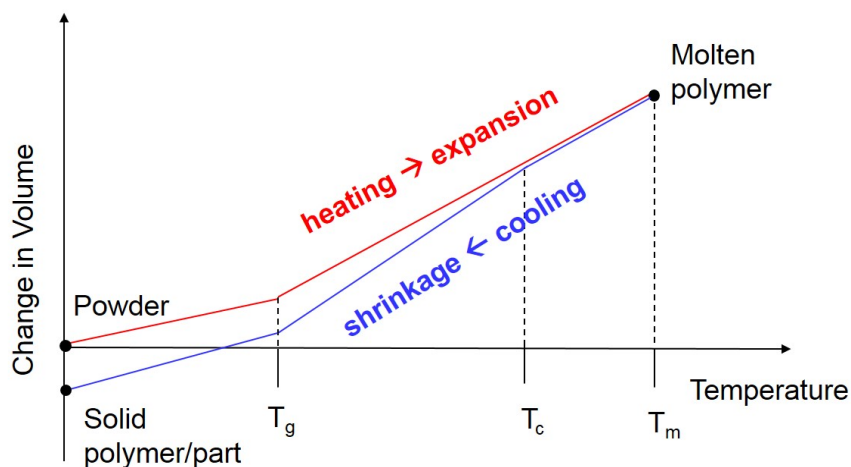


Fig. 8.1 Change in volume of semi-crystalline polymers subjected to heating and cooling.

In addition to the kinetics of crystallisation, particles in the LS bed are not fully compact and present a degree of porosity at room temperature as well as bed temperature. These

voids in the structure lead to a lower expansion during heating and may affect cooling. This chapter attempts to experimentally measure the leading causes of shrinkage occurring from bed temperature in LS, going through melting by applying laser heating, and then cooling down to room temperature. Therefore, the stages in the study concern two phases' transformation: a solid at almost T_m to molten phase, and a molten material to solid at room temperature. The factors taken into account are shown in Eq.(8.1):

$$\beta_{total} = \beta_T + \beta_c + \beta_{powder}, \quad (8.1)$$

in which β_T is the shrinkage caused by thermal retraction, β_c corresponds to the shrinkage due to crystallisation and β_{powder} is the shrinkage resulting from powder bulk and particle characteristics at T_{bed} .

This equation aims to measure the effect of powder bulk in overall shrinkage during cooling. β_T is an intrinsic property of the material and is attributed to the retraction observed with changes in temperature. This parameter was assessed using DMA equipment (Section 3.3.7) operating in compression mode. β_c was measured using a TMA equipment (Section 3.3.8) in dilatometry mode and evaluating the changes in dimension within the material crystallisation range. Finally, β_{total} was calculated by producing LS specimens and measuring their dimension; this is described in Section 8.2.1. Knowing the impact of each of these variables in the overall shrinkage helps to understand the behaviour of PEKK in the LS process, but also enables optimising mechanical properties and dimensional accuracy.

The influence of intrinsic material properties during cooling in LS was analysed by studying elementary geometries. Following the same logic, one combination of laser parameters and temperatures was selected for each material to avoid other variables in the system. The temperature fluctuations in the system were addressed by distributing the parts at various locations within the powder bed.

8.2.1 Measuring shrinkage in laser sintering: β_{total}

Two different systems were used to produce LS specimens. Kepstan 6002 PEKK was processed in an EOSINT P800 HT-LS system [234], whereas Orgasol PA12 specimens were manufactured using an EOS Formiga P100 system [311]. The parameters selected for each are found in Table 8.1.

The effect of anisotropy extensively reported in the literature [258, 312, 255, 313] was accounted for by producing parallelepipeds of different heights. The dimensions chosen for X and Y are of 10 mm each, whilst the height in Z orientation varied from 10 mm to 100 mm in a 10 mm interval. Two parallelepipeds were produced for each height, one located in the central part of the building area, and the other closer to the corners to account for potential temperature differences. A total of 20 parallelepipeds were manufactured for each material, Kepstan 6002 PEKK, and Orgasol PA12.

All samples were produced using the standard parameters available in Table 8.1 and standard cooling process as recommended by the equipment manufacturer. The paral-

Table 8.1 Laser sintering parameters for PEKK and PA12.

Parameters	Grade	
	Kepstan 6002 PEKK	Orgasol PA12
Laser power	12 W	21 W
Scan spacing	0.2 mm	0.2 mm
Scan speed	2550 mms ⁻¹	2500 mms ⁻¹
Energy density	23.5 mJmm ⁻²	42 mJmm ⁻²
Layer thickness	120 μ m	100 μ m
Part bed temperature	292 °C	168 °C
Building platform temperature	265 °C	152 °C

lelepipeds were then removed from the build, and their dimensions were measured and compared with the design size of the .STL file.

8.3 Results and Discussions

8.3.1 Shrinkage in laser sintering: β_{total}

The average shrinkage varying with the height of the parallelepiped (Z orientation) was plotted for Kepstan 6002 PEKK and Orgasol PA12 in Fig.8.2.

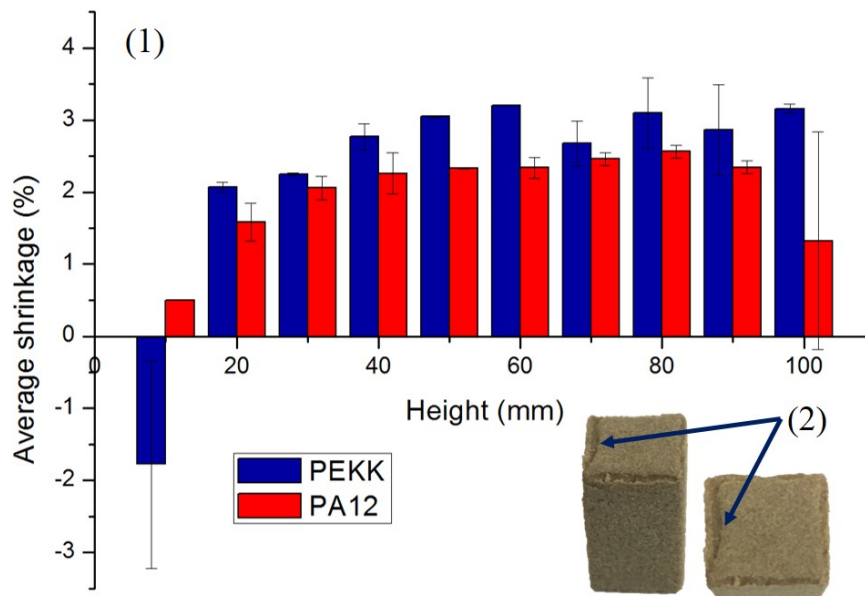


Fig. 8.2 (1) Shrinkage in Z orientation for PEKK and PA12 parallelepipeds; (2) downskin and upskin effect observed in the PEKK parts.

Kepstan 6002 PEKK parallelepipeds show a plateau from 50 mm height, in which shrinkage is approximately 3%. Several factors may be contributing to this, such as crystallisation, thermal contraction, and powder characteristics, e.g., particle size and shape. Parallelepipeds with lower heights, however, have a significantly lower shrinkage, and at 10 mm height, an expansion of 2.8% is obtained during cooling. Such difference might be due to the layer-by-layer nature of the LS process, but especially the downskin and upskin effect (Fig.8.2(2)), which corresponds to the adhesion of extra layers at the bottom and on the top of the sintered object, respectively, due to the transmission of laser energy beyond the sintered layer of particles (downskin effect) and the adhesion of extra layers resultant from melting of the upper layer (upskin effect) [264–266]. From 50 mm height, however, upskin and downskin effect are stable and can be negligible, remaining thermal contraction, powder characteristics, and crystallisation as the main factors contributing to overall shrinkage.

Most of the Orgasol PA12 parallelepipeds show a shrinkage of around 2% in the Z direction. Such shrinkage is visible from 10 mm but seems to achieve a linear and controllable behaviour at 40 mm, 10 mm before PEKK parallelepipeds. The upskin and downskin effect is less pronounced in Orgasol PA12, as no expansion is observed even at lower heights. Once the plateau is achieved, the shrinkage values in Z orientation are also lower for this grade, 2% against 3% for PEKK.

In addition to Z orientation, shrinkage was monitored in X and Y direction, and a final volumetric shrinkage was computed. This volumetric shrinkage considered the values for all the parallelepipeds in X, Y, and Z heights after achieving a plateau, which is at 50 mm for PEKK and 40 mm for PA12. The results are shown in Table 8.2.

Table 8.2 Average shrinkage in the laser sintering of PEKK and PA12.

Material	Shrinkage in laser sintering (%)				Volumetric
	X	Y (10 - 100 mm)	Z	Z (50/40 - 100 mm)	
PEKK	1.14 ± 0.12	1.39 ± 0.14	2.34 ± 0.13	3.01 ± 0.15	5.45 ± 0.07
PA12	2.72 ± 0.01	2.85 ± 0.01	1.98 ± 0.3	2.23 ± 0.36	7.6 ± 0.17

The shrinkage seems to be slightly higher in the Y direction than in the X direction for PEKK and PA12 parallelepipeds, but the more significant difference is observed for PEKK. Such differences can be associated with the sintering strategy, powder spread, and arrangement in the bed of EOS P800 systems. The final volumetric shrinkage is higher for PA12; this can be attributed to the intrinsic properties of this material as crystallisation and thermal contraction [19]. In Z direction, however, PEKK seems to shrink more and is possibly associated with the powder structure and the layer-by-layer nature of LS.

8.3.2 Shrinkage due to thermal contraction: β_T

One of the parameters of Eq.(8.1) is β_T ; it consists of the shrinkage caused by temperature change during cooling, not considering phase transformation. This parameter was calculated as described in Section 3.3.7; the coefficient of thermal contraction and the overall shrinkage are presented in Table 8.3.

Table 8.3 Thermal contraction during cooling for PEKK and PA12.

Parameters	Materials	
	Kepstan 6002 PEKK	Orgasol PA12
Coefficient of thermal contraction [$^{\circ}\text{C}^{-1}$]	6.48×10^{-5}	1.2×10^{-4}
Overall thermal shrinkage [%]	0.55 ± 0.02	1.41 ± 0.35

The thermal expansion coefficient of both materials is close in value to literature [12, 19]. The shrinkage of amorphous PEKK is significantly lower than PA12, and the standard deviation of the latter is higher, possibly due to the lower cooling rates. The thermal shrinkage of Kepstan 6002 PEKK corresponds to approximately 10% of the overall shrinkage visible in LS, whilst this value is of 18% for PA12.

8.3.3 Shrinkage due to crystallisation: β_c

Shrinkage due to crystallisation is the parameter measuring the effect of crystal morphology and degree of chain arrangement in shrinkage. Fig.8.3 shows the crystallisation obtained for Kepstan 6002 PEKK at slow (1) and rapid (2) cooling rates described in Table 3.5 (Section 3.3.8). The slow cooling method had a significant decrease in dimension at the crystallisation range of PEKK, with an average of 1.77% shrinkage after three repeats. The repeat measurements vary due to several factors: sample preparation, level of porosity within the sample at the end of the experiment, and slight variations in cooling rate. Regarding the rapid cooling method (Fig.8.3(2)), the change in dimension is negligible - Kepstan 6002 PEKK is usually amorphous when cooled at rates above $2^{\circ}\text{C min}^{-1}$ (see Section 6.2). The insignificant shrinkage is supported by the amorphous behaviour of this material when processed by conventional techniques, e.g., extrusion calendaring, thermoforming, or IM. PA12, on the other hand, crystallises quickly even at high cooling rates and when processed by other manufacturing techniques.

Table 8.4 shows the average shrinkage measured for Kepstan 6002 PEKK using the slow cooling method and the data achieved by Verbelen et al. [142] for Orgasol PA12. In the case of Orgasol PA12, the experiment was slightly adapted to compensate for the high flowability of PA12 [314]. Kepstan 6002 PEKK, on the other hand, is a highly self-supported polymer which flows significantly less when subjected to melt.

The measures match the expected crystalline behaviour of PEKK and PA12. The degree of crystallinity of PA12 is usually higher than PEKK, suggesting a higher degree of

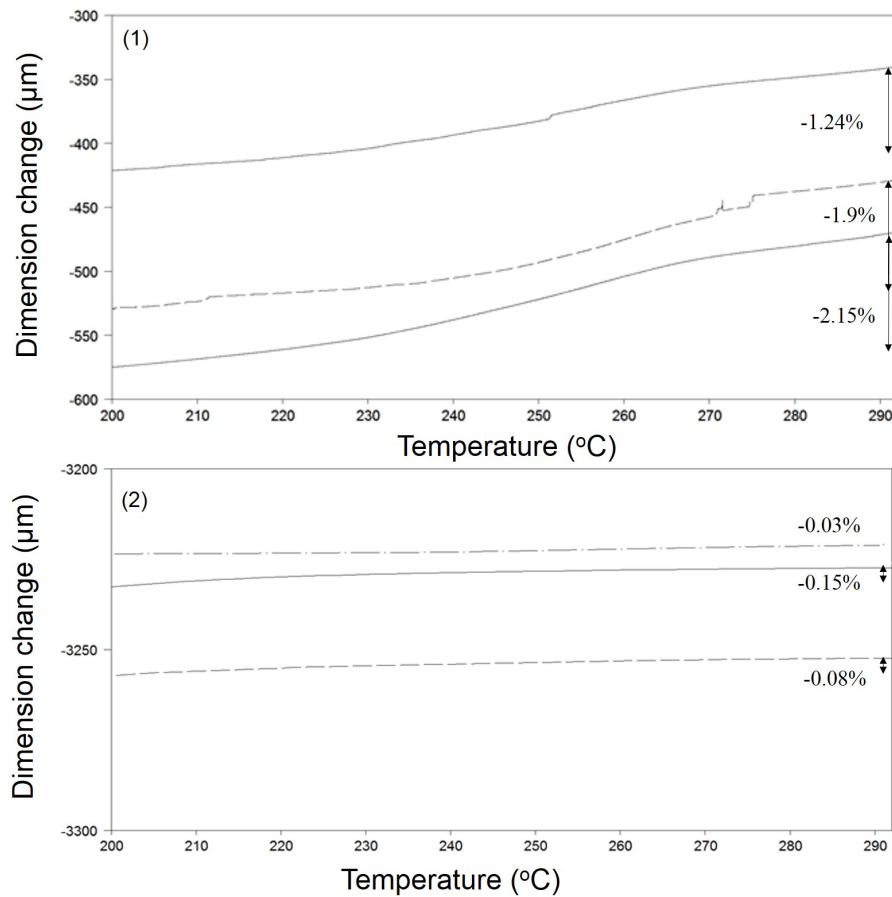


Fig. 8.3 Dimension change due to crystallisation of Kepstan 6002 PEKK at (1) slow cooling rate and (2) rapid cooling rate.

Table 8.4 Shrinkage due to crystallisation of Kepstan 6002 PEKK and Orgasol PA12 [142].

Parameter	Materials	
	Kepstan 6002 PEKK	Orgasol PA12
Overall shrinkage due to crystallisation [%]	1.77 ± 0.5	$4.6^{[142]}$

shrinkage at cooling from melting. Furthermore, the γ phase of PA12 presents a hexagonal structure whereof the packing factor is higher than the crystal structure of PEKKs.

Describing cooling in LS remains a challenge as it is not uniform and occurs at different stages: during manufacturing, after manufacturing until it reaches T_g and below T_g . This methodology, however, considers this issue by choosing similar cooling rates achieved during the crystallisation of PEKK. Such cooling is high enough to prevent PEKK flowability affecting the data on crystallisation but is still within the limit of the TMA equipment.

8.3.4 Calculation of powder bulk effect: β_{powder}

The experimental data measured for all the parameters of Eq.(8.1) were presented except for shrinkage due to powder bulk. This parameter describes the effect of powder

compaction in shrinkage during cooling and is a combination of particle size, distribution, morphology, degree of porosity, and arrangement on the powder bed. Indeed, particles have a very complex effect in LS, and several studies attempted to assess this effect [315, 114, 4]; most of them considered the same behaviour for particles at room temperature and at T_{bed} , which corresponds to the processing temperature. This chapter takes a top-bottom approach to measure the effect of powder bulk in LS shrinkage from the processing temperature. By experimentally measuring all the other parameters in Eq.(8.1), shrinkage due to powder bulk can be assessed. This value was calculated for Kepstan 6002 PEKK and Orgasol PA12; the summary of shrinkage values are presented in Table 8.5.

Table 8.5 Shrinkage (%) in Laser Sintering and the effect of powder bulk.

Material	β_{total}	β_c	β_T	β_{powder}
Kepstan 6002 PEKK	5.45	1.77	0.55	3.13
Orgasol PA12	7.6	4.6	1.41	1.59

The effect of shrinkage due to powder bulk is almost twice larger for Kepstan 6002 PEKK than for Orgasol PA12; this shrinkage is equivalent to almost 58% of the overall LS shrinkage during cooling of PEKK, whilst it corresponds to 21% of the overall shrinkage of Orgasol PA12. Such values are supported by the lower CBD of PEKK (0.36 g ml^{-1}) in comparison to PA12 (0.54 g ml^{-1}), as shown in Table 4.2 of Section 4.3.1, and the rough and porous powder structure of this material when compared to PA12 powder (Figs. 4.1 and 4.4, in Section 4.2.1).

Powder characteristics are extensively associated with powder flow and final part consolidation [98], but few studies attempted to relate dimensional accuracy of LS parts [99] with powder structure. The results presented in this chapter show that the intrinsic properties of particles also affect overall shrinkage, but this can be mitigated using rounder and solid particles with appropriate particle size distribution for LS.

8.4 Conclusions

In this chapter, a methodology was proposed to measure shrinkage due to material properties during cooling in LS. The method was experimentally applied to Kepstan 6002 PEKK and compared with Orgasol PA12; both grades are commercially available and are supplied by Arkema. With the measured parameters, shrinkage due to bulk density was assessed for each grade.

The impact of each shrinkage factor is different according to material and powder properties. Whilst crystallisation has the most significant impact in PA12 overall shrinkage during cooling, this parameter contributes to 32% of the overall shrinkage of PEKK. Previous literature highlights crystallisation as a factor preventing good dimensional

accuracy in final polymeric parts; hence, a lower degree of crystallinity would lead to less warpage and better dimension control.

Most of the shrinkage found in PEKK (~57%) was attributed to powder bulk, a parameter associated with powder structure - porosity, morphology, size, and distribution. For Orgasol PA12, such a parameter contributes to 21% of the overall shrinkage. These values are supported by SEM images, PSD, and CBD results provided in Chapter 4. This effect is also visible in the LS system: the shrinkage in the Z direction is larger for PEKK than for PA12, whilst in X and Y direction such values are more significant for PA12.

Kepstan 6002 PEKK is a promising candidate material for HT-LS, showing 30% less shrinkage than Orgasol PA12. These values can be further optimised by improving powder structure, such as shape and density. The results show the importance of powder properties not only for flowability and part density/consolidation but also for controlling shrinkage during cooling.

Chapter 9

Crystallisation, Mechanical Performance and Cooling Time of PEKK in LS

9.1 Summary

The LS process offers multiple advantages as enabling the production of complex geometries, integrating parts, and reducing cost. However, the nature of the process often leads to brittle parts with a low elongation at break. So far, the elongation achieved with the optimised process parameters of PEKK in this thesis is still below 3%. This chapter attempts to improve this brittle behaviour by developing a novel method using LS. A relationship between cooling time, mechanical properties, and crystallisation was developed to understand and therefore improve the properties of LS PEKK. The microstructure of PEKK subjected to different cooling times was investigated to support the effect material-process, and the kinetics of crystallisation curve of the LS process was developed for this material.

The structure of this chapter is shown in Fig.9.1. Specimens were manufactured in an HT-LS EOS P 800 system (Section 2.5.1) with slightly different temperature settings than previously processed PEKK. The mechanical performance was assessed using tensile testing (Section 3.3.11), and the fracture was investigated under SEM (Section 3.3.1). Regarding crystallisation, WXR (Section 3.3.9) and DSC (Section 3.3.6) were employed. The analysis of PEKK morphology included TEM (Section 3.3.10), and WXR (Section 3.3.9) analysis.

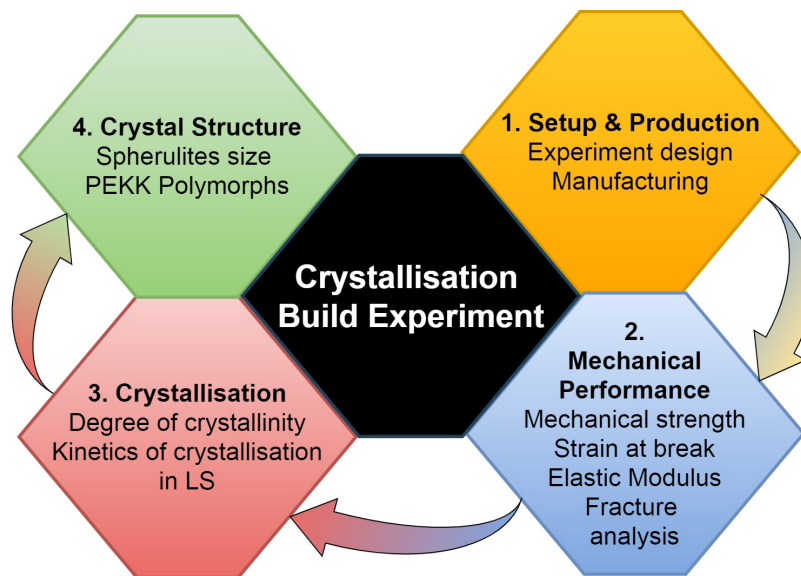


Fig. 9.1 Illustration of the topics discussed in Chapter 9.

The laser sintering process comprises pre-heating, manufacturing and cooling stages. By reducing the standard cooling time in LS, usually above 11 h, to 1 h of cooling, the elongation at break can be significantly increased to a maximum of 14% (more information regarding cooling in LS is available in Section 9.2). This value is a striking result never obtained for PAEKs in LS before. A calibration curve was successfully developed and can be used to correlate PEKK structure and mechanical properties to cooling conditions in LS according to the application. This study also showed that there is a discrepancy

in the kinetics of crystallisation of isothermally crystallised DSC samples of PEKK in comparison to the LS process, the latter being an order of ten times slower.

An investigation into the crystalline structure of LS PEKK reveals significantly less but larger spherulites with the reduction of cooling time, until almost no crystalline structure is found at 0 h of cooling. For the specimens subjected to shorter cooling times, form II could be identified through WXRd analysis. In literature, this form was claimed to be found only in cold crystallised or solvent crystallised samples [13].

The methodology developed in this chapter can be applied to select and/or optimise mechanical properties of other LS polymers sharing similar kinetics of crystallisation and processing temperatures. This study also suggests that there is enormous potential for a wide range of post-processing heat treatments to be used in AM to tailor the ultimate mechanical properties.

9.2 Cooling in High-Temperature Laser Sintering

Kepstan 6002 PEKK is amorphous when processed by IM, extrusion calendaring, sheet thermoforming, and other conventional techniques. However, the significantly slow cooling rate of LS allows Kepstan 6002 PEKK to crystallise, as observed by the opaque colour of Fig.9.2(4). This change in crystallisation behaviour may affect mechanical performance, density, and other properties of final PEKK parts.

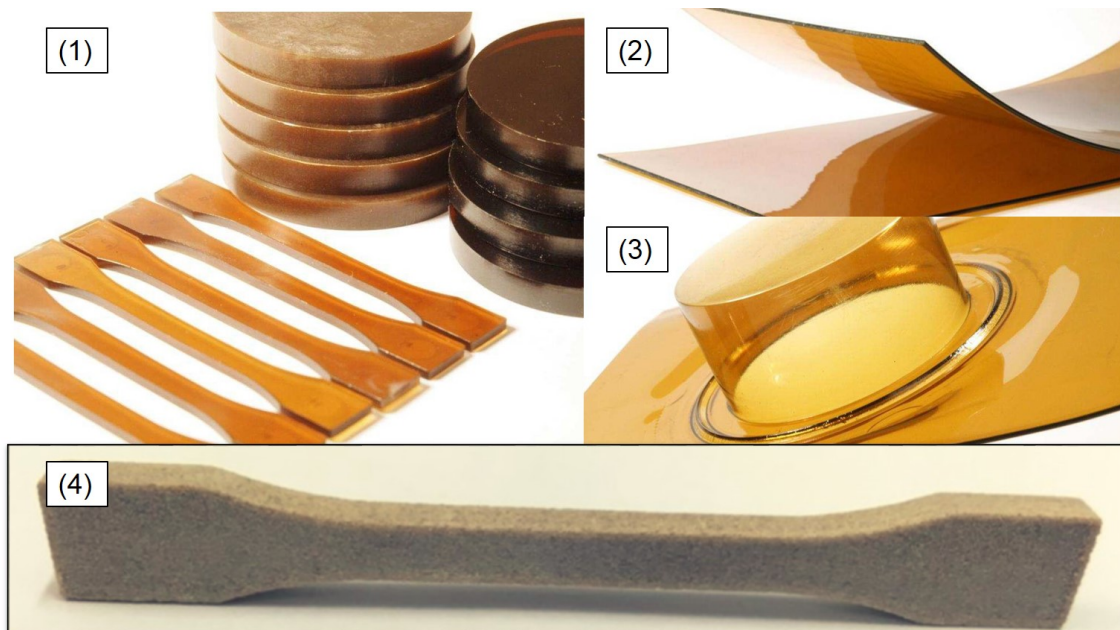


Fig. 9.2 Examples of the amorphous behaviour of Kepstan 6002 PEKK grade when processed by conventional polymer techniques such as (1) injection moulding, (2) extrusion calendaring, and (3) sheet thermoforming. The slow cooling of LS, however, provides enough time for PEKK crystallisation, as shown in (4).

The HT-LS process comprises three main cooling stages, as shown in Fig.9.3. The first stage (1) is in the order of milliseconds and starts from the laser application until the scanned layer reaches the bed temperature, T_{bed} . The second cooling stage (2) takes

place during manufacturing, whilst new parts are being built, and the specimens already sintered and located at the bottom of the build are gradually cooled down. This stage has a more controlled cooling rate determined by T_{bed} and the building platform temperature, T_{bp} , usually 15 to 30 °C below T_{bed} . Finally, the laser sintering is completed, and the build goes through the standard cooling phase (3) set by the system's software according to the volume and distribution of the built parts and the total height of the build in z-direction [178]. In addition to these considerations, the cooling rate in the EOS P 800 changes below T_g as the heatings are switched off.

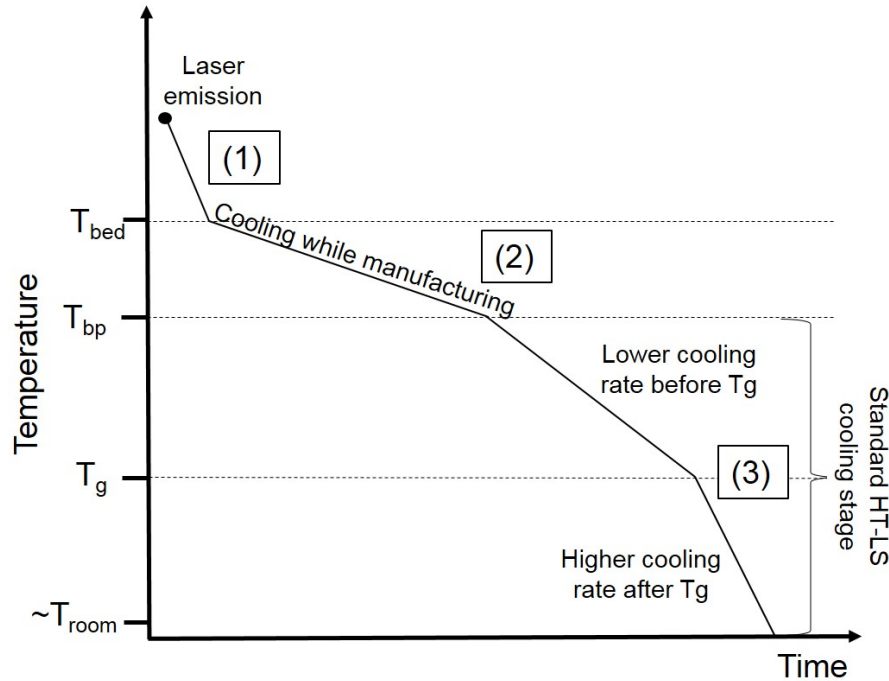


Fig. 9.3 Schematic representation of the cooling profile in an HT-LS system. Once the part production is finished (1-2), the system goes through the standard machine cooling (3), which comprises two cooling stages with different rates.

The first cooling phase is crucial as warping, and part distortion can take place if the powder bed is too cold [290, 4]. If shrinkage is controlled [316], however, cooling during the process determines the final part quality, as it significantly affects consolidation and mechanical performance. The slow cooling in LS should allow time for full particle coalescence and bonding as well as chain rearrangement for crystal formation and growth [185]. To avoid crystallisation at the first stage of cooling and promote full adhesion between layers, materials for LS can be chemically modified to delay solidification by slowing down the kinetics of crystallisation [135]. This is the case of Kepstan 6002 PEKK, which is usually amorphous but crystallises during LS. The relationship between material and process is, therefore, crucial to obtain the desired properties of PEKK processed by LS.

9.3 Build Setup

This experiment was designed to investigate the change in crystallisation of Kepstan 6002 PEKK with cooling time in LS and the effect in the final mechanical properties. A HT EOS P 800 LS system was used in the reduced chamber configuration ($350 \times 230 \times 250 \text{ mm}^3$) as shown in Section 2.5.2.2. From Section 7.2.3, the best mechanical performance of Kepstan 6002 PEKK is achieved when a total energy density of 23.5 mJ mm^{-2} is applied to each layer. Using the first derivative method described by Berretta et al. [152], the ideal T_{bed} for PEKK corresponds to $292 \text{ }^\circ\text{C}$ (see Section 6.2), which is the temperature that guarantees full coalescence, minimum warp, and best mechanical properties [317]. These parameters were applied to all the specimens produced in this experimental setup.

Considering the crystallisation behaviour of PEKK shown in Chapter 6 and aiming to investigate the entire spectrum of crystallisation during manufacture, the T_{bp} selected was of $190 \text{ }^\circ\text{C}$. It is important to note that the temperature distribution across the powder bed of LS systems, especially the EOS P 800, is not uniform, and temperature fluctuations of $\pm 5 \text{ }^\circ\text{C}$ are observed [2].

The build setup consisted of 16 groups of specimens stacked on top of each other in Z orientation. In each group, ten ISO 527-2-1BA specimens were produced in X orientation. These specimens experienced the same cooling time, therefore combined into groups. Each specimen is 4 mm thick. As the layer thickness of P 800 systems is fixed to $120 \text{ }\mu\text{m}$, the total number of layers for one specimen production is ~ 33 . Half of the specimens were produced in the corner of the build and were labelled as *a*; the other half were manufactured in the middle of the build and were labelled as *b*. The time to complete one empty layer by applying 12 s of post-sintering time was monitored and is equal to 35 s. The time to complete one layer full of specimens from the build setup was also monitored and corresponded to 55 s. Therefore, it takes approximately 30 minutes to build each group of specimens. By adding 25 empty layers in between each group of specimens (~ 15 minutes), this adds up to 45 minutes.

The groups were sequentially ordered from the bottom (group 1) to the top (group 16). The build setup took approximately 10.75 h to complete, excluding the pre-heating stage. Fig.9.4 shows the complete build configuration as loaded to be manufactured.

Once the last layer of the sixteenth group of specimens was produced, the process was interrupted as quickly as possible, so no powder was added to the top. Each group was exposed to different cooling times, as shown in Fig.9.5. The build was removed from the system, and quenched in water at approximately $15 \text{ }^\circ\text{C}$. The cake was broken into small parts to help with homogeneous cooling and allow water to penetrate it and interrupt further crystallisation.

The specimens were left cooling in water for approximately 12 hours and then removed, cleaned and sandblasted. Fig.9.6 shows the manufactured specimens after quenching in water. The significant changes in colour are a result of different degrees of crystallinity. Whilst the first groups are light beige, the specimens from group 5 assume a darker beige colour which turns to grey from groups 8/9. Interestingly, the specimens from group 16

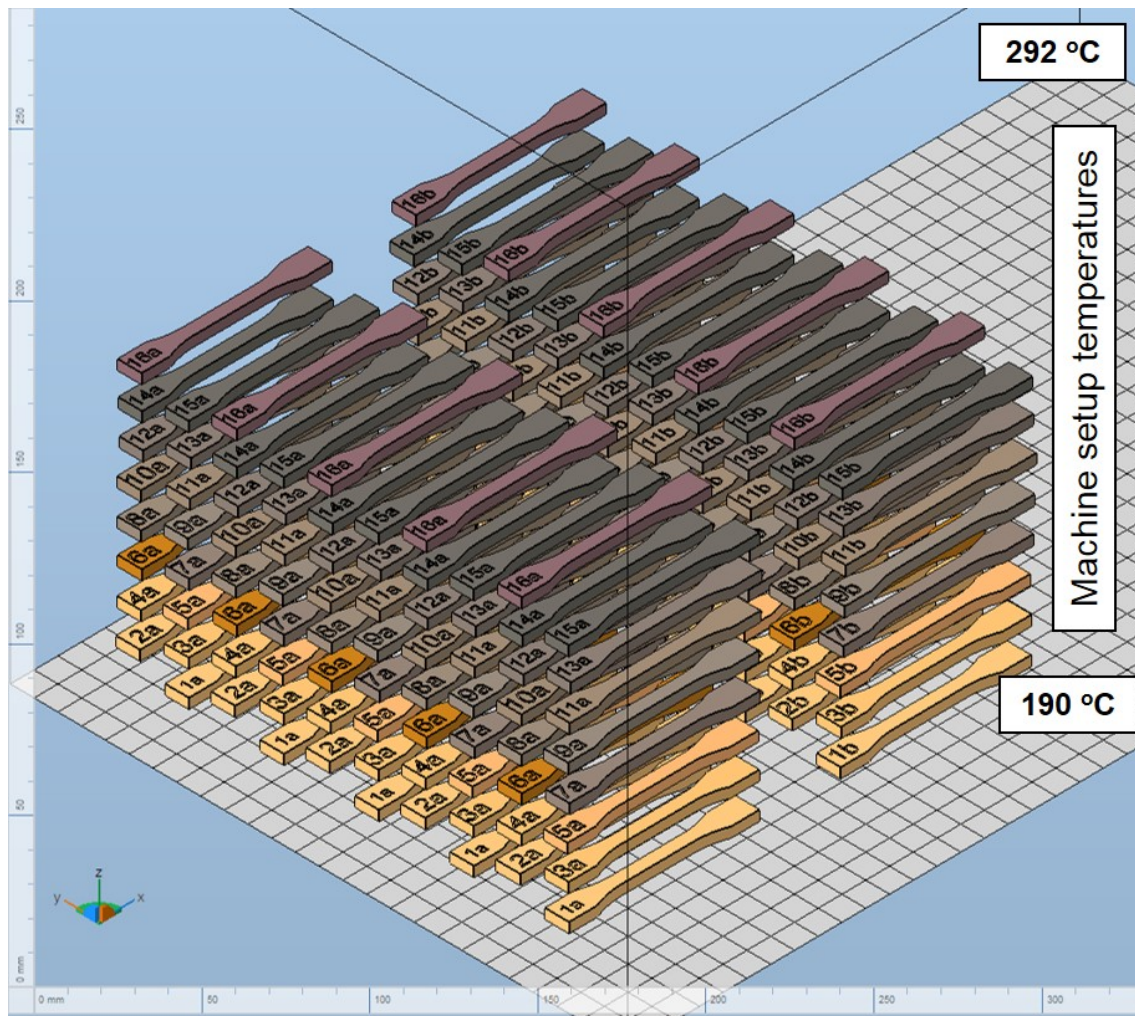


Fig. 9.4 Crystallisation build setup. The temperatures of manufacturing, T_{bed} and T_{bp} , are indicated on the right. Group one was the first to be built, following a sequential order until group 16 is completed. Therefore, the first group was exposed to the longest time of cooling, as opposed to group 16. The colour of the specimens attempted to match their real colours when removed from quenching.

are translucent on the top, but opaque in the bottom. This shade of colours suggests that the upper group is amorphous, but crystallisation begins quickly after; this is illustrated in Fig.9.4 regarding their location in the build across Z orientation. The experiment was repeated twice.

9.4 Results and Discussions

9.4.1 Mechanical performance varying with cooling time

Fig.9.7 presents the average mechanical performance results separated by each group of specimens (1) and by their location in the powder bed, corner (specimens *a*), or middle (specimens *b*) (2).

The majority of the build shows an inverse correlation between mechanical strength and elongation at break, as expected. At extended cooling periods, sufficient time is given

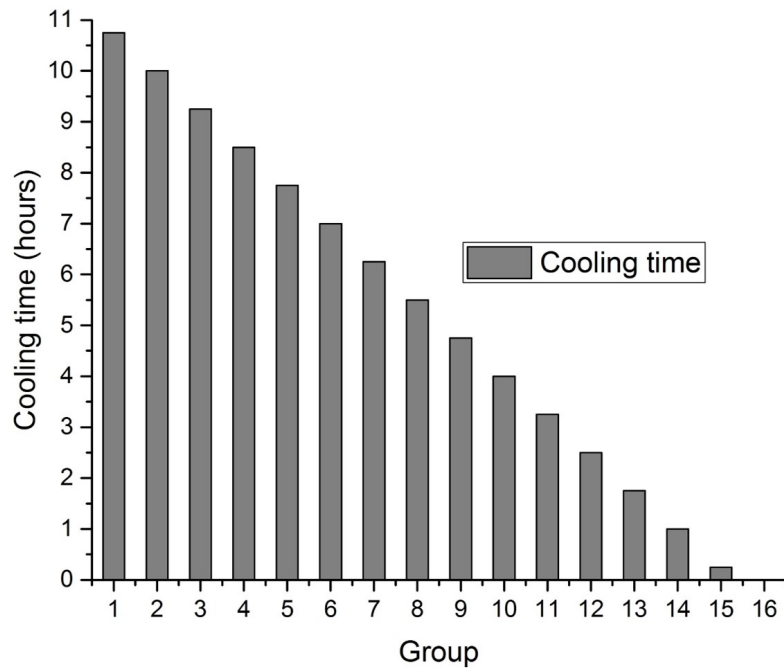


Fig. 9.5 Relationship between cooling time and groups of specimens in the build setup.



Fig. 9.6 Specimens removed from the cake, cleaned, and sandblasted. Note the change in color with cooling time. The specimens of lighter color remained cooling in the system for a longer time; therefore, they are more crystalline. In contrast, the darker specimens are less crystalline due to the shorter cooling time.

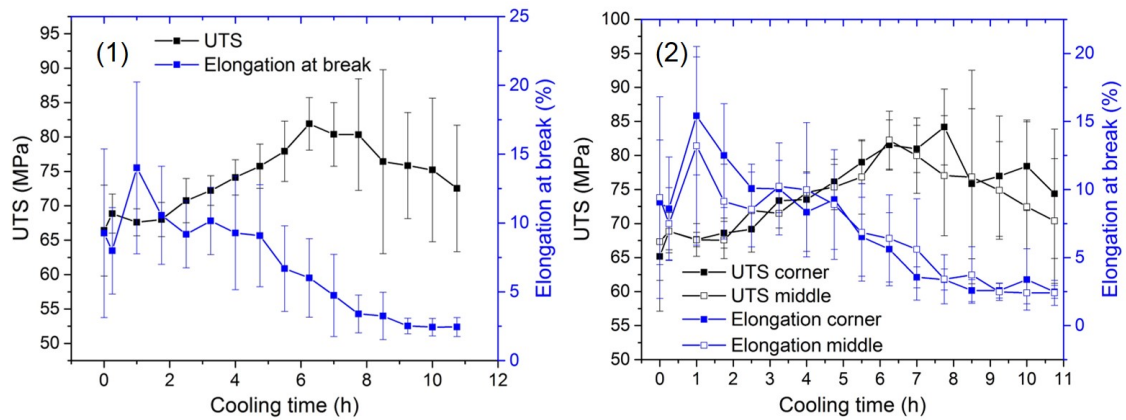


Fig. 9.7 Mechanical performance of specimens produced at different cooling times; (1) average tensile strength and elongation at break for each cooling time and (2) average mechanical performance separated by location in the powder bed, corner, and middle.

to reach the maximum degree of crystallinity of PEKK, as shown by the first three groups in the bottom (9.5-10.75 h). These groups have a brittle behaviour with elongation at break below 2.5%, characteristic of LS PAEKs [149, 280]. At slightly shorter cooling times, the elongation at break more than doubles (5.6% at 7 h of cooling) while mechanical strength ranges around 80 MPa. The maximum strength (~ 82 MPa) is obtained at 6.25 h of cooling, whilst the elongation at break reaches 14% at one hour of cooling, values never achieved in literature before for LS PAEKs.

Regardless of the clear and mostly linear trend observed with the mechanical properties of the specimens manufactured across Z orientation, the high standard deviations mostly overlap these differences in performance with cooling time. Such a large variation is mostly justified by the sudden and heterogeneous cooling in water. Therefore, one-way ANOVA was performed to confirm statistical differences in the data. The parameter chosen for the analysis was elongation at break since this is the factor of primary importance in this study. Table 9.1 summarises the data in terms of significant and non-significant differences, considering P values with 95% confidence. For the post hoc test, the Tukey method was employed, as described in Section 3.3.16. Table 9.1 compares the specimens produced at a specific cooling time (left column) with the other specimens of the build produced with different cooling times.

The values suggest that elongation at break only becomes statistically different in groups separated by an interval of at least 4 h from each other, with few exceptions mostly at low cooling times (~ 1 h and below). The trend, however, highlights the potential differences between groups, which may be statistically insignificant because of the heterogeneous quench in water. The group of specimens subjected to 1 h of cooling, however, was mostly different from the other groups; this may be due to the striking elongation of 14% in comparison with the other specimens. From all the groups, the ones exposed to 4.75 h and 7.75 h presented remarkable differences possibly associated with changes in material structure, such as the degree of crystallinity (see Section 9.4.2 for further details).

Table 9.1 One-way ANOVA analysis of the elongation at break of specimens subjected to different cooling times. The specimens manufactured at a specific cooling time (left column) were compared with the other specimens of the build in terms of their cooling time.

Cooling time	Statistically different ($P < 0.05$) from groups subjected to cooling times of:
0 h	1 h; ≥ 7.75 h
0.25 h	1 h; ≥ 7.75 h
1 h	0 h; 0.25 h; 1 h; ≥ 4 h
1.75 h	≥ 6.25 h
2.5 h	1 h; ≥ 7.75 h
3.25 h	≥ 7 h
4 h	1 h; ≥ 7.75 h
4.75 h	1 h; ≥ 7.75 h
5.5 h	1 h
6.25 h	1 h; 1.75 h
7 h	1 h; 1.75 h; 3.25 h
7.75 h	≤ 4.75 h
8.5 h	≤ 4.75 h
9.25 h	≤ 4.75 h
10 h	≤ 4.75 h
10.75 h	≤ 4.75 h

Fig.9.7(2) reveals the insignificant changes in the mechanical behaviour of specimens subjected to the same cooling time but manufactured at different locations in the powder bed, such as corner and middle. The variations in the final performance of PEKK specimens are minimum regardless of the higher heat dissipation in the corners of the build in the X-Y plane. In contrast, clear differences in heat fluctuation can be observed across Z orientation. The first two groups at the bottom, which should have the highest UTS, did not achieve as great results as the third group. The contact with T_{bed} was enough to prevent warp taking place, but the low T_{bp} of 190 °C accelerated the cooling rate for the specimens located at the bottom of the build, which did not have enough time to crystallise fully.

The specimens were also assessed in terms of elastic modulus against elongation at break. These results are shown in Fig.9.8. The elastic modulus is the highest at the fourth group (8.5 h of cooling) and corresponds to 4.3 GPa. Despite following the same trend as tensile strength, the variations are lower, and the minimum elastic modulus is achieved with group 13, of ~3 GPa.

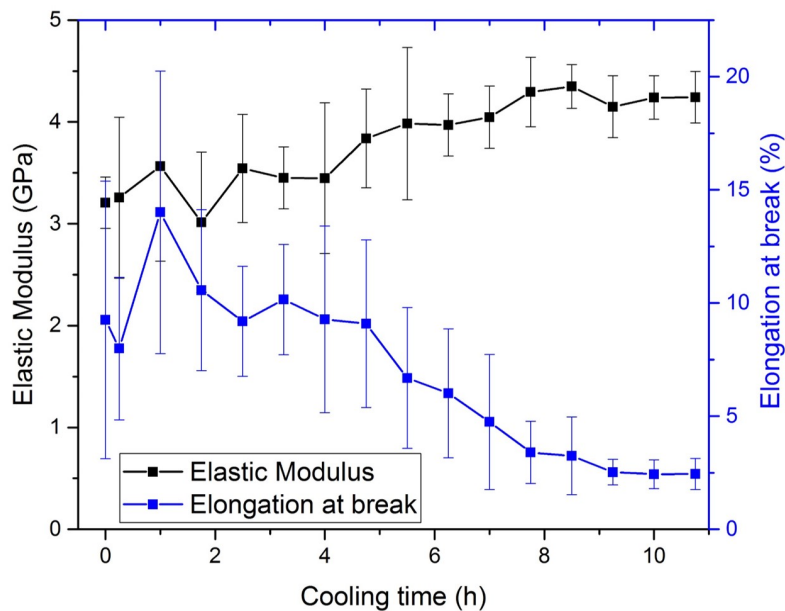


Fig. 9.8 Average elastic modulus versus elongation at break for specimens produced at different cooling times.

9.4.1.1 Fracture analysis of specimens with different cooling times

The fractures of specimens manufactured with different cooling times were investigated and presented in Fig.9.9. The specimens of Fig.9.9(1) and (2) show brittle failure typical from low elongation. The fracture resembles the ones achieved with the standard processing temperatures and cooling times of PEKK, reported in Fig.7.13. The failure of the specimen subjected to 9.25 h of cooling has possibly started on the top right corner as a result of surface imperfections. The specimen subjected to 6.25 h of cooling also showed a brittle failure despite the higher elongation of 6%. The failure seemed to have started from the bottom left corner, where a pore of almost 0.5 mm is located near the surface. This

specimen presents a few pores, but more importantly, fibrils which are holding the structure for longer, therefore enabling a more ductile behaviour confirmed by the higher elongation at break.

As opposed to the brittle failure observed in Fig.9.9(1-2), Fig.9.9(3) presents a ductile failure with layer delamination. Approximately half of the failure surface area shows a very plastic behaviour in which a large concentration of pores and layer delamination are observed. The pores are mostly located in the interlayer area, as pointed by previous studies [274], and in the ductile region. This specimen showed a significant increase in the elongation at break, from 6% at 6.25 h to 9.1% at 4.75 h of cooling. At 4.75 h of cooling, the degree of crystallinity is 14.2%. The crack may have initiated between the brittle and ductile area.

The plastic behaviour is intensified in the specimens of Fig.9.9(4-5), which show an evident ductile failure. The specimens subjected to 1 h of cooling have the highest elongation at break of 14%. For the specimen of Fig.9.9(4), failure seems to have started from the middle, as pores are present at a higher concentration in this region. Layer delamination may be contributing to failure as well. The specimen with minimum cooling time (Fig.9.9(5)) is very ductile as a result of its amorphous structure. On the top area near the surface, a brittle pattern can be observed. This area is free from pores, differently from the more ductile region in which porosity and layer delamination are observed. Fig.9.9(5b) shows a clear image of the fibrillar region, which is holding the structure before failure.

The SEM images of the fractures confirm the mechanical performance behaviour obtained for Kepstan 6002 PEKK under different cooling times. The absence of visible pores in the brittle failure of specimens with longer cooling times is possibly a result of the low elongation. In a ductile failure, however, necking is usually followed by void nucleation, growth, coalescence to form a crack, and finally, fracture [318]. Such stages are observed in ductile [319] and glassy polymers [320] due to their plastic behaviour that leads to more significant deformation. The delamination phenomenon confirms the poor adhesion between layers in LS, which leads to part anisotropy. This anisotropy can be associated with a higher concentration of pores in the interlayer area, as supported by Fig.9.9.

9.4.2 Crystallisation varying with cooling time

9.4.2.1 Degree of crystallinity

WXR analysis was used to measure the degree of crystallinity of two specimens of each group, one from the corner and one from the middle. The results are summarised in Fig.9.10.

The curve shows a correlation of 0.9 between cooling time and degree of crystallinity. By measuring crystallinity on the top layer of each specimen, group 16 was almost 100% amorphous, as expected by the extremely reduced cooling times combined with the slow crystallisation kinetics of PEKK. One-way ANOVA was conducted by comparing the degree of crystallinity of the specimen groups subjected to different cooling times. The

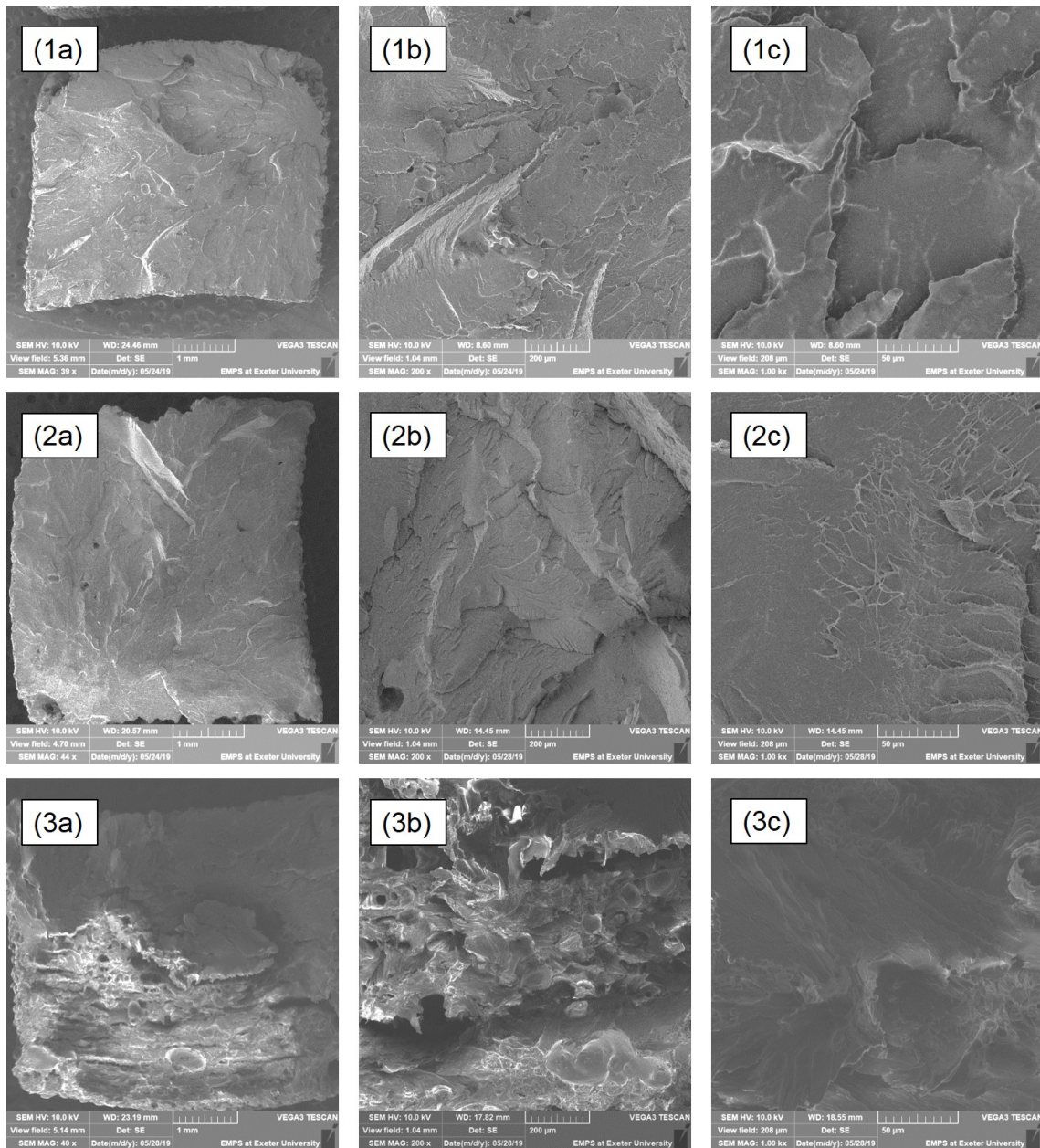


Fig. 9.9 SEM images of the fracture for specimens manufactured at (1) 9.25 h, (2) 6.25 h, (3) 4.75 h, (4) 1 h, and (5) 0 h of cooling time. Note the scale bars of (a) 1 mm, (b) 200 μm and (c) 50 μm.

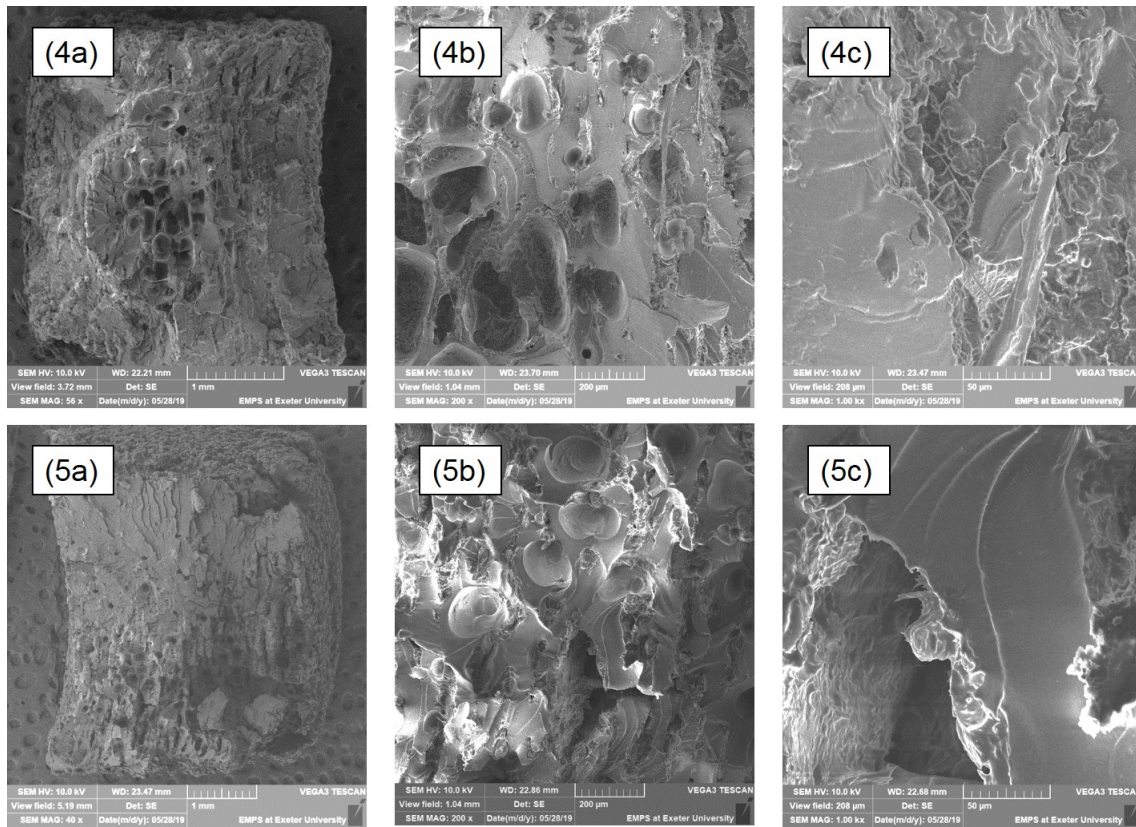


Fig. 9.9 SEM images of the fracture for specimens manufactured at (1) 9.25 h, (2) 6.25 h, (3) 4.75 h, (4) 1 h, and (5) 0 h of cooling time. Note the scale bars of (a) 1 mm, (b) 200 μm and (c) 50 μm (cont.).

results are shown in Table 9.2. As opposed to the elongation at break results, the differences between each group is more significant for the level of crystallinity. This result is possibly caused by the exclusion of manufacturing defects, i.e., warping, crack, and porosity affecting intrinsic material properties. For most of the groups, a difference of three hours in cooling time is sufficient to result in statistically significant data, and several groups are already different with cooling times lower than two hours. From 6.25 h to 7 h, a clear jump in the level of crystallinity is observed, from $\sim 16\%$ to almost 26%. This sudden change in the level of crystallinity can be associated with secondary crystallisation, also known as the crystallisation occurring within the spherulites [13, 29].

The maximum degree of crystallinity is found for the specimens manufactured in the third group (9.25 h) and corresponds to 32%. The first two groups (10.75 h and 10 h of cooling) were slightly affected by the low T_{bp} of 190 $^{\circ}\text{C}$, which may have increased the cooling rate. The lower level of crystallinity of the first two groups is supported by the mechanical test results shown in Section 9.4.1.

9.4.2.2 Crystallinity versus mechanical performance

The increase in the level of crystallinity is associated with an increase in strength, whilst elongation at break is compromised. The relation between the degree of crystallinity and tensile strength is plotted in Fig.9.11(1); Fig. 9.11(2) assesses elongation at break and degree of crystallinity varying with cooling time.

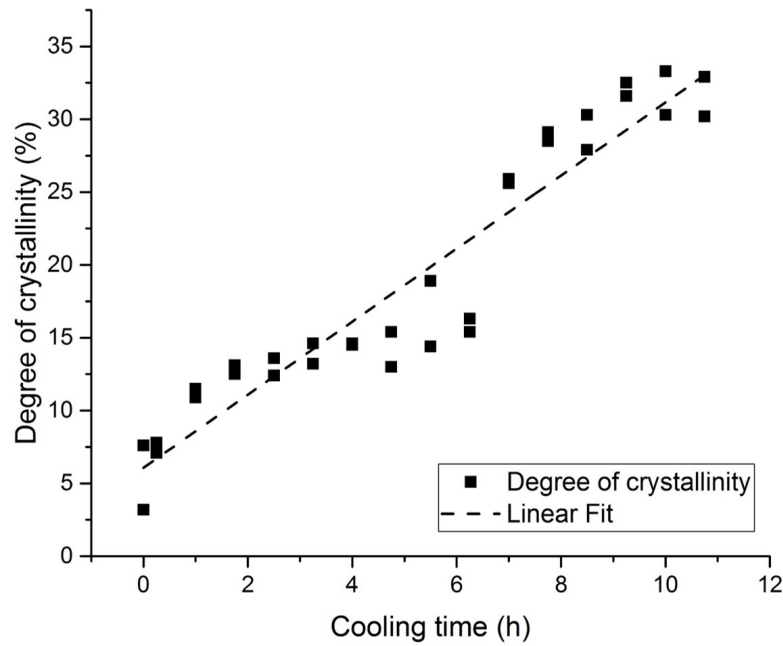


Fig. 9.10 Degree of crystallinity measured using WXR D for specimens produced at different cooling times.

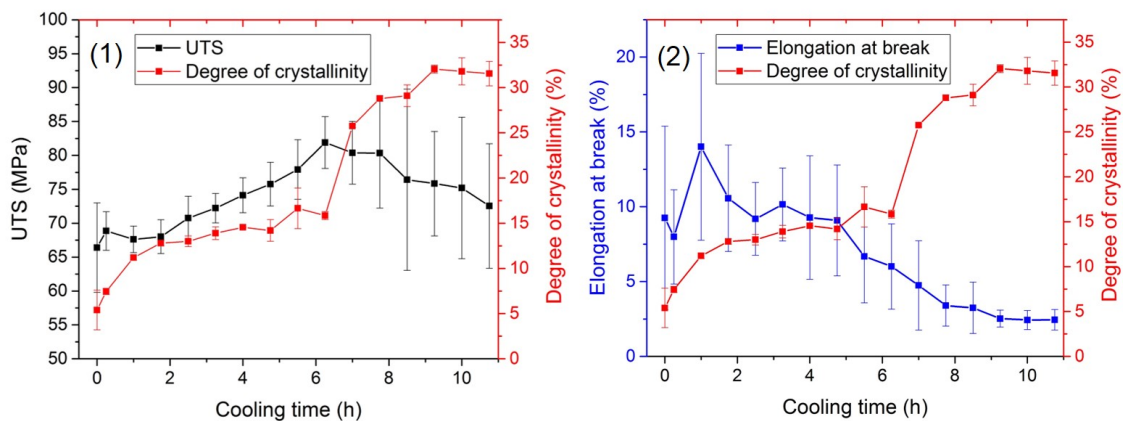


Fig. 9.11 Average degree of crystallinity versus (1) tensile strength and (2) elongation at break for specimens produced at different cooling times.

The increase in mechanical strength leads to an optimum degree of crystallinity of $\sim 16\%$ at 6.25 h of cooling time. Interestingly, the crystallinity rapidly increases from 6.25 h to 7 h of cooling (group 6) and reaches almost 26%, whilst mechanical strength starts to reduce. The elongation at break (Fig. 9.11(2)) is maximum at an almost amorphous structure, in which the level of crystallinity is of 11.2%, while in group 6 and 7 (degree of crystallinity of $\sim 26\%$ and $\sim 16\%$, respectively), elongation at break varies between 4.7 and 6%. This range (1 h to 7 h of cooling) has a variation of crystallinity of 15%. The results show that it is possible to control the crystallisation of Kepstan 6002 PEKK in LS and, therefore, significantly change the strength and mainly the poor elongation associated with this process.

Table 9.2 One-way ANOVA analysis of the degree of crystallinity of specimens subjected to different cooling times. The specimens manufactured at a specific cooling time (left column) were compared with the other specimens of the build in terms of cooling time.

Cooling time	Statistically different ($P < 0.05$) from groups subjected to cooling times of:
0 h	≥ 1.75 h
0.25 h	≥ 3.25 h
1 h	≥ 7 h
1.75 h	0 h; ≥ 7 h
2.5 h	0 h; ≥ 7 h
3.25 h	≤ 0.25 h; ≥ 7 h
4 h	≤ 0.25 h; ≥ 7 h
4.75 h	≤ 0.25 h; ≥ 7 h
5.5 h	≤ 0.25 h; ≥ 7 h
6.25 h	≤ 0.25 h; ≥ 7 h
7 h	≤ 6.25 h
7.75 h	≤ 6.25 h
8.5 h	≤ 6.25 h
9.25 h	≤ 7 h
10 h	≤ 6.25 h
10.75 h	≤ 6.25 h

9.4.2.3 Crystallisation kinetics in laser sintering

The slow cooling rate of LS provides sufficient time for chain rearrangement, therefore crystallisation of Kepstan 6002 PEKK. As shown in Section 6.2, crystallinity is only observed in dynamic DSC rates below $2\text{ }^{\circ}\text{C min}^{-1}$. As PEKK crystallises in LS, one can conclude that the cooling rate of this process is even slower than $2\text{ }^{\circ}\text{C min}^{-1}$. The cooling rate of LS during part fabrication (see Fig.9.3(2)) is quasi-static and can reach values of $0.15\text{ }^{\circ}\text{C min}^{-1}$ at standard LS conditions (temperatures as described in Section 7.2.2) for a building time of three hours, and considering cooling as linear throughout the build. Therefore, the most accurate method to simulate the kinetics of crystallisation of PEKK in LS is by assuming it as a process of successive isothermal steps.

The curves of the isothermally crystallised samples in the DSC were compared with the data obtained for PEKK crystallisation in LS. For this analysis, the group with the maximum level of crystallinity (9.25 h, 32% of crystallinity) was considered to have a relative volumetric crystallinity of 100%, i.e., the maximum possible crystallinity obtained

with the LS of PEKK. The degree of crystallinity of the LS specimens was measured under WXRd rather than DSC. Fig.9.12 presents some isothermal curves from DSC samples of PEKK against the volumetric crystallinity versus time of LS PEKK (black curve).

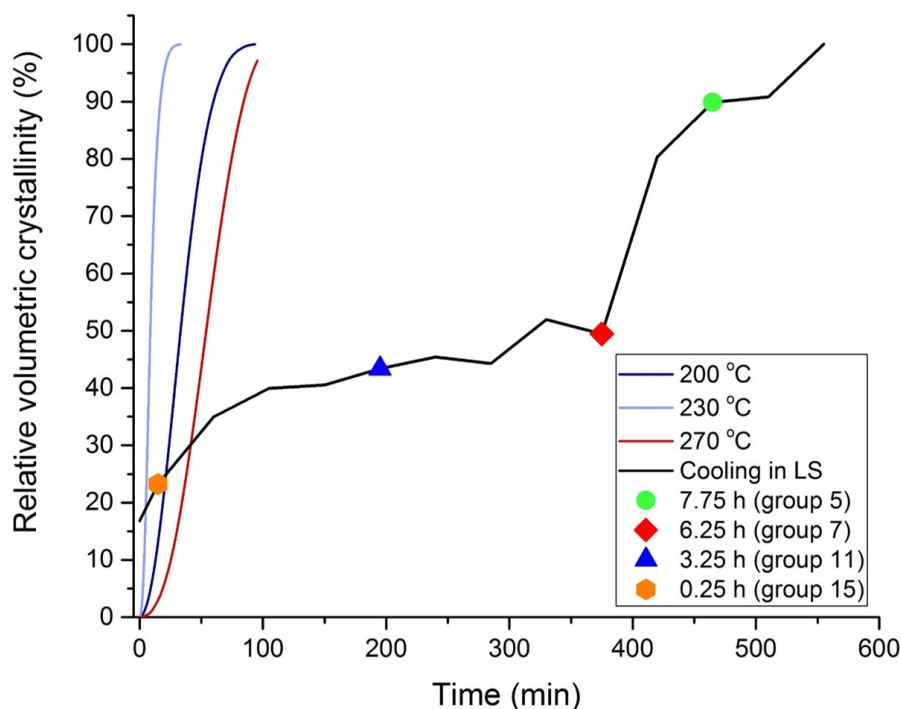


Fig. 9.12 Relative volumetric crystallinity of isothermally crystallised Kepstan 6002 PEKK compared with the LS process. The time to crystallise some of the LS groups is highlighted in the LS line by points of different colours and shapes.

The time to achieve the same relative volumetric crystallinity for the LS process is in the order of 10 times longer than the isothermally crystallised samples. Recent models used to describe crystallisation in LS [321, 322] were validated using isothermal profiles taken from flash DSC data, but they do not seem to correspond with the actual crystallisation in LS. Indeed, there is a striking difference between them. A small part of this difference can be explained by the assumptions considered to develop the LS curve. These assumptions include the method applied to compute volumetric crystallinity, i.e., DSC versus WXRd, the process in LS being quasi-static but not isothermal, the extra few minutes to remove the build from the system and interrupt crystallisation, the variance in the calculation of crystallinity using WXRd and the errors originated from the sudden cooling interruption of the experimental process.

A more significant reason for the discrepancy between the curves can be attributed to a punctual source of heat potentially melting the surface of the particles only [270], a complex heat transfer phenomenon taking place between the layers and leading to recrystallisation, and an increase in molecular weight with processing (see Appendix D for more information). These differences probably affect more polymers with a slow kinetics of crystallisation such as Kepstan 6002 PEKK, in which crystallisation can take several minutes to start (induction time), depending on the processing temperatures selected.

9.4.3 Crystal structure varying with cooling time

9.4.3.1 Spherulites

Similarly to other polymers from the PAEK family [76], PEKK crystallises in the form of spherulites. These crystal structures can be observed under TEM, and their dimensions can be measured. Samples of the specimens with cooling times of 10 h, 5.5 h, and 0 h (almost amorphous specimens) were taken to TEM analysis, as shown in Figs. 9.13 - 9.15.

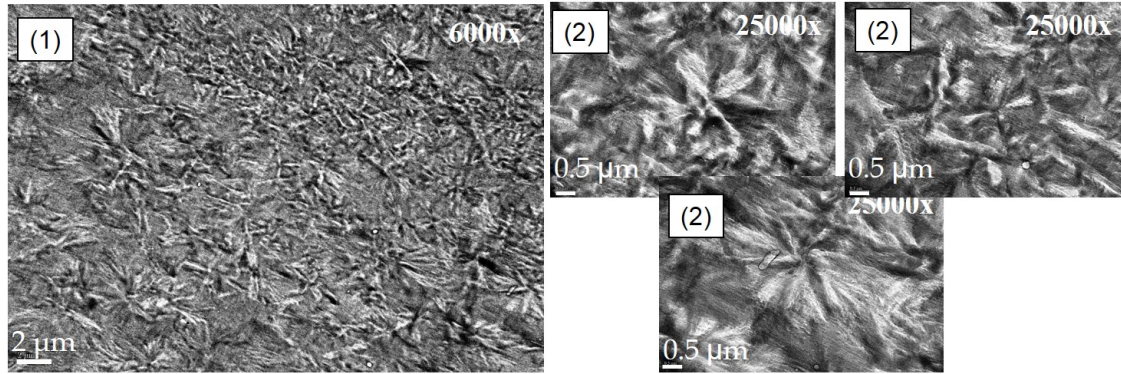


Fig. 9.13 PEKK spherulites formed after 10 h of cooling in LS. (1) General morphology of the spherulites and (2) magnified images of individual spherulites. The spherulites are homogeneously distributed at varying sizes from 5.4 to 5.7 μm in diameter.

The crystalline structure achieved with 10 h of cooling resembles those obtained when cooling PEKK at standard LS conditions, as shown in Fig.7.20. The diameter of the spherulites resulting from the process at T_{bp} of 265 $^{\circ}\text{C}$ varies between 2.8 and 5.8 μm ; the diameter of the spherulites resulting from the process at T_{bp} of 286 $^{\circ}\text{C}$ varies between 3.7 and 7.5 μm . When interrupting the cooling after 10 h, the spherulites show a variable size from 5.4 to 5.7 μm , which corresponds to intermediate values between the standard cooling process of both T_{bp} tested in Section 7.4. A possible explanation for the more uniform diameter of these spherulites is the uniform cooling during manufacture, which is slower and more controlled than when the LS system goes through the standard cooling cycle set by the software. The degree of crystallinity is also similar, as after 10 h of cooling, $32 \pm 0.6\%$ of crystallinity is obtained against $28 \pm 2.8\%$ at T_{bp} of 265 $^{\circ}\text{C}$ and $30.8 \pm 1.9\%$ at T_{bp} of 286 $^{\circ}\text{C}$.

At 5.5 h of cooling (Fig. 9.14), the spherulites reach diameters of 16.6 μm as impingement during growth is significantly reduced. Interestingly, the cores from which the spherulites start to grow assume a different format from the rest of the spherulites. Zarringhalam et al. [270] observed a similar phenomenon in the LS of recycled PA12 and attributed these cores to unmolten particles triggering heterogeneous nucleation. In their case, however, the solid cores are a result of an increase in T_m of the recycled powder. In this experiment, only virgin PEKK particles were used. Furthermore, these cores are not present in the specimens subjected to 10 h of cooling, which are part of the same build. It may be possible that the formed crystal structure did not go through secondary crystallisation, and the evident cores are a result of stable nuclei going through the growth

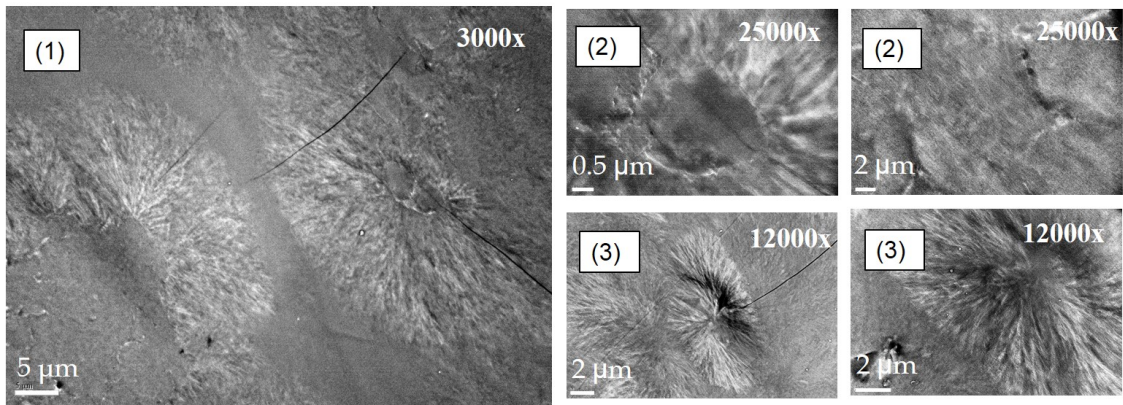


Fig. 9.14 PEKK spherulites formed after 5.5 h of cooling in LS. (1) General morphology of the spherulites, (2) magnified images of the core structures, (3) magnified images of the spherulites' structure. The spherulites assume a larger diameter, which starts growing from very clear cores.

phase during primary crystallisation. As cooling was interrupted, they assumed a different structure from the rest of the spherulites. From the WXR analysis, one can observe a reduction of almost half of the crystallinity achieved with 10 h of cooling, to $16.7 \pm 3.2\%$. Such a decrease is supported by the vast areas of amorphous PEKK shown in the TEM images.

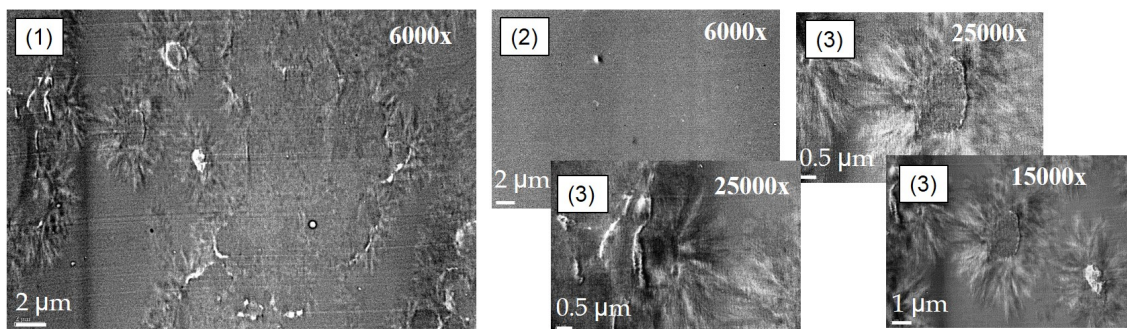


Fig. 9.15 PEKK spherulites formed with minimal LS cooling time approaching 0 h. (1) General morphology of the crystallised region, (2) image of the amorphous region, and (3) magnified images of the nuclei being formed. The quenching was not enough to prevent crystallisation.

The TEM images of the specimens approaching 0 h of cooling are shown in Fig.9.15. PEKK assumes a largely amorphous structure (Fig. 9.15(2)), although nuclei formation is observed in particular regions. In the upper left corner of Fig.9.15(1), stable nuclei were formed, and growth was interrupted. The other nuclei of Fig.9.15(1) (middle-right region) were not able to achieve the critical radius and become stable; therefore, they were re-dissolved in the molten structure. Due to the rapid cooling, solidification took place during the dissolution process; and a pattern similar to crystals 'exploding' is observed. The images of Fig.9.15(3) present similar 'cores' to the ones achieved in Fig.9.14; they were also attributed to stable nuclei with reduced time to grow and form a spherulite.

All the stages of crystallisation - primary nucleation, secondary nucleation, crystal growth - are present throughout this experiment. The spherulites of PEKK obtained with LS usually vary between 3 and 7 μm in diameter. By controlling the cooling time in LS, however, they can reach diameters of $\sim 17 \mu\text{m}$, resulting in a successful increase in elongation. Just as in conventional manufacturing techniques, the crystal structure is directly associated with performance in LS and can be controlled to attend different application needs.

9.4.3.2 Polymorphism of PEKK in LS

Previous studies mentioned that the crystalline structure of PEKK, known as form II, can only be obtained under cold crystallisation or when PEKK is exposed to solvents [71, 275]. Garcia-Leiner et al. [84], however, claimed that form II could be present when processing PEKK by LS or FDM. In this section, the potential for different PEKK morphologies will be explored under WXR analysis. Fig. 9.16 compares different WXR patterns of LS samples manufactured in a range of cooling times. The patterns were acquired from the top surface of a few specimens produced in the middle of the LS build.

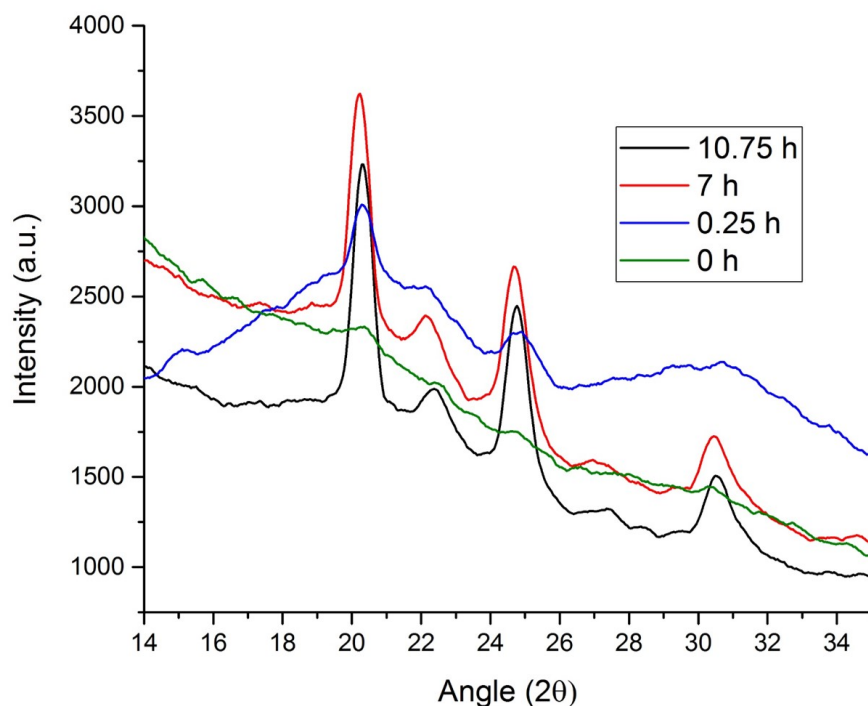


Fig. 9.16 WXR spectra of LS Kepstan 6002 PEKK specimens subjected to different cooling times.

The longer the cooling time (e.g., 10.75 h), the more pronounced are the peaks of the PEKK patterns, until very shallow peaks are found at 0 h of cooling. Before achieving an almost 100% amorphous structure, however, PEKK shows an additional shallow peak at $\sim 15.6^\circ$, at 0.25 h of cooling. This peak is attributed to the presence of form II in the structure; such a peak is not observed in the other patterns of Fig.9.16. Therefore, it is

possible to have PEKK organised into form II under certain conditions in LS, i.e., low cooling times followed by quenching in water. More information regarding polymorphism of PEKK in LS is provided in Appendix B.

9.5 Conclusions

This chapter has successfully developed a new method to correlate part properties (crystallinity and mechanical performance) with the process (cooling time) of Kepstan 6002 PEKK by LS. The degree of crystallinity shows a direct relation to mechanical properties, e.g., tensile strength and elongation at break. The poor elongation at break usually found in PAEKs processed by LS [149] is overcome by controlling the cooling time and interrupting crystallisation.

Cooling times below 5 h led to elongation at break from 9% with a low reduction of $\sim 17\%$ in tensile strength [317]. At 1 h of cooling, the strain is increased to 14%. Such an increase is a striking achievement as elongation at break was never above 5% for LS PAEKs [149]. However, 82 MPa of tensile strength is still attained with an elongation at break of 6% and a cooling time of 6.25 h.

The kinetics of crystallisation of PEKK is directly influenced by the process, as LS does not follow the same trend obtained with isothermally crystallised samples in the DSC. In fact, the time taken to crystallise PEKK specimens in LS is about ten times longer. This chapter highlights that isothermal DSC cannot be used to study LS crystallisation, as a few studies [322, 323] attempted to do. The striking difference between the kinetics of crystallisation in LS and isothermally crystallised samples in DSC can be justified by the punctual heat application of the laser, which is not able to melt the particles fully, the complex heat transfer phenomenon occurring between the layers, and the change in molecular weight.

A close investigation of LS PEKK microstructure reveals spherulites with completely different diameters varying with cooling time. The TEM analysis was able to capture the different stages of crystallisation: primary nucleation, secondary nucleation, and crystal growth. At prolonged cooling times, the microstructure is composed of small spherulites (5.4 - 5.7 μm) resulting from the several nucleation points, which limit their growth due to crystal impingement. At lower cooling times, the amorphous region is increased, and the spherulites are free to grow and achieve larger diameters of up to 17 μm . As cooling was interrupted, only primary crystallisation is identified in these PEKK samples, and the nuclei remain with a different structure from the rest of the spherulite. The specimens subjected to almost no cooling are mainly amorphous. Interestingly, recently formed nuclei are contrasted with unstable nuclei re-dissolving in the quenched structure. Different crystal structures were investigated, and form II can be obtained at short cooling times in LS; this was supported by WXR analysis.

This chapter developed a successful relationship between process and material properties. The calibration curve is a useful method to control the degree of crystallinity of PEKK in the LS process. Furthermore, it infers the ideal cooling time required to achieve the

desired mechanical properties for different applications. This introduces a novel feature to AM processing - the "tailoring" of mechanical properties to a vast range of possibilities.

The understanding of crystal structure and material properties is crucial for successful improvement of final part performance. This study provides an example of the effect of the degree of crystallinity and microstructure in the mechanical properties of Kepstan 6002 PEKK and shows that it is possible, up to an extent, to control the slow cooling stage of LS to favour the desired properties according to the application. A compromise might be possible, e.g., smaller builds (shorter cooling times) or maybe changes to new LS systems to allow the control of crystallisation (controlled cooling rate), and therefore apply a similar method to other LS materials with slow crystallisation kinetics and processing temperatures.

Chapter 10

Recyclability of LS PEKK Powder

10.1 Summary

High-performance polymers can replace metallic parts in several industries as automotive, aerospace, and medical. For most applications, this change is fundamentally dependent on the polymer's capability of reuse after LS, since it drastically reduces production cost. In the case of PAEKs, recyclability is particularly crucial as their processing temperatures are above the onset temperature of melting [152]. This industrial interest led to the research developed in this chapter, which concludes the optimisation of PEKK for HT-LS of this thesis.

Assessing and understanding particle and powder changes when subjected to LS is crucial for powder recycling, but also of significant importance when selecting the appropriate pre-heating temperatures, T_{bed} and T_{bp} . Previous studies [149, 150, 324] highlighted how powder reuse affects surface quality, mechanical properties, and shrinkage of LS parts. By exposing polymer material to temperatures above T_g and often near T_m , degradation can occur [146, 325, 326, 147] and change the structure of the polymeric powder with time, thus compromising final performance during reuse. The prolonged exposure to high temperatures can affect viscosity [189], sintering window in a reuse cycle [173], particle shape [121], size and distribution, packing density [148], and flow.

This chapter provides insights into size, distribution, morphology, thermal changes and crystallisation of PEKK powder exposed at processing temperatures (T_{bed} of 292 °C) and different T_{bp} in LS, of 265 °C and 286 °C, as selected in Section 7.2.2. Bulk density and flow were assessed for these conditions and compared with the virgin PEKK powder. A schematic illustration of this chapter's structure is shown in Fig.10.1.

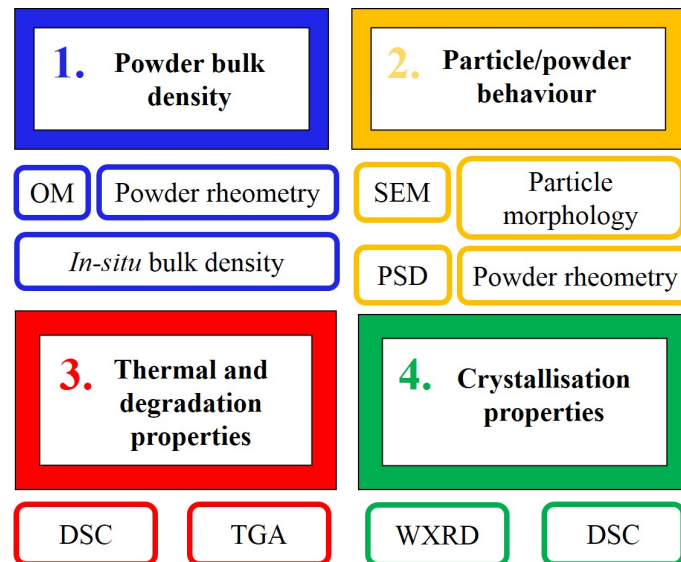


Fig. 10.1 Schematic illustration of Chapter 10 structure and the characterisation techniques employed to investigate powder, particle, and material properties.

The results revealed that powder is more affected by the increase of T_{bp} than with reuse. The particle size distribution of the processed powders was shifted to larger sizes as a result of partially sintered particles in the powder bulk, which led to a reduction in

the density and flow performance. The melting peak and degradation temperature were also shifted to higher temperatures with processing, whilst crystallisation was reasonably delayed for the cake exposed to T_{bp} of 286 °C. This delay, however, does not affect the level of crystallinity of PEKK processed by LS. A closer SEM investigation of the particles from the post-processed cakes reveals a change in particle surface at the nanometre scale and the presence of fibrillar structures bridging the voids within the particles. The selection of T_{bed} and T_{bp} are essential when processing PEKK as they may affect particle size, bulk density, flow performance, thermal behaviour, and crystallisation. Sieving is crucial for powder reuse as it breaks agglomeration resulting from pre-heating in LS.

10.2 Results and Discussions

10.2.1 Investigation of bulk density

Bulk density was assessed using three different methods. The first method consists of an optical microscopy analysis of the cake (Section 3.3.17), the second method assessed *in situ* bulk density (Section 3.3.18), and the last method used an FT4 powder rheometer to measure conditioned bulk density of virgin and processed powders during stability and flow rate test (Section 3.3.5.2).

Fig.10.2 shows a typical image of the cakes processed at a T_{bp} of (1) 265 °C and (2) 286 °C. The analysis of the images reveals a cake porosity of $28.63 \pm 2.4 \%$ for the cake processed at T_{bp} of 265 °C and a porosity of $23.77 \pm 1.96 \%$ for the cake processed at T_{bp} of 286 °C. These results suggest that the increase of T_{bp} improves powder layer consolidation, even with T_{bed} being the same for both cakes in analysis.

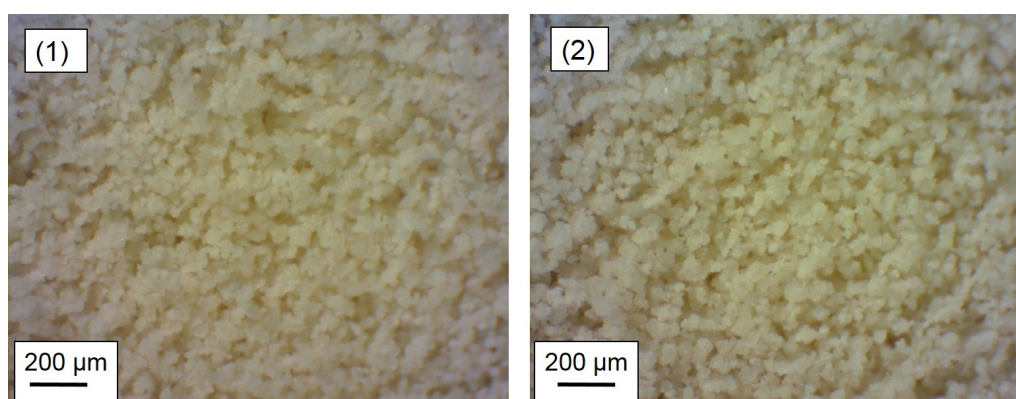


Fig. 10.2 Optical analysis of cakes processed at (1) 265 °C and (2) 286 °C of T_{bp} .

A second approach was conducted, which consists of measuring bulk density inside the LS process. The *in situ* measurement is possibly the most accurate method to monitor bed density. This test was performed according to the description in Section 3.3.18. The average weight of the six boxes resulted in a bulk density of $0.37 \pm 0.01 \text{ g cm}^{-3}$. The *in situ* results are compared to powder rheology measurements of the virgin and processed PEKK powders in Table 10.1. Bulk density is the highest for the virgin PEKK, as expected.

The increase in T_{bp} hindered packing; this is possibly a result of particle size change with processing.

Table 10.1 Bulk density of Kepstan 6002 PEKK achieved with different methods and conditions.

Method and condition	Bulk Density (g cm^{-3})
<i>In situ</i> with virgin powder	0.37 ± 0.01
Powder rheometry of virgin powder	0.37 ± 0
Powder rheometry of powder from the cake exposed to T_{bp} of 265 °C	0.34 ± 0
Powder rheometry of powder from the cake exposed to T_{bp} of 286 °C	0.33 ± 0

By comparing the bulk density values of the *in situ* measurements with the density of the virgin PEKK powder obtained with the powder rheometer, no variation was observed in the data. This result infers that any temperature effect or pre-compaction in the hopper is insufficient to change bed compaction of PEKK powder.

10.2.2 SEM analysis

Fig.10.3 presents SEM images of the virgin and processed Kepstan 6002 PEKK powders at different magnifications. The particles are irregular and porous, but overall show a similar structure and size at reduced magnifications. At 15,000 \times of magnification, however, significant changes appear regarding surface irregularities and the presence of fibrils in the particle interstices, as shown in Fig.10.3(6). Whilst virgin PEKK maintained its structure found at lower magnifications, the surface of processed PEKK particles seems to present an increase in surface roughness in the nanometre size. This change in roughness can be an indication of heat starting to change the initial morphology of the particles and is intensified by increasing T_{bp} , as observed in Fig.10.3(9). Similar findings were noticed by Mielicki et al. [121], who registered a change in the shape of larger PA12 particles after processing.

In addition to changes in surface roughness, fibrillar shapes were formed in the interstices of processed particles, particularly at 265 °C of T_{bp} . Siegmann et al. [221] found a fibrillar network in the structure of UHMWPE particles (see Fig.2.17) and attributed them to the highly oriented chains. The fibres in their study, however, are present throughout the particles due to the high degree of crystallinity of UHMWPE. Caddock and Evans [327] identified a fibrillar structure in polytetrafluoroethylene (PTFE) under expansion/compression. According to them, the individual particles are coalescing together and crossing from one cluster to another through this fibrillar network, which is largely responsible for the negative Poisson's ratio of PTFE. These studies support the idea that

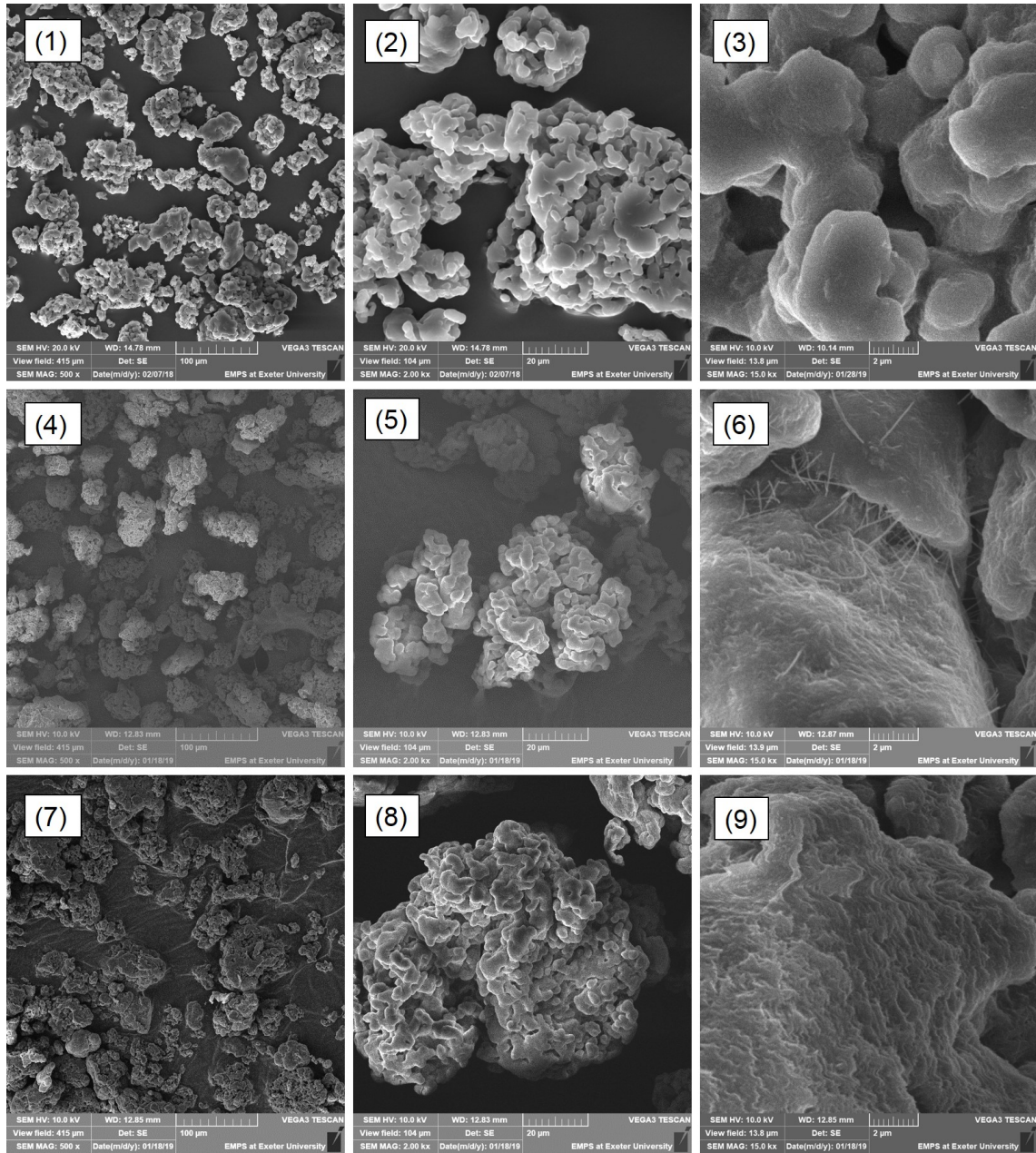


Fig. 10.3 Typical SEM images of Kepstan 6002 PEKK powder. Note the scale bars of 100 μm (left), 20 μm (middle) and 2 μm (right) for (1-3) virgin particles, (4-6) processed particles at T_{bp} of 265 °C and (7-9) processed particles at T_{bp} of 286 °C.

PEKK particles exposed to heat during LS attempt to reduce internal porosity by forming fibrils to bridge the voids in the particles' interstices.

10.2.3 Particle size distribution

A Microtrac Turbosync system was used to measure particle size distribution (Section 3.3.2) of virgin and processed Kepstan 6002 PEKK powder. The results are shown in Fig.10.4 and summarised in Table 10.2. The distribution curve of virgin PEKK shows a D(50) of 51.23 μm , whilst the powder processed at T_{bp} of 265 $^{\circ}\text{C}$ has a D(50) of 67.04 μm . Such an increase is even higher for the PEKK powder processed at 286 $^{\circ}\text{C}$ of T_{bp} , in which D(50) is of 85.16 μm .

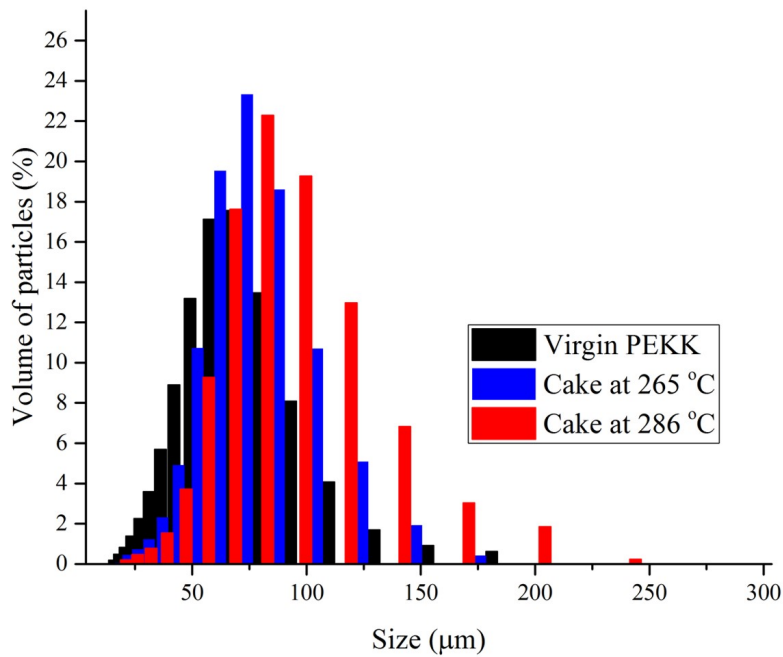


Fig. 10.4 Particle size distribution analysis for virgin and processed Kepstan 6002 PEKK powder at 265 $^{\circ}\text{C}$ and 286 $^{\circ}\text{C}$ of T_{bp} .

Table 10.2 Summary of the particle size distribution of Kepstan 6002 PEKK powder.

Volumetric parameter	Virgin PEKK	Processed PEKK at 265 $^{\circ}\text{C}$	Processed PEKK at 286 $^{\circ}\text{C}$
D(10) (μm)	28.64	44.32	57.24
D(50) (μm)	51.23	67.04	85.16
D(90) (μm)	83.88	99.28	137.5
D(90) - D(10) (μm)	55.24	54.96	80.26

The virgin PEKK shows a higher amount of finer particles than the cake powders, whilst PEKK processed at T_{bp} of 286 $^{\circ}\text{C}$ shows a significant increase in particle size. These

findings are different from what reported in the literature for PA12, in which no change in particle size distribution is observed with aging [132, 121].

For processed PEKK powder, the volume of particles increases in the central area of the curve, and less small particles are observed. A plausible explanation for the lower amount of small particles is the partial sintering of the processed powders. This phenomenon is not surprising considering that T_{bed} is well within the melting peak of PEKK (Fig.7.2). As smaller particles have a lower surface area, they are easier to melt; therefore, they partially sinter or coalesce in the pre-heating stage. The images of individual particles in Fig.10.5 confirms this phenomenon.



Fig. 10.5 Images of semi-sintered particles from the processed cake at (1-2) 265 °C and (3-4) 286 °C. The dashed lines represent the assumed partial sintering region between particles in the processed powder.

The particles from the cake processed at 286 °C show a broader end-tail, from 150 to 250 μm . Although with a volume distribution below 7%, the extension of the curve supports the presence of partial sintering, which can be possibly reversed through a more aggressive sieving process than the standard. It is important to highlight that a T_{bp} of 286 °C is above the conventional values of T_{bp} for HT-LS. The effect of processing and T_{bp} in particle morphology will be investigated next.

10.2.4 Morphology investigation

Morphology was investigated using the images captured by the high-speed camera of Microtrac TurboSync equipment. The shape descriptors under consideration are perimeter and convexity, in which convexity is calculated by Eq.(3.5). The results are shown in Fig.10.6 and Fig.10.7. The end-tail behaviour shown in Fig.10.4 for the powder processed at 286 °C is present again when assessing perimeter (Fig.10.6). For the cake particles processed at T_{bp} of 265 °C, perimeter achieves a plateau when the diameter is increased to above 80 μm . The plateau in the perimeter suggests that particles become smoother with the increase in particle size. The surface smoothness is explained by the prolonged heat provided by the T_{bp} of 265 °C, which is sufficient to round the surface of the particles, but not enough to cause agglomeration, as observed for the particles subjected to T_{bp} of 286 °C. This finding does not contradict the SEM images presented in Fig.10.3 as the high-speed camera in the Microtrac system is not able to capture surface roughness in the nanometre size.

The scatter graph of convexity in Fig.10.7 presents virgin PEKK particles with irregular morphology and convexity values varying from 0.77 to 1.0 at smaller particle sizes. The

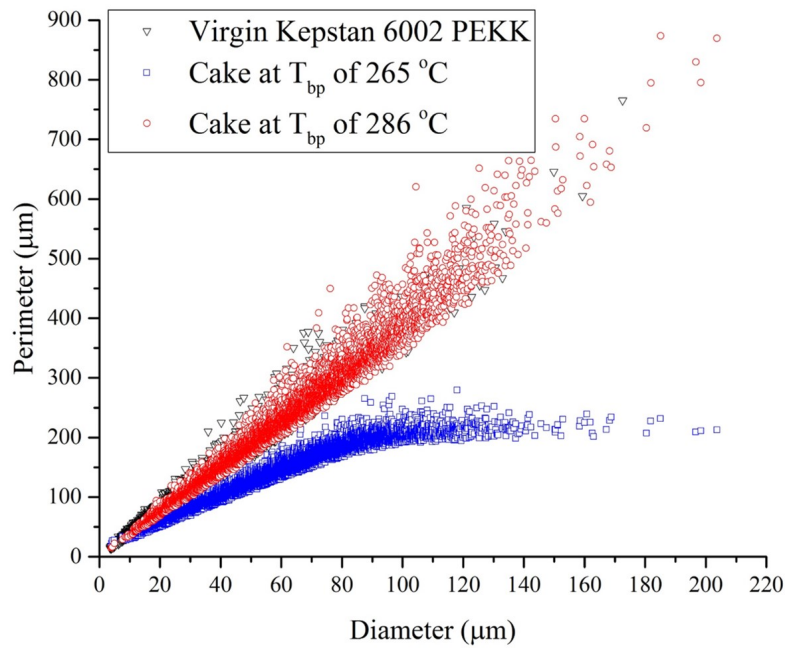


Fig. 10.6 Perimeter varying with particle diameter for virgin and processed PEKK.

PEKK powder processed at 265 °C and 286 °C had their surface improved, as a large concentration of particles presents higher values of convexity varying from 0.83 to 1.0. The improvement of particle morphology in the micrometric size can be a result of the fibrillar network bridging the interstices of the particles. The low values of convexity for the large particles of the powder processed at 286 °C support the presence of partial sintering in the cake, which is compromising final morphology.

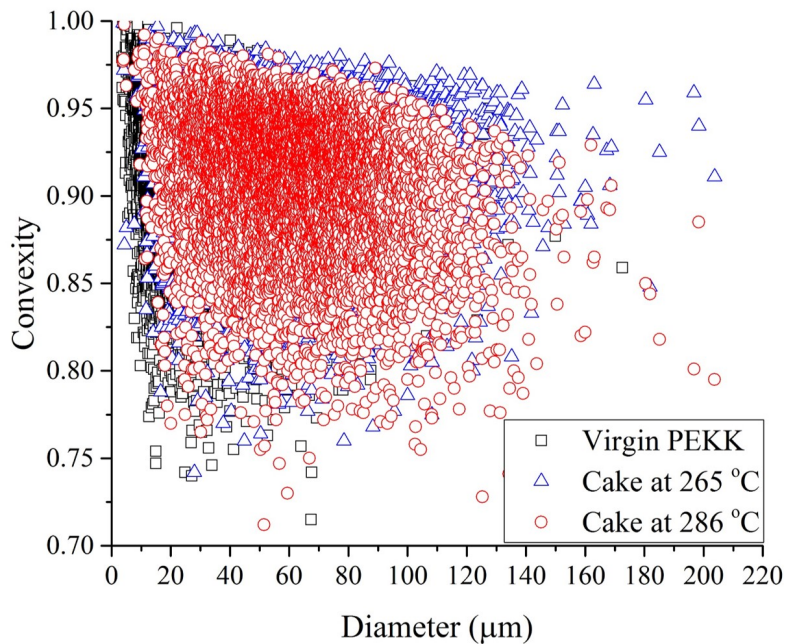


Fig. 10.7 Convexity varying with particle diameter for virgin and processed PEKK.

10.2.5 Powder flow performance

A Freeman FT4 system was used to perform stability and flow rate test, as described in Section 3.3.5.2. The test was modified to a larger amount of cycles until a plateau was found for all conditions. The summary of results is shown in Table 10.3. Following the standard practice in the industry, the powders were sieved and tested again; the results are summarised in Table 10.4.

Table 10.3 Summary of flow performance for Kepstan 6002 PEKK processed at different conditions.

Parameters	Virgin PEKK	Cake powder at 265 °C	Cake powder at 286 °C
Stability Index	1.32 ± 0.18	1.79 ± 0.06	1.81 ± 0.26
BFE (mJ)	154.6 ± 9.0	183.2 ± 4.4	239.3 ± 7.6
SE (mJ/g)	6.41 ± 0.29	6.56 ± 0.08	7.13 ± 0.36
Flow Rate Index	1.27 ± 0.02	1.17 ± 0.01	1.11 ± 0.04

Table 10.4 Summary of flow performance for sieved Kepstan 6002 PEKK powder processed at different conditions.

Parameters	Sieved cake powder at 265 °C	Sieved cake powder at 286 °C
Stability Index	1.05 ± 0.08	1.80 ± 0.28
BFE (mJ)	137.13 ± 5.6	220.02 ± 27.3
SE (mJ/g)	5.28 ± 0.43	7.12 ± 0.59
Flow Rate Index	1.18 ± 0.01	1.12 ± 0.01

The number of cycles required to stable virgin and processed powder at 265 °C is the same, of eleven cycles in total. For the cake powder processed at 286 °C, stability was achieved with thirteen cycles as the exposure to higher temperatures changed particle size and distribution (Section 10.2.3). The sieved cake processed at 265 °C does not present any significant difference in the stability curve when compared to virgin PEKK. For this condition, sieving was sufficient to break the cohesive forces between particles, hence loosen the agglomerated powder; this is supported by the SI values for this cake after sieving (Table 10.4), which is even more stable than the virgin PEKK powder. In the case of PEKK processed at 286 °C of T_{bp} , sieving reduced the effect of agglomeration but the total energy to displace the particles remains above the other powders. Such behaviour may be a result of changes in particle size, distribution and shape, and only a more aggressive sieving would be able to break the semi-sintered particles apart.

Fig.10.9(1) presents the flow behaviour of Kepstan 6002 PEKK powder processed at different conditions. The rate of change in flow follows the trend shown in Fig.10.8(1), with

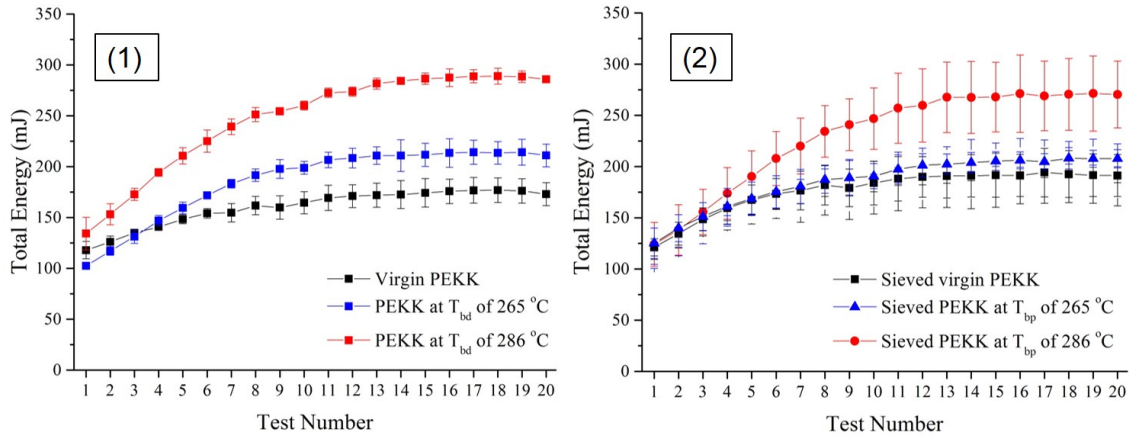


Fig. 10.8 Stability results of Kepstan 6002 PEKK powder processed at different conditions and tested (1) before and (2) after sieving.

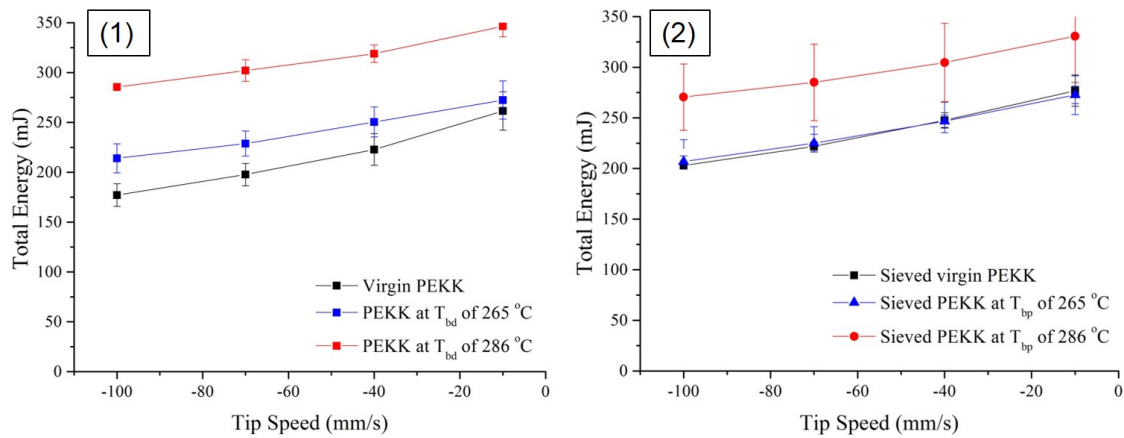


Fig. 10.9 Flow rate performance of Kepstan 6002 PEKK powder processed at different conditions and tested (1) before and (2) after sieving.

very similar flow performance for the virgin PEKK and PEKK processed at a T_{bp} of 265 °C. The higher the tip speed, the more air penetrates the bulk, which reduces interparticle contact and enables higher compressibility, thus less energy is required to produce flow. At low flow rates, interlocking forces are dominant in powder flow as the effect of air is excluded. This property is associated with morphology and surface roughness, which at the micrometric scale seems to be similar for the virgin and processed powder before sieving, despite far from the spherical and smooth shape desired for LS. The virgin and the cake powder processed at 265 °C show less interlocking and better consolidation than the cake powder processed at 286 °C.

When the processed powders go through sieving, the slight difference between virgin PEKK powder and PEKK processed at T_{bp} of 265 °C disappears, and the air is able to penetrate the structure in the same way. The values of BFE and SE support such behaviour. After sieving, the cake processed at 265 °C presents even better flow properties than the virgin PEKK powder, which suggests that the pre-existent agglomeration of powder is broken during sieving. For the cake processed at 286 °C, however, sieving is insufficient to disrupt the agglomerated structure resultant from heating, and flow is compromised.

These results highlight the importance of sieving the reused powder and selecting appropriate processing temperatures. As shown by the cakes processed at different conditions, T_{bp} is equally vital to T_{bed} and must be carefully chosen to avoid sintering during the pre-heating stage as well as to enable powder reuse. By analysing the BFE and SE values shown in Table 10.3 and Table 10.4, a clear difference is found for the cake processed at 286 °C of T_{bp} in comparison to the other powders, and the first needs more energy to be displaced. Similar results were reported by Clayton et al. [328] when investigating BFE values with different ratios of virgin/reused polymer powders. They concluded that any addition of recycled material to the structure could change BFE values, therefore being relevant to describe the flow of virgin/processed polymer powders for AM. In their analysis, however, the changes in flow performance did not vary linearly with the concentration of recycled powder in the sample.

10.2.6 Thermal changes

DSC and TGA analyses were performed to investigate changes in thermal behaviour and degradation with processing. The results are summarised in Table 10.5. The melting curve of the virgin PEKK powder was compared with the PEKK powders processed at different T_{bp} in Fig.10.10.

Table 10.5 Summary of thermal and degradation properties of virgin and processed PEKK powder.

Parameter	Virgin PEKK	Cake powder at 265 °C	Cake powder at 286 °C
Melting temperature (°C)	296 ± 1	301.1 ± 0	306.6 ± 0.4
Integral of the peak (J g ⁻¹)	-29.3 ± 3.3	-30.4 ± 5.1	-19.8 ± 1
Width of the melting peak (°C)	13.9 ± 2.1	10.7 ± 2.0	5.9 ± 1.8
Peak of degradation temperature (°C)	570	571	574

The melting peak is shifting to higher temperatures with processing. Whilst virgin PEKK has an average T_m of 296 ± 1.0 °C, the T_m for the cake processed at 265 °C and 286 °C are, respectively, ~301 °C and ~307 °C. Similar results were obtained with used powder of PA12 [329]. For this material, however, the peak broadens with aging, as reported by Dadbakhsh et al. [176]. In the case of Kepstan 6002 PEKK, the peak becomes narrower with processing and with the increase of T_{bp} , varying from ~14 °C for the virgin PEKK to ~6 °C for the cake powder processed at 286 °C. Such change is supported by the integral values of the peak, as reported in Table 10.5. A plausible explanation for the shift in T_m is the post-crystallisation of the powder exposed to T_{bed} , which may lead to lamellar growth. Regarding the width of the melting peak, it is possibly associated with an increase

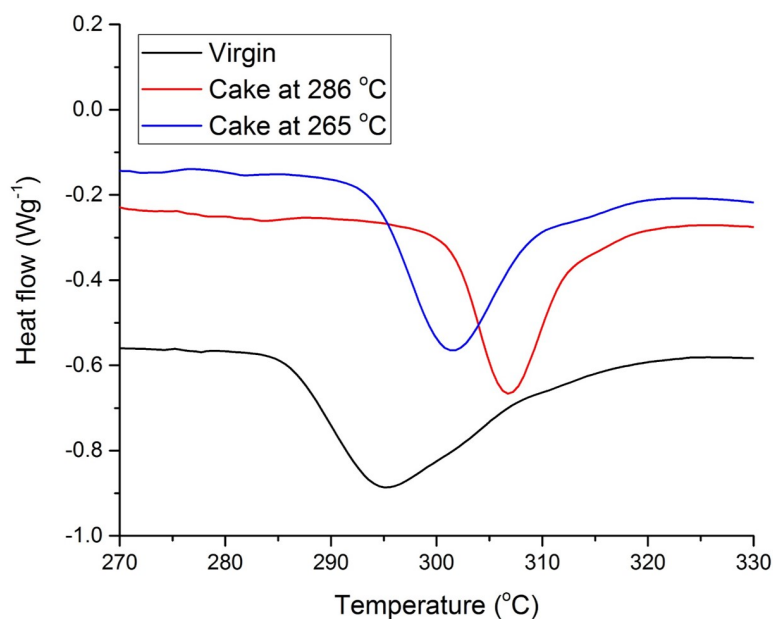


Fig. 10.10 DSC thermoscan of the heating curve for Kepstan 6002 PEKK powder processed at different T_{bp} .

in the molecular weight with ageing [176]; the M_w data for Kepstan 6002 PEKK is shown in Appendix D.

Changes in degradation with powder reuse were also conducted using TGA; the results are shown in Fig.10.11. The mass loss with degradation is approximately 37% for virgin and processed cake powders, and no significant differences can be observed in the profiles of Fig.10.11(1). The first derivative curves, however, suggest an increase in degradation temperature with processing, from 570 °C for the virgin PEKK powder to 574 °C for the cake powder processed at T_{bp} of 286 °C. The change in degradation temperature of virgin and processed cake powder at 265 °C is minimum; this supports the need for a careful selection of T_{bp} to avoid changing in the polymer chemical structure after processing.

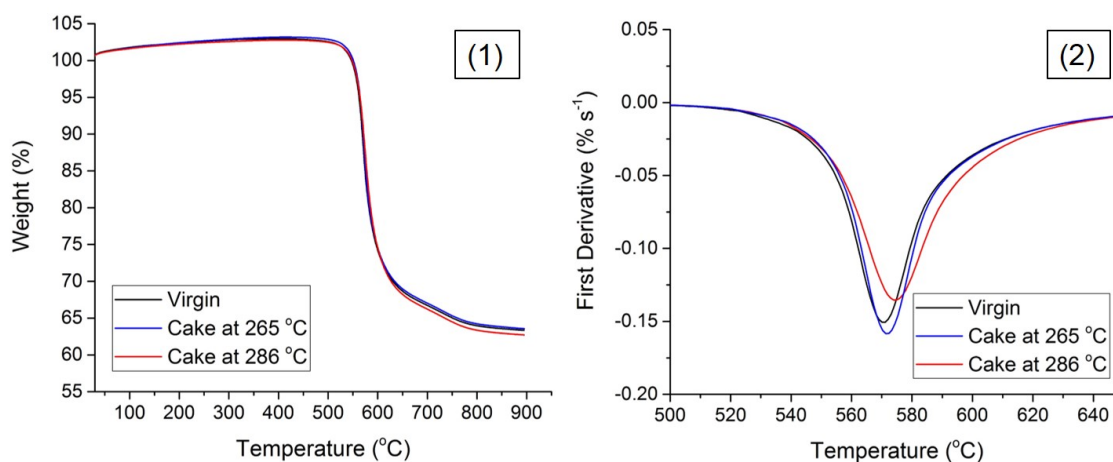


Fig. 10.11 (1) TGA profile of Kepstan 6002 PEKK powder processed at different T_{bp} and (2) the first derivative of the TGA curves.

10.2.7 Crystallisation changes

Due to the amorphous behaviour of Kepstan 6002 PEKK powder when cooled at standard rates, crystallisation was investigated in isothermal conditions, as described in Section 3.3.6.2. The half-time crystallisation curve, which is the curve that measures the time taken to crystallise to half of the maximum crystallisation at different isotherms, is shown in Fig.10.12 for virgin and processed Kepstan 6002 PEKK.

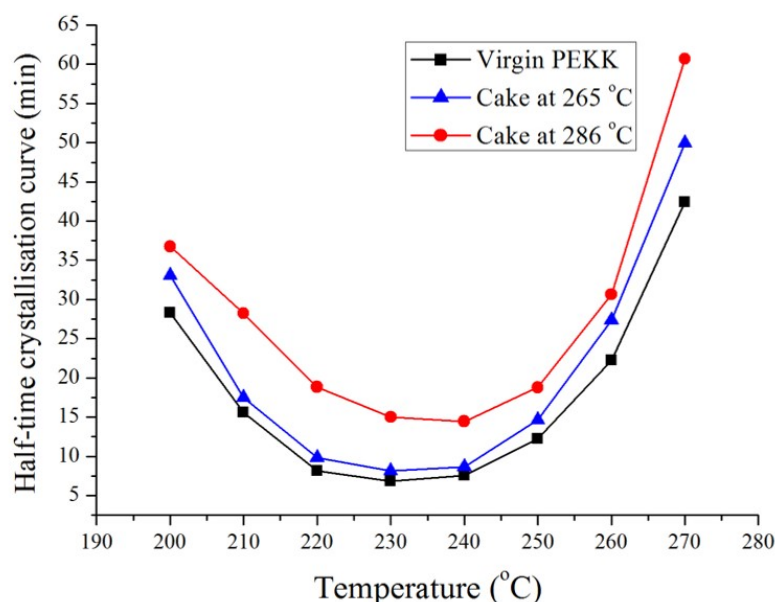


Fig. 10.12 Half-time crystallisation curve of Kepstan 6002 PEKK powder before and after being processed at different T_{bp} .

The kinetics of crystallisation change with processing and T_{bp} , and the cake powder subjected to T_{bp} of 286 °C takes at least 7 min longer to crystallise at the region of the maximum rate of crystallisation. This difference is reduced at higher temperatures as more heat is given for chain mobility, and increases at lower temperatures. Previous works [330, 331] identified an increase in molecular weight, hence viscosity, with powder reuse and an increase in processing temperatures. Such a phenomenon is also applied to Kepstan 6002 PEKK as by increasing M_w (see Appendix D), chain organisation is hindered at lower temperatures of crystallisation.

Wudy and Drummer [330] found a delay on crystallisation with temperature increase and powder reuse. According to them, the reduced molecular mobility with increasing M_w requires that polymer backbones are closer to each other to create a crystalline structure. The approach of the polymer backbones occurs at lower temperatures, hence explaining such a reduction in the temperature of crystallisation. This phenomenon would also explain the delay on crystallisation observed for the cake powder of Kepstan 6002 PEKK.

The change in the crystallisation kinetics of PEKK with the increase of T_{bp} might affect the crystal lattice of this polymer, as M_w changes. Therefore, WXR D was performed using the methodology described in Section 3.3.9. The WXR D scans of the cake powders were compared with the virgin PEKK in Fig.10.13.

The virgin PEKK powder shows a shallow peak at (010) attributed to form II [13]. As the melting of the cake powder is minimum and only occurs on the surface of the particles, the less evident (010) peak in the cake processed at 286 °C and the absence of form II in the cake processed at 265 °C are a result of cold-crystallisation. This phenomenon is occurring in the powder exposed to processing temperatures above or within the crystallisation range of PEKK. The exposure to T_{bed} and T_{bp} followed by cooling during or after manufacture leads to recrystallisation of the chains into a more organised structure known as form I.

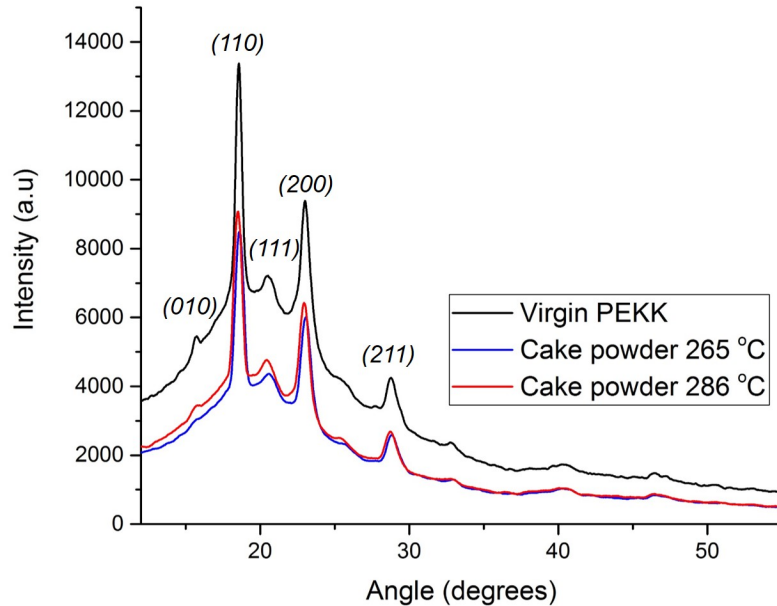


Fig. 10.13 WXR D spectra of Kepstan 6002 PEKK powder before and after being processed at different T_{bp} .

Interestingly, the exposure of the cake powder to higher temperatures (286 °C) maintained part of the structure present in the virgin PEKK powder. As 286 °C is located in the onset of the melt of PEKK, cold-crystallisation takes place in the cooling stage of the process (Fig.9.3(3)), which is significantly faster than the potential recrystallisation during manufacturing (Fig.9.3(2)). The rapid cooling prevents the complete reorganisation of form II into form I, therefore still visible in the spectrum of the cake powder processed at T_{bp} of 286 °C. For the cake processed at T_{bp} of 265 °C, cold-crystallisation occurs during manufacture, in which sufficient time is given for the alignment of the chains into form I, the most stable crystalline form of Kepstan 6002 PEKK.

The degree of crystallinity measured with WXR D for each condition is compared in Fig.10.14. The difference in the level of crystallinity for the cake powders is insignificant but slightly higher than for the virgin PEKK powder. Although negligible, this might infer that the thermal history of the powder is changing slightly with processing.

10.3 Conclusions

Understanding powder behaviour and the effect of temperature on its properties is crucial to select appropriate processing temperatures in LS and enable powder reuse.

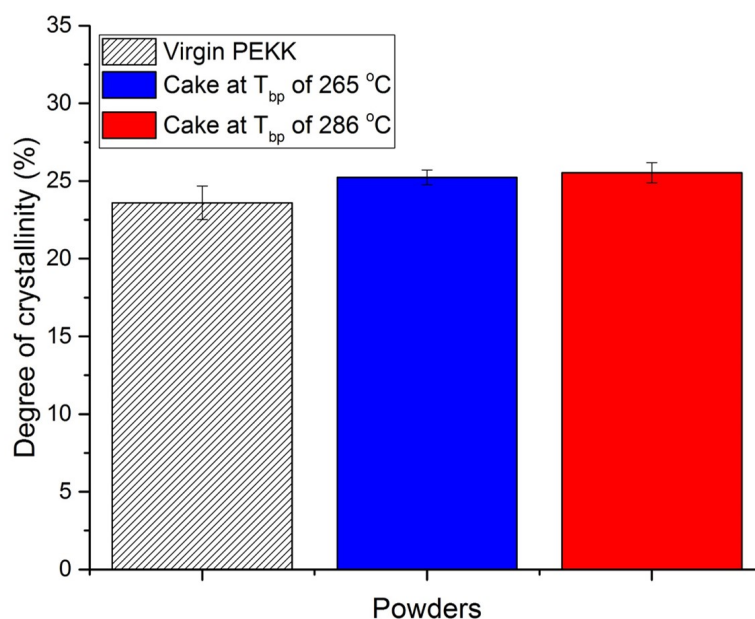


Fig. 10.14 Average degree of crystallinity of Kepstan 6002 PEKK powder processed at different conditions and compared with the virgin powder.

This chapter uses a series of characterisation techniques to control powder performance regarding bulk density, flow, thermal properties, and crystallisation.

The set of results infer that processing temperature can have a more significant effect in powder behaviour than the reusing process itself, as shown by the more significant differences between the cake powders processed at different T_{bp} than if comparing virgin PEKK powder with the cake powder exposed to T_{bp} of 265 °C. The increase of T_{bp} to the onset of the melt (286 °C) reduced bulk density as the particles shifted to larger size distribution. A closer investigation reveals semi-sintered particles in the cakes, which compromise particle morphology and powder flow and stability results. Furthermore, the particles subjected to processing showed an irregular surface in the nanometre scale, not observed for the virgin PEKK powder under SEM. The SEM images also revealed a fibrillar network in the interstices of the powder cake. It is possible that prolonged exposures to temperatures near the melt of the polymer creates these fibrils and can change the powder's ability to flow.

From a thermal perspective, T_m is slightly shifting to higher temperatures after being processed by LS; a similar phenomenon is observed for the degradation temperature. The changes in thermal behaviour are also affecting crystallisation, and particles processed at T_{bp} of 286 °C take longer to crystallise than the other conditions. This slower kinetics of crystallisation, however, does not affect the LS process as the cooling stage in LS is significantly longer than the time required to crystallise Kepstan 6002 PEKK, reused or not. The crystalline structure is also different, and the cake processed at T_{bp} of 286 °C seems to have part of the polymer chains organised into form II, known as the form obtained from cold or solvent crystallisation [13]. This peak is present in the virgin PEKK powder, but not in the cake processed at T_{bp} of 265 °C, in which cold-crystallisation occurs, and the chains crystallised in form II are reorganised into form I.

It is fundamentally important to sieve the powders before reuse to avoid agglomerated particles affecting powder stability and flow. For higher processing temperatures, more aggressive sieving is required to break the semi-sintered particles apart. It is important to notice, however, that a T_{bp} of 286 °C is significantly above the usual T_{bp} applied to process PEKK. Like any other polymeric powder, PEKK is susceptible to changes at higher temperatures, as shown in this study. By maintaining T_{bp} at the ideal range, e.g., 265 °C, such aggressive sieving is not required. Finally, PEKK particles of any condition (virgin or processed) present an irregular morphology and undesired shape for LS. Nevertheless, these properties do not prevent flow or manufacturing, as supported by the study developed in this chapter.

Chapter 11

Conclusions and Future Remarks

11.1 General Conclusions

The present thesis comprises an in-depth study relating PEKK physico-chemical properties, particle and powder behaviour, and the HT-LS process, to optimise final LS part performance by fundamentally understanding intrinsic material characteristics.

Kepstan 6002 PEKK [12] for LS was a PEKK grade under development by Arkema until 2019 when it became commercially available under the name of PEKK HPS1. This study contributed to identifying the capability of this material when processed by HT-LS and successfully optimised PEKK polymer to achieve outstanding performance never obtained with LS of PAEKs in literature.

The first part of this thesis focused on investigating particle/powder properties of three different grades of Kepstan 6002 PEKK - HL1327, P12S959a, and HL1320. Particle characteristics such as size, distribution, and morphology were measured and associated with bulk density, flow performance, and moisture uptake of the PEKK powders in the analysis. Then, these properties were assessed at processing temperatures (T_{bed}) in HT-LS and during coalescence, with the assistance of a hot-stage microscope. High heating rates were applied, and different substrates were tested, including PEKK films, to simulate the LS process. Furthermore, individual particles were monitored during the melt, and shape was accounted for by measuring particle size in terms of the perimeter. These characterisation techniques were able to determine the most suitable grade for LS, HL1327, to then optimise the process. Lastly, the thermal properties of PEKK, crystallisation, in particular, were investigated by DSC and WXR analysis to conclude material characterisation.

The second part of this study focused on the optimisation of the HT-LS process for Kepstan 6002 PEKK by applying different combinations of laser parameters, processing temperatures, and multiple laser exposure and assessing their effectiveness in part consolidation, mechanical properties, surface roughness, and crystallisation. The changes were assessed with respect to final part properties and material behaviour, therefore comprising a complete investigation of the relationship process-material. As part of process optimisation, multiple laser exposures were explored using an *in situ* step-by-step mode.

Chapter 8 used the information obtained with PEKK particle/powder characterisation in combination with process optimisation to develop an equation and explore the leading causes for shrinkage during cooling in LS. This research deepened into fundamental material differences, the effect of each property, and discusses how to mitigate or control shrinkage of PEKK by comparing it with the well-established Orgasol PA12 grade.

As part of the optimisation process, a novel route was developed to improve the poor elongation commonly obtained with LS. This methodology combined the careful selection of the processing temperatures with the slow kinetics of crystallisation of PEKK to improve the elongation at break by interrupting the cooling stage in HT-LS. With this method, Kepstan 6002 PEKK specimens were able to achieve striking elongations at break of up to 14%. A close investigation into material crystallisation revealed significantly slower crystallisation kinetics of LS PEKK than the isothermally crystallised specimens in the DSC. Furthermore, spherulites growth was directly related to the final mechanical

properties of the LS specimens. This study demonstrates the enormous potential for a wide range of "heat treatments" to be used in LS to tailor the ultimate mechanical properties. It is also the first study to highlight the differences between crystallisation models and the crystallisation within LS with experimental LS data.

Lastly, powder reuse was investigated to help reducing feedstock cost. The physical and chemical properties of reused powders were compared with the virgin PEKK powder. The results highlight the importance of selecting appropriate processing temperatures, which in this study had a more significant effect in final powder performance than the reuse cycle itself. An investigation on the physical and chemical properties support the recycling capability of PEKK, extremely desired for industrial application.

The optimisation of PEKK grade resulted in successful performance in LS. The excellent performance is supported by the recent launching of the commercially available PEKK HPS1 grade. This thesis helps in understanding some unique properties of PEKK and the multiple advantages attained with processing this grade with optimised parameters in LS. The methodologies and procedures developed in this research project increase the knowledge of PEKK, HT-LS, and the effect of material-process at the academic level and can be extended to multiple areas of study, including particles, polymers, and process. The characterisation and optimisation results have a clear industrial application and can facilitate further development in the manufacturing, design, and performance of final parts, therefore contributing to innovation in AM.

11.2 Specific Conclusions

11.2.1 Powder and particle behaviour at room temperature

The grades under development supplied by Arkema were characterised regarding particle and powder behaviour at room temperature. Particle size distribution, surface area, flow, stability, and bulk density were assessed, followed by thermal and crystallisation behaviour of powder samples. Three different PEKK grades were evaluated and compared with commercially available LS grades. The comparison aims to assist the selection of the most suitable PEKK grade for LS.

The morphology of HL1327 is very similar to HL1320 particles, which present a rough surface and a porous structure. P12S959a and PEK HP3 particles have a fully solid interior and a smooth surface. When compared to Orgasol PA12, all these grades show more convex morphology and broader size distribution. Except for P12S959a, all PAEKs present similar distribution with D(50) of $\sim 55 \mu\text{m}$. Orgasol PA12 has an average D(50) of $\sim 37 \mu\text{m}$, whilst P12S959a has a D(50) of $84.7 \mu\text{m}$. The increase in particle size for the latter grade significantly affects stability and flow despite the smoother surface and the solid structure. As particles are larger and denser, more energy is required to displace them, therefore harder to promote flow. On the other hand, rough surface, as shown by HL1320 and HL1327 grades, compromise packing and may cause interlocking. From the data,

however, rough but smaller particles, as observed for HL1327 and HL1320 grades, are preferable over larger particle size, as shown by P12S959a.

The high chemical resistance of PAEKs is supported by the moisture uptake analysis performed in Chapter 4. When assessing flow, moisture seemed to have filled the interstices of HL1327 and HL1320 particles, assisting flow by preventing interlocking. PEKK powders subjected to drying performed worse in terms of flow; this can be explained by agglomeration resulting from interparticle forces acting in the system.

11.2.2 Particle and powder behaviour during coalescence and at processing temperature

Coalescence was investigated for a pair of particles under high heating rates ($120\text{ }^{\circ}\text{C min}^{-1}$) and over different substrates using HSM. The results suggest that particles shrink from $8\text{ }^{\circ}\text{C}$ before melting and reduce up to 30% in perimeter size. This shrinkage is followed by an expansion driven by viscous flow. This phenomenon was not caused by the porous structure of two of the PEKK grades, as it was observed for all the grades on different substrates. Literature seems to attribute this behaviour to the recovering of elastic deformation of the chains just before melt [208, 206, 205].

Regarding the method of analysis, perimeter seems to give more accurate results when measuring the changes in dimensions of highly irregular particles as the grades in this study. The values of the perimeter, however, were assessed with changes in temperature, as mentioned by Pokluda [194]. Particles on top of glass and glass coated silicone substrates presented similar trends for neck growth, and so did the PEKK particles monitored on top of PEKK film until they reach $(T+4)$. After $(T+4)$, these particles suddenly 'sink in' the film and prevent further analysis. From the beginning of the analysis until melt takes place, the use of different substrates does not seem to affect neck growth, and any change is overlapped by particle size and shape differences. The distinct behaviour of PEKK grades can be explained by viscosity and particle size; the lower the viscosity (HL1320 grade), the faster is coalescence, and larger particle size prolongs the time to complete coalescence (P12S959a grade).

The results obtained by experimentally monitoring coalescence shows a delay if compared to the models from literature [197, 332]. This discrepancy is explained by the shrinkage observed before the melt, which draws particles apart and continuously acts as a barrier whilst the neck is being formed. In addition to shrinkage, the neck can be delayed in the later stages of coalescence due to the diffusion of chains across the interface and the establishment of an equilibrium distribution of chain entanglements [206].

Particle and powder characterisation at room temperature, and while melting occurs, led to the selection of HL1327 grade for LS optimisation. This selection considered particle size distribution, the higher viscosity, which can lead to a higher mechanical performance of final LS parts, and the similar flow rate index to PEK HP3 powder. Furthermore, melt compounding is required to produce fully solid particles such as the ones from P12S959a

grade, which significantly increases production time and cost, therefore not desired for scaling up to industrial needs.

HL1327 particle were also investigated at processing temperatures ($T_{bed} = 292\text{ }^{\circ}\text{C}$) over prolonged periods of six hours under HSM. The results point to an insignificant decrease in dimension dependent on unique particle morphology and size.

11.2.3 Crystallisation properties of PEKK

DSC tests were performed at dynamic and isothermal conditions for Kepstan 6002 PEKK (HL1327 grade). The dynamic DSC presents a melting peak at $\sim 300\text{ }^{\circ}\text{C}$ for the PEKK grades, which is $\sim 70\text{ }^{\circ}\text{C}$ below the PEK HP3 melting peak. At standard cooling rates, PEKK shows a completely amorphous structure; however, a shallow crystallisation peak is obtained below $2\text{ }^{\circ}\text{C min}^{-1}$. The first derivative of the heating scan was applied [18] to determine the processing temperature of PEKK. The minimum of the derivative corresponds to $292\text{ }^{\circ}\text{C}$, the chosen T_{bed} for future LS trials.

Isothermal DSC analysis was conducted to investigate crystallisation of PEKK. The isothermal curves indicate a maximum rate of crystallisation around $230\text{ }^{\circ}\text{C}$ and a prolonged time above 30 min to achieve half of the maximum crystallisation at isotherms of $200\text{ }^{\circ}\text{C}$ and $270\text{ }^{\circ}\text{C}$. The WXR analysis supports the results obtained with DSC, and the degree of crystallinity of PEKK is approximately 30%. The spectra of PEKK powders presented a shallow peak at 15.6° , which was attributed to the presence of form II in the structure.

11.2.4 Process optimisation

The HT-LS process was optimised for HL1327 PEKK grade. Different combinations of laser parameters were investigated at T_{bed} of $292\text{ }^{\circ}\text{C}$ and T_{bp} of $265\text{ }^{\circ}\text{C}$. The optimised ED of $\sim 23.53\text{ mJ mm}^{-2}$ (power: 12 W; scanning speed: 2550 mm s^{-1} ; hatching spacing: 0.2 mm) resulted in an outstanding tensile strength of 91 MPa and an elongation at break of 2.6% for specimens built in X orientation; the flexural and compressive strength results support such results. The specimens built in Z orientation, however, had their strength compromised by half; this supports the anisotropic behaviour caused by the layer-by-layer nature of LS. The poor elongation at break results in a flat failure characteristic of brittle materials. However, for the specimens built in X orientation, localised plastic zones were found. These specimens also presented the highest elongation at break, the lowest surface roughness, and the lowest porosity content.

The prolonged time for coalescence and adhesion between layers caused by increasing T_{bp} to $286\text{ }^{\circ}\text{C}$ led to significantly lower mechanical performance and completely brittle behavior. Despite the less porous structures, the increase in surface roughness led to cracks initiation from the surface of the specimens. A possible explanation for surface roughness increase is the partial sintering of particles on the top and in the bottom layers in contact with the specimens, caused by a T_{bp} corresponding to the onset of the melt of PEKK. The increase in T_{bp} also led to an increase in the diameter of the spherulites, from 2.8 - 5.8 μm at T_{bp} of $265\text{ }^{\circ}\text{C}$ to 3.7 - 7.5 μm at T_{bp} of $286\text{ }^{\circ}\text{C}$.

The multiple scan exposures experiments reveal a worse mechanical strength but similar elongation at break for the specimens subjected to multiple scan counts but the same final ED. The SEM analysis of the film's surface presents a porous structure when the first scan has a laser power of 3 W. Above 3 W, micro-pores are still found but in a less continuous pattern. The mechanical strength seems to contradict porosity values and is higher for (3+9) W than (8+4) W specimens. Furthermore, double laser exposure does not seem to reduce surface smoothness. The exposure to three scan counts, however, showed significantly worse performance.

11.2.5 Shrinkage in laser sintering

One of the major issues in LS is the shrinkage associated with the process [257, 258, 103]. When curling and warping are under control, shrinkage is usually compensated by adding scaling factors to the parts, which vary according to part orientation and material selection. The present work developed an equation to measure the main factors causing shrinkage of PEKK produced by LS - thermal retraction, crystallisation, and powder bulk. These factors were determined using different characterisation methods in combination with the production of LS PEKK parallelepipeds of different heights. The shrinkage in X and Y orientations vary between 1.1 to 1.4% but strongly depends on the height for Z orientation. Whilst an expansion is observed at heights of 10 mm due to upskin and downskin effect, a plateau of $\sim 3\%$ is obtained above 40-50 mm height, which leads to a total volumetric shrinkage of 5.45%. These values are lower than measured for Orgasol PA12 and are possibly associated with the higher degree of crystallinity of this polymer in comparison to PEKKs. The thermal retraction of PEKK is minimum (0.55%), whilst shrinkage resulting from crystallisation is approximately 1.8%, 2.6 times lower than for Orgasol PA12. The shrinkage due to bulk density, however, is almost twice as large for PEKK than for PA12, corresponding to 58% of the total LS shrinkage. These results are supported by the lower bulk density of PEKK resulting from its irregular particle morphology and highlight the significant differences in shrinkage values for different materials with distinct crystallisation and bulk properties.

11.2.6 Crystallisation affecting the performance of LS PEKK

The brittle failure characterised by reduced or nonexistent plastic regions of LS PEKK specimens led to the development of a novel route to improve elongation at break. The experiment idea consisted of providing different cooling times by interrupting the LS process and quenching the specimens in water. Specimens with cooling times varying from 0 to 10.75 h were produced. The elongation at break reached up to 14% at one hour of cooling, striking values never achieved in literature for LS PAEKs. At 6.25 h of cooling, an average elongation at break of 6% is achieved with a slight reduction in strength when compared to the standard LS process. The elastic modulus at this cooling time is of 4 GPa, supporting the high performance of PEKK. The fracture analysis reveals a mixture of ductile and brittle failure from 4.75 h of cooling and shifts to an even more ductile

behaviour at lower cooling times. The specimens located in the middle of the build setup present a linear behaviour in terms of mechanical performance; such behaviour slightly changes in the edges of the build (top and bottom groups).

The degree of crystallinity linearly decreases with the reduction in the cooling time, as expected. The higher the strength, the higher the degree of crystallinity, and the lower the elongation. It seems, however, that specimens with a degree of crystallinity above 25% showed a lower mechanical strength as well as lower elongation; this was associated with secondary crystallisation. At 6.25 h of cooling time, a crystallinity of $\sim 16\%$ is obtained, which is reduced to $\sim 11\%$ at one hour and 5.4% at no cooling time.

The kinetics of crystallisation of isothermally crystallised samples in the DSC were compared with the LS process. The results highlight the striking difference in the time required to crystallise the same amount of the structure with LS, approximately ten times longer. This increase is mostly justified by the punctual heat applied by the laser, the complex heat transfer between LS layers, and the increase in the molecular weight of PEKK with processing.

The crystalline structure was investigated. The diameter of the spherulites drastically changes with cooling time. At ten hours of cooling, the spherulites show a similar pattern to the crystal structure obtained at standard LS process, with a uniform diameter varying between 5.4 to 5.7 μm . At cooling times of 5.5 h, the crystal structures are significantly larger and achieve 16.6 μm of diameter. The increase in diameter is justified by the reduced impingement of the spherulites (larger amorphous regions). The different structure observed in the core of the spherulites can be attributed to insufficient time for secondary crystallisation to occur due to cooling interruption. The sudden quench is even more pronounced for the specimens with no cooling time, in which the unstable nuclei redissolved in the molten structure. The WXR analysis reveals form II for the specimens subjected to cooling times equal or below 3.25 hours.

11.2.7 Recyclability of PEKK powder

Recycling polymer powder is crucial to reduce the production cost of polymeric parts and to broaden the market for polymeric powders with high-performance properties. For these reasons, powder reuse was assessed regarding particle and powder structure and physical and chemical changes. Virgin HL1327 powder was compared with cake powder subjected to different T_{bp} : 265 and 286 °C. The bulk density measurements reveal a less packed structure for reused powders; these results are supported by the increase in particle size led by the partial sintering of particles subjected to processing. The partial sintering can be disrupted by regular sieving applied to the powder processed at T_{bp} of 265 °C. The powder processed at T_{bp} of 286 °C, however, presented partially sintered particles even after sieving, affecting stability and flow rate data as more energy is required for powder displacement.

The melting peak narrows and slightly shifts to higher temperatures with processing; the latter was also noticed for PA12 powders [329]. The degradation curves are very similar

in shape; however, an increase in degradation temperature is observed for PEKK processed at T_{bp} of 286 °C. The crystallisation time significantly increases with higher processing temperature and takes at least 7 min longer to crystallise half of the maximum crystalline structure at the region of the maximum rate of crystallisation (~ 230 °C). Despite the slight increase in the degree of crystallinity between virgin and reused powders (23.6 to 25.2%), the cake powders do not show any significant difference between themselves. The WXR spectrum for the virgin PEKK powder reveals the presence of form II; this form is less pronounced in the cake processed at 286 °C of T_{bp} , and non-existent in the cake processed at 265 °C. This change in the crystalline structure reveals that cold-crystallisation is taking place during and after exposure of the cake powder to T_{bed} and T_{bp} . In conclusion, PEKK can be successfully recycled by choosing appropriate processing temperatures. Before recycling, however, sieving is recommended to loosen the particles and break agglomeration, therefore assisting powder flow.

11.3 Limitations

11.3.1 Limitations of experimental methods

Despite the successful development and application of different methods applied in this thesis, some limitations were found:

- The quantitative description of powder flow and bulk density measurements performed using Freeman FT4 powder rheometer are often difficult to interpret due to several properties (particle texture, size, porosity, etc.) affecting the data simultaneously;
- The monitoring of coalescence requires a lot of manual work which prevents the analysis of larger sample sizes to reduce experimental errors;
- The investigation of a pair of particles does not represent the coalescence process taking place in HT-LS, in which multiple particles are coalescing simultaneously and in a different environment condition from HSM experiments. These factors prevent a defined correlation between coalescence data and the LS process;
- Several complex factors affect powder bulk. They are difficult to be isolated when measuring shrinkage during cooling. Therefore, shrinkage due to powder bulk was not experimentally validated, but calculated from the other factors in the equation developed to assess shrinkage in LS;
- The improved elongation values achieved by varying cooling time in LS do not apply to an industrial setup, although extremely valuable as a calibration methodology.

11.3.2 Limitations of PEKK optimisation for HT-LS

The commercially available PEKK HPS1 showed successful properties for LS application. The characterisation and optimisation results, however, highlight some areas of improvement to reduce processing issues and optimise final performance.

The stability, flow, and bulk density performance of Kepstan 6002 PEKK are not yet optimised for LS; this becomes clearer if compared to the flow and stability results achieved with Orgasol PA12 powder, a commercial and well-established LS grade. Despite the successful recoating at high processing temperatures, the relative poor flow performance of PEKK can block the hopper damper after long hours of manufacturing, and powder can agglomerate around the spreading mechanism, as shown in Fig.11.1. Powder agglomeration in the hopper damper and around the recoater is possibly caused by interparticle forces in contact with the metal surface from the hopper damper and the recoater. As already mentioned, hopper blocking is only observed when Kepstan 6002 PEKK powder remains in the hopper for prolonged periods, therefore aggravating the effect of powder compaction and of the slightly higher temperatures in which the powder inside the hoppers is exposed.

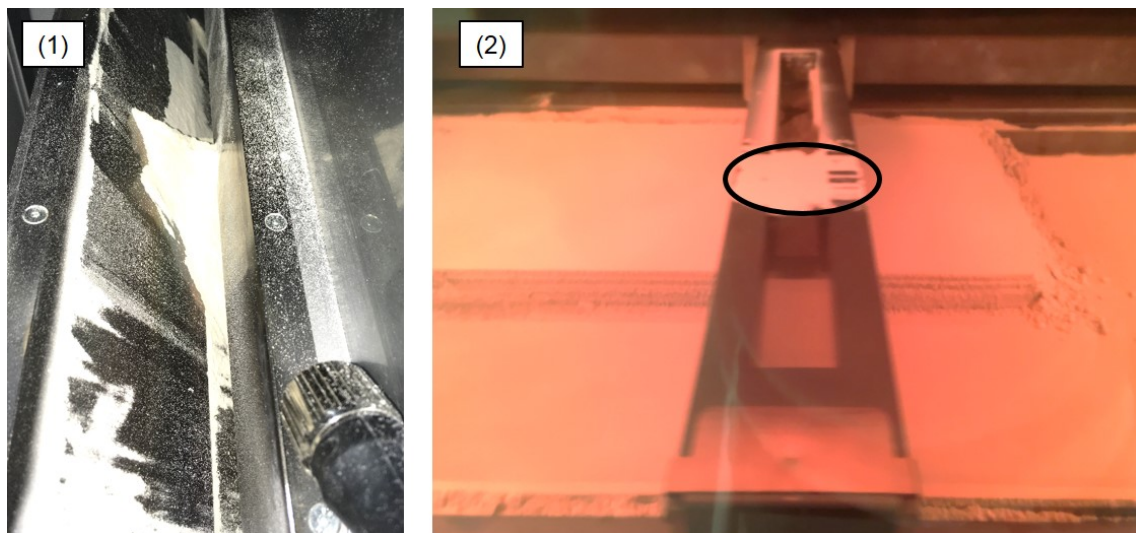


Fig. 11.1 Virgin PEKK powder agglomerating in the (1) hopper damper and (2) around the recoater during manufacturing using the EOS P 800 system.

Spherical particle morphology can reduce interparticle forces and prevent interlocking in the hopper and around the recoater. However, the surface roughness of the particles must be improved whilst maintaining the desired particle size for LS. Sachs et al. [86] developed a methodology to produce spherical particles for LS application described in Section 2.3.5. The use of a downer reactor may offer a cheaper and better alternative than melt-compounding. Another method to improve flow can be the inclusion of flowing additives, e.g., silica, to the powder bulk.

Chapter 9 showed outstanding mechanical performance data acquired with controlled cooling time in LS. Despite the improved elongation, cooling time cannot be controlled in a standard HT-LS process, and the procedure used in this work cannot be replicated on an industrial scale. Additional post-processing steps would be required to translate

the results into an industrially feasible process. Appendix C presents a method developed with the attempt to replicate the crystallisation behaviour achieved with the best specimens subjected to quenching in water. This attempt, however, did not succeed in improving the final performance. Alternatively, a collaboration between industry and academia can be developed to tailor the HT-LS systems (variable cooling time and cooling rate) to specific material properties. By acquiring a more controlled process, issues such as warping and large deviations in the mechanical properties can be addressed.

11.4 Future Work

This research project provided new insights and valuable information on HT-LS of PEKK. The following topics may guide upcoming studies with the same or similar PAEK materials.

- Interparticle forces not explored in this work seem to fundamentally affect powder packing and flow. Some examples of relevant interparticle forces for this study include friction and interlocking, which directly affect particle movement. Tensile strength is a commonly employed parameter to measure these interparticle forces [3] and can be applied to the PEKK grades used in this research;
- Powder flow was only assessed at room temperatures. The flow promoted by the recoater during LS, however, occurs at processing temperatures, a factor that can drastically affect performance. A powder spreader set-up operating at LS processing temperatures was developed and adapted by Van Den Eynde et al. [136, 151]. An equivalent or similar system can be used to assess flow properties of PEKK particles and experimentally simulate the HT-LS process;
- The coalescence study performed using HSM is not able to replicate the HT-LS. Besides only being applied to a pair of particles, the heat from the hot-stage platform differs from the punctual laser heating in LS, and only 2D images of the particles can be obtained. With the attempt to address many of these limitations of HSM analysis, Hejmady et al. [225] developed a complex system to monitor 3D coalescence in LS using a laser beam and a heated chamber. Such systems are preferred to associate the coalescence behaviour of this study with HT-LS, and could provide a more reliable description of particle interaction, neck formation, coalescence, and growth;
- Mechanical performance can be further optimised by varying T_{bp} . It is possible that reducing T_{bp} to near the crystallisation of PEKK not only increases elongation at break whilst maintaining mechanical strength but can assist in preserving thermal and crystallisation properties of the powder;
- All the specimens in this study were tested as removed from the system. As highlighted in this work, the crack can be initiated from the surface, hence polishing the

specimens before testing may increase performance and avoid surface defects to propagate throughout the PEKK structure;

- Considering the resulting calibration curve obtained for PEKK subjected to different cooling times, novel routes can be explored to achieve similar performance in an industrially scalable process. These routes can be developed inside the process by changing processing temperatures or the LS cooling set-up. Alternatively, adding post-processing stages can optimise PEKK performance according to the application needs;
- The discrepancy in the crystallisation time of isothermally crystallised samples in comparison to HT-LS specimens reveals the need to develop crystallisation models tailored to the LS process. The models should be validated with experimental LS data as provided in this work.

Appendix A

Summary of Coalescence Mechanisms driven by Viscous Flow

Table A.1 Analytical solutions and numerical studies to predict particle coalescence driven by viscous sintering.

Study	Method	Theory Description	Assumptions	Conclusions
1945, Frenkel [183]	Analytical	<ul style="list-style-type: none"> $\left(\frac{y}{a_0}\right)^2 = \frac{3}{2} \frac{\Gamma t}{\eta_0}$ Viscous flow under the action of surface tension 	<ul style="list-style-type: none"> Two identical spheres with constant radius Volume is constant through time Small dihedral angle 	<ul style="list-style-type: none"> The model is only valid for early stages of sintering Conservation of mass is not satisfied
1949, Frenkel-Eshelby [193]	Analytical	<ul style="list-style-type: none"> $\left(\frac{y}{a_0}\right)^2 = \frac{\Gamma t}{\eta_0}$ Frenkel model satisfying conservation of mass 	<ul style="list-style-type: none"> Constant strain rate Constant elongation flow 	<ul style="list-style-type: none"> Only valid for early stages of sintering
1949, Mackenzie and Shuttleworth [184]	Analytical	<ul style="list-style-type: none"> $\frac{dp}{dt} = \frac{3}{2} \left(\frac{4\pi}{3}\right)^{1/3} \frac{\gamma n^{1/3}}{\eta} (1-p)^{2/3} p^{1/3}$ [1] $\frac{dp}{dt} = \frac{3}{2} \left(\frac{4\pi}{3}\right)^{1/3} \frac{\gamma n^{1/3}}{\eta_\infty} (1-p)^{2/3} p^{1/3} \left[1 - a \left(\frac{1}{p} - 1\right)^{1/3} \ln\left[\frac{1}{(1-p)}\right]\right]$ [2] Flow with Newtonian [1] or Bingham Solid behaviour [2] Model to describe later stages of sintering 	<ul style="list-style-type: none"> Pores as equal spheres Uniform densification Newtonian behaviour or Bingham solid behaviour 	<ul style="list-style-type: none"> Pores interactions are crucial to understand final consolidation Viscous models are not able to explain the sintering of metals
1955/1959, Kingery and Berg [333, 195]	Analytical	<ul style="list-style-type: none"> $\frac{\Delta L}{L_0} = \frac{1}{3} \frac{\Delta V}{V_0}$ Describes the rate of approach of the centres of two spheres at the initial stage of sintering 	<ul style="list-style-type: none"> Volume diffusion as the main mechanism driving sintering Neck curvature is considered a tangent of circle models Particles are spherical 	<ul style="list-style-type: none"> Particle approach is dependent of shrinkage rate and time Volume diffusion is dominant for $d > 0.05 \mu\text{m}$
1971, Johnson, Kendall and [334] Roberts	Analytical	<ul style="list-style-type: none"> $\frac{x}{a} = \left(\frac{18\pi\gamma(1-\nu^2)}{\alpha E}\right)^{1/3}$ Solve the equilibrium deformation of two elastic bodies under surface tension Experimental validation with spherical rubber particles, and flat latex particles 	<ul style="list-style-type: none"> Elastic behaviour Time invariant modulus, valid only for early regime or slow coalescence evolution 	<ul style="list-style-type: none"> Theory supports experimental analysis with rubber and gelatine spheres
1976, Cosgrove [198]	Analytical	<ul style="list-style-type: none"> $\left(\frac{x}{R}\right) + \ln\left(1 - \frac{x}{R}\right) = \frac{2t}{t_{visc}}$ Predicts later stages of sintering on a linear array of rods 	<ul style="list-style-type: none"> Locally planar interface 	<ul style="list-style-type: none"> Non-linear behaviour at later stages of sintering, explaining the lower rate of neck grow at this stage

Study	Method	Theory Description	Assumptions	Conclusions
1981, Ross [204]	Numerical	<ul style="list-style-type: none"> • FEM to solve Navier-Stokes Equation for an infinite line of cylinders with their morphology and neck being monitored with time • Viscoelastic effects were considered 	<ul style="list-style-type: none"> • Particle shrinkage is neglected • Starts from $\frac{x}{a} = 0.16$ • Model as two-dimensional 	<ul style="list-style-type: none"> • Model yielded higher neck growth rates due to small radii of curvature at the neck • Frenkel model is not suitable for all sintering stages
1984, Hopper [199]	Analytical	<ul style="list-style-type: none"> • $\frac{x}{a_f} = \frac{(1-\alpha)}{\sqrt{1+\alpha^2}}$ • $\left(\frac{t\Gamma}{\eta_0 a_f}\right)^2 = \frac{\pi}{4} \int_0^1 \frac{1}{(\beta\sqrt{(1+\beta)K(\beta)})} d\beta$ • $K(\beta) = \int_0^1 [(1-x^2)(1-\beta x^2)]^{-1/2} dx$ • Coalescence of two cylinders using Navier-Stokes equation • Viscous flow is driven by capillary forces 	<ul style="list-style-type: none"> • System of two equal particles • Negligible inertial and body forces • Flow is planar • Surfaces behave classically • Initial contact has little effect on subsequent flow 	<ul style="list-style-type: none"> • Good approximation with modeling the coalescence of cylinders
1988/1990, Jagota and Dawson [210, 209]	Numerical	<ul style="list-style-type: none"> • FEM of viscous sintering for two initially spherical particles • Deformation is modelled based on external tractions and local surface tension forces 	<ul style="list-style-type: none"> • Only valid for amorphous materials • Pressure from the boundary has no contribution to sintering. This is only valid for smooth boundary 	<ul style="list-style-type: none"> • Model predicts experimental behaviour well • Frenkel model captures the nature of the velocity field but is quantitatively an error
1991/1992/1993 Hopper [200, 335, 332]	Analytical	<ul style="list-style-type: none"> • Model of viscous coalescence of cylinders driven by surface tension • Based on Stoke's Equation of momentum and continuity for planar flow 	<ul style="list-style-type: none"> • Planar flow • Classical surface traction • Classical boundary condition • Inertial flow is negligible 	<ul style="list-style-type: none"> • The theory is in agreement with experimental observation of glass fibres • To assess coalescence of cylinders, a parametric form for the time-evolving domain was guessed

Study	Method	Theory Description	Assumptions	Conclusions
1994, Mazur and Plazek [206]	Analytical	<ul style="list-style-type: none"> • $\left(\frac{x}{a}\right)_e = \left(\frac{9\pi\gamma(1-\nu^2)J_r(t)}{a(1+\nu)}\right)^{1/3}$ [1] • $\frac{x}{a} = \left(\frac{2\gamma}{\eta_0 a}\right)^{1/2}$ [2] • Study on the role of viscoelasticity in polymer coalescence • Equation [1] to account for the elastic behaviour • Equation [2] to account for the viscous behaviour 	<ul style="list-style-type: none"> • Specific to some M_w, structure and particle size • All volumetric elements experience the same stress history • Boltzmann superposition is negligible 	<ul style="list-style-type: none"> • Stress relaxation is crucial in the equilibration kinetics • Viscous flow becomes important at times on the order of the terminal relaxation time • Coalescence mechanisms differ for larger particles and colloids
1994, Martínez-Herrera and Derby [211]	Numerical	<ul style="list-style-type: none"> • $\frac{\rho\gamma R_0}{\eta^2} \left(\frac{\delta v}{\delta t} + v\dot{\Delta}v\right) = \nabla\dot{T} + \frac{\rho R_0^2 g}{\gamma} e_g$ • FEM to measure the effect of initial geometry on flow and sintering rate • Viscous flow driven by capillary forces to minimise surface area • Particles have initial arbitrary geometry • Flow is driven by gradients of neck curvature 	<ul style="list-style-type: none"> • Incompressible planar flow • Two-dimensional particles • Isothermal flow • Newtonian fluid 	<ul style="list-style-type: none"> • Successful development of an FEM to solve viscous plane flows • Successfully validated with Hopper model • Enables the study of arbitrary initial geometries • Rate of coalescence is quicker for smaller particles than larger ones
1994, Van der Vorst	Numerical	<ul style="list-style-type: none"> • BEM applied to linear or quadratic boundary elements • Creeping flow equations transformed into a system of integral equations • Navier-stokes equations were used for different geometries and packing 	<ul style="list-style-type: none"> • Incompressible Newtonian viscous fluid • Dimensionless Navier-Stokes equations • Two-particle system 	<ul style="list-style-type: none"> • Model shows good agreement with Hopper study, but the neck curvature and time dependence for neck growth differs
1997, Pokluda [194]	Analytical	<ul style="list-style-type: none"> • $\frac{x}{a_f} = \sin(\theta) \left(\frac{2}{[1+\cos(\theta)]^2[2-\cos(\theta)]}\right)^{1/3}$ • Sintering process of two spherical particles • Based on Frenkel-Eshelby approach • Considers particle radius change with time in the coalescence process • Based on the work of surface tension and viscous dissipation • Use of Runge-Kutta-Fehlberg numerical integration for solution 	<ul style="list-style-type: none"> • Gravity and other forces are neglected • Constant density • Extensional flow field • Constant strain rate • Dimensionless time 	<ul style="list-style-type: none"> • Predictions are similar to other models for the early stages of sintering • Better approach to describe the later stages of sintering, especially for viscous-dominant polymer coalescence

Study	Method	Theory Description	Assumptions	Conclusions
1998, Jagota et al. [208]	Numerical	<ul style="list-style-type: none"> • $\frac{r_c}{R} = \left(\frac{9\pi\gamma(1-\nu^2)}{ER}\right)^{1/3}$ [1] • $\frac{\tau}{\tau'} = \left(\frac{3}{4\pi}\right)^{1/3} \frac{\gamma}{RG}$ [2] • Coalescence is described using the Maxwell viscoelastic model, in which [1] considers the elastic contact radius contribution and [2] the viscous time constant 	<ul style="list-style-type: none"> • Spherical particles • Bulk modulus does not change with time • Γ is zero for elements in contact • Poisson's ratio = 0.3 	<ul style="list-style-type: none"> • Two stages in particle coalescence: elastic adhesion and viscous sintering • Two modes of contact growth in viscous sintering: zipping mode, governed by attractive forces and stretching mode, ruled by curvature-based tractions • Particle size affects contact growth led by curvature-based tractions
Bellehumeur et al. [215]	Analytical	<ul style="list-style-type: none"> • $\frac{d\left(\frac{x}{R}\right)^2}{dt} = \frac{-R\gamma - 2t_{visc} + [(3R\lambda)^2 + 4R\lambda t_{visc} + 4t_{visc}^2]^{1/2}}{2(R\lambda)^2}$ • Model following Frenkel's and Pokluda's approach but considering the convected Maxwell constitutive equations to account for viscoelastic behaviour 	<ul style="list-style-type: none"> • Extensional and quasi-steady flow field • Constant density • Constant strain rate 	<ul style="list-style-type: none"> • The use of Maxwell's model in Frenkel's model is able to describe the behaviour observed with the experimental data • Melt elasticity slows down the process
1999, Eggers et al. [336]	Analytical	<ul style="list-style-type: none"> • $\frac{x}{R_0} = -C_{visc} \frac{t}{t_{visc}} \ln\left(\frac{t}{t_{visc}}\right)$ [1] • $\frac{x}{R_0} = -C_{visc} \left(\frac{t}{t_{inert}}\right)^{1/2}$ [2] • Model to predict the early stages of coalescence using Stokes equations • Splits Stokes equations into initial spherical shape [1] and when shape evolves rapidly [2] 	<ul style="list-style-type: none"> • Spherical particles joining each other in their symmetry axis • Zero-stress condition 	<ul style="list-style-type: none"> • Particle shape evolves rapidly in the second stage of sintering • Demonstrates that Hopper model is valid for 3D when changing the constants in the equation • Two-particle system cannot be described by single equation models
2001, Garabedian and Helble [337]	Numerical	<ul style="list-style-type: none"> • BEM to study coalescence of two equal particles in two dimensions • Modified BEM to solve equations for surface velocities • Incorporation of an empirical analytical function to describe the fluid interface throughout the growth process • Provides a basis for multi-particle models 	<ul style="list-style-type: none"> • Invariant internal axial velocity with cylindrical radius, which is valid for outer regions of the particles only • Particles of spherical shape 	<ul style="list-style-type: none"> • The model shows a good agreement with other models found in literature • Guess of geometric evolution of the interface

Study	Method	Theory Description	Assumptions	Conclusions
2006, Scribber et al. [338]	Analytical	<ul style="list-style-type: none"> • $\frac{d\theta}{dt} = \frac{\sigma}{R\mu} \frac{K_2}{K_1^2}$ • $K_1 = \frac{\tan(\theta) \sin(\theta)}{2} \frac{1}{6} \left[\frac{2(2-\cos(\theta))+(1+\cos(\theta))}{(1+\cos(\theta))(2-\cos(\theta))} \right]$ • $K_2 = \left[\frac{2^{-5/3} \cos(\theta) \sin(\theta)}{(2-\cos(\theta))^{5/3} (1+\cos(\theta))^{4/3}} \right]$ • General viscoelastic constitutive model at transient mode by assuming elongational flow 	<ul style="list-style-type: none"> • Homogeneous biaxial extensional flow • Negligible external stresses • Negligible gravitational effects • Internal energy is only a function of surface area • Extension rate is constant over time 	<ul style="list-style-type: none"> • The influence of viscoelasticity is limited to short times • At long times, it converges to a Newtonian solution • Coalescence accelerates by increasing relaxation time
2009, Kirchhof et al. [182]	Numerical	<ul style="list-style-type: none"> • $\frac{d\bar{S}_0}{dt} = K_0 \frac{\bar{N}_k t}{t_{visc}}$ • Fractional VOF to study 3D bridge growth between particles in different arrangements • First stage of sintering described as a function of \bar{N}_k 	<ul style="list-style-type: none"> • Sintering necks are dependent from each other even in first stages of sintering • First stage of sintering is characterised by surface area reduction at constant sintering rate • Later stages of sintering are characterised by dense particle morphologies and faster sintering rate 	
2009, Djohari et al. [339]	Numerical	<ul style="list-style-type: none"> • Meso-scale FEM based on rigorous formulations of coupled equations for continuum transport and interfacial phenomena • Comparison between viscous flow and vacancy diffusion mechanisms 	<ul style="list-style-type: none"> • Negligible inertial and gravitational forces • Isothermal system • Material with isotropic properties • Dihedral angle of 180° 	<ul style="list-style-type: none"> • Coalescence driven by viscous flow gives instantaneous shrinkage and neck growth • When diffusion mechanism is dominant, shrinkage occurs with delay and neck is formed with very little densification until the late stages of sintering
2010, Wang et al. [340]	Numerical	<ul style="list-style-type: none"> • 2D transient simulations employing VOF method to investigate coalescence of two water droplets of equal size on a homogeneous plate surface • Morphology changes were monitored 	<ul style="list-style-type: none"> • Unsteady, isothermal and laminar flow • Heat generation and heat transfer are negligible 	<ul style="list-style-type: none"> • Coalescence is driven by surface tension and pressure gradient • Good agreement with experimental data in the same conditions established by the model
2011, Eggersdorfer et al. [341]	Analytical	<ul style="list-style-type: none"> • Sintering simulation of fractal-like particles using a model conserving volume (Eq. 8) and energy (Eq. 14) • $\frac{dr_i}{dt} = B_i \frac{dd_{ij}}{dt}$ • Model considers two particles with different sizes and irregular multi-particle sintering 	<ul style="list-style-type: none"> • Surface energy is independent from primary particle radius • Extensional flow with complex morphology • Constant strain rate inside the particles 	<ul style="list-style-type: none"> • Aggregate densification is driven by surface area reduction • The change in surface energy equals the energy dissipated by viscous flow • Model was validated qualitatively by investigating amorphous material

Study	Method	Theory Description	Assumptions	Conclusions
2012, Kirchhof et al. [216]	Numerical	<ul style="list-style-type: none"> VOF method coupled with Hamaker summation to investigate sintering of vitreous nanoparticles Experimental validation using high temperature sintering flow reactor and doublet shape analysis in TEM 	<ul style="list-style-type: none"> Negligible intraparticle forces Model limited to initial stages of sintering 	<ul style="list-style-type: none"> Coalescence of vitreous particles is driven by viscous flow and van der Waals forces Nanoparticulate sintering is dominant in particles up to 200 - 300 nm of diameter Sintering kinetics scales with the inverse square of particle radius
2013, Varnik et al. [342]	Numerical	<ul style="list-style-type: none"> Non-ideal LBM applied to simulate 3D coalescence driven by viscous flow The force driving viscous flow comes from the curvature of the contact zone between particles Applicable to pair of particles and multi-particle systems 	<ul style="list-style-type: none"> Meniscus shape is approximated to half circle Negligible explicit time derivative of the fluid velocity at early times of sintering 	<ul style="list-style-type: none"> Simulation showed faster densification than experiment Simulation results are explained by the absence of intergranular friction Model predicts relative density and effective viscosity for multi-particle system
2013, Gross et al. [343]	Numerical	<ul style="list-style-type: none"> Non-ideal LBM to investigate 2D and 3D viscous coalescence of two equal droplets in a saturated vapour phase 	<ul style="list-style-type: none"> Isothermal fluid Pressure varies between zero and the Laplace pressure Smooth variance of velocity 	<ul style="list-style-type: none"> The time evolution of the bridge can be described by a $t^{1/2}$ scaling law Results do not match the available theory of viscous coalescence Results do not match experimental observations
2015, Katsura et al. [344]	Numerical	<ul style="list-style-type: none"> FEM to simulate shape changes of axisymmetric ellipsoidal glass particles in a two particle system during the later stages of sintering 	<ul style="list-style-type: none"> Spheroidal particles evolving under uniform deformation Incompressible flow 	<ul style="list-style-type: none"> Development of a method to determine sintering forces from experiments Radial growth rate is proportional to a stress equal to the sintering force
2016, Wakai et al. [201]	Numerical	<ul style="list-style-type: none"> $F_s = -\bar{P}a + \gamma_s l$ FEM to investigate neck growth and shrinkage of two identical and spherical particles driven by viscous flow 	<ul style="list-style-type: none"> Constant surface energy Radius of curvature is constant near the notch root 	<ul style="list-style-type: none"> Sintering force F_s drives neck growth and shrinkage in a non-equilibrium sintering Anisotropic deformation can be described by the tensor virial equation viscous flow

Appendix B

Polymorphism of PEKK produced by LS

This appendix is a continuation of Section 9.4.3.2, Chapter 9. Further analysis was performed to investigate different crystalline structures of PEKK manufactured by LS and exposed to different cooling times. The samples were analysed under WXR D and DSC, as described in Section 3.3.9 and Section 3.3.6, respectively. Firstly, the measurements were performed on the upper surface of the specimens, which were placed in X orientation. The results are shown in Fig.B.1.

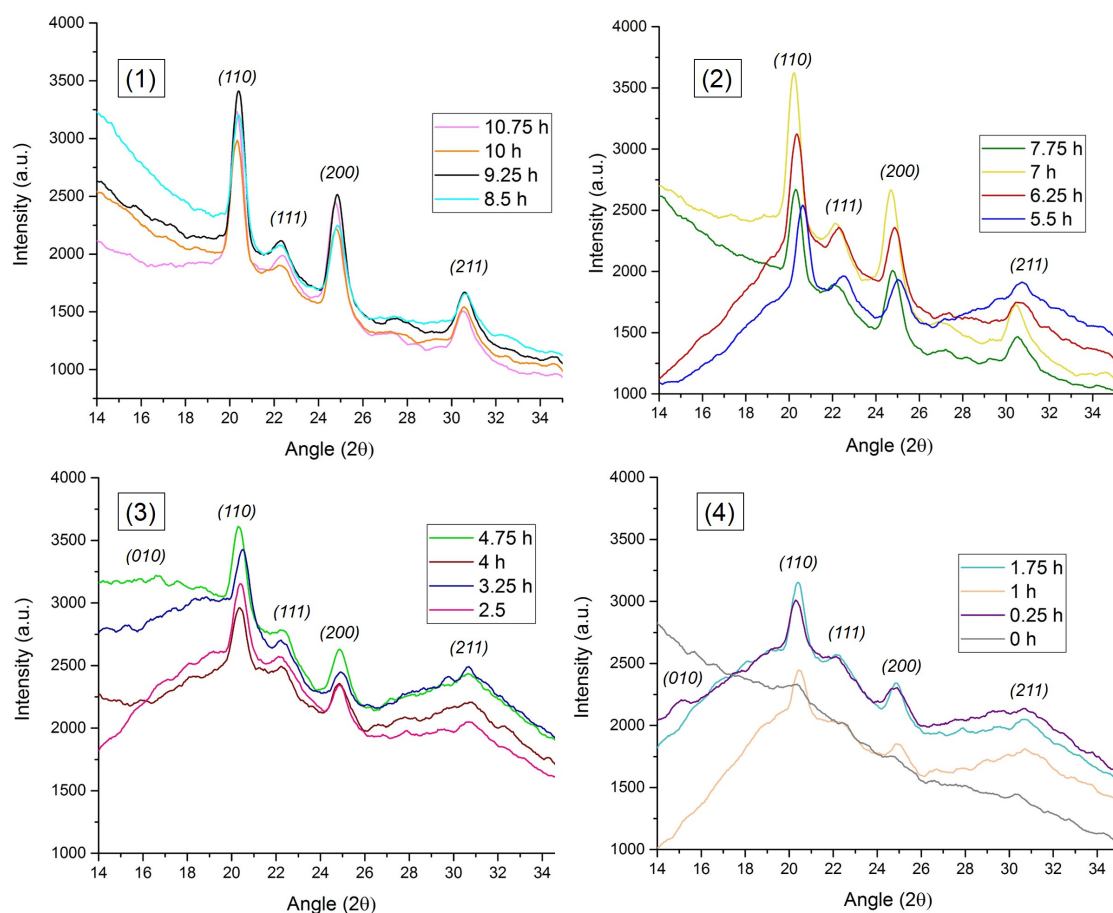


Fig. B.1 WXR D patterns of LS Kepstan 6002 PEKK specimens subjected to different cooling times. (1) 10.75 h, 10 h, 9.25 h and 8.5 h; (2) 7.75 h, 7 h, 6.25 h and 5.5 h; (3) 4.75 h, 4 h, 3.25 h and 2.5 h; (4) 1.75 h, 1 h, 0.25 h, and 0 h.

Peaks (111) and (211) become broader and less pronounced from 7.75 h of cooling (group 5). The other peaks gradually disappear until they reach 0 h of cooling, in which only traces of peak (110) can be identified. Peak (010) ($2\theta = 15.6^\circ$) is evident at 0.25 h of cooling, but might be present at 3.25 h as well.

The patterns are not very clear. There may be some variation from sample to sample of the same group. Furthermore, the crystal structure is likely to change according to the orientation of the WXR analysis - the analysis of a surface in Z orientation might reveal different structures. Therefore, samples near the fracture were transversally cut using a diamond cutting disc. The patterns for each group are presented in Fig.B.2.

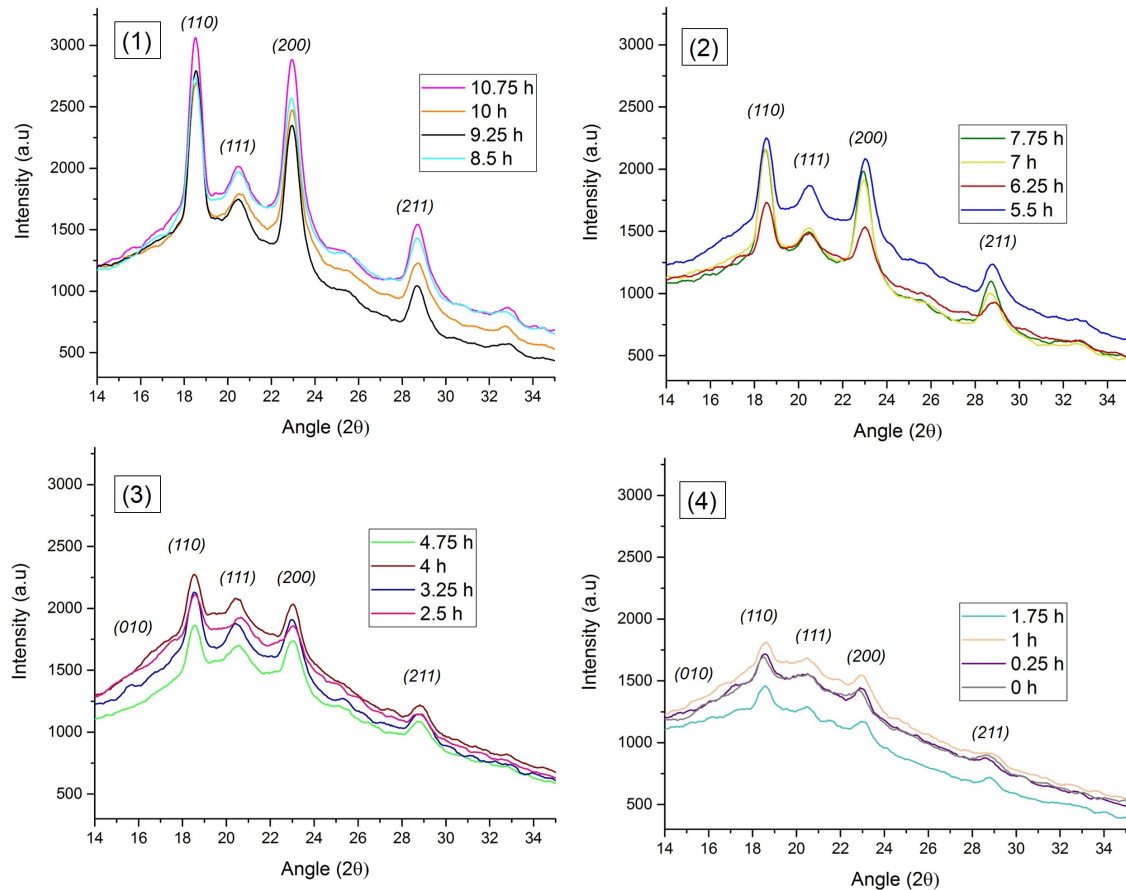


Fig. B.2 WXR patterns of LS Kepstan 6002 PEKK specimens analysed along Z orientation with varying cooling time. (1) 10.75 h, 10 h, 9.25 h and 8.5 h; (2) 7.75 h, 7 h, 6.25 h and 5.5 h; (3) 4.75 h, 4 h, 3.25 h and 2.5 h; (4) 1.75 h, 1 h, 0.25 h, and 0 h.

The crystal structure and degree of crystallinity are very similar to the WXR patterns in X orientation. The sample in Z exposed to 0 h of cooling, however, presented clear peaks in (110), (111), and (200). The difference between X and Z orientation is explained by the little cooling to which the top layer was subjected when compared to the other layers. This difference provides additional evidence that solidification does not take long to occur when laser sintering PEKK.

A peak at (010) is identified for the group subjected to 3.25 h. A very shallow peak at 2θ of 15.6° might be present in the patterns of 1 h and 0.25 h of cooling as well, but it is unclear. It is possible that form II, associated with this peak, is present in low quantities

and in specific regions of the specimens exposed to lower cooling times. As form II is less stable, this crystal structure is usually obtained when not enough time is given for a full arrangement of the chains into a more ordered structure [13].

The unclear results of some WXR patterns led to the analysis of Kepstan 6002 PEKK using DSC. Samples taken from the fracture of the specimens were prepared according to Section 3.3.6, but heated at $50\text{ }^{\circ}\text{C min}^{-1}$. The thermograms of the heating segments are shown in Fig.B.3.

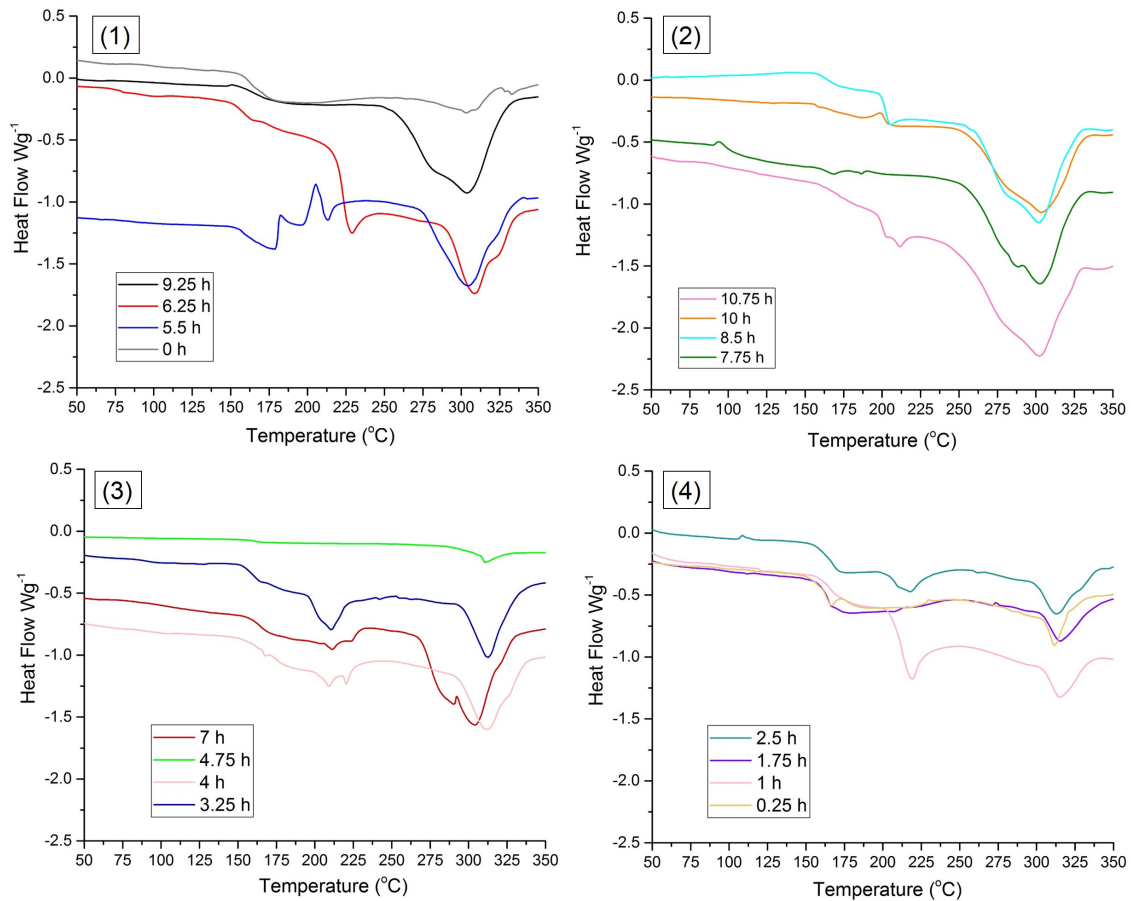


Fig. B.3 DSC thermograms of the melt for LS Kepstan 6002 PEKK specimens produced at different cooling times. (1) 10.75 h, 10 h, 9.25 h and 8.5 h; (2) 7.75 h, 7 h, 6.25 h and 5.5 h; (3) 4.75 h, 4 h, 3.25 h and 2.5 h; (4) 1.75 h, 1 h, 0.25 h, and 0 h.

The DSC curves reveal a series of phenomena taking place during the melt of LS PEKK subjected to different cooling times. These phenomena were explored and described in previous studies using different manufacturing techniques [71, 83, 13]. The specimens exposed to prolonged times of cooling showed a clear peak at $\sim 300\text{ }^{\circ}\text{C}$ attributed to the melt of the most stable form of PEKK crystal structure, also known as form I. The same form can be reorganised into a more compact structure due to the chain flexibility of PEKK at 60/40 T/I concentration. This organisation can lead to the formation of an additional peak at $330\text{ }^{\circ}\text{C}$, also attributed to the melt of form I. This peak can be observed at 1.75 h and below. Other groups (6.25 h, 4.75 h, 4 h, 3.25 h, and 2.5 h) showed a slight shift of the main endotherm at $300\text{ }^{\circ}\text{C}$ to higher temperatures [13]. In these groups, the melting rate of

$50\text{ }^{\circ}\text{C min}^{-1}$ was probably insufficient to separate the peak at $300\text{ }^{\circ}\text{C}$ from the one at $330\text{ }^{\circ}\text{C}$, both related to the melting of form I.

Merged peaks are also observed from 10.75 h to 7 h of cooling, however easier to distinguish at 7.75 and 7 h. This peak is a result of merging $300\text{ }^{\circ}\text{C}$ peak with a peak at $\sim 280\text{ }^{\circ}\text{C}$. Previous literature associated the peak at $280\text{ }^{\circ}\text{C}$ to the melt of form II or another phenomenon known as double-melting [13]. The WXR patterns for these cooling times do not show a peak at $2\theta = 15.6^{\circ}$, which suggests that form II is not present in the structure. Therefore, double-melting occurs. Double-melting is attributed to the melting of a secondary structure within the spherulites and is a result of annealing at temperatures $10\text{ }^{\circ}\text{C}$ below the endotherm [13]. It may be possible that, due to the slow cooling of the LS process, a similar phenomenon to annealing is creating the structure obtained at prolonged cooling times (above 7 h). Interestingly, if considering a linear cooling between T_{bed} and T_{bp} , 7 h of cooling would correspond to a temperature of $266\text{ }^{\circ}\text{C}$. Therefore, it is likely that most of the crystallisation structure of the specimens exposed to cooling times above 7 h would be formed at temperatures close to $270\text{ }^{\circ}\text{C}$.

The double-melting behaviour can also take place at $\sim 220\text{ }^{\circ}\text{C}$ due to the melting of a secondary structure within the spherulites of both forms, form I and II [13]. Such a phenomenon can be identified in most of the endotherms (10.75, 8.5, 7, 6.25, 5.5, 4, 3.25, 2.5, and 1 h of cooling). Excluding the endotherms with cooling times below 3.25 h, only the secondary structure present in form I is being melted. At shorter cooling times, however, the secondary structure of both forms can melt.

A very particular behaviour is observed at 5.5 h of cooling. Right after T_g , PEKK goes through double-melting followed by a crystalline peak at $\sim 220\text{ }^{\circ}\text{C}$. This peak is a clear indication of cold crystallisation, which is crystallising the amorphous chains into form I. A less pronounced exothermic peak is also obtained at 10 h of cooling, suggesting a similar phenomenon.

A different sample subjected to 5.5 h of cooling in LS was tested under the same DSC conditions. The test was also repeated for samples from LS specimens subjected to 10.75, 7, and 3.25 h of cooling. The thermograms are shown in Fig.B.4. The results confirm the broad behaviour of LS specimens even when subjected to the same cooling time. The double-melting peak previously observed is not recorded in the repeated curves at 10.75 h, 7 h, and 3.25 h of cooling. For 5.5 h of cooling, the exothermic peak disappears in the repeated sample and is replaced by a steep endotherm at $\sim 220\text{ }^{\circ}\text{C}$.

To conclude, the softening point (T_g) is around $160\text{ }^{\circ}\text{C}$ for all the cooling times, and becomes clearer the shorter the cooling time, as crystal arrangement is hindered. Table B.1 relates the peaks obtained in DSC with their respective physical phenomenon [13].

Garcia-Leiner et al. [84] mention the existence of both crystal structure arrangements when PEKK is processed by LS. This section suggests that form II can be present at short cooling times, in which the chains are not able to reorganise into form I due to insufficient time before stable solidification.

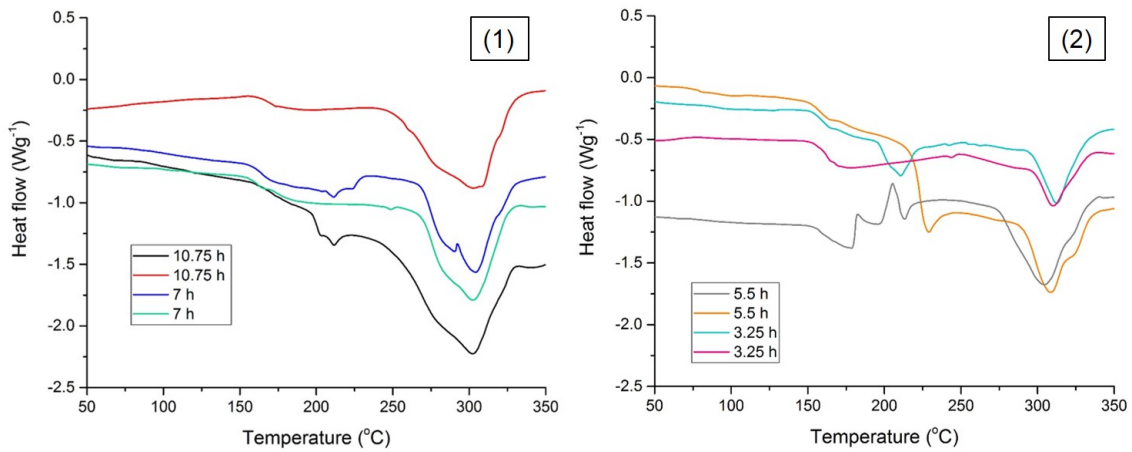


Fig. B.4 DSC thermograms of the melt for LS Kepstan 6002 PEKK specimens. The thermograms were repeated for different samples subjected to the same cooling time. (1) 10.75 h and 7 h samples and (2) 5.5 and 3.25 h samples. Note that different phenomena are occurring despite the samples being subjected to the same cooling time.

Table B.1 Relation between thermogram peaks and crystallisation phenomenon of PEKK [13].

Peak nature	Temperature	Crystal form	Description
Endotherm	300 °C	Form I	Melting of the primary and main form of PEKK crystal
Endotherm	330 °C	Form I	Associated with recrystallisation/reorganisation of the crystals into a more compact structure due to increased chain flexibility
Endotherm	280 °C	Form II/form I	Melting of form II or double-melting behaviour resulting from annealing at 270 °C
Endotherm	220 °C	Form I and/or form II	Double-melting behaviour attributed to the melting of a secondary structure within the spherulite
Exotherm	~225 °C	Form I and form II	Cold crystallisation peak

Appendix C

Replicating Final Performance of Optimised Quenched Specimens under Scalable LS Setup

This Appendix is a continuation of Chapter 9, in which the mechanical performance of PEKK specimens was significantly improved by varying cooling time in LS. The experiment consisted of manufacturing a build with 16 groups of specimens stacked on top of each other in Z orientation and interrupting the cooling phase by quenching all specimens in cold water. In this methodology, different levels of crystallisation were obtained for each group, elongation was significantly improved, and a calibration curve was developed associating cooling time, mechanical performance, and degree of crystallinity of PEKK.

Despite proving the relationship between kinetics of crystallisation, mechanical performance, and the LS process (cooling time), this experiment is only possible in a research environment, and interrupting the cooling phase of LS is not industrially scalable. Furthermore, a few specimens warped due to the rapid cooling, and dimensional accuracy was compromised.

For these reasons stated above, a few attempts were performed to replicate the optimal mechanical performance of some of the groups quenched in water, but in an industrially feasible setup. From Chapter 9, the combination of improved elongation and good mechanical strength is achieved around 5.5 to 6.25 h of cooling time. By making a rough approximation and considering a linear decrease in temperature from T_{bed} to T_{bp} , the groups subjected to such cooling were possibly at temperatures varying between 246 and 280 °C before quenching. These temperatures are located between the maximum rate of crystallisation to the far-right side of the half-time crystallisation curve of PEKK (Fig. 6.7).

Two different experimental setups were designed and manufactured simultaneously. For this experiment, the build volume of $350 \times 380 \times 400 \text{ mm}^3$ was used rather than the smaller volume configuration. The build setup is shown in Fig.C.1. The same processing temperatures selected in Chapter 9 (T_{bed} of 292 °C and T_{bp} of 190 °C) were used. Half of the build was left in the system to cool according to the standard cooling phases in LS but being interrupted after 3.5 h. The other half was removed and placed in the oven at 230

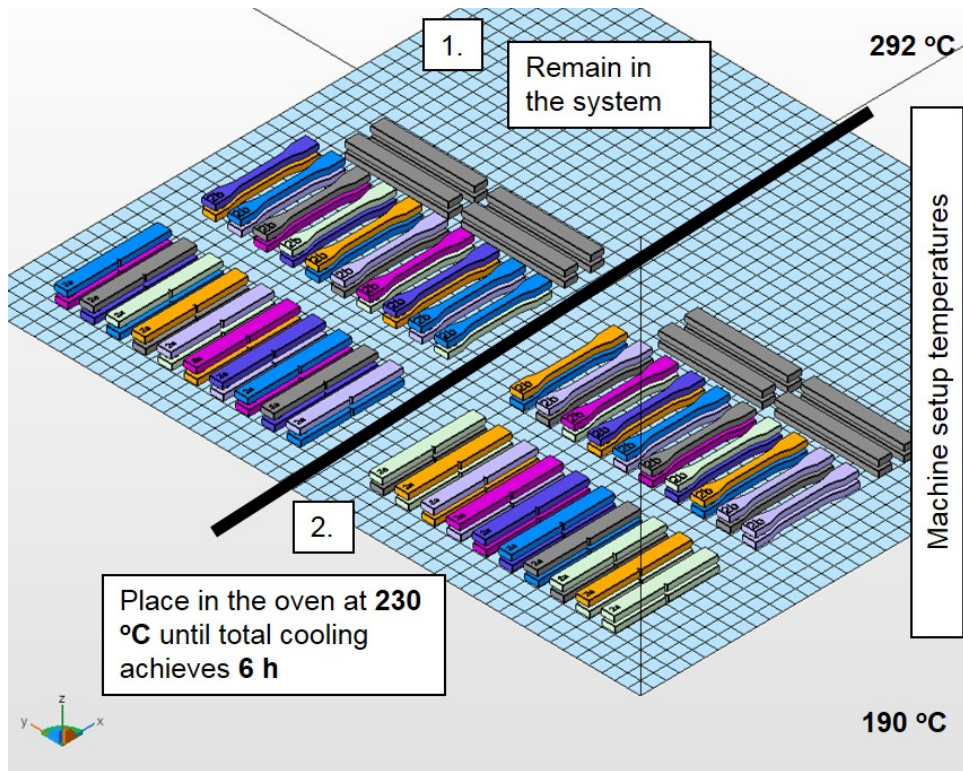


Fig. C.1 Configuration of the experimental build. The temperatures of manufacturing, T_{bed} and T_{bp} are indicated on the right. The half of the build located on the upper left region remained in the system for 3.5 h, whilst the other half was removed and placed in the oven at 230 °C for the same period.

°C for 3.5 h. The chosen period of cooling summed with the manufacturing time of ~ 2 h is equivalent to the cooling time in which specimens from groups 7-8 of Chapter 9 were exposed. The experimental setup is shown in Fig.C.1.

The mechanical strength and elongation at break of the sandblasted specimens were measured according to Section 3.3.11. The results were compared with the optimised standard LS and with PEKK quenched in water after 5.5 and 6.25 h of cooling; they are shown in Fig. C.2.

Despite sharing similar UTS than the specimens quenched in water, the elongation at break was not improved in either of the attempts. In both trials, the strain at break was of approximately 2%. Therefore, the level of crystallinity was investigated using WXR, as described in Section 3.3.9. The results were plotted in comparison with all the specimens quenched in water as well as the crystallinity achieved with standard LS production; they are shown in Fig.C.3. Note the standard cooling time in LS is variable according to the build size. In Fig. C.3, a 9 h cooling was selected for comparison reasons.

The results of the degree of crystallinity explain the low elongation at break achieved with the two attempts performed. Although being subjected to reduced cooling times, the level of crystallinity was higher than predicted, of $\sim 25\%$. This degree of crystallinity is equivalent to the obtained for the specimens quenched in water after 7 h of cooling. The elongation at break after 7 h of cooling, however, is almost 5%, as opposed to the 2% obtained with the experiment setups presented in this section. It is possible that the crystal

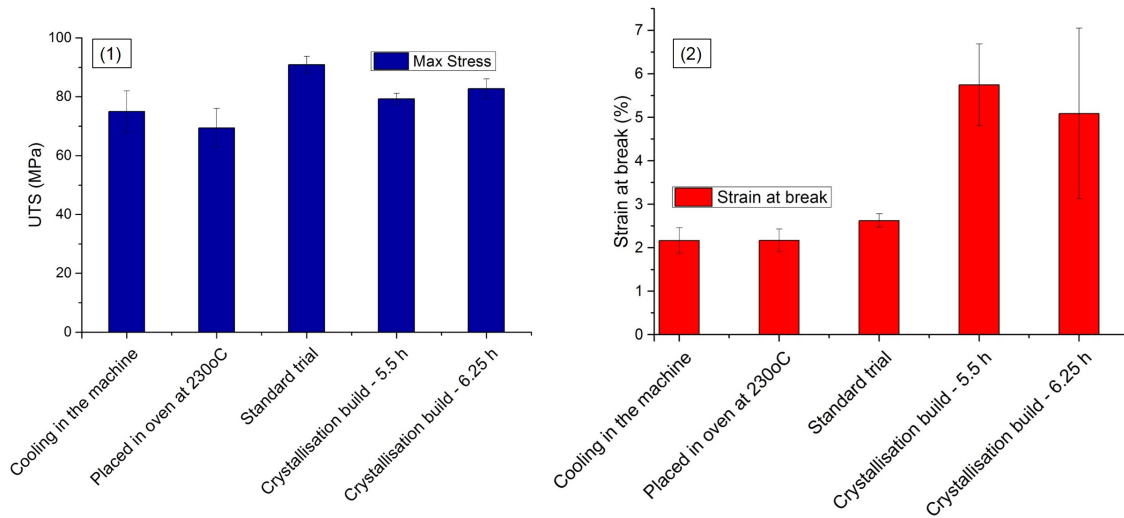


Fig. C.2 (1) UTS and (2) strain at break properties of specimens produced with the two different setups - cooling in the machine and placed in the oven at 230 °C. The results were compared for the specimens produced at standard LS cooling, and for the specimens subjected to 5.5 and 6.25 h of cooling before quenching in water.

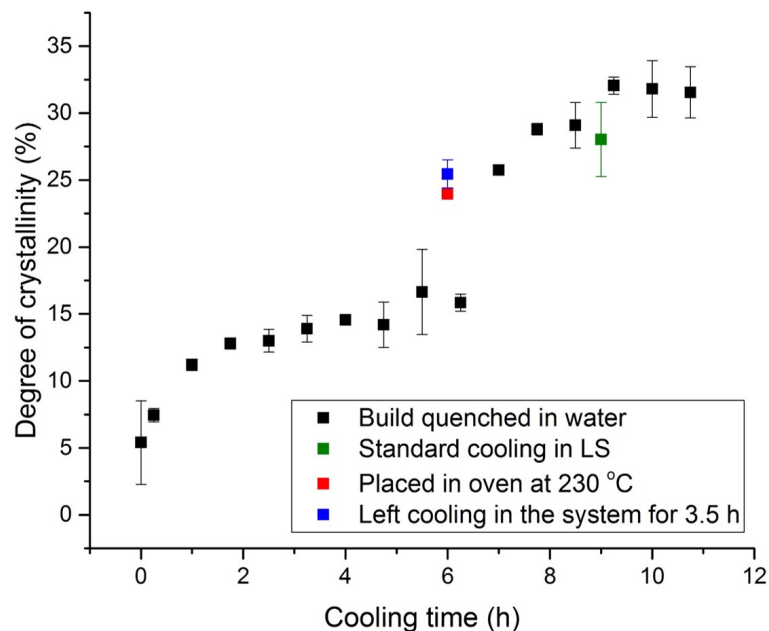


Fig. C.3 Degree of crystallinity obtained with the specimens left in the system and placed in the oven for 3.5 h. The results were compared with the specimens quenched in water and with the standard LS process with a cooling time of 9 h.

arrangement is significantly different, as different conditions were applied to each system. These results suggest that optimising LS is not trivial, and additional research is required to understand and optimise the performance of polymeric material according to the process.

Appendix D

Molecular Weight Change with Powder Reuse

This Appendix supports some of the discussions raised in Chapter 10 regarding powder reuse and its potential effect on molecular weight distribution. Gel permeation chromatography (GPC) test was performed in samples of virgin and reused PEKK powder manufactured at T_{bp} of 265 °C and 286 °C. The results are shown in Table D.1.

Table D.1 GPC values for PEKK powder processed at different conditions and compared with the virgin powder.

Condition	M_n (g mol ⁻¹)	M_w (g mol ⁻¹)	M_z (g mol ⁻¹)
Virgin	28,200	67,200	125,900
Cake processed at 265 °C	28,800	68,400	127,000
Cake processed at 286 °C	28,800	68,800	128,700

As expected, the molecular weight increases with powder reuse. The difference, however, is not significant, but sufficient to change the melting temperature, degradation temperature, and the kinetics of crystallisation slightly, as shown in Chapter 10. The values of GPC help to support the discussion provided in Chapter 10 and highlight the importance of selecting appropriate processing temperatures in LS.

References

- [1] M. Attaran. The rise of 3-D printing: The advantages of additive manufacturing over traditional manufacturing. *Business Horizons*, 60(5):677–688, 2017.
- [2] D. L. Bourell, T. J. Watt, D. K. Leigh, and B. Fulcher. Performance Limitations in Polymer Laser Sintering. *Physics Procedia*, 56:147–156, 2014.
- [3] J. Schmidt, M. Sachs, S. Fanselow, K. E. Wirth, and W. Peukert. New approaches towards production of polymer powders for selective laser beam melting of polymers. In *AIP Conference Proceedings*, volume 1914, pages 762–769, 2017.
- [4] R. D. Goodridge, C. J. Tuck, and R. J. M. Hague. Laser sintering of polyamides and other polymers, 2012.
- [5] J. Kruth, G. Levy, R. Schindel, T. Craeghs, and E. Yasa. Consolidation of Polymer Powders by Selective Laser Sintering. In *International Conference on Polymers and Moulds Innovations*, pages 15–30, 2008.
- [6] D. Drummer, D. Rietzel, and F. Kühnlein. Development of a characterization approach for the sintering behavior of new thermoplastics for selective laser sintering. *Physics Procedia*, 5(PART 2):533–542, 2010.
- [7] M. Berzins, T. H. C. Childs, and G. R. Ryder. The selective laser sintering of polycarbonate. *Annals of the CIRP*, 45(1):187–190, 1996.
- [8] S. Arai, S. Tsunoda, R. Kawamura, K. Kuboyama, and T. Ougizawa. Comparison of crystallization characteristics and mechanical properties of poly(butylene terephthalate) processed by laser sintering and injection molding. *Materials and Design*, 113:214–222, 2017.
- [9] S. Berretta, K. E. Evans, and O. Ghita. Processability of PEEK, a new polymer for high temperature laser sintering (HT-LS). *European Polymer Journal*, 68:243–266, 2015.
- [10] O. Ghita, E. James, R. Davies, S. Berretta, B. Singh, S. Flint, and K. E. Evans. High Temperature Laser Sintering (HT-LS): An investigation into mechanical properties and shrinkage characteristics of Poly (Ether Ketone) (PEK) structures. *Materials and Design*, 61:124–132, 2014.
- [11] T. Wohlers and T. Gornet. History of Additive Manufacturing. Technical report, 2014.
- [12] Arkema. Kepstan 6000 Series, 2013.
- [13] K. H. Gardner, B. S. Hsiao, R. R. Matheson Jr., and B. A. Wood. Structure, crystallization and morphology of Poly (aryl ether ether ketone). *Polymer*, 33(12):1752–1758, 1992.

- [14] C. M. González-Henríquez, M. A. Sarabia-Vallejos, and J. Rodríguez-Hernández. Polymers for additive manufacturing and 4D-printing: Materials, methodologies, and biomedical applications. *Progress in Polymer Science*, 94:57–116, 2019.
- [15] S. K. Tiwari, S. Pande, S. Agrawal, and S. M. Bobade. Selection of selective laser sintering materials for different applications. *Rapid Prototyping Journal*, 216(21):630–648, 2015.
- [16] S. Thomas and P. M. Visakh. *Handbook of Engineering and Specialty Thermoplastics, Volume 3: Polyethers and Polyesters*. Wiley, 2011.
- [17] H. X. Nguyen and H. Ishida. Poly(aryl-ether-ether-ketone) and its advanced composites: a review. *Polymer Composites*, 8(2):57–73, 1987.
- [18] National Research Council. *Polymer Science and Engineering: The Shifting Research Frontiers*. National Research Council, 1994.
- [19] Oxford University Press Inc. *Polymer Data Handbook*. New York, 1999.
- [20] J. Yang. *Part One: Synthesis of Aromatic Polyketones Via Soluble Precursors Derived From Bis(α -Aminonitrile)s*. PhD thesis, Virginia Polytechnic Institute and State University, 1998.
- [21] D. F. Williams, A. McNamara, and R. M. Turner. Potential of poly ether ether ketone (PEEK) carbon-fiber-reinforced PEEK in medical applications. *Journal of Materials Science Letters*, 6(2):188–190, 1987.
- [22] A. R. McLauchlin, O. R. Ghita, and L. Savage. Studies on the reprocessability of poly(ether ether ketone) (PEEK). *Journal of Materials Processing Technology*, 214(1):75–80, 2014.
- [23] Y. Wang, E. James, and O. R. Ghita. Glass bead filled Polyetherketone (PEK) composite by High Temperature Laser Sintering (HT-LS), 2015.
- [24] J. E. Harris and L. M. Robeson. Miscible Blends of Poly(aryl Ether Ketone)s and Polyetherimides. *Journal of Applied Polymer Science*, 35:1877–1891, 1988.
- [25] Victrex High Performance Polymers. Victrex® PEEK 150PF, 2014.
- [26] K. J. Dahl and V. Jansons. *Poly(arylene ether ketone) Chemistry: Recent Advances in Synthesis and Applications*, pages 69–81. Springer US, Boston, MA, 1995.
- [27] T. Choupin, B. Fayolle, G. Régnier, C. Paris, J. Cinquin, and B. Brulé. Isothermal crystallization kinetic modeling of poly(etherketoneketone) (PEKK) copolymer. *Polymer*, 111:73–82, 2017.
- [28] P. A. Staniland, C. J. Wilde, F. A. Bottino, G. Di Pasquale, A. Pollicino, and A. Recca. Synthesis, characterization and study of the thermal properties of new polyarylene ethers. *Polymer*, 33(9):1976–1981, 1992.
- [29] B. S. Hsiao, I. Y. Chang, and B. B. Sauer. Isothermal crystallization kinetics of poly (ether ketone ketone) and its carbon-fibre-reinforced composites. *Polymer*, 32(15):2799–2805, 1991.
- [30] T. Choupin, B. Fayolle, G. Régnier, C. Paris, J. Cinquin, and B. Brulé. A more reliable DSC-based methodology to study crystallization kinetics: Application to poly(ether ketone ketone) (PEKK) copolymers. *Polymer*, 2018.
- [31] Arkema. Glass fiber reinforced grade 6010G30 Preliminary Technical Data Sheet, 2014.

- [32] Arkema. Carbon fibre reinforced grade 8010C30 Preliminary Technical Data Sheet, 2013.
- [33] Arkema. Kepstan 7000 Series, 2012.
- [34] Arkema. Technical Data 8000 Series, 2013.
- [35] W. H. Bonner Jr. Aromatic polyketones and preparation thereof, 1962.
- [36] T. E. Attwood, P. C. Dawson, J. L. Freeman, L. R. J. Hoy, J. B. Rose, and P. A. Staniland. Synthesis and properties of polyaryletherketones. *Polymer*, 22(August):1096–1103, 1981.
- [37] B. M. Marks. Boron trifluoride - hydrogen fluoride catalyzed synthesis of poly(aromatic ketone) and poly(aromatic sulfone) polymers, 1969.
- [38] P. Gay and C. M. Brunette. Ordered Polyetherketones, 1989.
- [39] R. N. Johnson, A. G. Farnham, R. A. Clendinning, W. F. Hale, and C. N. Merriam. Poly(aryl Ethers) by Nucleophilic Aromatic Substitution. I. Synthesis and Properties. *Journal of Polymer Science: Part A-1*, 5:2375–2398, 1967.
- [40] I. Fukawa, T. Tanabe, and T. Dozono. Preparation of Aromatic Poly(ether ketones) from an Aromatic Dihalide and Sodium Carbonate. *Macromolecules*, 24:3838–3844, 1991.
- [41] H. R. Kricheldorf and G. Bier. New polymer syntheses : II. Preparation of aromatic poly(ether ketone)s from silylated bisphenols. *Polymer*, 25(8):1151–1156, 1984.
- [42] D. R. Kelsey, L. M. Robeson, R. A. Clendinning, and C. S. Blackwell. "Defect-Free", Crystalline Aromatic Poly(ether ketones): A Synthetic Strategy Based on Acetal Monomers. *Macromolecules*, 20:1204–1212, 1987.
- [43] W. Risse and D. Y. Sogah. Synthesis of soluble high molecular weight poly(aryl ether ketones) containing bulky substituents. *Macromolecules*, 23(18):4029–4033, 1990.
- [44] A. Pandyat, J. Yang, and H. W. Gibson. A New Polyketone Synthesis Involving Nucleophilic Substitution via Carbanions Derived from Bis(waminonitrile)s. 1. Semicrystalline Poly(arylene ketone sulfone)s112. *Macromolecules*, 27:1367–1375, 1994.
- [45] M. Chen, I. Guzei, A. L. Rheingold, and H. W. Gibson. Novel macrocycle by Friedel-Crafts acylation cyclization. *Macromolecules*, 30:2516–2518, 1997.
- [46] M. Chen and H. W. Gibson. Large-Sized Macrocyclic Monomeric Precursors of Poly(ether ether ketone): Synthesis and Polymerization. *Macromolecules*, 29:5502–5504, 1997.
- [47] M. Chen, F. Fronczekb, and H. W. Gibson. Concise synthesis and characterization of 30-membered macrocyclic monomer for poly(ether ether ketone). *Macromolecular chemistry and physics*, 197:4069–4078, 1996.
- [48] G. A. Deeter and J. S. Moore. A New Polymerization Reaction for the Synthesis of Aromatic Polyketones. *Macromolecules*, 26:2535–2541, 1993.
- [49] M. Ueda and F. Ichikawa. Synthesis of aromatic poly (ether ketone)s by nickel-catalyzed coupling polymerization of aromatic dichlorides. *Macromolecules*, 23:926–930, 1990.

- [50] D. W. Van Krevelen and K. Te Nijenhuis. Crystallisation and Recrystallisation. In *Properties of Polymers*, chapter 19, pages 703–746. Elsevier B.V., fourth edition, 2009.
- [51] R. Becker and W. Döring. Kinetische Behandlung der Keimbildung in übersättigten Dämpfen. *Annalen der physik*, 416(8):719–752, 1935.
- [52] M. Avrami. Kinetics of Phase Change. I General Theory. *Journal of Chemical Physics*, 7(12):1103, 1939.
- [53] M. Avrami. Kinetics of Phase Change. II Transformation-Time Relations for Random Distribution of Nuclei. *Journal of Chemical Physics*, 8(2):212, 1940.
- [54] M. Avrami. Granulation, Phase Change, and Microstructure Kinetics of Phase Change. III. *Journal of Chemical Physics*, 9(2):177, 1941.
- [55] D. Turnbull and J. C. Fisher. Rate of Nucleation in Condensed Systems. *The Journal of Chemical Physics*, 17:71–73, 1949.
- [56] I. H. Hillier. Modified Avrami Equation for the Bulk Crystallization Kinetics of Spherulitic Polymers. *Journal of Polymer Science: Part A*, 3:3067–3078, 1965.
- [57] J. D. Hoffman and J. I. Lauritzen Jr. Crystallization of Bulk Polymers With Chain Folding : Theory of Growth of Lamellar Spherulites. *Journal of Research of the National Bureau of Standards - A. Physics and Chemistry*, 65(August):1961, 1961.
- [58] J. I. Lauritzen Jr. and J. D. Hoffman. Extension of theory of growth of chain-folded polymer crystals to large undercoolings. *Journal of Applied Physics*, 44(10):4340–4352, 1973.
- [59] H. Motz and J. M. Schultz. The Solidification of PEEK. Part II: Kinetics. *Journal of Thermoplastic Composite Materials*, 2(4):267–280, 1989.
- [60] P. Altúzar and R. Valenzuela. Avrami and Kissinger theories for crystallization of metallic amorphous alloys. *Materials Letters*, 11(3-4):101–104, 1991.
- [61] P. Cebe and S.-D. Hong. Crystallization behaviour of poly(ether-ether-ketone). *Polymer*, 27(8):1183–1192, 1986.
- [62] A. Maffezzoli, J. M. Kenny, and L. Torre. On the physical dimensions of the Avrami constant. *Thermochimica Acta*, 269/270:185–190, 1995.
- [63] G. da Cunha Vasconcelos, R. L. Mazur, E. C. Botelho, M. C. Rezende, and M. L. Costa. Evaluation of crystallization kinetics of poly (ether-ketone- ketone) and poly (ether-ether- ketone) by DSC. *Journal of Aerospace Technology and Management*, 2(2):155–162, 2010.
- [64] D. C. Bassett. *Principles of polymer morphology*. Cambridge University Press, Cambridge, 1981.
- [65] C. N. Velisaris and J. C. Seferis. Crystallization kinetics of polyetheretherketone (PEEK) matrices. *Polymer Engineering & Science*, 26(22):1574–1581, 1986.
- [66] D. C. Bassett, R. H. Olley, and I. A. M. Al Raheil. On crystallization phenomena in PEEK. *Polymer*, 29(10):1745–1754, 1988.
- [67] D. J. Blundell and B. N. Osborn. The morphology of poly(aryl-ether-ether-ketone). *Polymer*, 24(8):953–958, 1983.

- [68] W. Wang, J. M. Schultz, and B. S. Hsiao. Dynamic study of crystallization- and melting-induced phase separation in PEEK/PEKK blends. *Macromolecules*, 30(16):4544–4550, 1997.
- [69] K. Konnecke. Crystallization of poly(aryl ether ketones). i. crystallization kinetics. *Journal of Macromolecular Science, Part B*, 33(1):37–62, 1994.
- [70] X. Tardif, B. Pignon, N. Boyard, J. W. P. Schmelzer, V. Sobotka, D. Delaunay, and C. Schick. Experimental study of crystallization of PolyEtherEtherKetone (PEEK) over a large temperature range using a nano-calorimeter. *Polymer Testing*, 36:10–19, 2014.
- [71] T. Choupin. *Mechanical performances of PEKK thermoplastic linked to their processing parameters*. PhD thesis, ParisTech, 2018.
- [72] J. P. Mercier. Nucleation in polymer crystallization: A physical or a chemical mechanism? *Polymer Engineering and Science*, 30(5):270–278, 1990.
- [73] R. H. Olley, D. C. Bassett, and D. J. Blundell. Permanganic etching of PEEK. *Polymer*, 27(3):344–348, 1986.
- [74] P. C. Dawson and D. J. Blundell. X-ray data for poly (aryl ether ketones). *Polymer*, 21(5):577–578, 1980.
- [75] A. J. Lovinger and D. D. Davis. Electron-microscopic investigation of the morphology of a melt-crystallized polyaryletherketone. *Journal of Applied Physics*, 58(8):2843–2853, 1985.
- [76] Y. Wang, J. D. Beard, K. E. Evans, and O. Ghita. Unusual crystalline morphology of Poly Aryl Ether Ketones (PAEKs). *RSC Adv.*, 6(4):3198–3209, 2016.
- [77] S. Z. D. Cheng, M. Y. Cao, and B. Wunderlich. Glass Transition and Melting Behavior of Poly(oxy-1,4-phenyleneoxy-1,4-phenylenecarbonyl-1,4-phenylene). *Macromolecules*, 19(7):1868–1876, 1986.
- [78] A. Jonas and R. Legras. Description of PEEK Semi-crystalline Morphology. *Crystallization of Polymers I*, pages 619–624, 1993.
- [79] Y. Deslandes, M. Day, N. F. Sabir, and T. Suprunchuk. Crystallization of poly(aryl-ether-ether-ketone): Effect of thermal history of the melt on crystallization kinetics. *Polymer Composites*, 10(5):360–366, 1989.
- [80] C. Li and A. Strachan. Prediction of PEKK properties related to crystallization by molecular dynamics simulations with a united-atom model. *Polymer*, 174(April):25–32, 2019.
- [81] D. J. Blundell and A. B. Newton. Variations in the crystal lattice of PEEK and related para-substituted aromatic polymers: 2. Effect of sequence and proportion of ether and ketone links. *Polymer*, 32(2):308–313, 1991.
- [82] P. Avakian, K. H. Gardner, and R. R. Matheson. A comment on crystallization in PEKK and PEEK resins. *Journal of Polymer Science Part C: Polymer Letters*, 28(8):243–246, jul 1990.
- [83] T. Liu, S. Wang, Z. Mo, and H. Zhang. Crystal structure and drawing-induced polymorphism in poly(aryl ether ether ketone). IV. *Journal of Applied Polymer Science*, 73(2):237–243, 1999.

- [84] M. Garcia-Leiner, D. P. Dennies, and A. Yardimci. High Performance Polymers in Additive Manufacturing Processes: Understanding Process, Structure and Property. *Microscopy and Microanalysis*, 21(S3):127–128, 2015.
- [85] B. Brulé, N. Decraemer, D. Huze, F. S. Jouy, B. Fr, and J. Pascal. Process for Densification of Poly(arylene ether ketone) Powders, 2017.
- [86] M. Sachs, J. Schmidt, F. Toni, C. Blümel, B. Winzer, W. Peukert, and K.-E. Wirth. Rounding of irregular polymer particles in a downer reactor. In *Procedia Engineering*, volume 102, pages 542–549, 2015.
- [87] J. Schmidt, M. Sachs, B. Winzer, and W. Peukert. A novel process route for the production of spherical SLS polymer powders. In *AIP Conference Proceedings*, number May, pages 16001–1 – 16001–5, 2015.
- [88] F. Müller, A. Pfister, and M. Leuterer. PAEK Powder, In Particular for the Use in a Method for a Layer-wise Manufacturing of a Three-dimensional Object, as well as Method for Producing it, 2010.
- [89] Finetal. Cryogenic Grinding Powder Production, 2016.
- [90] M. Schmid and K. Wegener. Additive Manufacturing: Polymers applicable for laser sintering (LS). *Procedia Engineering*, 149(June):457–464, 2016.
- [91] M. Wilczek, J. Bertling, and D. Hintemann. Optimised technologies for cryogenic grinding. *International Journal of Mineral Processing*, 74(SUPPL.):425–434, 2004.
- [92] S. Dadbakhsh, L. Verbelen, T. Vandeputte, D. Strobbe, P. Van Puyvelde, and J.-P. Kruth. Effect of powder size and shape on the SLS processability and mechanical properties of a TPU elastomer. *Physics Procedia*, 83:971–980, 2016.
- [93] S. Faselow, S. E. Emamjomeh, K. E. Wirth, J. Schmidt, and W. Peukert. Production of spherical wax and polyolefin microparticles by melt emulsification for additive manufacturing. *Chemical Engineering Science*, 141:282–292, 2016.
- [94] W. Christoph and H. Scholten. Using a Polyamide 12 for Selective Laser Sintering, 2007.
- [95] G. Sugano, T. Hosono, and K. Iwaki. System and method for producing composite powder, 2008.
- [96] M. S. Wahab, K. W. Dalgarno, and R. F. Cochrane. Development of Polymer Nanocomposites for Rapid Manufacturing Application. *International Journal of Integrated Engineering*, 1(1):51–59, 2009.
- [97] B. Badrinarayan and J. W. Barlow. Manufacture Of Injection Molds Using SLS. *Solid Freeform Fabrication Proceedings*, pages 371–378, 1994.
- [98] S. Ziegelmeier, P. Christou, F. Wöllecke, C. Tuck, R. Goodridge, R. Hague, E. Krampe, and E. Wintermantel. An experimental study into the effects of bulk and flow behaviour of laser sintering polymer powders on resulting part properties. *Journal of Materials Processing Technology*, 215(1):239–250, 2015.
- [99] V. K. Vashishtha, R. Makade, and N. Mehla. Advancement of Rapid Prototyping in Aerospace Industry -a Review. 3(3):2486–2493, 2011.
- [100] A. Amado, M. Schmid, G. Levy, and K. Wegener. Advances in SLS powder characterization. In *22nd Annual International Solid Freeform Fabrication Symposium - An Additive Manufacturing Conference*, pages 438–452, Austin, 2011.

- [101] S. Yang and J. R. G. Evans. Metering and dispensing of powder; the quest for new solid freeforming techniques. *Powder Technology*, 178(1):56–72, 2007.
- [102] R. D. Goodridge, K. W. Dalgarno, and D. J. Wood. Indirect selective laser sintering of an apatite-mullite glass-ceramic for potential use in bone replacement applications. *Journal of Engineering in Medicine*, 220(1):57–68, 2006.
- [103] Y. Shi, Z. Li, H. Sun, S. Huang, and F. Zeng. Effect of the properties of the polymer materials on the quality of selective laser sintering parts. *Journal of Materials: Design and Applications*, 218(3):247–252, 2004.
- [104] C. H. Clausen, D. J. Mickish, W. J. Nebe, and S. R. Vaidya. Laser Sinterable Thermoplastic Powder, 2000.
- [105] L. Fiedler, L. O. G. Correa, H.-J. Radusch, A. Wutzler, and J. Gerken. Evaluation of Polypropylene Powder Grades in Consideration of the Laser Sintering Processability. *Journal of plastic technology*, 3(4):1–14, 2007.
- [106] J. C. Nelson, S. Xue, J.W. Barlow, J. J. Beaman, H. L. Marcus, and D. L. Bourell. Model of the selective laser sintering of bisphenol-A polycarbonate. *Industrial & Engineering Chemistry Research*, 32(10):2305–2317, 1993.
- [107] A. Butscher, M. Bohner, S. Hofmann, L. Gauckler, and R. Müller. Structural and material approaches to bone tissue engineering in powder-based three-dimensional printing. *Acta Biomaterialia*, 7(3):907–920, 2011.
- [108] M. Schmid, A. Amado, and K. Wegener. Polymer powders for selective laser sintering (SLS). *AIP Conference Proceedings*, 1664(May 2015), 2015.
- [109] J. Schmidt, M. Sachs, S. Fanselow, M. Zhao, S. Romeis, D. Drummer, K. E. Wirth, and W. Peukert. Optimized polybutylene terephthalate powders for selective laser beam melting. *Chemical Engineering Science*, 156:1–10, 2016.
- [110] G. M. Vasquez, C. E. Majewski, B. Haworth, and N. Hopkinson. A targeted material selection process for polymers in laser sintering. *Additive Manufacturing*, 1(4):127–138, 2014.
- [111] L. Hao, M. M. Savalani, Y. Zhang, K. E. Tanner, and R. A. Harris. Effects of material morphology and processing conditions on the characteristics of hydroxyapatite and high-density polyethylene biocomposites by selective laser sintering. *Journal of Materials: Design and Applications*, 220(3):125 – 137, 2006.
- [112] E. J. R. Parteli and T. Pöschel. Particle-based simulation of powder application in additive manufacturing. *Powder Technology*, 288:96–102, 2016.
- [113] Z. Xiang, M. Yin, Z. Deng, X. Mei, and G. Yin. Simulation of Forming Process of Powder Bed for Additive Manufacturing. *Journal of Manufacturing Science and Engineering*, 138(8), 2016.
- [114] S. Haeri, Y. Wang, O. Ghita, and J. Sun. Discrete element simulation and experimental study of powder spreading process in additive manufacturing. *Powder Technology*, 306:45–54, 2016.
- [115] A. F. A. Becker. *Characterization and prediction of SLS processability of polymer powders with respect to powder flow and part warpage*. PhD thesis, ETH Zurich, 2016.
- [116] S. Berretta, Y. Wang, R. Davies, and O. R. Ghita. Polymer viscosity, particle coalescence and mechanical performance in high-temperature laser sintering. *Journal of Materials Science*, 51(10):4778–4794, 2016.

- [117] S. Berretta, O. Ghita, and K.E. Evans. Morphology of polymeric powders in Laser Sintering (LS): From Polyamide to new PEEK powders. *European Polymer Journal*, 59:218–229, 2014.
- [118] S. Ziegelmeier, F. Wollecke, C. Tuck, R. Goodridge, and R. Hague. Characterizing the Bulk & Flow Behaviour of LS Polymer Powders, 2013.
- [119] L. C. Y. Chan and N. W. Page. Particle fractal and load effects on internal friction in powders. *Powder Technology*, 90(3):259–266, 1997.
- [120] L. Verbelen, S. Dadbakhsh, M. Van den Eynde, D. Strobbe, J.-P. Kruth, B. Goderis, and P. Van Puyvelde. Analysis of the material properties involved in laser sintering of thermoplastic polyurethane. *Additive Manufacturing*, 15:12–19, 2017.
- [121] C. Mielicki, B. Gronhoff, and J. Wortberg. Effects of laser sintering processing time and temperature on changes in polyamide 12 powder particle size, shape and distribution. *AIP Conference Proceedings*, 1593(2014):728–731, 2014.
- [122] R. M. German. *Particle packing characteristics*. Metal Powder Industries Federation, Princeton, N.J., 1989.
- [123] M. Leturia, M. Benali, S. Lagarde, I. Ronga, and K. Saleh. Characterization of flow properties of cohesive powders: A comparative study of traditional and new testing methods. *Powder Technology*, 253:406–423, 2014.
- [124] Microtrac. Size and Shape Particle Analyser, 2019.
- [125] Retsch technology. Camsizer IP4, 2018.
- [126] Malvern Panalytical. Morphologi 4 range, 2009.
- [127] T. Ferreira and W. Rasband. ImageJ User Guide IJ 1.46r, 2012.
- [128] Microtrac. SI-RT-03: Imaging Parameters Reference Table, 2019.
- [129] A. Schweiger and I. Zimmermann. A new approach for the measurement of the tensile strength of powders. *Powder Technology*, 101(June 1998):1–9, 1998.
- [130] M. Pavan, T. Craeghs, J.-P. Kruth, and W. Dewulf. Investigating the influence of X-ray CT parameters on porosity measurement of laser sintered PA12 parts using a design-of-experiment approach. *Polymer Testing*, 66(January):203–212, 2018.
- [131] M. Pavan, M. Faes, D. Strobbe, B. Van Hooreweder, T. Craeghs, D. Moens, and W. Dewulf. On the influence of inter-layer time and energy density on selected critical-to-quality properties of PA12 parts produced via laser sintering. *Polymer Testing*, 61:386–395, 2017.
- [132] K. Wudy and D. Drummer. Aging Behavior of Polyamide 12: Interrelation between Bulk Characteristics and Part Properties. *2016: Proceedings of the 26th Annual International Solid Freeform Fabrication Symposium*, pages 770–781, 2016.
- [133] S. R. Athreya, K. Kalaitzidou, and S. Das. Processing and characterization of a carbon black-filled electrically conductive Nylon-12 nanocomposite produced by selective laser sintering. *Materials Science and Engineering A*, 527:2637–2642, 2010.
- [134] B. Chen, Y. Wang, S. Berretta, and O. Ghita. Poly Aryl Ether Ketones (PAEKs) and carbon-reinforced PAEK powders for laser sintering. *Journal of Materials Science*, 52(10):6004–6019, 2017.

- [135] S. Dupin, O. Lame, C. Barrès, and J. Y. Charneau. Microstructural origin of physical and mechanical properties of polyamide 12 processed by laser sintering. *European Polymer Journal*, 48(9):1611–1621, 2012.
- [136] M. Van Den Eynde, L. Verbelen, and P. Van Puyvelde. Influence of temperature on the flowability of polymer powders in laser sintering. *AIP Conference Proceedings*, 1914(December), 2017.
- [137] S. Vock, B. Klöden, Al. Kirchner, T. Weißgärber, and B. Kieback. Powders for powder bed fusion: a review. In *Progress in Additive Manufacturing*, volume 0, page 0. Springer International Publishing, 2019.
- [138] M. Schmid, F. Amado, G. Levy, and K. Wegener. Flowability of powders for Selective Laser Sintering (SLS) investigated by Round Robin Test. In *6th International Conference on Advanced Research in Virtual and Rapid Prototyping*, pages 12–19, 2014.
- [139] ASTM International. ASTM D1895-17: Standard Test Methods for Apparent Density, Bulk Factor, and Pourability of Plastic Materials, 2017.
- [140] C. A. Chatham, T. E. Long, and C. B. Williams. A review of the process physics and material screening methods for polymer powder bed fusion additive manufacturing. *Progress in Polymer Science*, 93:68–95, 2019.
- [141] D. Geldart, E. C. Abdullah, A. Hassanpour, L. C. Nwoke, and I. Wouters. Characterization of powder flowability using measurement of angle of repose. *China Particuology*, 4(3-4):104–107, 2006.
- [142] L. Verbelen, S. Dadbakhsh, M. Van Den Eynde, J-P. Kruth, B. Goderis, and P. Van Puyvelde. Characterization of polyamide powders for determination of laser sintering processability. *European Polymer Journal*, 75:163–174, 2016.
- [143] Mercury Scientific Inc. REVOLUTION Powder Analyzer, 2012.
- [144] Freeman Technology. About the FT4 Powder Rheometer, 2014.
- [145] I. F. Ituarte. Flowability characterization for SLS powders, 2017.
- [146] K. Wudy, S. Greiner, M. Zhao, and D. Drummer. Selective laser beam melting of polymers: In situ and offline measurements for process adapted thermal characterization. *Procedia CIRP*, 74:238–243, 2018.
- [147] D. Drummer, K. Wudy, and M. Drexler. Influence of energy input on degradation behavior of plastic components manufactured by selective laser melting. In *Physics Procedia*, volume 56, pages 176–183, 2014.
- [148] S. Ziegelmeier, F. Wöllecke, C. Tuck, R. Goodridge, and R. Hague. Aging behavior of thermoplastic elastomers in the laser sintering process. *Journal of Materials Research*, 29(17):1841–1851, 2014.
- [149] O. R. Ghita, E. James, R. Trimble, and K. E. Evans. Physico-chemical behaviour of Poly (Ether Ketone) (PEK) in High Temperature Laser Sintering (HT-LS). *Journal of Materials Processing Technology*, 214(4):969–978, 2014.
- [150] K. Wudy, D. Drummer, F. Kühnlein, and M. Drexler. Influence of degradation behavior of polyamide 12 powders in laser sintering process on produced parts. *AIP Conference Proceedings*, 1593(2014):691–695, 2014.
- [151] M. Van den Eynde, L. Verbelen, and P. Van Puyvelde. Assessing polymer powder flow for the application of laser sintering. *Powder Technology*, 286:151–155, 2015.

- [152] S. Berretta, K. E. Evans, and O. R. Ghita. Predicting processing parameters in high temperature laser sintering (HT-LS) from powder properties. *Materials and Design*, 105:301–314, 2016.
- [153] M. C. Coelho and N. Harnby. Moisture bonding in powders. *Powder Technology*, 20(2):201–205, 1978.
- [154] J. H. Koo, S. Lao, W. Ho, K. Ngyuen, J. Cheng, L. Pilato, G. Wissler, and M. Ervin. Polyamide nanocomposites for selective laser sintering. *Solid Freeform Fabrication Symposium Proceedings*, pages 392–409, 2006.
- [155] T. Niino and K. Sato. Effect of Powder Compaction in Plastic Laser Sintering Fabrication. In *Solid Freeform Fabrication Symposium*, pages 193–205, 2009.
- [156] Mercury Scientific Inc. PACKING Analysis with the REVOLUTION, 2012.
- [157] A. Amado, M. Schmid, and K. Wegener. Flowability of SLS Powders at Elevated Temperature. In *Solid Freeform Fabrication Proceedings*, pages 1–7, 2014.
- [158] M. Vasquez. Analysis and Development of New Materials for Polymer Laser Sintering. *Loughborough University*, 1:224, 2012.
- [159] A. Budding and T. H.J. Vaneker. New strategies for powder compaction in powder-based rapid prototyping techniques. *Procedia CIRP*, 6:527–532, 2013.
- [160] A. Castellanos. *The relationship between attractive interparticle forces and bulk behaviour in dry and uncharged fine powders*, volume 54. 2005.
- [161] P. K. Venuvinod and W. Ma. *Rapid Prototyping: Laser-based and Other Technologies*. Springer Science + Business Media, LLC, 2004.
- [162] N. P. Karapatis, G. Egger, P. E. Gyax, and R. Glardon. Optimization of powder layer density in selective laser sintering. *10th Solid Freeform Fabrication Symposium (SFF)*, pages 255–263, 1999.
- [163] S. C. Thakur, H. Ahmadian, J. Sun, and J. Y. Ooi. An experimental and numerical study of packing, compression, and caking behaviour of detergent powders. *Particuology*, 12(1):2–12, 2014.
- [164] M. Sigl, S. Lutzmann, and M. F. Zaeh. Transient physical effects in electron beam sintering. *17th Solid Freeform Fabrication Symposium, SFF 2006*, pages 464–477, 2006.
- [165] S. Greiner, K. Wudy, L. Lanzl, and D. Drummer. Selective laser sintering of polymer blends: Bulk properties and process behavior. *Polymer Testing*, 64(July):136–144, 2017.
- [166] L. Zhang, X. Bi, and J. R. Grace. Measurements of electrostatic charging of powder mixtures in a free-fall test device. *Procedia Engineering*, 102:295–304, 2015.
- [167] S. Yuan, F. Shen, C. K. Chua, and K. Zhou. Polymeric composites for powder-based additive manufacturing: Materials and applications. *Progress in Polymer Science*, 91:141–168, 2019.
- [168] J. P. K. Seville, C. D. Willett, and P. C. Knight. Interparticle forces in fluidisation: A review. *Powder Technology*, 113(3):261–268, 2000.
- [169] M. C. Coelho and N. Harnby. The effect of humidity on the form of water retention in a powder. *Powder Technology*, 20(2):197–200, 1978.

- [170] B. Armstrong and J. Clayton. Quantifying The Impact Of Humidity On Powder Properties, 2019.
- [171] H. Batzer and U. T. Kreibich. Influence of Water on Thermal Transitions in Natural Polymers and Synthetic Polyamides. *Polymer Bulletin*, 5:585–590, 1981.
- [172] R. D. Goodridge, R. J. M. Hague, and C. J. Tuck. Effect of long-term ageing on the tensile properties of a polyamide 12 laser sintering material. *Polymer Testing*, 29(4):483–493, 2010.
- [173] M. Vasquez, B. Haworth, and N. Hopkinson. Methods for Quantifying the Stable Sintering Region in Laser Sintered Polyamide-12. *Polymer Engineering and Science*, 53(6):1230 – 1240, 2013.
- [174] P. Chen, M. Tang, W. Zhu, L. Yang, S. Wen, C. Yan, Z. Ji, H. Nan, and Y. Shi. Systematical mechanism of Polyamide-12 aging and its micro-structural evolution during laser sintering. *Polymer Testing*, 67(March):370–379, 2018.
- [175] B. Haworth, N. Hopkinson, D. Hitt, and M. Vasquez. Influence of molecular weight and viscosity on particle coalescence for laser sintering of Nylon-12. *PPS-27 Polymer Processing Society*, pages 7.1–7.7, 2011.
- [176] S. Dadbakhsh, L. Verbelen, O. Verkinderen, D. Strobbe, P. Van Puyvelde, and J.-P. Kruth. Effect of PA12 powder reuse on coalescence behaviour and microstructure of SLS parts. *European Polymer Journal*, 92(May):250–262, 2017.
- [177] C. Yan, L. Hao, L. Xu, and Y. Shi. Preparation, characterisation and processing of carbon fibre/polyamide-12 composites for selective laser sintering. *Composites Science and Technology*, 71(16):1834–1841, 2011.
- [178] D. Drummer, S. Greiner, M. Zhao, and K. Wudy. A novel approach for understanding laser sintering of polymers. *Additive Manufacturing*, 27(November 2018):379–388, 2019.
- [179] H.-Y. Mi, M. R. Salick, X. Jing, B. R. Jacques, W. C. Crone, X.-F. Peng, and L.-S. Turng. Characterization of thermoplastic polyurethane/polylactic acid (TPU/PLA) tissue engineering scaffolds fabricated by microcellular injection molding. *Materials Science and Engineering: C*, 33(8):4767–4776, 2013.
- [180] Mettler Toledo. Thermogravimetry for Routine and Research, 2012.
- [181] J. Schmidt, M. Sachs, C. Blümel, B. Winzer, F. Toni, K. E. Wirth, and W. Peukert. A novel process route for the production of spherical LBM polymer powders with small size and good flowability. *Powder Technology*, 261:78–86, 2014.
- [182] M. J. Kirchhof, H.-J. Schmid, and W. Peukert. Three-dimensional simulation of viscous-flow agglomerate sintering. *Physical Review*, 80:1–9, 2009.
- [183] J. Frenkel. Viscous Flow of Crystalline Bodies Under the Action of Surface Tension. *Journal of Physics*, 9(5):385–391, 1945.
- [184] J. K. Mackenzie and R. Shuttleworth. A Phenomenological Theory of Sintering. *Proceedings of the Physical Society*, 62(B):833–852, 1949.
- [185] J. P. Kruth, G. Levy, F. Klocke, and T. H C Childs. Consolidation phenomena in laser and powder-bed based layered manufacturing. *CIRP Annals - Manufacturing Technology*, 56(2):730–759, 2007.
- [186] S. Mazur. Chapter 8: Coalescence of Polymer Particles. In *Polymer Powder Technology*, chapter 8, pages 158–216. Wiley, 1995.

- [187] C. T. Bellehumeur. *Polymer Sintering and its Role in Rotational Molding*. PhD thesis, McMaster university, 1997.
- [188] M. Narkis. Sintering behavior of poly(methyl methacrylate) particles. *Polymer Engineering & Science Science*, 19(13):889–892, 1979.
- [189] B. Haworth, N. Hopkinson, D. J. Hitt, and Z. Xiaotao. Shear viscosity measurements on Polyamide-12 polymers for laser sintering. *Rapid Prototyping Journal*, 19(1):28–36, 2013.
- [190] D. Defauchy. *Simulation du procédé de fabrication directe de pièces thermoplastiques par fusion laser de poudre*. PhD thesis, 2013.
- [191] S. Dupin. *Etude fondamentale de la transformation du polyamide 12 par frittage laser : mécanismes physico-chimiques et relations microstructures / propriétés Résumé*. PhD thesis, 2012.
- [192] M. Vasquez, N. Hopkinson, and B. Haworth. Laser sintering processes: Practical verification of particle coalescence for polyamides and thermoplastic elastomers. *Annual Technical Conference - ANTEC, Conference Proceedings*, 3:2458–2462, 2011.
- [193] A. J. Shaler. Seminar on the Kinetics of Sintering. *Metals Trans.*, 185(11):806, 1949.
- [194] O. Pokluda, C. T. Bellehumeur, and J. Machopoulos. Modification of Frenkel' s Model for Sintering. *AIChE Journal*, 43(12):3253–3256, 1997.
- [195] W. D. Kingery and M. Berg. Study of the Initial Stages of Sintering Solids by Viscous Flow, Evaporation-Condensation, and Self-Diffusion. *Journal of Applied Physics*, 26:1205, 1955.
- [196] H. E. Exner and G. Petzow. Shrinkage and Rearrangement during Sintering of Glass Spheres. In *Sintering and Catalysis*, pages 279–293. Springer, New York, 1975.
- [197] C. T. Bellehumeur, M. K. Bisaria, and J. Vlachopoulos. An Experimental Study and Model Assessment of Polymer Sintering. *Polymer Engineering & Science*, 36(17):2198–2207, 1996.
- [198] G. J. Cosgrove, J. A. S. Trozier, and L. L. Seigle. An approximate analytical model for the late-stage sintering of an array of rods by viscous flow. *Journal of Applied Physics*, 47(4):1258–1264, 1976.
- [199] R. W. Hopper. Coalescence of Two Equal Cylinders: Exact Results for Creeping Viscous Plane Flow Driven by Capillarity. *Journal of the American Ceramic Society*, 67(12):262–264, 1984.
- [200] R. W. Hopper. Plane Stokes flow driven by capillarity on a free surface. *Journal of Fluid Mechanics*, 230:355–364, 1991.
- [201] F. Wakai, K. Katsura, S. Kanchika, Y. Shinoda, T. Akatsu, and K. Shinagawa. Sintering force behind the viscous sintering of two particles. *Acta Materialia*, 109:292–299, 2016.
- [202] H. Zhou and J. J. Derby. Three-Dimensional Finite-Element Analysis of Viscous Sintering. *Journal of the American Ceramic Society*, 81(3):533–540, 2005.
- [203] G. A. L. van de Vorst. *Modelling and numerical simulation of viscous sintering*. PhD thesis, Eindhoven University, 1994.

- [204] J. W. Ross, W. A. Miller, and G. C. Weatherly. Dynamic computer simulation of viscous flow sintering kinetics. *Journal of Applied Physics*, 52(6):3884–3888, 1981.
- [205] G. C. Kuczynski, B. Neuville, and H. P. Toner. Study of sintering of poly(methyl methacrylate). *Journal of Applied Polymer Science*, 14(8):2069–2077, aug 1970.
- [206] S. Mazur and D. J. Plazek. Viscoelastic effects in the coalescence of polymer particles. *Progress in Organic Coatings*, 24(1-4):225–236, 1994.
- [207] A. Jagota and P. R. Dawson. Micromechanical modeling of powder compacts-I. Unit problems for sintering and traction induced deformation. *Acta Metallurgica*, 36(9):2551–2561, 1988.
- [208] A. Jagota, C. Argento, and S. Mazur. Growth of adhesive contacts for Maxwell viscoelastic spheres. *Journal of Applied Physics*, 83(1):250–259, 1998.
- [209] A. Jagota and P. Dawson. Simulation of the Viscous Sintering of Coated Particles. *Journal of the American Ceramic Society*, 73(1):173–177, 1990.
- [210] A. Jagota and P. R. Dawson. Micromechanical modeling of powder compacts-II. Truss formulation of discrete packings. *Acta Metallurgica*, 36(9):2563–2573, 1988.
- [211] J. I. Martínez-Herrera and J. J. Derby. Analysis of capillary-driven viscous flows during the sintering of ceramic powders. *AIChE Journal*, 40(11):1794–1803, 1994.
- [212] J. I. Martínez-Herrera and J. J. Derby. Viscous Sintering of Spherical Particles via Finite Element Analysis, 1995.
- [213] M. Kandis and T. L. Bergman. Observation, Prediction, and Correlation of Geometric Shape Evolution Induced by Non-Isothermal Sintering of Polymer Powder. *Journal of Heat Transfer*, 119(4):824–831, 1997.
- [214] R. M. Tarafdar and T. L. Bergman. Detailed Numerical and Experimental Investigation of Non-Isothermal Sintering of Amorphous Polymer Material. *Journal of Heat Transfer*, 124(3):553, 2002.
- [215] C. T. Bellehumeur, M. Kontopoulou, and J. Vlachopoulos. The role of viscoelasticity in polymer sintering. *Rheologica Acta*, 37(3):270–278, 1998.
- [216] M. J. Kirchhof, H. Förster, H. J. Schmid, and W. Peukert. Sintering kinetics and mechanism of vitreous nanoparticles. *Journal of Aerosol Science*, 45:26–39, 2012.
- [217] N. Rosenzweig and M. Narkis. Coalescence phenomenology of spherical polymer particles by sintering. *Polymer (United Kingdom)*, 21(9):988–989, 1980.
- [218] N. Rosenzweig and M. Narkis. Observation and analysis technique for studying sintering of polymeric particles. *Journal of Applied Polymer Science*, 26(8):2787–2789, 1981.
- [219] P. R. Hornsby and A. S. Maxwell. Mechanism of sintering between polypropylene beads. *Journal of Materials Science*, 27(9):2525–2533, 1992.
- [220] R. W. Truss, K. S. Han, J. F. Wallace, and P. H. Geil. Cold compaction molding and sintering of ultra high molecular weight polyethylene. *Polymer Engineering & Science Science*, 20(11):747–755, 1980.
- [221] A. Siegmann, I. Raiter, M. Narkis, and P. Eyerer. Effect of powder particle morphology on the sintering behaviour of polymers. *Journal of Materials Science*, 21(4):1180–1186, 1986.

- [222] S. Aid, A. Eddhahak, Z. Ortega, D. Froelich, and A. Tcharkhtchi. Predictive coalescence modeling of particles from different polymers: application to PVDF and PMMA pair. *Journal of Materials Science*, 52(19):11725–11736, 2017.
- [223] M. Van den Eynde, D. Strobbe, O. Verkinderen, L. Verbelen, B. Goderis, J.-P. Kruth, and P. Van Puyvelde. Effect of thermal treatments on the laser sinterability of cryogenically milled polybutene-1. *Materials & Design*, 153:15–23, 2018.
- [224] A. Barnetson and P. R. Hornsby. Observations on the sintering of ultra-high molecular weight polyethylene (UHMWPE) powders. *Journal of Materials Science Letters*, 14(2):80–84, 1995.
- [225] P. Hejmady, L. C. A. Van Breemen, P. D. Anderson, and R. Cardinaels. Laser sintering of polymer particle pairs studied by in situ visualization. *Soft Matter*, 15(6):1373–1387, 2019.
- [226] ASTM International. Standard Terminology for Additive Manufacturing Technologies, 2015.
- [227] I. Gibson, D. W. Rosen, and B. Stucker. *Additive Manufacturing Technologies: 3D Printing, Rapid Prototyping and Direct Digital Manufacturing*. Springer, New York, second edition, 2010.
- [228] R. Castells. DMLS vs SLM 3D Printing for Metal Manufacturing, 2016.
- [229] A. Lindstrom. Selective Laser Sintering, Birth of an Industry, 2012.
- [230] D. D. Gu, W. Meiners, K. Wissenbach, and R. Poprawe. Laser additive manufacturing of metallic components: materials, processes and mechanisms. *International Materials Reviews*, 57(3):133–164, 2012.
- [231] D. Drummer, K. Wudy, F. Kühnlein, and M. Drexler. Polymer Blends for Selective Laser Sintering: Material and Process Requirements. *Physics Procedia*, 39:509–517, 2012.
- [232] A. Franco, M. Lanzetta, and L. Romoli. Experimental analysis of selective laser sintering of polyamide powders: An energy perspective. *Journal of Cleaner Production*, 18(16-17):1722–1730, 2010.
- [233] F. Ma, H. Zhang, K. K. B. Hon, and Q. Gong. An optimization approach of selective laser sintering considering energy consumption and material cost. *Journal of Cleaner Production*, 199:529–537, 2018.
- [234] EOS. EOSINT P 800, 2003.
- [235] EOS. EOSINT P 800, 2011.
- [236] M. Schmidt, M. Merklein, D. Bourell, D. Dimitrov, T. Hausotte, K. Wegener, L. Overmeyer, F. Vollertsen, and G. N. Levy. Laser based additive manufacturing in industry and academia. *CIRP Annals*, 66(2):561–583, 2017.
- [237] S. H. Huang, P. Liu, A. Mokasdar, and L. Hou. Additive manufacturing and its societal impact: A literature review. *International Journal of Advanced Manufacturing Technology*, 67:1191–1203, 2013.
- [238] I. Jasiuk, D. W. Abueidda, C. Kozuch, S. Pang, F. Y. Su, and J. McKittrick. An Overview on Additive Manufacturing of Polymers. *Jom*, 70(3):275–283, 2018.
- [239] J. Meyer. Polymer Additive Layer Manufacturing, 2012.

- [240] S. Berretta. *Poly Ether Ether Ketone (PEEK) polymers for High Temperature Laser Sintering (HT-LS)*. PhD thesis, University of Exeter, 2015.
- [241] EOS e-manufacturing solutions. Industrial 3D printing of high-tech aerospace components.
- [242] S. Haeri. Optimisation of blade type spreaders for powder bed preparation in Additive Manufacturing using DEM simulations. *Powder Technology*, 321:94–104, 2017.
- [243] E. D. Dickens, B. L. Lee, G. A. Taylor, A. J. Magistro, H. Ng, K. P. McAlea, and P. F. Forderhase. Sinterable semi-crystalline powder and near-fully dense article formed therewith, 2000.
- [244] D. Rietzel, M. Drexler, F. Kühnlein, and D. Drummer. Influence of temperature fields on the processing of polymer powders by means of laser and mask sintering technology. *22nd Annual International Solid Freeform Fabrication Symposium - An Additive Manufacturing Conference, SFF 2011*, pages 252–262, 2011.
- [245] Y. C. Keshavamurthy, N. R. Arjun, M. Ganiger, and M. Idris. Studies on optimization of Selective Laser Sintering process to manufacture Fuel tanks. page 4.
- [246] T. Laumer, T. Stichel, K. Nagulin, and M. Schmidt. Optical analysis of polymer powder materials for Selective Laser Sintering. *Polymer Testing*, 56:207–213, 2016.
- [247] Y. Wang, D. Rouholamin, R. Davies, and O. R. Ghita. Powder characteristics, microstructure and properties of graphite platelet reinforced Poly Ether Ether Ketone composites in High Temperature Laser Sintering (HT-LS). *Materials and Design*, 88:1310–1320, 2015.
- [248] T. L. Starr, T. J. Gornet, and J. S. Usher. The effect of process conditions on mechanical properties of laser-sintered nylon. *Rapid Prototyping Journal*, 17(6):418–423, 2011.
- [249] S. Negi and R. K. Sharma. Study on shrinkage behaviour of laser sintered PA 3200GF specimens using RSM and ANN. *Rapid Prototyping Journal*, 22(4):645–659, 2016.
- [250] M. Drexler, M. Lexow, and D. Drummer. Selective Laser Melting of Polymer Powder – Part mechanics as function of exposure speed. *Physics Procedia*, 78(August):328–336, 2015.
- [251] E. C. Hofland, I. Baran, and D. A. Wismeijer. Correlation of Process Parameters with Mechanical Properties of Laser Sintered PA12 Parts. *Advances in Materials Science and Engineering*, 2017, 2017.
- [252] M. Schmidt, D. Pohle, and T. Rechtenwald. Selective laser sintering of PEEK. *CIRP Annals - Manufacturing Technology*, 56(1):205–208, 2007.
- [253] J. Sreedharan and A. K. Jeevanantham. Analysis of Shrinkages in ABS Injection Molding Parts for Automobile Applications. *Materials Today: Proceedings*, 5(5):12744–12749, 2018.
- [254] H. Hassan, N. Regnier, C. Pujos, E. Arquis, and G. Defaye. Modeling the effect of cooling system on the shrinkage and temperature of the polymer by injection molding. *Applied Thermal Engineering*, 30(13):1547–1557, 2010.
- [255] N. Raghunath and P. M. Pandey. Improving accuracy through shrinkage modelling by using Taguchi method in selective laser sintering. *International Journal of Machine Tools and Manufacture*, 47(6):985–995, 2007.

- [256] D. Drummer, M. Drexler, and K. Wudy. Density of laser molten polymer parts as function of powder coating process during additive manufacturing. *Procedia Engineering*, 102:1908–1917, 2015.
- [257] M. Schmidt, M. Merklein, D. Bourell, D. Dimitrov, T. Hausotte, K. Wegener, L. Overmeyer, F. Vollertsen, and G. N. Levy. CIRP Annals - Manufacturing Technology Laser based additive manufacturing in industry and academia. *CIRP Annals - Manufacturing Technology*, pages 1–23, 2017.
- [258] S. P. Soe, D. R. Eyers, and R. Setchi. Assessment of non-uniform shrinkage in the laser sintering of polymer materials. *International Journal of Additive Manufacturing Technology*, 68:111–125, 2013.
- [259] A. Mazzoli. Selective laser sintering in biomedical engineering. *Medical and Biological Engineering*, 51:245 – 256, 2012.
- [260] Y. Shi, Z. Li, H. Sun, S. Huang, and F. Zeng. Effect of the properties of the polymer materials on the quality of selective laser sintering parts, 2004.
- [261] SpecialChem. Shrinkage, 2019.
- [262] ASTM. ASTM D955 - Standard Test Method of Measuring Shrinkage from Mold Dimensions of Thermoplastics, 2014.
- [263] EOS E-Manufacturing Solutions. Parameter sheet, 2015.
- [264] A. Townsend, N. Senin, L. Blunt, R. K. Leach, and J. S. Taylor. Surface texture metrology for metal additive manufacturing: a review. *Precision Engineering*, 46:34–47, 2016.
- [265] T. Grimm, G. Wiora, and G. Witt. Characterization of typical surface effects in additive manufacturing with confocal microscopy. *Surface Topography: Metrology and Properties*, 3(1), 2015.
- [266] G. Strano, L. Hao, R. M. Everson, and K. E. Evans. Surface roughness analysis, modelling and prediction in selective laser melting. *Journal of Materials Processing Technology*, 213(4):589–597, 2013.
- [267] D. K. Leigh. A comparison of polyamide 11 mechanical properties between laser sintering and traditional molding. *23rd Annual International Solid Freeform Fabrication Symposium - An Additive Manufacturing Conference, SFF 2012*, pages 574–605, 2012.
- [268] T. Stichel, T. Frick, T. Laumer, F. Tenner, T. Hausotte, M. Merklein, and M. Schmidt. A Round Robin study for Selective Laser Sintering of polyamide 12: Microstructural origin of the mechanical properties. *Optics and Laser Technology*, 89(October 2016):31–40, 2017.
- [269] B. Van Hooreweder, D. Moens, R. Boonen, J.-P. Kruth, and P. Sas. On the difference in material structure and fatigue properties of nylon specimens produced by injection molding and selective laser sintering. *Polymer Testing*, 32(5):972–981, 2013.
- [270] H. Zarringhalam, N. Hopkinson, N. F. Kamperman, and J. J. de Vlieger. Effects of processing on microstructure and properties of SLS Nylon 12. *Materials Science and Engineering A*, 435-436:172–180, 2006.
- [271] U. Ajoku, N. Hopkinson, and M. Caine. Experimental measurement and finite element modelling of the compressive properties of laser sintered Nylon-12. *Materials Science and Engineering A*, 428(1-2):211–216, 2006.

- [272] W. Zhu, C. Yan, Y. Shi, S. Wen, J. Liu, and Y. Shi. Investigation into mechanical and microstructural properties of polypropylene manufactured by selective laser sintering in comparison with injection molding counterparts. *Materials and Design*, 82:37–45, 2015.
- [273] S. R. Athreya, K. Kalaitzidou, and S. Das. Mechanical and microstructural properties of Nylon-12/carbon black composites: Selective laser sintering versus melt compounding and injection molding. *Composites Science and Technology*, 71(4):506–510, 2011.
- [274] A. Wegner and G. Witt. Adjustment of isotropic part properties in laser sintering based on adapted double laser exposure strategies. *Optics and Laser Technology*, 109(June 2018):381–388, 2019.
- [275] M. Garcia-Leiner, M. T. F. Reitman, M. J. El-Hibri, and R. K. Roeder. Structure-Property Relationships in Commercial PEEK Resins. *Polymer Engineering and Science*, pages 955–964, 2017.
- [276] H. Zarringhalam. *Investigation into Crystallinity and Degree of Particle Melt in Selective Laser Sintering*. PhD thesis, University of Loughborough, 2007.
- [277] T. J. Hoskins, K. D. Dearn, and S. N. Kukureka. Mechanical performance of PEEK produced by additive manufacturing. *Polymer Testing*, 70(August):511–519, 2018.
- [278] Victrex High Performance Polymers. Victrex ® PEEK 450G, 2014.
- [279] EOS GmbH. PA 2200 Performance 1.0, 2010.
- [280] EOS E-Manufacturing Solutions. EOS PEEK HP3, the high-grade performer, 2008.
- [281] G. Nino and T. Blumenthal. 3D Printed Thermal Protection System on Composite Structures. *SAMPE Journal*, 50(7 - 17), 2014.
- [282] J. Coykendall, M. Cotteleer, L. Holdowsky, and M. Mahto. 3D opportunity for aerospace and defense, 2014.
- [283] N. Guo and M. C. Leu. Additive manufacturing: Technology, applications and research needs, 2013.
- [284] Automated Dynamics Performance in Composites. Automated Fiber Placement, 2017.
- [285] A. Lystrup and T. L. Andersen. Autoclave consolidation of fibre composites with a high temperature thermoplastic matrix. *Journal of Materials Processing Technology*, 77(1):80–85, 1998.
- [286] S. M. Kurtz and J. N. Devine. PEEK biomaterials in trauma, orthopedic, and spinal implants. *Biomaterials*, 28(32):4845–4869, 2007.
- [287] C. Weller, R. Kleer, and F. T. Piller. Economic Implications of 3D printing: Market structure Models in light of additive manufacturing Revisited. *International Journal of Production Economics*, 164:43–56, mar 2015.
- [288] W. Gao, Y. Zhang, D. Ramanujan, K. Ramani, Y. Chen, C. B. Williams, C. C. L. Wang, Y. C. Shin, S. Zhang, and P. D. Zavattieri. The status, challenges, and future of additive manufacturing in engineering. *Computer-Aided Design*, 69:65–89, 2015.
- [289] B. Wendel, D. Rietzel, F. Kühnlein, R. Feulner, G. Hülder, and E. Schmachtenberg. Additive processing of polymers. *Macromolecular Materials and Engineering*, 293(10):799–809, 2008.

- [290] M. Schmid, A. Amado, and K. Wegener. Materials perspective of polymers for additive manufacturing with selective laser sintering. *Journal of Materials Research*, 29(17):1824–1832, 2014.
- [291] R. N. Mathur. Design Considerations for Successfully Using Long Fiber Thermoplastic Composites as Substitutes for Metals.
- [292] P. Patel, T. R. Hull, R. E. Lyon, S. I. Stoliarov, R. N. Walters, S. Crowley, and N. Safronava. Investigation of the thermal decomposition and flammability of PEEK and its carbon and glass-fibre composites. *Polymer Degradation and Stability*, 96(1):12–22, 2011.
- [293] I. V. Panayotov, V. Orti, F. Cuisinier, and J. Yachouh. Polyetheretherketone (PEEK) for medical applications. *Journal of Materials Science: Materials in Medicine*, 27(7):117–127, 2016.
- [294] Arkema. ORGASOL Polyamide Powders - General Bulletin, 2000.
- [295] Arkema. Orgasol: Ultra-fine powders, 2015.
- [296] Victrex High Performance Polymers. Victrex HT G22, 2014.
- [297] Particle Technology Labs. LASER DIFFRACTION, 2019.
- [298] Mettler Toledo. Differential Scanning Calorimetry for all Requirements, 2011.
- [299] L. Q. Cortés, N. Caussé, E. Dantras, A. Lonjon, and C. Lacabanne. Morphology and dynamical mechanical properties of poly ether ketone ketone (PEKK) with meta phenyl links. *Journal of Applied Polymer Science*, 133(19), 2016.
- [300] S. Gogolewski, K. Czerniawska, and M. Gasiorek. Effect of annealing on thermal properties and crystalline structure of polyamides. Nylon 12 (polylauro lactam). 1136:1130–1136, 1980.
- [301] R. Kohli. Methods for Monitoring and Measuring Cleanliness of Surfaces. In *Developments in Surface Contamination and Cleaning: Detection, Characterization, and Analysis of Contaminants*, chapter 3, pages 107–178. William Andrew, 2012.
- [302] C. Y. Tang and Z. Yang. Transmission Electron Microscopy (TEM). *Membrane Characterization*, pages 145–159, jan 2017.
- [303] IBM. IBM SPSS software.
- [304] B. Chang, X. Wang, Z. Long, Z. Li, J. Gu, S. Ruan, and C. Shen. Constitutive modeling for the accurate characterization of the tension behavior of PEEK under small strain. *Polymer Testing*, 69(2):514–521, 2018.
- [305] R. Castro and K. Van Benthem. *Sintering: Mechanisms of Conventional Nanodensification and Field Assisted Processes*. Springer, New York, 2012.
- [306] H. J. Zimmermann and K. Könnecke. Crystallization of poly(aryl ether ketones): 3. The crystal structure of poly(ether ether ketone) (PEEK). *Polymer*, 32(17):3162–3169, 1991.
- [307] E. Atzeni and A. Salmi. Study on unsupported overhangs of AlSi10Mg parts processed by Direct Metal Laser Sintering (DMLS). *Journal of Manufacturing Processes*, 20(February 2014):500–506, 2015.
- [308] G. Flodberg, H. Pettersson, and L. Yang. Pore analysis and mechanical performance of selective laser sintered objects. *Additive Manufacturing*, 24(October):307–315, 2018.

- [309] J. Damon, S. Dietrich, F. Vollert, J. Gibmeier, and V. Schulze. Process dependent porosity and the influence of shot peening on porosity morphology regarding selective laser melted AlSi10Mg parts. *Additive Manufacturing*, 20(December 2017):77–89, 2018.
- [310] S. P. Soe, N. Martindale, C. Constantinou, and M. Robinson. Mechanical characterisation of Duraform Flex for FEA hyperelastic material modelling. *Polymer Testing*, 34:103–112, 2014.
- [311] EOS e-Manufacturing Solutions. Technical Description FORMIGA P 100, 2007.
- [312] K. Senthilkumaran, P. M. Pandey, and P. V. M. Rao. Shrinkage compensation along single direction dixel space for improving accuracy in Selective Laser Sintering. In *4th IEEE Conference on Automation Science and Engineering*, pages 827–832, 2008.
- [313] H. J. Yang, P. J. Hwang, and S. H. Lee. A study on shrinkage compensation of the SLS process by using the Taguchi method. *International Journal of Machine Tools and Manufacture*, 42(11):1203–1212, 2002.
- [314] L. Verbelen, J. Van Humbeeck, and P. Van Puyvelde. Development of a method for pressure-free volumetric dilatometry of polymer melts and solids. *Polymer Testing*, 69(March):219–224, 2018.
- [315] M. Schmid, R. Kleijnen, M. Vetterli, and K. Wegener. Influence of the Origin of Polyamide 12 Powder on the Laser Sintering Process and Laser Sintered Parts. *Applied Sc*, 7:1–15, 2017.
- [316] L. Benedetti, B. Brulé, N. Decreamer, K. E. Evans, and O. Ghita. Shrinkage behaviour of semi-crystalline polymers in laser sintering: PEKK and PA12. *Materials & Design*, 181:107906, 2019.
- [317] L. Benedetti, B. Brulé, N. Decraemer, R. Davies, and K. Evans. Mechanical Performance of Laser Sintered Poly (Ether Ketone Ketone). *30th Annual International Solid Freeform Fabrication Symposium*, 44(0):1–14, 2019.
- [318] P. G. Kossakowski. Influence of initial porosity on strength properties of S235JR steel at low stress triaxiality. *Archives of Civil Engineering*, 58(3):293–308, 2012.
- [319] H. G. H. Van Melick, L. E. Govaert, and H. E. H. Meijer. Prediction of brittle-to-ductile transitions in polystyrene. *Polymer*, 44(2):457–465, 2002.
- [320] Polymer properties database. BRITTLE-DUCTILE BEHAVIOR OF AMORPHOUS POLYMERS, 2015.
- [321] F. Paolucci, M. J. H. van Mook, L. E. Govaert, and G. W. M. Peters. Influence of post-condensation on the crystallization kinetics of PA12: From virgin to reused powder. *Polymer*, 175(March):161–170, 2019.
- [322] F. Paolucci, D. Baeten, P. C. Roozmond, B. Goderis, and G. W. M. Peters. Quantification of isothermal crystallization of polyamide 12: Modelling of crystallization kinetics and phase composition. *Polymer*, 155(June):187–198, 2018.
- [323] F. Amado, K. Wegener, M. Schmid, and G. Levy. Characterization and modeling of non-isothermal crystallization of Polyamide 12 and co-Polypropylene during the SLS process. *5th International Polymers and Moulds Innovations Conference*, pages 207–216, 2012.

- [324] J. Choren, V. Gervasi, T. Herman, S. Kamara, and J. Mitchell. SLS powder life study. In *Solid Freeform Fabrication Symposium*, number January, pages 39–45, 2001.
- [325] S. O. Akande, K. W. Dalgarno, J. Munguia, and J. Pallari. Assessment of tests for use in process and quality control systems for selective laser sintering of polyamide powders. *Journal of Materials Processing Technology*, 229:549–561, 2016.
- [326] W. Zhu, C. Yan, Y. Shi, S. Wen, C. Han, C. Cai, J. Liu, Y. Shi, R. I. Campbell, and I. Gibson. Study on the selective laser sintering of a low-isotacticity polypropylene powder. *Rapid Prototyping Journal*, 22(4):621–629, 2016.
- [327] B. D. Caddock and K. E. Evans. Microporous materials with negative Poisson's ratios. I. Microstructure and mechanical properties. *Journal of Physics D: Applied Physics*, 22(12):1877–1882, 1989.
- [328] J. Clayton, D. Millington-Smith, and B. Armstrong. The Application of Powder Rheology in Additive Manufacturing. *Jom*, 67(3):544–548, 2015.
- [329] P. Chen, H. Wu, W. Zhu, L. Yang, Z. Li, C. Yan, S. Wen, and Y. Shi. Investigation into the processability, recyclability and crystalline structure of selective laser sintered Polyamide 6 in comparison with Polyamide 12. *Polymer Testing*, 69(April):366–374, 2018.
- [330] K. Wudy and D. Drummer. Aging effects of polyamide 12 in selective laser sintering: Molecular weight distribution and thermal properties. *Additive Manufacturing*, 25(September 2018):1–9, 2019.
- [331] D. Drummer, K. Wudy, and M. Drexler. Modelling of the aging behavior of polyamide 12 powder during laser melting process. In *AIP Conference Proceedings*, volume 1664, pages 1–5, 2015.
- [332] R. W. Hopper. Coalescence of Two Viscous Cylinders. 1993.
- [333] W. D. Kingery. Densification during Sintering in the Presence of a Liquid Phase. I. Theory. *Journal of Applied Physics*, 30(1959):301–306, 1959.
- [334] K. L. Johnson, K. Kendall, and A. D. Roberts. Surface Energy and the Contact of Elastic Solids. In *The Royal Society of London*, volume 324, pages 301–313. The Royal Society Publishing, 1971.
- [335] R. W. Hopper. Stokes flow of a cylinder and half-space driven by capillarity. *Journal of Fluid Mechanics*, 243:171–181, 1992.
- [336] J. Eggers, J. R. Lister, and H. A. Stone. Coalescence of Liquid Drops. *Journal of Fluid*, 401:293–310, 1999.
- [337] R. S. Garabedian and J. J. Helble. A model for the viscous coalescence of amorphous particles. *Journal of Colloid and Interface Science*, 234(2):248–260, 2001.
- [338] E. Scribner, D. Baird, and P. Wapperom. The role of transient rheology in polymeric sintering. *Rheologica Acta*, 45(6):825–839, 2006.
- [339] H. Djohari and J. J. Derby. Transport mechanisms and densification during sintering: II. Grain boundaries. *Chemical Engineering Science*, 64(17):3810–3816, 2009.
- [340] H. Wang, X. Zhu, Q. Liao, and P. C. Sui. Numerical simulation on coalescence between a pair of drops on homogeneous horizontal surface with volume-of-fluid method. *Journal of Superconductivity and Novel Magnetism*, 23(6):1137–1140, 2010.

- [341] M. L. Eggersdorfer, D. Kadau, H. J. Herrmann, and S. E. Pratsinis. Multiparticle sintering dynamics: From fractal-like aggregates to compact structures. *Langmuir*, 27(10):6358–6367, 2011.
- [342] F. Varnik, A. Rios, M. Gross, and I. Steinbach. Simulation of viscous sintering using the lattice Boltzmann method. *Modelling and Simulation in Materials Science and Engineering*, 21(2):0–17, 2013.
- [343] M. Gross, I. Steinbach, D. Raabe, and F. Varnik. Viscous coalescence of droplets: A lattice Boltzmann study. *Physics of Fluids*, 25(5), 2013.
- [344] K. Katsura, Y. Shinoda, T. Akatsu, and F. Wakai. Sintering force behind shape evolution by viscous flow. *Journal of the European Ceramic Society*, 35(3):1119–1122, 2015.

